Aspects of Spectroscopic and Polarimetric Instrumentation for Ground Based Optical Telescopes with related Observations

A thesis submitted in partial fulfillment of

the requirements for the degree of

Doctor of Philosophy

by

Vipin Kumar

(Roll No. 17330039)

Under the supervision of

Dr. Mudit K. Srivastava

Associate Professor

Astronomy and Astrophysics

Physical Research Laboratory, Ahmedabad, India.

DEPARTMENT OF PHYSICS

INDIAN INSTITUTE OF TECHNOLOGY GANDHINAGAR

2022

Dedicated to

My Family & Teachers

DECLARATION

I declare that this written submission represents my ideas in my own words and where others' ideas or words have been included, I have adequately cited and referenced the original sources. I also declare that I have adhered to all principles of academic honesty and integrity and have not misrepresented or fabricated or falsified any idea/data/fact/source in my submission. I understand that any violation of the above will be cause for disciplinary action by the Institute and can also evoke penal action from the sources which have thus not been properly cited or from whom proper permission has not been taken when needed.

Vipin Kumar
30/03/2023

(Name: Vipin Kumar)

(Roll No: 17330039)

Date: 30/03/2023

CERTIFICATE

It is certified that the work contained in the thesis titled **"Aspects of Spectroscopic and Polarimetric Instrumentation for Ground Based Optical Telescopes with related Observations"** by **Vipin Kumar** (Roll no: 17330039), has been carried out under my supervision and that this work has not been submitted elsewhere for degree.

I have read this dissertation and in my opinion, it is fully adequate in scope and quality as a dissertation for the degree of Doctor of Philosophy.

Dr. Mudit K. Srivastava

(Thesis Supervisor)

Associate Professor

Astronomy & Astrophysics Division

Physical Research Laboratory

Navarangpura, Ahmedabad, India

Date:

Acknowledgements

These five years at PRL have been an explosion of experiences that allowed me to grow up both professionally and personally and that I will never forget. The research included in this dissertation could not have been possible without many individuals' assistance, patience, and support. I would like to take this opportunity to thank several people who have supported me in getting to this point in my life.

I would like first and foremost to extend my deepest gratitude and a heartfelt thanks to my supervisor, Dr. Mudit K. Srivastava, for the patience, motivation, inspiration, encouragement, and continuous support during my Ph.D. study. I appreciate his vast knowledge and skills in many areas, which have added so much to my Ph.D. experience. I have learned a lot from you as a person & an academician, and will always try to build those qualities within me. I will always remember the instrument assembly time spend in the laboratory, Mt. Abu visits to take observations, and many more moments during these five years.

I would also like to thank my group members Ms. Ankita Patel, Mr. Bhavesh Kumar Mistry, former group member Mr. Mohan Lal, and especially Mr. Vaibhav Dixit for being there for any of my work-related doubts and discussion and helping me with full sincerity over these five years. I express my heartfelt gratitude to my DSC members - Prof. Santosh Vadawale, Prof. Shashikiran Ganesh, and Dr. K. Durga Prasad for reviewing my academic work and giving valuable suggestions which made it better and helps to improve my research skills.

I thank the current Chairman of the Astronomy & Astrophysics division, Prof. Abhijit Chakraborty for his support towards the requirements of my research work. I am grateful to the current PRL Director, Prof. Anil Bharadwaj for his timely support and guidance. I thank the current Dean, PRL, Prof. D. Pallamraju for his academic support. I also thank the current Academic committee chairman Dr. B. K. Sahoo & all the members of the Academic Committee for reviewing and providing us with ideas to improve the research work during annual reviews at PRL. I thank the Head Academic Services, PRL, Dr. Bhushit Vaishnav for managing our academic activities. I thank all the PRL staff members for the support and facilities I received from the institute during my stay at PRL. I express my heartfelt gratitude and thanks to the PRL doctors, Dr. Samir Dani and Dr. Sheetal Patel for their medical support at any time, even on holidays, and stand with us during the critical COVID period.

I am thankful to my course work project supervisor, Dr. Lokesh Kumar Dewangan, and Prof. Dibyendu Chakrabarty for making me understand in detail the work I completed as my project, and have been always present to clarify my doubts. I would also like to thank the Honorary Scientist, Prof. D. P. K. Banerjee, and Dr. Arvind Singh Rajpurohit for their support and suggestions during the collaborative work on some of the research projects. I would also like to thank all the course-work instructors - Dr. Vishal Joshi, Dr. Veeresh Singh, Dr. Aveek Sarkar, Dr. Sachindra Naik, and Dr. Manash Samal, who taught me the basics of Astronomy and Astrophysics. I also thank Kevi kumar, Rishikesh Sharma, Kapil Kumar, Prashanth Kumar, and Nirbhay Kumar Upadhyay for the discussion during some of the research projects on different aspects. I express my heartfelt thanks to the Mt. Abu observatory technical staff with special mention to Rajesh Sir, Mathur Sir, Jain Sir, Purohit Sir, Nafees Sir, Mr. Vivek Mishra, Mr. Dinesh Yadav, and TOTs, especially Mitesh Kavaiya & Vikram for their immense help during instrument commissioning and observations times.

Thanks to all my friends/batch-mates and colleagues that make this place special and with whom I shared not only scientific chats but also cultural exchanges and laughs: Sushant, Abhijit, Neeraj, Biswajit, Aravind, Shanwlee, Abhay, Ankit, Alka, Rituparna, Anshika, Sarika, Satyajeet, Kamlesh, Suraj, Ramanuj, Subith, Madhusudhan, Partha, Himanshu, Shivani, Sana, Atif, Milan, Amit, Sovan, Hrushikesh, Tanmay, Sudipta, Vishal, Deepak, Hirdesh. I would also like to thank my seniors: Archita di, Shivangi di, Subir bhaiya, Nisha di, Sandeep bhaiya, Parveen Bhai, Aditya bhaiya, and my loving juniors: Naval, Binal, Akanksha, Namita, Arup, Birendra, Vineet, Sanjay, Arijit, Ashish, Yash, Vikas, Anupam.

I would also like to thank the caring couples Abhijit & Ghazal and Subir bhaiya & Tuli di for their help and support over the years during different phases of the life. Of course, I cannot forget to thank some of my close schoolmates, Dharmraj, Satendra, Shyam, and Abhishek for their support at each stage and up-and-downs of my life. I would also like to thank some of my close motivators Mr. Mohit Kumar, Mr. Dharmendra Chaudhary (V2 Sir), Dr. Rishipal Singh, and Mrs. Bala Rani (Madam Ji) for their motivation to work hard, giving the direction and help to reach this point.

And finally, I express my sincere, loving, heartfelt thanks to my parents and my younger brother Manish (Joni) for all their support and encouragement over the years. I would also like to thank my mother-in-law, father-in-law, brother-in-law Neeraj and his wife Shivani for their support. Last but not least, I would also like to give special thanks to my loving and caring wife Rekha for her continuous support and understanding when undertaking my research and writing my projects/thesis. Your prayer for me was what sustained me this far.

(Vipin Kumar)

Abstract

Physical Research Laboratory (PRL) has been operating a 1.2m aperture diameter telescope and is recently in the process of setting up another 2.5m aperture diameter telescope at Gurushikhar, Mt. Abu, India. The 1.2m telescope is equipped with various back-end instruments capable of studying the visible and NIR regime of the spectrum. A variety of observational astrophysical research programs have been successfully explored with the existing telescope over the last couple of decades, such as star formation, novae & supernovae, active galactic nuclei, cometary sciences, exo-planets, etc. The upcoming 2.5m telescope would further enhance the prospects of these research domains as well as in new avenues like observations of transients (novae, supernovae, etc.), exoplanets, and their host stars, M dwarfs, etc.

The Faint Object Spectrograph and Camera (FOSC) type of instrument has been one of the most sought-after general-purpose, versatile instruments on any small or medium aperture telescope due to its ability to provide imaging and spectroscopy in a single focal reducer-based optical chain. As the requirements of a full-fledged FOSC instrument for the upcoming 2.5m telescope were being considered around late 2014, it was decided to develop a pathfinder instrument, named Mt. Abu Faint Object Spectrograph and Camera-Pathfinder (MFOSC-P) for the existing 1.2m telescope. MFOSC-P had been designed to provide low-resolution spectroscopy in three resolution modes (R$\sim$500, 1000, 2000) and seeing limited imaging in astronomy standard Bessell's B, V, R, I, and a narrow band Hα filters. At the time of starting this thesis work in mid-2018, the design of MFOSC-P was completed, and various components were being procured. Thus the overall structure of this thesis was planned around the MFOSC-P instrument and can be summarized in four broad projects,

1. Assembly-Integration-Test (AIT) of MFOSC-P instrument in the laboratory.

2. On-sky characterization and performance verification program of MFOSC-P using a sample of M dwarfs.

3. Science verification of MFOSC-P with the observational studies of Nova V2891 Cyg and a suspected symbiotic system SU Lyn.

4. Optical design of an extended version of FOSC instrument for the upcoming 2.5m telescope, named - Mt. Abu Faint Object Spectrograph and Camera-Echelle Polarimeter (M-FOSC-EP) and its prototype- named ProtoPol.

The Assembly-Integration-Test (AIT) of MFOSC-P in the laboratory formed **the early part of the thesis**. AIT is an important and essential phase of the instrument development process. It includes quality tests for various components, sub-assemblies, instrument integration, etc. It also includes various performance tests to cross-verify the photometric and spectroscopic performance of the instrument with their designed values. During the AIT procedure of MFOSC-P, various sub-systems were assembled and characterized on the optical test bench set-up. These sub-systems were then assembled within the instrument's enclosure, and the performance verification of the instrument was done in the laboratory. The imaging & spectroscopic performance had been verified & were determined as per the designed values. The AIT and laboratory characterization of MFOSC-P was conducted from October 2018 to January 2019. Optical performance verification of the optics components (e.g., lenses and lens sub-assemblies), motion sub-systems testing, imaging and spectroscopy performance verification, etc., were done during this period (see Fig. 1).

The next project of the thesis work was to commission the instrument on PRL 1.2m telescope (see Fig. 2). This was done through a long-term performance verification (PV) program, wherein a sample of M dwarfs were observed during February-June 2019. The primary goal of the PV observations is to ensure the functionalities of the instrument in varying observing conditions. Observations of various astrophysical objects conducted during this program were also utilized to evaluate the performance of MFOSC-P, such as its efficiency, signal-to-noise-ratio (SNR), etc.

During the MFOSC-P performance verification program, 80 M dwarfs were observed during February-June 2019 for their spectral type classification &

Figure 1: Panels (a.), (b.) & (c.) show the development of MFOSC-P lens barrels. Panels (d.), (e.) and (f.) show the completed lens barrels and their cage-rod assemblies. Panels (g.) and (h.) show the assembled MFOSC-P instrument in the laboratory.

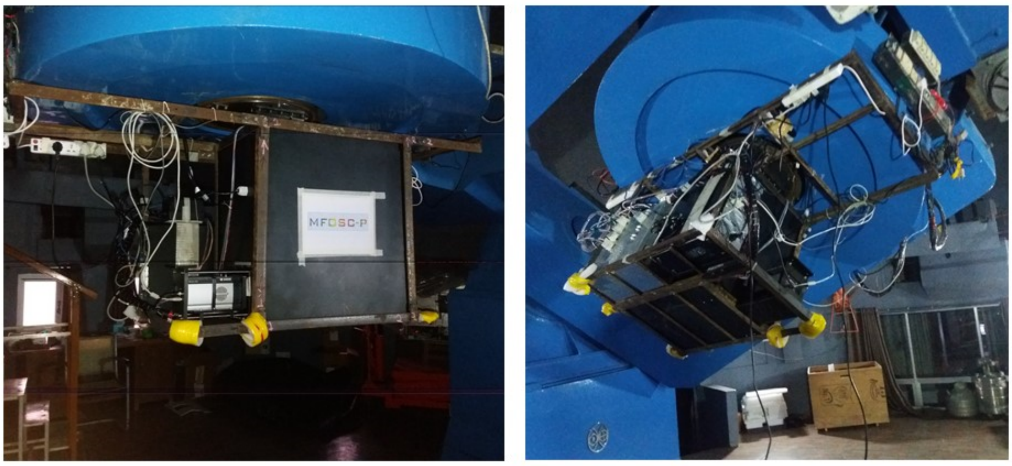

Figure 2: MFOSC-P on the PRL 1.2m telescope.

atmospheric properties using spectroscopy. Hα emission was noticed in ten of these sources, indicating the activity in M dwarfs. As very few studies had been carried out to explore the short-term Hα variability in M dwarfs. Therefore, it was decided to perform a follow-up spectroscopic study of the variability of the Hα and Hβ emissions at shorter time scales in a different sample of M dwarfs. Therefore, in another program, 83 active M dwarfs were observed from March

2020 to March 2021. In this program, we have performed the spectroscopic monitoring of 83 early M dwarfs to study the short-term ($\sim$5 minutes) variability of Hα and Hβ emissions over a few hours of time scales. This study was further complemented with the use of archival photometric light curves from TESS and Kepler/K2 missions. The derived variability parameters are then explored for any plausible systematics for their rotation periods and star-spot filling factors.

An automated data reduction pipeline was developed during the PV phase to reduce these raw observational data to science-ready data. The pipeline has been developed in PYTHON using open-source image processing libraries (e.g. ASTROPY, etc.). The pipeline consists of a series of tasks (codes) to be applied to the raw data in pre-determined sequences. It includes various spectroscopy data reduction steps like bias subtraction, cosmic ray removal, tracing and extracting the spectra, sky background subtraction, wavelength calibration, instrument response correction, etc.

Subsequently, **a science verification (SV) program** was undertaken with MFOSC-P to demonstrate the instrument's scientific potential, capabilities, and performance. Nova V2891 Cyg was selected as a science target for this purpose, and it was monitored for 13 months (November 2019 - December 2020) since its discovery using various imaging and spectroscopy modes of MFOSC-P. Supporting data from several other observatories were also used in this study. Novae are the outburst transients and show significant variations in their magnitudes and optical spectrum. Various phases of the nova outburst were, thus, traced and studied with MFOSC-P. The analysis showed that the coronal emission lines, most likely, are due to shock heating rather than photo-ionization, and the episode of dust formation is shock-induced. These phenomena are rare in the evolution of the novae.

An additional short-term program with MFOSC-P was the study of a suspected symbiotic system- SU Lyn. In this study, we have also utilized the UV spectroscopic data from the UVIT (Ultra-Violet Imaging Telescope) payload of the AstroSat mission. Using this multi-wavelength data, we have successfully confirmed the symbiotic nature of SU Lyn and established that it belongs to a rare non-shell burning symbiotic system. These results are significant as they firmly establish the existence of non-shell-burning symbiotics without any prominent emission lines in optical.

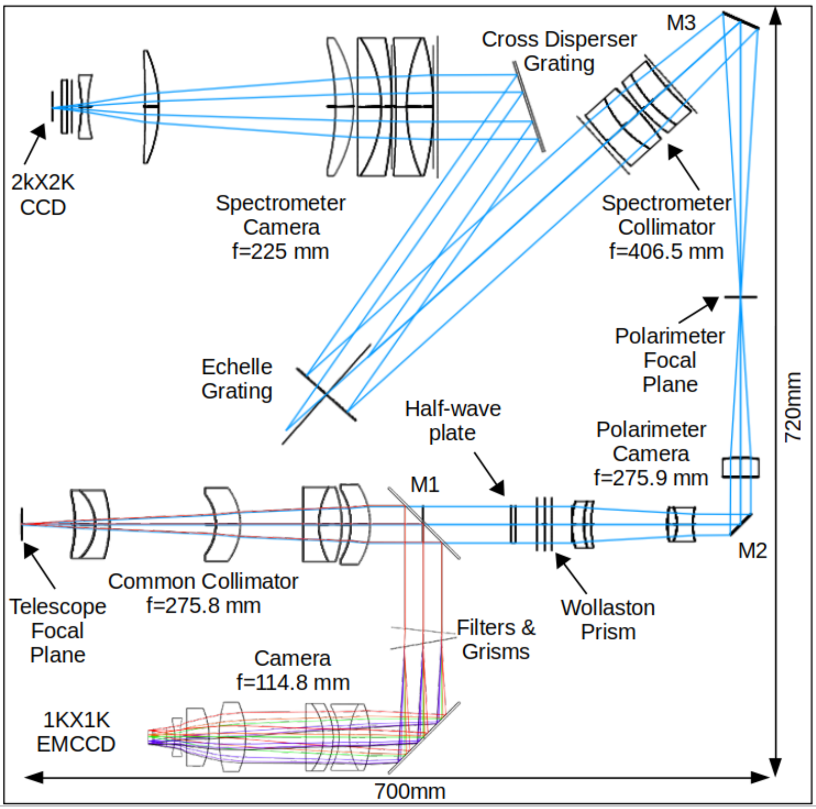

Figure 3: The figure shows ZEMAX optical design model of the M-FOSC-EP instrument. Fold mirrors are used to fold the design within the constraints of the mechanical dimensions. The movable fold mirror M1 would be used to choose the required mode between LRA & Spectro-polarimetry.

As the last part of the thesis, following the success of the MFOSC-P instrument on a 1.2m telescope, we have subsequently developed the optical design of a two-channel multi-mode instrument named Mt. Abu Faint Object Spectrograph and Camera - Echelle Polarimeter (M-FOSC-EP). M-FOSC-EP would have the capabilities of a typical FOSC instrument and the functionalities of an intermediate-resolution spectro-polarimeter. It would be having two detector systems for two of the optical arms. The first arm, the low-resolution arm (LRA), would provide low-resolution spectroscopy (∼500-800) and seeing limited imaging in various filters. The second arm is designed for intermediate resolution (∼15000) spectro-polarimetry.

The instrument's optical design has been completed and analyzed to ensure the required performance. The optical ZEMAX design is shown in Fig. 3. The instrument is being developed as a common facility instrument with wide-ranging science cases such as symbiotics, M dwarfs, AGNs, novae, supernovae, etc.

As a precursor of the M-FOSC-EP instrument, a prototype instrument-ProtoPol has also been designed with completely off-the-shelf optical components. ProtoPol can be used on the upcoming PRL 2.5m telescope and the existing PRL 1.2m telescope. We have completed the optical design of ProtoPol using ZEMAX software (see left panel of Fig. 4). An initial version of the 3-D mechanical CAD model was also developed using the "Autodesk Inventor" software (see right panel of Fig. 4). The ProtoPol would perform the spectro-polarimetry in the visible domain with a resolution of ∼6000-7000. ProtoPol is currently being developed, and its various parts are being fabricated.

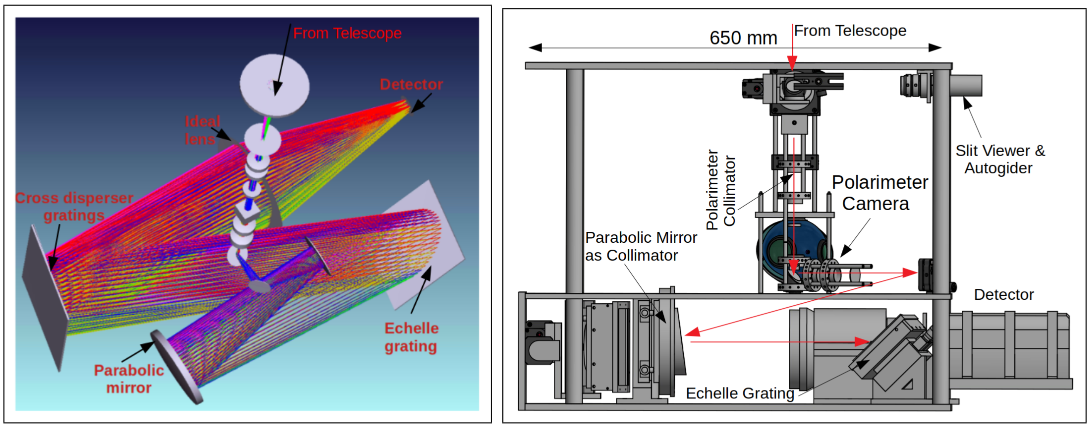

Figure 4: Left panel shows the ZEMAX 3-D model of the Echelle-polarimeter prototype instrument - ProtoPol for upcoming PRL 2.5m telescope. Right panel shows the opto-mechanical design of ProtoPol. The telescope beam enters from the top into the vertical polarimeter arm and then travels through the horizontal spectrograph section.

The thesis is organized into six chapters, as briefly described below:

Chapter 1 - Introduction: This chapter will describe the baseline optical and opto-mechanical designs of the MFOSC-P instrument. We will also discuss the requirements of intermediate resolution spectro-polarimeters on small to moderate aperture telescopes. Various science programs that can be executed with the M-FOSC-EP on the upcoming PRL 2.5m telescope are briefly described here, along with the primary design considerations of the intermediate resolution spectro-polarimeter.

Chapter 2 - Assembly-Integration-Test & laboratory characterization of MFOSC-P: We shall discuss the details of the AIT procedure of MFOSC-P in this chapter. This includes the development of optics/lens sub-assemblies, their quality checks, the laboratory characterization of MFOSC-P on the optical bench as well as within the instrument envelope, etc. The on-sky commissioning and characterization tests of MFOSC-P on the 1.2m telescope will also be discussed, along with the development of the MFOSC-P spectroscopy data reduction pipeline.

Chapter 3 - Performance verification of MFOSC-P with the statistical samples of M dwarfs: In this chapter, we will describe the performance verification studies of MFOSC-P with the sample of M dwarfs. Two observing programs will be discussed: (A.) the low-resolution spectroscopy program of a sample of M dwarfs to characterize them with the determination of their fundamental parameters, viz. effective temperature and surface gravity, and (B.) a follow-up spectroscopic study of short-term Hα /Hβ variability in another sample of M dwarfs.

Chapter 4 - Science verification of MFOSC-P: multi-wavelength studies of Nova V2891 Cyg & Suspected Symbiotic - SU Lyn: The two science programs will be discussed in this chapter that were chosen for science verification of MFOSC-P. First, the observing program for Nova V2891 Cyg will be discussed. The observations of this nova include observations with various spectroscopy and photometry modes of MFOSC-P, along with various data from other national and international observational facilities. In the second section, the multi-wavelength science observations of SU Lyn will be discussed, which include (in addition to MFOSC-P observations) the UV spectroscopy data from the UVIT payload on-board the AstroSat mission.

Chapter 5 - Design of spectro-polarimeters for PRL telescopes: The optical design and analyses of M-FOSC-EP and its prototype instrument will be presented in this chapter. In the first section, the optical designs of various sub-modules of M-FOSC-EP -namely, the Low-Resolution Arm (LRA), Polarimeter module, and the Echelle spectrograph module, will be discussed, along with their optical performance and various design analyses. Several other aspects of the optical design like efficiency, resolutions, cross-talk of orders in Echelle spectroscopy, etc., will also be discussed for this instrument. In the second part of the chapter, the optical design of ProtoPol will be described along with its expected performance. A preliminary opto-mechanical design of ProtoPol will also be discussed.

Chapter 6 - Summary & Future Work: This chapter will summarize the content of this thesis and will also discuss some of the promising future research prospects that arise with the successful completion of this work.

List of Publications

To be included in the thesis

1. A. S. Rajpurohit, **Vipin Kumar**, Mudit K. Srivastava, F. Allard, D. Homeier, Vaibhav Dixit and Ankita Patel, "First results from MFOSC-P: low-resolution optical spectroscopy of a sample of M dwarfs within 100 parsecs" (MNRAS 492, 5844-5852 (2020); doi:10.1093/mnras/staa163)

2. **Vipin Kumar**, Mudit K. Srivastava, Dipankar P.K. Banerjee and Vishal Joshi, "UV spectroscopy confirms SU Lyn to be a symbiotic star" (MNRAS Letters, 500, L12-L16 (2021); doi:10.1093/mnrasl/slaa159)

3. Mudit K. Srivastava, **Vipin Kumar**, Vaibhav Dixit, Ankita Patel, Mohanlal Jangra, A.S. Rajpurohit, and S. N. Mathur, "Design and Development of Mt. Abu Faint Object Spectrograph and Camera - Pathfinder (MFOSC-P) for PRL 1.2m Mt. Abu Telescope" (Experimental Astronomy, 51, 345-382 (2021); doi:10.1007/s10686-021-09753-5)

4. **Vipin Kumar**, Mudit K. Srivastava, Dipankar P.K. Banerjee, C. E. Woodward, Ulisse Munari, Nye Evans, Vishal Joshi, Sergio Dallaporta, and Kim Page, "Optical and near-infrared spectroscopy of Nova V2891 Cygni: evidence for shock-induced dust formation" (MNRAS, 510, 3, 4265-4283 (2022); doi:10.1093/mnras/stab3772)

5. **Vipin Kumar**, Mudit K. Srivastava, Vaibhav Dixit, Bhavesh Mistry, Kevikumar Lad, Ankita Patel, Arvind S. Rajpurohit, "Designs of Mt. Abu faint object spectrograph and camera - echelle polarimeter (M-FOSC-EP) and its prototype: spectro-polarimeters for PRL 1.2m and 2.5m Mt. Abu Telescopes, India" (Proceedings Volume 12184, Ground-based and Airborne Instrumentation for Astronomy IX; 121845B (2022); doi:10.1117/12.2629090)

Under Preparation/Revision

1. **Vipin Kumar**, A. S. Rajpurohit, Mudit K. Srivastava, "Exploring the short term variabilities in Hα and Hβ emissions in a sample of M Dwarfs" (Submitted to MNRAS, Manuscript ID: MN-22-0437-MJ, currently under review)

Others (not to be included in the thesis)

1. Guenther, E. W. ; Wockel, D. ; Chaturvedi, P. ; **Kumar, V.** ; Srivastava, M. K. ; Muheki, P., "The flare-activity of 2MASS J16111534-1757214 in the upper Scorpius association" (MNRAS, 507, 2, 2103-2114 (2021); doi:10.1093/mnras/stab1973)

2. Ankita Patel, Vaibhav Dixit, Mohan Lal, **Vipin Kumar**, and Mudit K. Srivastava, "Development of an Instrument Control System: Automation of MFOSC-P Instrument to Facilitate Remote Operation at Mt. Abu" (published in PRL Technical Reports; PRL-TN-2022-116)

Conference Talk / Division Seminar / Posters

1. **Poster**, "Assembly-Integration-Testing (AIT) and Characterization of Mt. Abu Faint Object Spectrograph and Camera-Pathfinder (MFOSC-P)", 37th Meeting of Astronomical Society of India, 18-22 February 2019, hosted by Christ (Deemed to be University), Bengaluru, India.

2. **Division Seminar**, "Development of FOSC Instrumentation for PRL Telescope: Commissioning of MFOSC-P & Optical Design of M-FOSC-EP", 31 July 2019, Astronomy & Astrophysics Division, Physical Research Laboratory, Ahmedabad, India.

3. **Division Seminar**, "Confirming the suspected symbiotic nature of SU Lyn : A new kind of symbiotic system", 13 September 2020, Astronomy & Astrophysics Division, Physical Research Laboratory, Ahmedabad, India.

4. **Conference talk**, “The symbiotic nature of SU Lyn : Confirmation from UVIT spectroscopy”, UVIT: 5 years of operation, 1-3 December 2020, hosted by Indian Institute of Astrophysics, Bengaluru, India.

5. **Conference talk**, “Optical and near-infrared spectroscopy studies of a very slow Nova V2891 Cyg”, February 2021, 39th meeting of the Astronomical Society of India, 18-23 February 2021, hosted jointly by ICTS - TIFR Bengaluru, IISER Mohali, IIT Indore and IUCAA Pune.

6. **Division Seminar**, “Optical and near-infrared spectroscopy studies of a very slow Nova V2891 Cyg”, 29 July 2021, Astronomy & Astrophysics Division, Physical Research Laboratory, Ahmedabad, India.

7. **Conference talk**, “Exploring the short term H-alpha variability in a sample of M Dwarfs”, 40th meeting of the Astronomical Society of India, 25-29 March 2022, hosted jointly by IIT-Roorkee and ARIES at the campus of IIT-Roorkee.

8. **Poster**, “Designs of Mt. Abu Faint Object Spectrograph and Camera - Echelle Polarimeter (M-FOSC-EP) and its prototype for PRL telescopes”, 40th meeting of the Astronomical Society of India, 25-29 March 2022, hosted jointly by IIT-Roorkee and ARIES at the campus of IIT-Roorkee.

List of Figures

List of Tables

Contents

Chapter 1

Introduction

Physical Research Laboratory (PRL), Ahmedabad, operates the PRL Mt. Abu observatory at Gurushikhar, Mt. Abu, Rajasthan, India. Gurushikhar peak is located nearly 230 km north of Ahmedabad and has an altitude of ∼1680 m. The observatory currently hosts a 1.2m optical-near infrared (NIR) telescope and two smaller 43cm and 50cm diameter telescopes. PRL is also currently in the process of setting up another 2.5m aperture diameter optical-NIR telescope at the same site. A variety of observational astrophysical research programs have been successfully explored with these telescopes over the last couple of decades, such as star formations, novae & supernovae (Srivastava et al., 2016; Joshi et al., 2017; Banerjee et al., 2018b), active galactic nuclei (Kaur et al., 2017), cometary sciences (Venkataramani et al., 2019), exo-planets (Chakraborty et al., 2018a), etc. The upcoming 2.5m telescope would further enhance the prospects of these research domains.

Faint object spectrograph and camera (FOSC) class of instrument have been proven to be one of the most sought-after general-purpose, versatile instruments in the visible wavelength domain. As the FOSC instruments provide the capability for imaging and spectroscopy in a single optical chain, they have been very successful on various telescopes around the world (e.g., EFOSC on ESO 3.6m telescope (Buzzoni et al., 1984), DFOSC on Danish 1.54m Telescope (Andersen et al., 1995), FOCAS on 8.2m Subaru telescope (Kashikawa et al., 2000) etc.) as well on several Indian facilities (e.g., IFOSC on IUCAA 2m telescope

Figure 1.1: The figure shows the PRL Mt. Abu observatory at Gurushikhar, Mt. Abu, Rajasthan, India. PRL 1.2m telescope building and PRL 2.5m telescope building can be seen on the left and right-hand sides in the figure, respectively (Source: https://www.amos.be/project/mont-abu-observatory-2).

(Gupta et al., 2002), HFOSC on IIA-HCT Hanle telescope (Prabhu & Anupama, 2010), ADFOSC on ARIES Devasthal 3.6m Telescope (Kumar, 2016; Omar et al., 2017) etc.). Considering the diverse scientific applications of a FOSC, a similar kind of instrument was envisaged for PRL 2.5m telescope. However, as the specifications of the FOSC for the new 2.5m telescope were being deliberated in late 2014, a similar instrument was also required for the 1.2m telescope to provide the facility for imaging and low/medium resolution spectroscopy in the optical domain. Thus, as a precursor of a FOSC for the 2.5m telescopes, it was decided to develop a scaled-down version of a typical FOSC instrument named – Mt. Abu Faint Object Spectrograph and Camera-Pathfinder (MFOSC-P) for the 1.2m telescope with a relatively smaller budget and development period.

This thesis work was, thus, planned around the MFOSC-P instrument, which includes the Assembly-Integration-Test (AIT) of the instrument, its on-sky characterization and performance verification, and subsequently, the science-verification with the studies of a suitable astrophysical source utilizing MFOSC-P. Owing to the various science cases with a 2.5m telescope, an extended version of FOSC has been designed, which also offers the capability of intermediate resolution spectro-polarimeter. These aspects will be described in later chapters.

In this chapter, we shall first briefly describe the basic specification of PRL telescopes and then the need, and scientific requirements of a Faint Object Spectrograph and Camera (FOSC) kind of instrument for PRL telescope, which led us to develop a pathfinder instrument named MFOSC-P for the 1.2m telescope. We shall describe its optical and opto-mechanical design, which were completed by the engineering team of MFOSC-P prior to the start of this thesis work. The later part of this chapter will discuss some of the perspective science cases that demand beyond FOSC type of instrumentation and led us to propose an extended version of FOSC with an additional mode of intermediate resolution spectro-polarimetry. A basic theoretical framework required for the spectro-polarimetry instrumentation is also briefly discussed.

1.1 PRL's 1.2m and upcoming 2.5m telescopes

The existing 1.2m telescope consists of 1.2m primary and 0.3m secondary mirrors with the final f/13 beam at its focal plane (Deshpande, 1995). The telescope is equatorial mounted. The position of the focal plane of the telescope can be adjusted by motorized movement of the secondary mirror along the optics axis. The telescope has a plate scale of 76 μm per arc-second and aberration-free field-of-view (FOV) of $\sim$10.0 arc-minutes of diameter (Banerjee et al., 1997). The weight of the focal plane instrumentation is typically restricted to up to 125 kg. The physical space beneath the primary mirror cell for any instrumentation set-up is $\sim$1.0m diameter $\times$ 0.8m depth. Thus, any back-end instrument on the 1.2m telescope has to be designed within these weight and volume constraints.

The upcoming 2.5m telescope is currently being installed at the same site but in a new telescope building. The telescope is of the altitude-azimuth type and has Ritchey-Chretien optical configuration Pirnay et al. (2018) i.e., a hyperbolic concave primary mirror (2.5m, f/2) with a hyperbolic convex secondary mirror (0.779m, f/2.4). The final beam is f/8 at the focal plane, and the telescope provides a total scientific FOV of 25 arc-minutes in diameter. The telescope is equipped with active support for the mirrors. The primary mirror is kept in the desired shape at various orientations by a number of axial and radial actuators. The secondary mirror is also equipped with a hexapod for its

Figure 1.2: The left panel shows the existing PRL 1.2m telescope, and the right panel shows the upcoming 2.5m telescope (Source: https://www.prl.res.in/ miro/telescopes.html).

positioning and fine alignments. This active support system uses the feedback of a wavefront sensor which in turn uses an off-axis guide star for wavefront sensing. The telescope can host three instruments: one at the main Cassegrain port and two others on the two side ports. The instrument's weight limits on the main and side ports are 400kg and 150kg, respectively.

1.2 Mt. Abu Faint Object Spectrograph and Camera - Pathfinder (MFOSC-P) for PRL 1.2m telescope : The science requirements

The pathfinder instrument (MFOSC-P) was conceived to provide low/medium resolution optical spectroscopy and imaging on the PRL 1.2m telescope and to supplement the ongoing observational programs of the Astronomy & Astrophysics (A&A) division, e.g., optical/NIR studies of novae and supernovae, photometric variability studies of AGNs, high-resolution spectroscopy studies of exo-planet/host star, etc. Therefore, the desired imaging and spectroscopy capabilities of MFOSC-P were chosen not only to complement these existing programs but also to open up new areas of research, like optical studies of symbiotic stars. For example, in the past, a NIR instrument- Near Infrared Camera and Spectrometer (NICS) has extensively been used for the observational studies of novae, like, the NIR studies of the novae ejecta, understanding the physical processes, astrochemistry of dust formation, etc. NIR spectroscopy has also successfully provided a NIR classification scheme of early novae spectra (especially useful for obscured novae which are faint in the optical but bright in the NIR) (Banerjee & Ashok, 2012; Banerjee et al., 2018a). However, optical spectroscopy is also an extremely desired technique for studying such objects. Early optical spectroscopy categorizes novae spectra into the He/N or Fe II classes (Williams, 1992). Identification and evolution of emission lines of various species in novae ejecta, the temporal evolution of continuum, and line profile variations seen in various emission lines are useful diagnostics of the evolution of physical conditions in such transient events. These lines cover the complete visible spectrum, e.g., Hydrogen Balmer series including Hβ 4861Å and Hα 6563Å, low ionization lines of Mg I 5184Å, Na I 5890Å, O I 5577/7773/8446 Å along with Fe II multiplets in Fe II class of novae, high excitation lines of N III 4640Å, He II 4686Å, N II 5001Å, N II 5679Å, He I 5876Å, in He/N class of novae, etc. The spectral coverage and resolution of MFOSC-P were thus determined from the requirements of such science cases.

A typical resolution of ∼5Å over the optical region was considered to be adequate to address the scientific issues discussed above while ensuring a good signal-to-noise ratio (SNR) over a range of magnitudes (see section 2.3.2). This resolution range is also suitable for studying potential exo-planet host targets like M dwarfs. A lower resolution of ∼10Å mode was also incorporated for supernovae studies where the emission lines are considerably broad (10,000 kms^{-1} or more). This low-resolution mode was also required to determine the spectral energy distribution (SED) over a broader wavelength range. At the outburst, novae show broad lines with the full width at half maximum (FWHM) of few thousand kms^{-1}, which in some cases (e.g., symbiotic novae (Srivastava et al., 2015)) decreases with time to a few hundred kms^{-1}. The evolution of the width and shape of the emission line profiles in symbiotic systems carries significance in understanding the propagation of shock waves into the dense ambient medium surrounding the white dwarf (Bode & Kahn, 1985). A relatively higher resolution mode around Hα was also chosen with a velocity resolution of $\sim 100-200$ kms^{-1} to study such a scenario (among other possible ones).

MFOSC-P uses 1K×1K CCD images sensor at the focal plane detector with a sampling scale of 3.3 pixels per arc-second for the reasons discussed in sections 1.3 and 1.3.1; therefore, the imaging FOV of MFOSC-P turned out to be 5.2×5.2 arc-minutes^2, which was consistent with our other existing instrumentation set-up (as mentioned above). Bessell's astronomy standard B-V-R-I filters and a narrow Hα filter are used for imaging purposes.

1.3 MFOSC-P: The system design

As MFOSC-P was conceptualized as the pathfinder instrument, thus it was much required to keep the systems' cost low and the fabrication/development period within 2 to 3 years. Therefore commercial off-the-shelf solutions for various components and sub-systems were chosen wherever possible, e.g., detector systems, gratings, filters, calibration optics, motion controllers, etc. For similar reasons, gratings were chosen as the dispersive element instead of grisms, and a commercially available off-the-shelf (COTS) CCD camera system, along with its read-out electronics and data acquisition software, was decided to be used in MFOSC-P. However, such a commercial camera system comes with protective glass windows, and the image sensor is typically kept 4-8mm inside in a vacuum enclosure. This prohibits the use of any field-corrector lens close to the sensor, which is usually incorporated in the FOSC optical design to reduce the aberrations of the imaging system, e.g., field curvature for larger FOVs. Therefore, We adopted a FOV of 5.2×5.2 arc-minutes^2 on a 1K×1K CCD image sensor, with a sampling scale of 3.3 pixels per arc-second (see section 1.3.1). The choice of this FOV also did not require any field corrector lens for aberrations control. It also allowed us to develop a simpler, cost-effective optical design using only spherical singlet and

Table 1.1: Design parameters of MFOSC-P. Table is reproduced from Srivastava et al. (2021).

Parameters	Values
Optimized wavelength range	4500 – 8500 Å
Imaging FOV	$\sim 5.2 \times 5.2$ arc-minute^2
Imaging pixel scale	3.3 pixels per arc-second
Image quality requirement	$\sim$ 80% Encircled Energy Diameter (EE80) is to be within 1.5 pixels
Magnification of the MFOSC-P optical chain	0.57
Camera F/number	7.4
CCD detector	1K × 1K ANDOR CCD with 13μm pixel size
Filters	Astronomy standard Bessell's BVRI filters. Narrow band Hα filter
Spectral coverage of gratings	∼4500-8500Å using three different gratings
Spectral Resolutions ($\lambda/\delta\lambda$)	∼2000, 1000 and 500 around 6500Å, 5500Å and 6000Å respectively for 1 arc-second ($\sim 76\mu m$) slit width
Pupil diameter	∼33 mm
Grating's specifications	Three plane reflection gratings, named R2000, R1000 and R500 with 500, 300, and 150-line pairs per mm (lp/mm) blazed at ∼6500Å, 5500Å and 6000Å respectively

doublet lenses. Further, given the small aperture of the telescope and minimal throughput in the U band, the instrument's optical design was not optimized for the deep blue part or U band of the spectrum.

Thus, MFOSC-P had been conceptualized to provide grating-based spectroscopy and seeing limited imaging in standard Bessell's B, V, R, and I filters. A narrow band Hα filter had also been added to the design. The wavelength range for the spectroscopy modes was chosen to be 4500-8500Å, which is sufficient to address the science goals as described above. Three plane reflection gratings with different groove-densities, viz. 500 lp/mm, 300 lp/mm, and 150 lp/mm (hereafter R2000, R1000, and R500 grating modes, respectively) were selected to cover this wavelength range. R2000 grating mode of MFOSC-P covers the wavelength range of ∼6000-7000Å with a resolution of $\sim$ 3.3Å. This corresponds to a velocity resolution of ∼150 kms^{-1} around Hα . R1000 grating mode has a resolution of $\sim$ 5.0Å over the wavelength range of ∼4500-6500Å. This grating can also be centered appropriately so that Hβ and Hα wavelengths can be covered in a single exposure. R500 grating mode has the lowest resolution (∼12Å), and the largest spectral range of $\sim 4500-8500$Å to provide spectral energy distribution (SED) and spectroscopy of broad lines astrophysical objects. The optical design of MFOSC-P is discussed in the next section. Table 1.1 gives primary design parameters of MFOSC-P.

Table 1.2: Parameters of the gratings used in MFOSC-P. All the gratings are procured from Richardson Gratings (M/S Newport Corporation). Table is reproduced from Srivastava et al. (2021).

Parameters	Values		
Grating mode	R2000	R1000	R500
Catalog No.	53-*-396R	53-*-204R	53-*-426R
Groove density (line-pairs per mm)	500	300	150
Grating order	1	1	1
Blaze wavelength[a] (Å)	∼6500	∼5500	∼8000
Nominal blaze angle[a] (degree)	11.1	4.7	3.4
Angle of incident (degrees) (with respect to grating normal)	24.7	20.1	17.9
On-axis wavelength[b] (Å)	∼6510	∼5730	∼6520
Angle of dispersion (degrees) (for on-axis wavelengths)	5.3	9.9	12.1
Dispersion (Å per pixel)	∼1.1	∼1.9	∼3.8
Spectral range(Å)	∼5950-7100	∼4700-6650	∼4600-8450

a: As per manufacturer's (Richardson Gratings, M/S Newport Corporation) grating specification sheets.
b: On-axis wavelengths for the given grating mode would fall in the centre of the detector in the spectral direction. For these, the sum of angles of incident and angle of dispersion would be 30 degrees.

1.3.1 Optical Design of MFOSC-P

Like many of the FOSC instruments, MFOSC-P optical design is based on the focal reducer concept to achieve a proper sampling of the seeing disc on the CCD. For the PRL 1.2m f/13 telescope, the seeing of 1.0 arc-second corresponds to 76μm on the telescope focal plane. For the CCD pixel size of 13μm $\times$ 13μm and, considering the gratings' anamorphic magnification (∼0.90-0.95)(Schweizer, 1979) for the spectroscopy modes, the MFOSC-P optical chain has been designed to provide a magnification of $\times$0.57. In this way, the imaging mode has a sampling scale of 3.3 pixels per arc-second, while in the spectroscopy modes, a slit width of 1.0 arc-second maps on to ∼3 pixels.

The optical design of MFOSC-P is shown in Fig. 1.3 along with the dimensions of the optical system. The optical design has been developed in-house, prior to the start of this thesis work, by the MFOSC-P engineering team. The collimator section is designed using a singlet lens and two cemented doublet lenses to produce a collimated beam. It also makes the pupil image (diameter

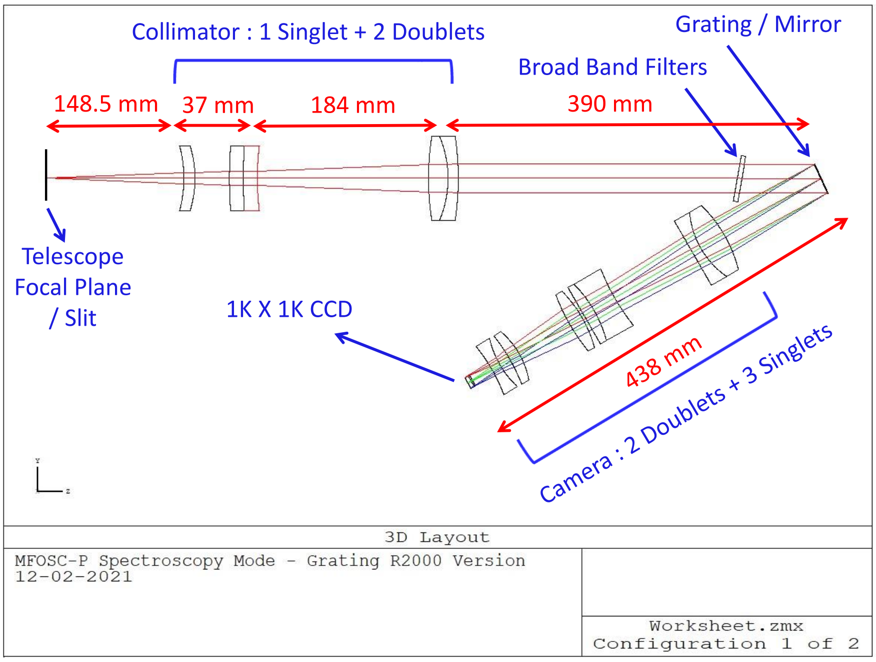

Figure 1.3: The optical design of MFOSC-P. An additional fold mirror (not shown in the figure) is also kept immediately after the last lens of collimator to fold the design mechanically. Distances mentioned here are to show the scale of the optical system. Exact values are given in Table 1.3. Figure is reproduced from Srivastava et al. (2021).

~33.0mm) at the grating's positions. Three suitable off-the-shelf plane reflection gratings (see Table 1.2) are used to provide the slit-limited resolutions of ~2000, 1000, and 500 at the wavelengths of 6500Å, 5500Å, and 6000Å respectively in the first order. These gratings and a fold mirror for imaging mode are mounted on the purpose-designed stepper-motor driven turret-like mechanism. This mechanism is rotated to select the desired spectroscopy or imaging mode. The optics axes of the collimator and camera system are designed to be kept at an angle of 30 degrees. Thus, for the on-axis wavelengths of the gratings modes (in the center of the detector on the spectral axis), the sum of the angle of incident (α) and angle of dispersion (β) is fixed at 30 degrees.

A filter wheel, with Bessell's B, V, R, I, and Hα filters, is placed before the gratings in parallel beam space. The camera optics is designed with two doublet and three singlet lenses to produce an f/7.4 beam. The image is finally formed at a detector system consisting of a 1024×1024 pixels CCD image sensor with 13 μm pixel size (ANDOR Model No. iKon-M 934, M/S Oxford Instru-

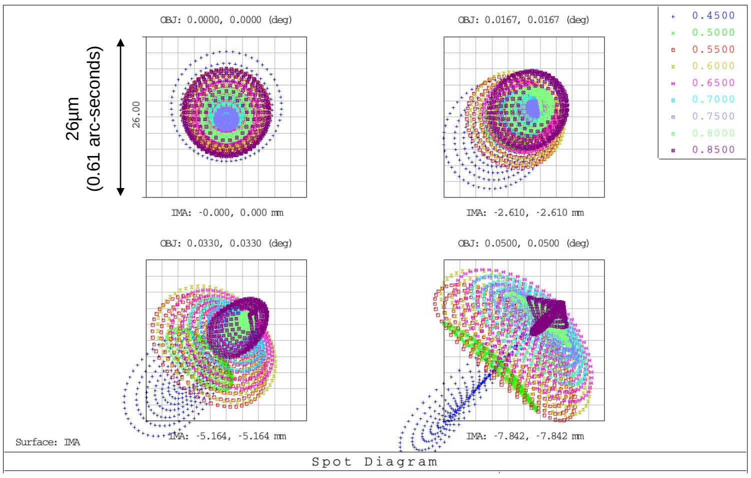

Figure 1.4: Poly-chromatic imaging mode spot diagram of MFOSC-P optics at the detector plane, for the design wavelength range 4500-8500Å. Four radial field points are chosen as top-left for on-axis (0,0) arc-minutes field, top-right for (1,1) arc-minutes, bottom-left for (2,2) arc-minutes and bottom-right for (3,3) arc-minutes field coordinates. Box size is 26 μm (2 pixels) a side. The CCD detector has pixel size of 13μm a side in size and spans $\sim 5.2 \times 5.2$ arc-minute^2. The details of RMS spot diameters for various field points are given in Table 1.4. Figure is reproduced from Srivastava et al. (2021).

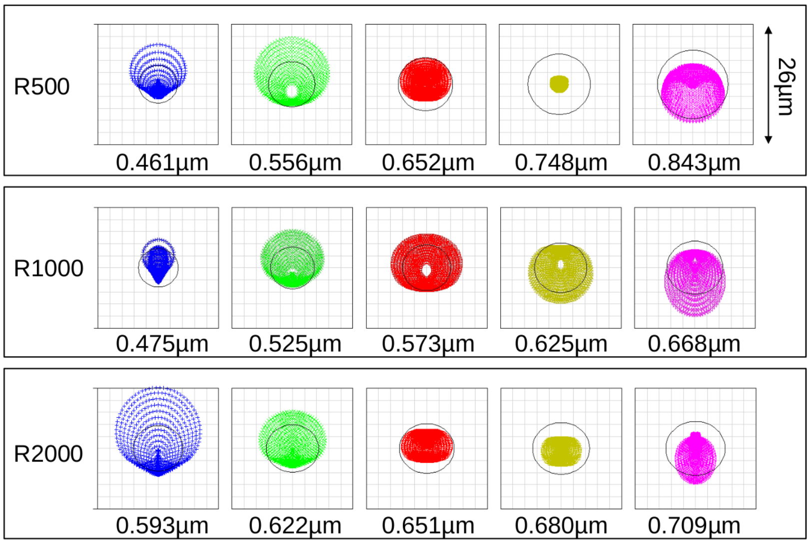

Figure 1.5: Matrix spot diagram for R500, R1000 and R2000 grating modes of MFOSC-P. Box size is 26 μm (2 pixels) a side. The details of RMS spot diameters for all the spectroscopy modes are given in Table 1.4. Figure is reproduced from Srivastava et al. (2021).

Table 1.3: Lens parameters for the MFOSC-P optical chain: this table contains ZEMAX optical designdata. Table is reproduced from Srivastava et al. (2021).

Element	Surface	Glass	Catalog	Radius of Curvature (mm)	Thickness
Collimator-Singlet-1	First	N-PK51	SCHOTT	-135.0 (CC)[a]	12.0
Collimator-Singlet-1	Second			-116.0 (CX)[a]	37.0
Collimator-Doublet-1	First	S-FTM16	OHARA	478.0 (CX)	15.0
Collimator-Doublet-1	Second	S-NSL36	OHARA	700.0 (CC-CX)	15.0
Collimator-Doublet-1	Third			290.0 (CC)	184.0
Collimator-Doublet-2	First	S-FPL53	OHARA	286.0 (CX)	21.0
Collimator-Doublet-2	Second	S-NSL36	OHARA	-115.6 (CX-CC)	11.0
Collimator-Doublet-2	Third			-307.0 (CX)	510.0[c]
Camera-Doublet-1	First	S-FPM3	OHARA	147.0 (CX)	29.0
Camera-Doublet-1	Second	S-BSM28	OHARA	-93.3 (CX-CC)	10.0
Camera-Doublet-1	Third			Inf (Plano)	96.8
Camera-Doublet-2	First	N-KZFS4	SCHOTT	-237.0 (CC)	26.0
Camera-Doublet-2	Second	K-GFK70	SUMITA	135.0 (CC-CX)	12.0
Camera-Doublet-2	Third			Inf (Plano)	3.0
Camera-Singlet-1	First	N-KF9	SCHOTT	136.8 (CX)	15.0
Camera-Singlet-1	Second			-218.8 (CX)	63.0
Camera-Singlet-2	First	N-LASF44	SCHOTT	90.4 (CX)	11.7
Camera-Singlet-2	Second			205.3 (CC)	12.1
Camera-Singlet-3	First	S-LAH60	OHARA	-102.0 (CC)	10.0
Camera-Singlet-3	Second			185.0 (CC)	29.65[d]

a : CC : Concave surface. CX : Convex surface. The intermediate surface of a doublet lens is described as CC-CX or CX-CC.
b : Thickness in mm (distance to the next surface)
c : The 510.0mm (= 300.0+5.0+85.0+120.0 mm) is the distance between last surface of the collimator lens to first surface of camera lens. 300.0mm is the distance between collimtor to 5.0mm thick imaging filter, 85.0mm is from filter to grating and 120.0mm is from grating to camera lens surface.
d : The last distance from camera lens surface to the image sensor (29.65mm = 24.0+1.5+4.15 mm) is the distance from lens to the protective glass window (24.0mm), thickness of glass window (1.5mm) and from glass window to the image sensor (4.15mm).

ments) [1]. Off-the-shelf slits from M/S Thorlabs and M/S Edmund Optics are used at the instrument's object plane. Two slits of 75 μm and 100μm width are used in MFOSC-P for varying seeing conditions. The slits are 3mm in length, projecting onto 132 pixels at the CCD. Though the slits do not cover the entire length of the CCD, they were found suitable for the spectroscopy of Galactic point sources and extra-galactic bright super-novae. Given the moderate aperture of the telescope, spatially resolved spectroscopy of extended diffuse sources

[1] https://andor.oxinst.com/products/ikon-xl-and-ikon-large-ccd-series/ikon-m-934; Accessed 2020-03-18

are usually not done with the telescope. The telescope is also not equipped with a Cassegrain rotator to re-orient the slit. Thus, this off-the-shelf, readily available solution for the slits was adopted. Table 1.1 gives the baseline design parameters of MFOSC-P. The details of optical design parameters, lens specifications, glass types, etc., of the MFOSC-P optical chain, are given in Table 1.3.

1.3.2 Image Quality and Tolerances

MFOSC-P optics image quality requirement was to have the root-mean-square (RMS) spot diameters within one-third of the seeing profile. Thus, for a seeing profile of 1.0 arc-second FWHM, and with the sampling scale of 3.3 pixels per arc-second, this corresponds to an RMS spot diameter requirement of 1.1 pixels. It must, however, be mentioned that the final PSF on the 1.2m telescope focal plane also includes the contributions from the telescope optics, its opto-mechanical arrangement, tracking system, etc. These extra factors further degrade the FWHM of the PSF on the telescope focal plane (see section 2.3.1). The polychromatic spot diagrams for imaging mode and matrix spot diagram for three spectroscopy modes are shown in Fig. 1.4 and 1.5 respectively. Table 1.4 describes RMS diameters for all the modes of imaging and spectroscopy. The throughput of the instrument is estimated $\sim 30\%$ for spectroscopy modes. A throughput curve is shown in Fig. 1.6 for the instrument in R500 spectroscopy mode.

MFOSC-P optics was designed with typical industry-standard manufacturing errors of $\pm 25\mu$m /3 fringes on the radii of curvatures and $\pm 50\mu$m on the lens elements' thickness. Several other optics specifications were chosen as per the requirement of scientific imaging applications, such as power/irregularity of 4/1, the surface quality of $\lambda/4$ per inch, Scratch/Dig of 40/20, etc. At the component level, tolerances of $\pm 100\mu$m and ± 0.1 degrees were considered for the positioning accuracy and tilt of the individual lens elements, respectively, during their opto-mechanical assembly process. All the lenses were coated with broadband anti-reflection coating with less than 1.5% reflectance over the wavelength range of 4500-8500Å. The optical system was analyzed for these tolerance val-

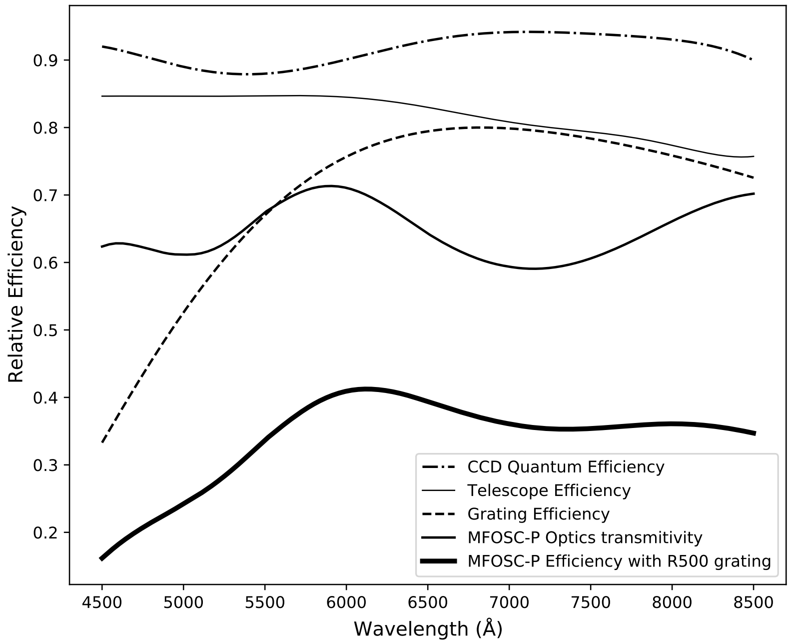

Figure 1.6: The throughput variation (solid thick dark curve) of MFOSC-P is shown for R500 grating mode. Various contributors are shown in thin curves. Grating response is for R500 grating. The other modes of spectroscopy have the similar throughput profiles. Figure is reproduced from Srivastava et al. (2021).

ues, including the thermal variations i.e., 5 to 30 degrees C as nominal observing conditions and -2 to +35 degrees C for extreme conditions. The statistical performance of simulated systems using ZEMAX Monte Carlo analysis yields the mean of RMS spot diameters within ∼1.1 pixels with a standard deviation of 0.3 pixels (for all the modes of imaging and spectroscopy). The 90% of the simulated systems showed the RMS spot diameter values within 1.5 pixels. The back focal distance of the camera optics was used as a compensator in the tolerance analyses. Its variation was found in the range of ±1.5mm for various cases.

1.3.3 Opto-mechanical design of MFOSC-P

Opto-mechanical design of MFOSC-P is shown in Fig 1.7. The telescope beam enters the instrument through an optical protective glass window. The focal plane of the telescope is formed inside the instrument. The slits are positioned on the focal plane using a stepper motor-based linear translational stage to be

Table 1.4: Image quality performance of MFOSC-P optical chain: RMS spot diameter (μm). Pixel Size is 13 μm a side. Table is reproduced from Srivastava et al. (2021).

Imaging					
Radial Field Height (arc-minutes)	0	1	2	3	4
Wavelength (Å)					
4500	11.92	11.79	11.51	11.73	13.73
5500	9.98	10.34	11.68	13.64	15.86
6500	6.50	7.00	8.79	11.41	14.42
7500	2.94	2.52	2.37	4.32	7.61
8500	12.36	11.73	9.79	6.98	4.71
Spectroscopy					
Grating Mode	R500		R1000		R2000
Wavelength (Å)					
4500	10.80		-		-
5000	7.20		7.49		-
5500	10.56		9.90		-
6000	9.42		9.17		11.52
6500	6.29		8.06		5.98
7000	2.62		8.52		5.47
7500	2.46		-		-
8000	6.16		-		-
8500	9.90		-		-

driven in and out of the optics axis. Due to the mechanical design constraints, the field stop is mounted just below this translational stage at the telescope focal plane to limit the FOV and stray light. The collimator optical system then picks the beam from the focal plane and provides a parallel beam space for the filters and gratings requirements. The linear translational stage and collimator optics barrel are mounted on the vertical plate of the L-shape chassis. A 45-degree fold mirror bends the parallel beam in a horizontal plane. The beam passes through a stepper motor-driven filter wheel with Bessell's B-V-R-I-Hα filters (50mm diameter) and an empty slot for spectroscopy purposes. The beam forms the pupil image after the filter onto the grating/imaging mirror surface. Three different plane reflection gratings and a fold mirror are mounted on the four faces (90 degrees apart) of a rotation mechanism driven by a stepper motor. Desired grating (for spectroscopy) or mirror (for imaging) can be brought into the path of the beam by rotating the mechanism. The dispersed or reflected beam is directed into camera optics and forms the image on the ANDOR CCD detector system. The instrument's dimensions are 680mm $\times$ 608mm $\times$ 429mm, and it weighs 68 kg. The opto-mechanical structure is made of aluminum (6061T), and an inner enclosure is added for dust contamination. MFOSC-P is mounted on the telescope along with its control system and control computer using a mild steel support structure (Fig. 1.7). The entire assembly weighs around 121 kg. The finite element analysis of the MFOSC-P mechanical system (including its external support cage system) was also done to ensure its structural integrity and desired tolerances. The details of structural analysis are described in Srivastava et al. (2018).

MFOSC-P is also equipped with an off-axis guider system. Before the beam enters into MFOSC-P, a 45-degree pick-up mirror selects an off-axis field and directly image it onto the Lodestar X2 auto-guider camera[2]. The 45-degree pick-up mirror and the Lodestar camera are mounted on a stepper motor-based motion mechanism. This mechanism allows movement of the auto-guider system around 90 degrees along the periphery to scan the off-axis field for a suitable guide star.

1.3.4 Instrument control system and graphical user's interface of MFOSC-P

The automation and controls of MFOSC-P's sub-systems (e.g., slit motion, calibration motion, grating motion, filter motion, etc.) are provided through an in-house developed control system that operates the instrument with a Graphical User Interface (GUI). The hardware and GUI are developed by the engineering team of MFOSC-P and are described in Srivastava et al. (2021). Here we briefly discuss these automation aspects.

MFOSC-P has five motion systems, viz. filter wheel, grating motion system, slit & aperture positioning system, calibration mirror positioning system, and the off-axis auto-guider pick-up mirror. All the motion systems are driven by stepper motors or stepper motor-based linear translational stages. Ex-

[2]https://www.sxccd.com/lodestar-x2-autoguider; Accessed: 2020-03-19

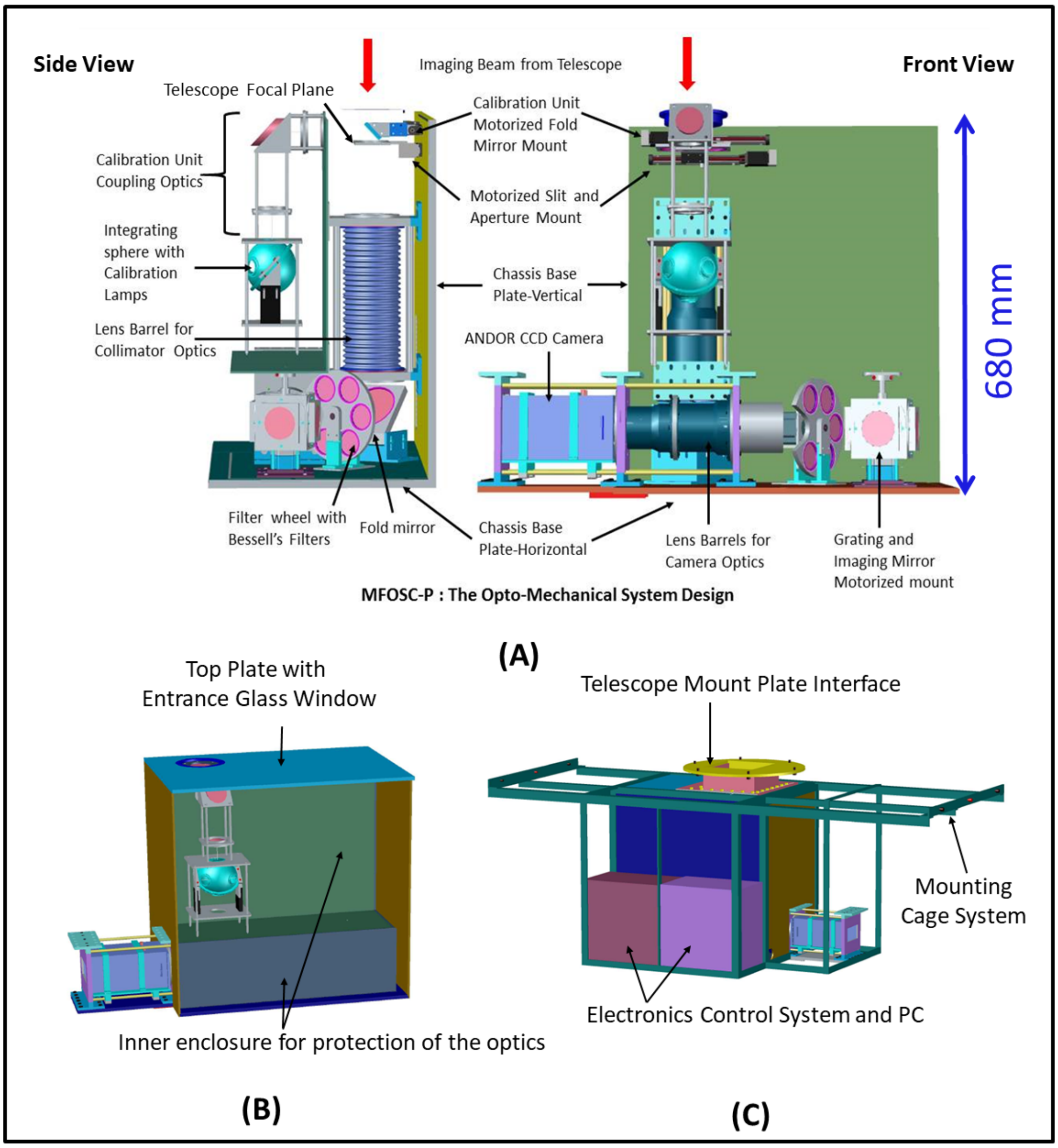

Figure 1.7: Opto-mechanical system design of MFOSC-P instrument. Top panel (A) shows the inner design and components of MFOSC-P. Panel (B) shows the outline of the instrument, the inner enclosure for protection of the optics and the outer enclosure. Panel (C) is the final configuration of MFOSC-P with its support structure. Figure is reproduced from Srivastava et al. (2021).

cept for the auto-guider system, all other motors are equipped with quadrature encoders. Limits and home sensors are also used in all motion systems. These motion systems and the lamps in the calibration unit are being operated through the instrument control system. The hardware of the control system (Fig. 1.8) is developed with two ARCUS make PMX-4EX-SA series of motion controllers [3] and eight stepper motor driver units. These drivers can be individually con-

[3]https://www.arcus-technology.com/ Accessed: 2020-01-23

Figure 1.8: The hardware set-up of MFOSC-P control system. Figure is reproduced from Srivastava et al. (2021).

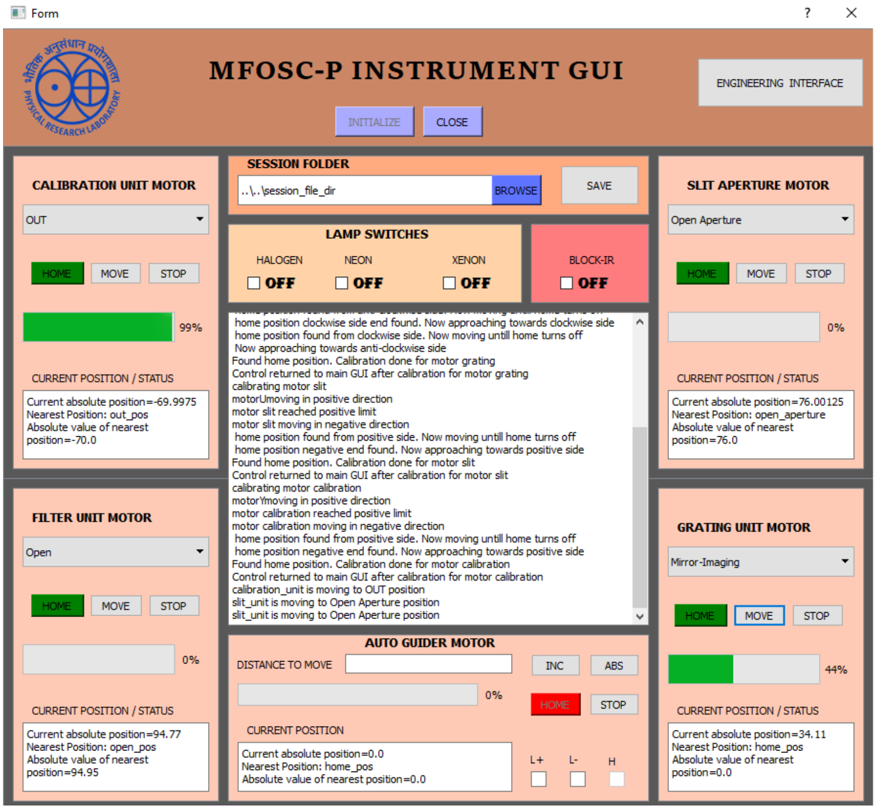

Figure 1.9: The graphical user interface (GUI) for MFOSC-P. The GUI has been developed using Python-PyQT framework and acts as the front end of MFOSC-P control software. Figure is reproduced from Srivastava et al. (2021).

figured in desired micro-stepping modes for better positioning accuracy of the motion system. Four different optically isolated power supplies from TRACO power supplies [4] are used for controller operations, relay circuit operations, limit

[4]https://www.tracopower.com/home/;Accessed 2020-01-23

sensor operations, and motor operations, respectively. The CCD detector system has built-in read-out electronics. It is accessed through the control software - SOLIS - provided by M/S Andor Technology Ltd [5].

The GUI and its application software have been developed using Python 2.7 with the PyQt4 framework. The front facade is the main front-end GUI window, which is designed as per the requirements of the MFOSC-P instrument (see Fig. 1.9). It provides the visualization and status of various motion sub-systems. The progress of any motion system while changing modes can be monitored on the GUI screen. Provisions are made in the front-end GUI to access the password-protected engineering interface directly to access the hardware component (e.g., individual motors, limit sensors, lamp control, etc.) separately for engineering tests and debug purposes. A USB communication is used to communicate with the hardware control system using the USB2.0 interface.

1.3.5 MFOSC-P: AIT, On-sky commissioning, Science verification etc.

The assembly-integration-test (AIT) of MFOSC-P in the laboratory, its on-sky commissioning, performance & characterization observations, and science verification observations form a major content of this thesis work. These are discussed in detail in the following chapters.

1.4 Moving beyond FOSC Instrumentation: Requirements of intermediate resolution spectro-polarimeter for PRL 2.5m telescope

PRL 1.2m telescope has been extremely successful over the past decades in probing a variety of observational astrophysical research domains such as star formations, planetary nebulae, novae, active galactic nuclei (AGNs), cometary sciences, exo-planets, etc. Given this heritage, the upcoming 2.5m telescope is

[5]https://andor.oxinst.com/products/solis-software/; Accessed: 2020-01-23

not only expected to enhance the prospects of observational research in these areas but would also be a major observational facility for avenues like observations of transients (novae, supernovae, etc.), exo-planets, etc. A few newer back-end instruments are being planned for the 2.5m telescope. A wide-field camera and a very high-resolution spectrograph (resolution∼100000) are being developed as the first light instruments for the visible regime of the spectrum (Chakraborty et al., 2018b). A multi-purpose instrument named NISP (Near Infrared Spectrometer and Polarimeter) is being developed to provide imaging, low-resolution spectroscopy (resolution∼2000-3000), and imaging polarimetry capabilities in NIR spectral range(Rai et al., 2020). In addition, a need was felt for a multi-mode instrument in visible bands, with basic observing modes of imaging and spectroscopy with quick switchover time. Though the FOSC series of instruments would have been the obvious choice, they are preliminarily designed for medium to low-resolution spectroscopy (generally for resolutions <3000). As some of the newer science programs with PRL 2.5m telescope require imaging and spectroscopy functionalities beyond the regular FOSC operational mode, this led us to explore instrumentation aspects beyond FOSC capabilities.

There are several scientific cases for objects like symbiotic systems, M dwarfs, AGNs, novae, supernovae, etc., that would greatly benefit from having a higher resolution mode (resolutions∼10000-15000) and/or having a spectro-polarimetry capability on the telescope. The studies of spectral line profile variabilities to probe symbiotics morphology and kinematics, the use of spectro-polarimetry to trace the surrounding environments of obscure objects (e.g., novae, supernovae, symbiotics, etc.), spectroscopic studies of M dwarfs, etc. are some of the key science goals that require the intermediate resolution spectroscopy capability as well, in addition to few traditional modes of FOSC instrument. Some of these goals will also benefit if the choice of detector system provides a fast, low-noise readout for fast photometric timing studies (time resolution ∼1 second). Therefore, an extended version of FOSC was envisaged for the 2.5m telescope, which would also include an arm for intermediate resolution (R∼10000-15000) spectro-polarimetry. The instrument, named Mt. Abu Faint Object Spectrograph and Camera- Echelle Polarimeter (M-FOSC-EP), has been designed as a facility instrument having capabilities of a FOSC (imaging and low-resolution spectroscopy) along with an optical arm for the intermediate-resolution spectro-polarimetry.

Spectro-polarimetry, being a photon-hungry technique, has been mostly utilized on large aperture (>3m diameter) telescopes such as HARPSpol-High Accuracy Radial velocity Planet Searcher (R$\sim$120000) at ESO 3.6m-Telescope, La Silla, Chile; ESPaDOnS- Echelle SpectroPolarimetric Device for the Observation of Stars (R$\sim$120000) at 3.6m Canada-France-Hawaii Telescope, Mauna Kea; SARG (R$\sim$160000) at 3.55m telescopes, on the Roque de Los Muchachos, La Palma, Canary Islands, Spain; HRS: High-Resolution Spectrograph (R$\sim$16000,37000,67000) at 11m Southern African Large Telescope (SALT), etc. While these instruments have been very successful in exploring the spectro-polarimetry regime of the observational sciences, most of these instruments have specific science programs and may not be an ideal facility for the transient target of opportunity (ToO) observations, which generally requires high cadence observations. Small to moderate aperture telescopes (2-3m diameters) equipped with relatively lower resolution spectro-polarimeters (R$\sim$10000-15000) can be a great facility, in particular for the high cadence observation of the transients such as novae or supernovae, due to the relative ease of observing time on such telescopes. Few such instruments exist on similar telescopes around the world. e.g., BOES-BOAO Echelle Spectrograph (R$\sim$60000) at 1.8m telescope, Bohyunsan Optical Astronomy Observatory, Korea; MuSiCoS- MUlti SIte COntinous Spectroscopy (R$\sim$35000) at 2m Telescope Bernard Lyot, Pic du Midi in France; VESPolA-Very precise Echelle SpectroPolarimeter (R$\sim$8000) at 1.3m Araki telescope at the Koyama Astronomical Observatory of Kyoto Sangyo University (Kyoto, Japan); LIPS-LIne Polarimeter and Spectrograph (R$\sim$7000) at 2.2m telescope of University of Hawaii, etc.

Below we shall discuss some of the science cases that would benefit from an instrument like M-FOSC-EP on the upcoming PRL 2.5m telescope. Later we shall discuss the basics of polarization measurements in astronomy and the design concepts of spectro-polarimeters. These concepts are later utilized while developing the optical design of M-FOSC-EP and a prototype spectro-polarimeter (see chapter 5).

1.5 Science programs to be explored with M-FOSC-EP

As mentioned above, the perspective science cases with M-FOSC-EP include several ongoing programs on existing PRL 1.2m telescope that would benefit from the larger aperture of the newer telescope, e.g., spectroscopy of novae and supernovae, photometric variability studies of AGNs, spectroscopic studies of M dwarfs, etc. The larger aperture of the telescope also opens up several newer avenues like spectro-polarimetry studies of symbiotic systems, fast photometric studies of symbiotics, higher-resolution spectroscopy/spectro-polarimetry studies of novae, spectro-polarimetry studies of super-novae, AGNs, etc. These goals are discussed below.

1.5.1 Studies of novae & symbiotic systems

(a) Intermediate resolution spectroscopy of novae & symbiotic stars

Symbiotic stars are a class of binary star systems consisting of a very hot compact white dwarf and a very cool red giant star. Observations of the interaction between these two components, like mass transfer from the cool giant to the white dwarf, their ionization environment, etc., are essential to understand the mechanism of mass accretion onto the compact object, ejected material propagation in their surrounding, etc. Some binary systems also show the novae outbursts caused by thermonuclear runaway events on the surface of a degenerate white dwarf, which has accreted material from the secondary star (e.g., main sequence, cool giant star) in a close binary system. Several emission lines are present in the optical spectrum of these two astronomical objects/phenomena, which are caused by the ionization of the surrounding of the secondary star due to radiation from the hot white dwarf or from exploded ejecta. Temporal variation in these lines can provide information about the physical conditions of the system. A recent study presented in Gałan et al. (2022) shows the temporal evolution of several spectral lines present in the symbiotic binary St 2-22 (see fig.1.10). This is a good example to show that M-FOSC-EP with a resolution of around 10000-15000 can do such studies showing temporal variation in emission lines in symbiotic stars (the profile variation shown in the figure has been taken with an intermediate-resolution spectrograph (R∼14000)).

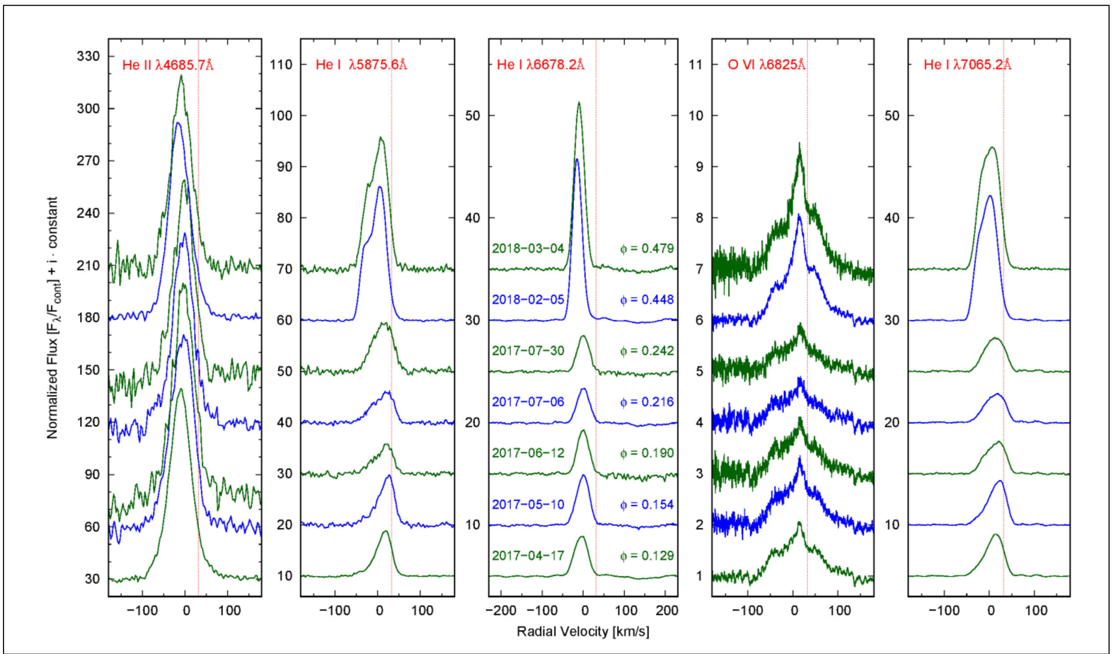

Figure 1.10: Evolution of several line profiles including Raman scattered O VI line (the figure is reproduced from Gałan et al. (2022)) in the spectra of a symbiotics system St 2-22. The spectra are recorded with the HRS instrument on the South African Large Telescope.

(b) Spectro-polarimetry of novae & symbiotic stars

The line profile variation in novae & symbiotics could arise due to changes in the optical depth morphology. Spectro-polarimetry is a suitable technique to explore such possibilities by measuring the wavelength-dependent polarization, thereby probing their geometry. The O VI Raman scattered line in symbiotic systems is polarized. Harries & Howarth (1996) shows that the line was found to be stable in intensity profiles, but there were significant changes in both magnitude and direction of the polarization. As shown in Fig. 1.11), the

RGO Cassegrain spectrograph observed this phenomenon with a polarimeter module having the resolution of ∼5500. M-FOSC-EP with a resolution of 12000-15000 can also resolve these lines with better detail.

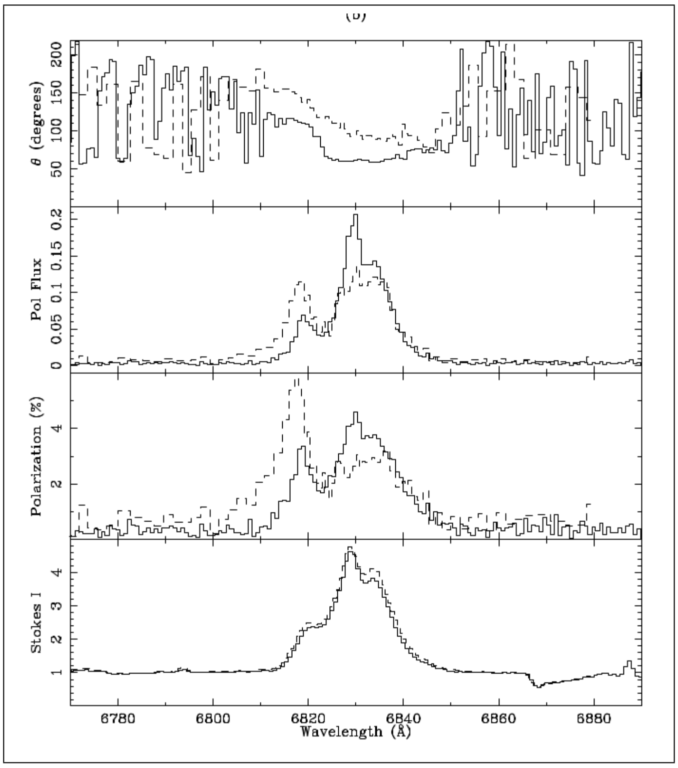

Figure 1.11: Plots of Raman scattered O VI line 6825 Å line in the symbiotics stars Hen 1242. plot shows two observations: May 1994 (solid line) and March 1992 (dashed line). The polarization spectra have the continuum vector subtracted. This figure is reproduced from Harries & Howarth (1996)

(c) Fast photometry of symbiotic stars

While symbiotic stars have traditionally been identified with intense emission lines of highly ionized species, recent developments Mukai et al. (2016) also brought forward a class of non-shell burning symbiotic systems having extremely weak emission lines which are usually not detectable in low-resolution spectroscopy. Therefore the more prevalent low-resolution spectroscopy may not be an ideal tool for their detection. However, fast photometric observations in bluer bands (U/B bands) at the time scale of a few seconds are suggested to be a good probe for the accretion disk instabilities, which points toward the symbiotic nature of the underlying stellar system. One such flickering observation of a symbiotic star ZZ Cmi (Zamanov et al., 2021) is shown in Fig. 1.12. Such studies require a detector system with faster readouts; therefore, an EMCCD-based detector system is being considered for the FOSC arm of M-FOSC-EP.

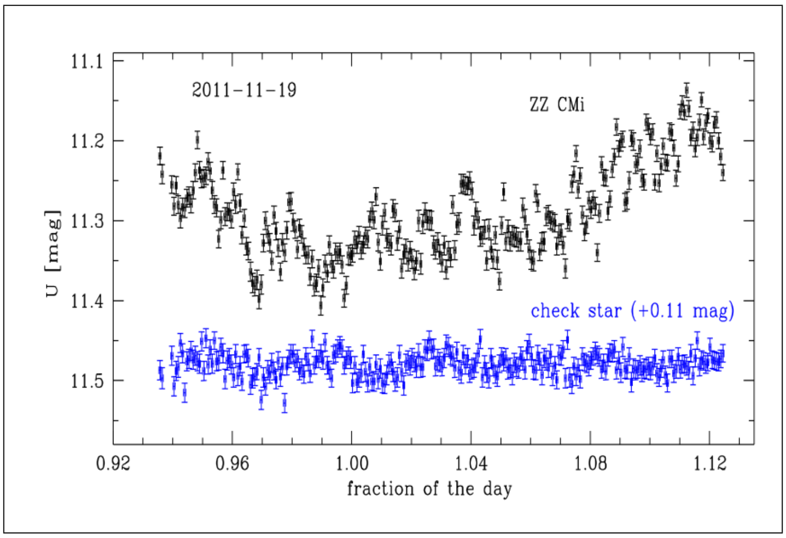

Figure 1.12: Detection of flickering in U band light-curve of a symbiotic binary ZZ CMi (Figure is reproduced from Zamanov et al. (2021)).

1.5.2 Studies of M dwarfs

M dwarfs are the lowest mass stars located at the bottom of the main sequence stars in the HR diagram. 70% stars of our Galaxy consist of M dwarfs, which represent about 40% of the total stellar mass of our Galaxy. Their small size and low mass range make them a suitable candidate to detect planets around them in the habitable zone, and thus their study may help to understand exoplanet formation. The determination of stellar parameters such as effective temperature, surface gravity, and metallicity of M dwarfs play a crucial role in their studies. While the effective temperature and the surface gravity can be derived with low-resolution spectroscopy using the synthetic models, the metallicity measurements require medium-high resolution spectroscopy. The high-resolution spectra and broad wavelength coverage allow an understanding of the onset of dust and cloud formation at cool temperatures. Furthermore, these studies give a path to understanding the physical processes in the cool atmosphere of M dwarfs. Recently, Rajpurohit et al. (2018a), have done such kind of study for 292 M dwarfs to find the stellar parameters (see fig.1.13). M-FOSC-EP shall be able to do such kind of study with the resolution of 10000-15000.

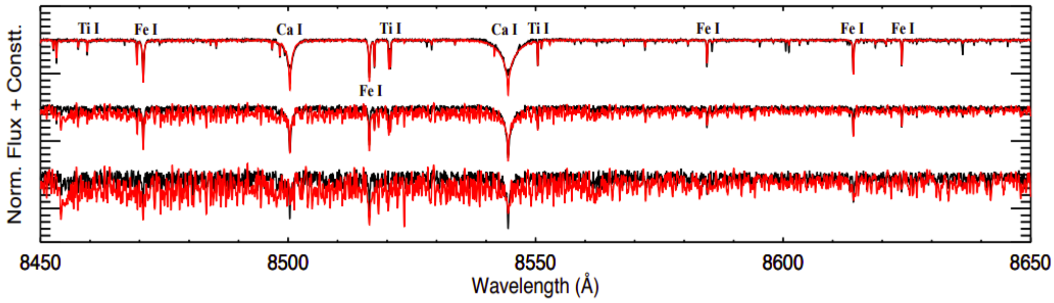

Figure 1.13: CARMENES spectra of GJ 180 (M1.0, top), Ross 128 (M4.0, middle), and HD 180617 (M8.0, bottom) in black is compared with the best-fit BT-Settl model (red). Figure is reproduced from Rajpurohit et al. (2018a).

1.5.3 Spectro-polarimetry of Super Novae

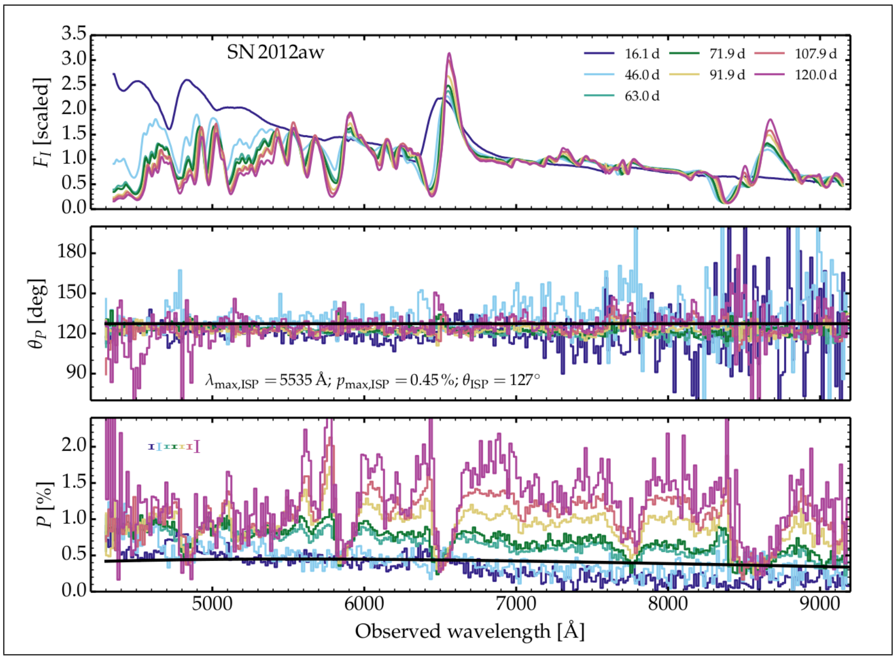

Figure 1.14: Multiepoch VLT spectro-polarimetric observations of SN2012aw showing the total flux at the top, the observed polarization angle, and the observed degree of polarization. Each epoch is color coded and mentioned as the label of top panel. Figure is reproduced from Dessart et al. (2021).

Conventional photometry and spectroscopy methods only give limited ideas about the structures of the Supernovae (SNe) ejecta that are expected to be present in their morphology due to complex ejecta geometry, circumstellar surrounding, kinematics, etc. The observable emission is expected to be polarized since the asymmetry is present in the SNe ejecta. Thus, spectro-polarimetry may be a helpful technique to provide the SNe explosion geometry. The asymmetry present in SNe ejecta and various element formed in the ejecta can be traced by the continuum polarization and polarization profiles of associated spectral lines, respectively. Recently, some of the low-resolution spectro-polarimetry has been done using FORS1 and FORS2 (see fig.1.14) instruments on VLT, which describe the asymmetry of the ejecta (Patra et al., 2022; Dessart et al., 2021). Such studies can also be attempted with M-FOSC-EP (R∼10000-15000), albeit with brighter supernovae.

1.5.4 Spectroscopy & Spectro-polarimetry of AGNs

It is generally accepted that supermassive black holes (SMBH) are located in the center of massive galaxies. Active galactic nuclei (AGNs) are the most powerful and steady radiation sources in the Universe. A tremendous amount of energy is produced by the accretion of matter onto supermassive black holes. The optical spectrum of AGN shows a broad emission line having a velocity range of thousands to tens of thousands of km/s, coming from the gas clouds present in the Broad Line Region (BLR). While this simple picture is useful, the internal dynamic of AGNs is not well understood, as a very high spatial resolution is required to resolve the central part. AGN variability is generally used to investigate their internal structure, the mass of the SMBH, the size of the BLR, etc. M-FOSC-EP could be used for reverberation mapping (RM) technique to record the change in emission line flux in response to change in continuum flux. The emission line profile variability and RM measurement can be used to study the dynamics of BLR, etc. The higher resolution mode of M-FOSC-EP could also be used to study the narrow-line Seyfert 1 galaxies. Some recent studies, e.g., Songsheng & Wang (2018), have also pointed out the importance of spectro-polarimetry observations in such measurements. Such studies can be done either by spectroscopy or spectro-polarimetry mode of M-FOSC-EP.

1.6 Polarization in Astronomy

Several phenomena could cause polarized light in astrophysical situations. As polarization is a property of light in which the vibration of the electric field vector has a preferred orientation, measuring the degree of polarization and/or polarization angle is a great probe to determine the orientation or morphology of the underlying astrophysical system. Some of the majorly observed phenomena in optical astronomy (Eversberg & Vollmann (2015) and reference therein) are discussed below:

1) Zeeman effect: It is a phenomenon in which a spectral line splits into two or more components in a uniform & strong magnetic field. The number of split lines depends on the strength of the magnetic field and hence helps to estimate the magnetic field of the stars. Depending on the relative observing geometry, the Zeeman effect can be the transverse or longitudinal Zeeman effect. This phenomenon is commonly seen in various astrophysical bodies such as Sun, magnetic A_P stars, HI clouds, galactic molecular clouds, etc.

2) Synchrotron & Cyclotron radiation: Accelerated charged particles in the magnetic field emit polarized radiation. Cyclotron radiation (particle moving with non-relativistic velocities) or Synchrotron radiation (particle moving with relativistic velocities) are some of the most common forms of astrophysical continuum radiation and are observed in a number of astrophysical sources like radio galaxies, pulsars, AGNs, Quasars, neutron stars, X-ray binaries, etc.

3) Rayleigh scattering: Scattering is a major cause of polarization in astrophysical situations. For example, in Rayleigh scattering, the light is scattered if it passes through a medium having particles of comparable size to the wavelength of the light. Rayleigh scattering exhibit the wavelength dependency of $1/\lambda^4$, and thus it affects the blue light more compared to red. The scattered light is partially or completely linear polarized in the plane perpendicular to the incident light direction. This scattering is primarily seen in comets, reflection nebulae, atmospheres of late-type stars, spiral galaxies, etc.

4) Dichroic absorption: Polarization also arises when the starlight travels through a magnetized, dusty interstellar medium (ISM), and it occurs as a result of dust scattering (Rayleigh scattering) or dichroic extinction. Dichroic extinction refers to interstellar dust, which consists of elongated particles aligned with their short axes parallel to the magnetic field. As light passes through these aligned grains, the component of the electric field vector partially absorbed along their long axis. Thus, the light becomes linearly polarized parallel to the magnetic field direction. The light absorbed by the dust grain is re-emitted as thermal radiation having linear polarization perpendicular to the magnetic field. This mechanism is used to characterize the magnetic field of the ISM as it is observed towards many stars in our Galaxy.

In addition, there are several other effects that can give rise to polarized light, e.g., the Cherenkov effect, Stark effect, Raman scattering, Thomson scattering, Hanle effect, grey-body magneto-emission, gyro-resonance emission, etc.

1.7 Polarization measurements in Astronomy

1.7.1 The Stokes parameters

The different causes of the polarization in astronomy have been discussed in the previous section. Here we describe some terminologies used to define polarized light and the theoretical framework of polarization measurement. In the vector wave theory of light, the electric field and magnetic field vectors are perpendicular to each other and to the direction of the propagation. The polarization state of light can be described by using the electric field vector. The orthogonal components of an electric field vector of light propagating in $+z$ direction at a time t, can be written as,

$$\vec{E_x}(z,t) = E_{0x} cos(kz - \omega t)\hat{\mathbf{x}} \tag{1.1}$$

$$\vec{E_y}(z,t) = E_{0y} cos(kz - \omega t + \epsilon)\hat{\mathbf{y}} \tag{1.2}$$

Where E_{0x} and E_{0y} are the amplitudes, ϵ is the phase difference between the x and y components of $\vec{E}$, $k = 2\pi/\lambda$ is the wave number, and ω is the angular frequency of the wave. Depending upon the phase difference and amplitude of these orthogonal components, the light is defined linearly, circularly, and elliptically polarized as follows:

a)If ϵ=0°, then light is linearly polarized,

b)if ϵ=90° and $E_{0x} = E_{0y}$, then light is circularly polarized.

c)if ϵ=90° and $E_{0x} \neq E_{0y}$, then light is eliptically polarized.

Re-arranging the equations 1.1 and 1.2,

$$\left(\frac{E_x(t)}{E_{0x}}\right)^2 + \left(\frac{E_y(t)}{E_{0y}}\right)^2 - 2\frac{E_x(t)E_y(t)}{E_{0x}E_{0y}} = sin^2\epsilon \tag{1.3}$$

This is an ellipse equation, and since it describes the polarization state of light, it is called a polarization ellipse. The polarization ellipse is shown in Fig. 1.15, where the orientation angle ψ and ellipticity angle χ can describe the polarization state of light.

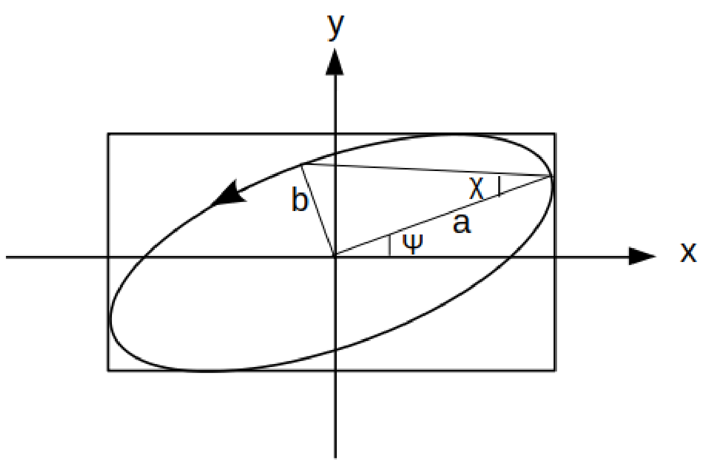

Figure 1.15: Figure shows the left handed polarization ellipse.

If we take an average over a single time period of oscillation of equation 1.3,

$$(E_{0x}^2 + E_{0y}^2)^2 - (E_{0x}^2 - E_{0y}^2)^2 - (2E_{0x}E_{0y}cos\epsilon)^2 = (2E_{0x}E_{0y}sin\epsilon)^2 \tag{1.4}$$

Each term of this equation is denoted by (Goldstein, 2003),

$$I = E_{0x}^2 + E_{0y}^2 = I_{0^\circ} + I_{90^\circ} \tag{1.5a}$$

$$Q = E_{0x}^2 - E_{0y}^2 = I_{0^\circ} - I_{90^\circ} \tag{1.5b}$$

$$U = 2E_{0x}E_{0y}cos\epsilon = I_{45^\circ} - I_{135^\circ} \tag{1.5c}$$

$$V = 2E_{0x}E_{0y}sin\epsilon = I_{RCP} - I_{LCP} \tag{1.5d}$$

These parameters I (total intensity), Q (majority of linear horizontal polarization over linear vertical polarization), U (majority of linear +45° polarization over linear −45° polarization), and V (majority of right-handed circular polarization over left-handed circular polarization) are the Stokes parameters and can be estimated by observations. Sir George Gabriel Stokes introduced these parameters in 1852 to measure the state of polarization. The orientation angle ψ, ellipticity angle χ and the degree of polarization p can be estimated with the help of stokes parameters as follows (Goldstein, 2003):

$$\tan 2\psi = \frac{2E_{0x}E_{0y}\cos\epsilon}{E_{0x}^2 - E_{0y}^2} = \frac{U}{Q} \tag{1.6}$$

$$\sin 2\chi = \frac{2E_{0x}E_{0y}\sin\epsilon}{E_{0x}^2 + E_{0y}^2} = \frac{V}{I} \tag{1.7}$$

$$p = \frac{\sqrt{Q^2 + U^2 + V^2}}{I} \tag{1.8}$$

1.7.2 The optical setup

Usually, the fraction of circularly polarized light for astrophysical objects is very low, and it is mostly the linear polarization which is mostly measured. Therefore, here we will discuss a basic optical set-up used to measure the linear polarization in the incoming stellar radiation. Three stokes parameters (or four intensities I_0, I_{90}, I_{45}, and I_{145}) are required to measure the state of linear polarization. These intensities can be observed by rotating a polarizer at four appropriate angles; thus, four sets of observations are required. A rotatable HWP followed by a fixed Wollaston Prism (WP) is a commonly used set-up in optical instrumentation. As WP provides two orthogonal intensities, (I_0, I_{90} or I_{45}, I_{135}) can be measured in one observation snap-shot, thereby reducing the number of observations from four to two. Below we briefly discuss the basic characteristics of these two components.

Half Wave Plate (HWP): Half-wave plate, also known as a retarder, is an optical device that can change the polarization angle of linearly polarized light. It works based on the birefringence property of the materials (Quartz, Calcite, etc.). It is an optical property of material showing the refractive index dependency on the polarization state of light passing through it. HWP introduces a phase shift of 180° between two orthogonal polarization components of the light. If there is a polarized light having polarization vector $\hat{\mathbf{p}}$ and it incident on HWP such that it makes an angle θ with its fast axis, then the incident electric field vector can be defined as,

$$\vec{E} = Ee^{i(kz-\omega t)}\hat{\mathbf{p}} = E(\cos\theta\hat{\mathbf{f}} + \sin\theta\hat{\mathbf{s}})e^{i(kz-\omega t)} \tag{1.9}$$

Where $\hat{\mathbf{f}}$ and $\hat{\mathbf{s}}$ are the vectors along the fast and slow axis, respectively. Here, the fast axis refers to the axis along which the electric field vector propagates faster than the slow axis. After passing through the HWP, it will introduce a phase shift term -1 ($=e^{i\pi}$) between $\hat{\mathbf{f}}$ and $\hat{\mathbf{s}}$, and hence the electric field vector becomes,

$$\vec{E'} = E(\cos\theta\hat{\mathbf{f}} - \sin\theta\hat{\mathbf{s}})e^{i(kz-\omega t)} = E[\cos(-\theta)\hat{\mathbf{f}} + \sin(-\theta)\hat{\mathbf{s}})]e^{i(kz-\omega t)} \tag{1.10}$$

Equation 1.10 shows that after passing through HWP, the electric field vector makes an angle of $-\theta$ with $\hat{\mathbf{f}}$. It means the HWP changes the polarization angle by 2θ (Goldstein, 2003) as shown in Fig. 1.16.

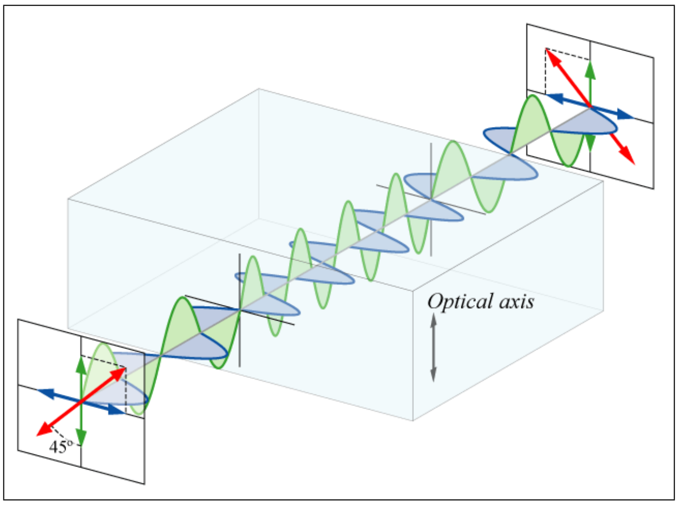

Figure 1.16: Figure shows a half wave plate, rotating polarization angle by 90° (Source: https://en.wikipedia.org/wiki/Waveplate).

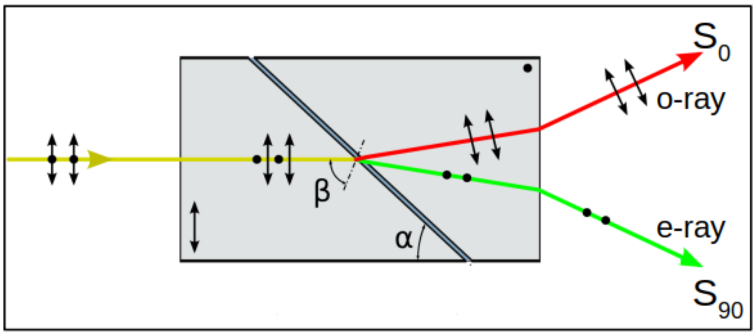

Figure 1.17: Figure shows the Wollaston prism splitting ordinary and extra-ordinary (Source: https://commons.wikimedia.org/wiki/File:Wollaston_Prism_DE.svg).

Wollaston prism (WP): Wollaston prism is also an optical device made up of two orthogonal prisms of birefringent material. They are cemented together such that the optic axis of prisms are perpendicular to each other. When a linearly polarized light enters the prism and hits the interface of the prism, then the orthogonal components of light experience an increase and decrease in their refractive indices. Due to the difference in refractive indices for ordinary ray (o-ray) and extra-ordinary ray (e-ray), the o-ray and e-ray are refracted in the opposite direction and split into two beams (see Fig. 1.17). The splitting angle between o-ray and e-ray can be estimated as (Simon, 1986),

$$\delta = 2\sin^{-1}(n_e - n_o)tan\alpha \tag{1.11}$$

In a typical polarization measuring set-up, an HWP + WP combination is placed in the path of the collimated beam. If no rotation is given to the HWP, it provides I_0 and I_{90}. However, if HWP rotated by 22.5°, the polarization angle is changed by 45° (HWP changed the polarization angle by 2θ), and hence I_{45} and I_{135} can be measured. The stokes parameters then can be estimated by using equations 1.5a, 1.5b, and 1.5c. Lastly, these stokes parameters provides the polarization angle (ψ) and degree of polarization (p) using equations 1.6, and 1.8.

1.7.3 Spectro-polarimeter: High resolution spectrometer using Echelle gratings - A theoretical perspective

In a typical spectro-polarimeter, a spectrometer is coupled to the polarimeter optical set-up (as discussed above) to provide the spectra of the separated o- and e-rays. Subsequent comparison of their recorded flux with respect to the wavelength would then provide the Stokes parameters. A typical high-resolution spectrometer uses Echelle gratings to disperse the spectra in the higher orders and employs a cross-disperser element (prism or grating) to spatially separate the overlapping higher orders. Below we discuss some of the concepts related to the design of an echelle spectrometer, which has been used to design the M-FOSC-EP and its prototype (see chapter 5).

Echelle gratings

The diffraction grating is an optical device used to disperse the light, based on the concept of interference between the diffracted light by a large number of grooves present on its surface. The gratings may be transmissive or reflective in nature. If an incoming light beam hits the surface of grating at angle α (see left Fig. 1.18) and is refracted to an angle β (in case of transmission grating), then for the constructive interference, the grating equation can be written as,

$$m\lambda = d(\sin\alpha + \sin\beta) \tag{1.12}$$

Where m is the diffraction order, λ is the wavelength, and d is the groove spacing of the grating. This relation is known as a grating equation. If we give an off-axis angle γ to the grating, as shown in the right panel of Fig. 1.18, then the more general form of the grating equation becomes,

$$m\lambda = d\cos\gamma(\sin\alpha + \sin\beta) \tag{1.13}$$

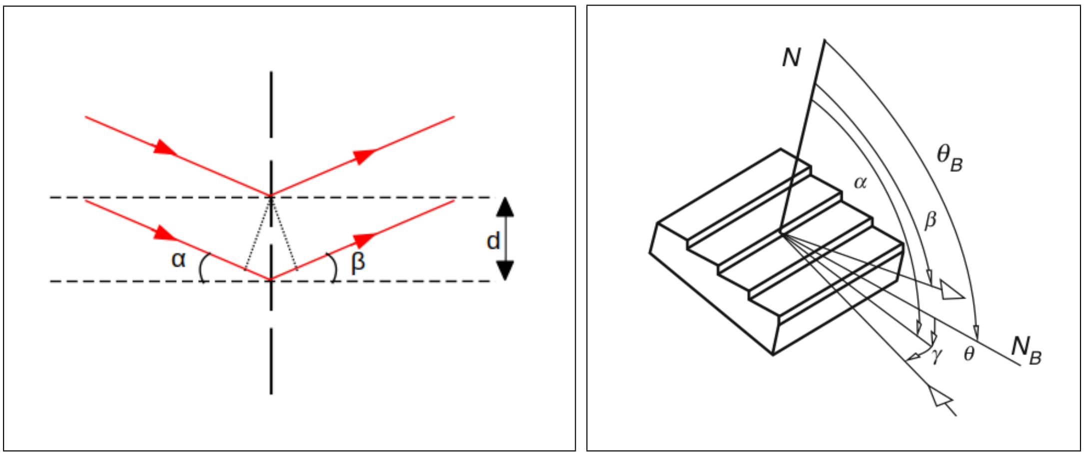

Figure 1.18: The left panel shows the schematic diagram of a transmission grating. The right panel shows the reflection grating showing the various angles. Figure is reproduced from Eversberg & Vollmann (2015). γ is the off-axis angle, θ is the difference between α and β, θ_B is the blaze angle, N is the grating normal, and N_B is the groove facet normal.

The angular dispersion of the grating can be estimated by differentiating equation 1.13,

$$\frac{d\beta}{d\lambda} = \frac{m}{d\cos\gamma\cos\beta} \tag{1.14}$$

This equation indicates that the higher orders have high dispersion, but one must take care of the efficiencies in these orders. The blaze angle of the gratings helps to employ the maximum efficiency in a given direction. If we choose the blaze angle θ_B and considering $\alpha = \beta = \theta_B$, then using equations 1.13 and 1.14,

$$\frac{d\beta}{d\lambda} = \frac{2}{\lambda}\tan\theta_B \tag{1.15}$$

Hence, gratings with larger blaze angles are required to achieve large angular dispersions. Such gratings having large blaze angles, angles of incidence and diffraction, and working at high order numbers, are known as Echelle gratings.

Overlapping of higher orders: the concept of cross dispersion

The central wavelength of each order is inversely proportional to the order number (equation 1.13). At the same time, the separation between adjacent orders can be estimated by differentiating equation 1.13 with respect to the order number ($d\lambda/dm$) and found to be proportional to 1/m^2. It means the wavelength intervals will overlap in higher orders. Since each order has its own specific wavelength range, another dispersive element (grating or prism) having dispersing direction perpendicular to the Echelle dispersion can be used to separate the orders. The second dispersive element is called the cross disperser, and this technique is called the Echelle spectroscopy.

If the cross-disperser has an angular dispersion $d\beta_c/d\lambda$, the distance between two adjacent orders i and j on the CCD plane is given as:

$$\Delta x_{ij} = f_{cam}.\Delta\lambda_{ij}.d\beta_c/d\lambda$$

where f_{cam} is the focal length of the camera optics, and $\Delta\lambda_{ij}$ is the wavelength difference between the central wavelengths of the two adjacent orders. The distances Δx_{ij} for various orders can vary differently for prism and grating cross-dispersers, as the above equation shows that spacing between successive orders is determined by the wavelength dependence of the angular dispersion of the cross-disperser. While the prism has the advantages of offering relatively higher efficiency as compared to the gratings, they have non-linear dispersion. On the other hand, the gratings give sufficiently high linear dispersion, ensuring that the orders are well separated, even in extreme wavelength ranges.

In the case of the prism cross-disperser, the order distances are reduced because the prism dispersion is proportional to dn/dλ (n is the refractive index), which in turn is inversely proportional to the wavelength, thereby decreasing the inter-order spacing in the red wavelength range. The orders may come very close (or, in the worst case, overlap) to cause undesirable "cross-talk". Gratings cross-disperser would be having a separation between the orders in proportion to λ^2; thus, once the spectral order separation is ensured at the lowest λ, it would only be increased subsequently. For the above reasons, grating cross-disperser was found suitable to be used in the Echelle spectro-polarimeter, as the simultaneous recording of two spectra (for o and e rays) in multiple orders demands sufficient order separation across all the orders.

Spectral Resolution

The spectral resolution (R) is an important parameter for a spectrograph, and it is given by,

$$R = \frac{\lambda}{\Delta\lambda} = \frac{f_{cam}}{d_D}.\lambda.\frac{d\beta}{d\lambda} \tag{1.16}$$

where $\Delta\lambda$ is the resolution element, f_{cam} is the focal length of the camera optics, d_D is the physical size of the slit at the telescope focal plane. Using equation 1.13, 1.14, and 1.16,

$$R = \frac{f_{cam}}{d_D}\frac{(\sin\alpha + \sin\beta)}{\cos\gamma\cos\beta} \tag{1.17}$$

For littrow configuration, where $\alpha = \beta = \theta_B$, the spectral resolution is proportional to $\tan\theta_B$. It means a high blaze angle provides a higher resolution.

The Slit-tilt

Echelle gratings are used in the spectrometer with an out-of-plane angle γ to separate the incident and dispersed beams by 2γ. However, this angle also results in an effect of line-tilt/slit-tilt, which effectively increases the projected slit width and lowers the resolution. This effect is shown in Fig. 1.19.

If χ is the tilt in the slit with respect to the order normal, then this angle can be estimated as:

$$tan\chi = 2tan\Theta_B tan\gamma \tag{1.18}$$

This tilt in the projected slit would increase the effective slit width on the CCD plane by a factor of $1/\cos\chi$. This would, thus, lowers the resolution by the same factor if the slit is circular, e.g., fiber core. However, in the case of the long slit, where there is also intensity spread in the cross-dispersion direction, this tilt may

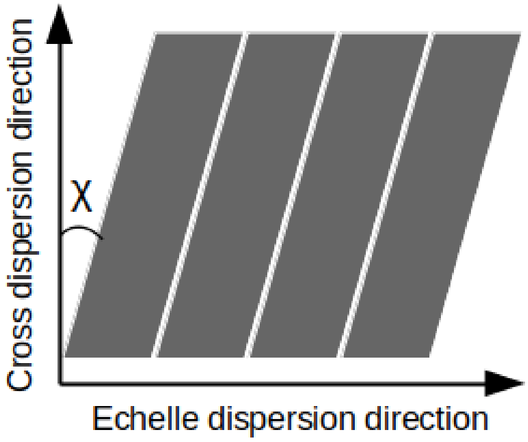

Figure 1.19: The tilt of the spectroscopy slit on the detector plane of echelle spectrometer.

further lower the resolution if the intensity is summed along the cross dispersion direction. However, this effect can be removed by counter-rotating the slit at the input plane of the echelle spectrometer.

The Grating Efficiency

The efficiency pattern in gratings can be formulated as the combination of a blaze function (or diffraction pattern of a single groove) and interference function. The blaze function $B(\delta)$ modulates the intensity of the interference function $G(\psi)$, and then it gives a combined efficiency profile within a diffraction order. The observed intensity from a grating is given by (Eversberg & Vollmann, 2015),

$$I = I_0 \frac{sin^2\delta}{\delta^2} \frac{sin^2 N\psi}{sin^2\psi} = I_0 B(\delta) G(\psi) \tag{1.19}$$

where,

$$\delta = \frac{kb}{2}(sin(\alpha - \Theta_B) + sin(\beta - \Theta_B))$$

$$\psi = \frac{kd}{2}(sin\alpha + sin\beta)$$

Here, I_0 is the incident intensity, $k = 2\pi/\lambda$ is the wave vector, d is the groove spacing and b is the illuminated size of groove facet. Although a more general relative efficiency expression is given by Bottema (1981) and can be written as,

$$E(\alpha,\beta,m) = \frac{\cos\alpha}{\cos\beta} sinc^2 \left[m\pi\cos\alpha \frac{\sin\{1/2(\alpha+\beta)-\theta_B\}}{\sin\{1/2(\alpha+\beta)\}} \right] \qquad \alpha > \beta \quad (1.20)$$

$$E(\alpha,\beta,m) = \frac{\cos\beta}{\cos\alpha} sinc^2 \left[m\pi\cos\beta \frac{\sin\{1/2(\alpha+\beta)-\theta_B\}}{\sin\{1/2(\alpha+\beta)\}} \right] \qquad \alpha < \beta \quad (1.21)$$

1.8 Chapter Conclusions

This chapter describes the objectives and rationale behind MFOSC-P development. The optical and opto-mechanical designs of the instrument are presented, along with its electrical controls and software interface. The design and development routes adopted for MFOSC-P are rather unconventional for a FOSC kind of instrument. Some of the features of MFOSC-P which make it a noteworthy development for the astronomical community; in particular for the users of small aperture telescopes, are as follows: a simple optical design, relaxed opto-mechanical tolerances, use of an off-the-shelf detector system, and a robust control system based on commercially available components. MFOSC-P was successfully developed and commissioned on the PRL 1.2m telescope in February 2019 after three and a half years of fabrication and development. The subsequent chapters of this thesis will describe these development activities, laboratory and on-sky commissioning, and a science verification program with this instrument.

As soon as the MFOSC-P was commissioned on the PRL 1.2m telescope, the efforts began to develop an extended FOSC - named M-FOSC-EP for the upcoming 2.5m telescope, which would also incorporate the provisions for an intermediate resolution spectrometer. A prototype instrument - named ProtoPol was also designed, which could be used on both 1.2m and 2.5m PRL telescopes. In this chapter, we have discussed the scientific objectives for developing such instruments and provided a basic theoretical framework used to develop the designs of these instruments. The designs will be discussed in chapter 5.

Chapter 2

Assembly-Integration-Test (AIT) & Characterization of MFOSC-P

We have discussed (Chapter 1, section 1.2 and 1.3) the requirements and optical/opto-mechanical designs of MFOSC-P on the PRL 1.2m telescope. MFOSC-P was designed to provide low/medium resolution optical spectroscopy and seeing limited imaging in visible wavebands. It was assembled and characterized in the laboratory between October 2018 to January 2019. Performance verification of the optics components (e.g., lenses, lens sub-assemblies, etc.), motion subsystems testing, imaging and spectroscopy performance verification, etc., were conducted in the laboratory during this period.

The Assembly-Integration-Test (AIT) is an important and essential phase of the instrument development process. During the AIT phase, each component and subsystem of the instrument is thoroughly characterized before integrating within the instrument system. It consists of sequential integration and various test plans for each component/subsystem to verify the designed specifications and required performance. During the AIT procedure of MFOSC-P, various subsystems were assembled and characterized, first on the optical test bench setup & later within the instrument's enclosure. The laboratory performance verification was done after the assembly of the instrument on the chassis plate. Various components of MFOSC-P like lens assembly/sub-assemblies, detector-camera system, motion systems, control electronics, and control software were tested for their designed performance. A series of experimental tests were carried out before the instrument was fully integrated into the laboratory. Once the instrument was assembled in the laboratory, its laboratory characterization was done with a series of calibration exercises. Subsequently, MFOSC-P was commissioned on the telescope in February 2019. Regular characterization and preliminary science observations were made from February 2019 to June 2019.

In this chapter, the AIT procedure will be discussed in detail, including the characterization of the motion systems, the lenses/lens-assemblies quality check, and the laboratory characterization of MFOSC-P on the optical bench as well as in the instrument envelope. After the commissioning of MFOSC-P on the 1.2m telescope, the on-sky characterization of the instrument was done, and the MFOSC-P data reduction pipeline was developed. These aspects shall also be discussed.

2.1 Assembly-Integration-Test (AIT) of MFOSC-P

2.1.1 Image quality tests of lenses/lens-assemblies

The lenses of the MFOSC-P optical chain were manufactured as per design by a commercial optics manufacturer (M/S Gooch and Housego PLC, UK [1]) and later assembled into the collimator and camera barrels in the laboratory. The lens mounts and barrel were designed and fabricated using the in-house PRL workshop facility. Thus, the first step of the AIT was to assemble the lenses to their respective lens barrels and to check the first-order lens parameters, such as focal lengths, with their designed values. The lenses were assembled into the barrels in a two-step process. First, each of the lenses was mounted to their respective mounts. As required, a mark was made on the edge of the lenses by the manufacturer to identify the surfaces. Accordingly, we put the lenses into their respective mounts and then applied a thin Teflon spacer followed by tightening with a retainer ring as shown in Fig. 2.1. In some cases, two lenses

[1]https://gandh.com/; Accessed: 2020-03-20

were designed to be kept very close to each other. These lenses were housed in a single mount, forming a sub-assembly lens system. These mounts and sub-assemblies were later housed in the barrels.

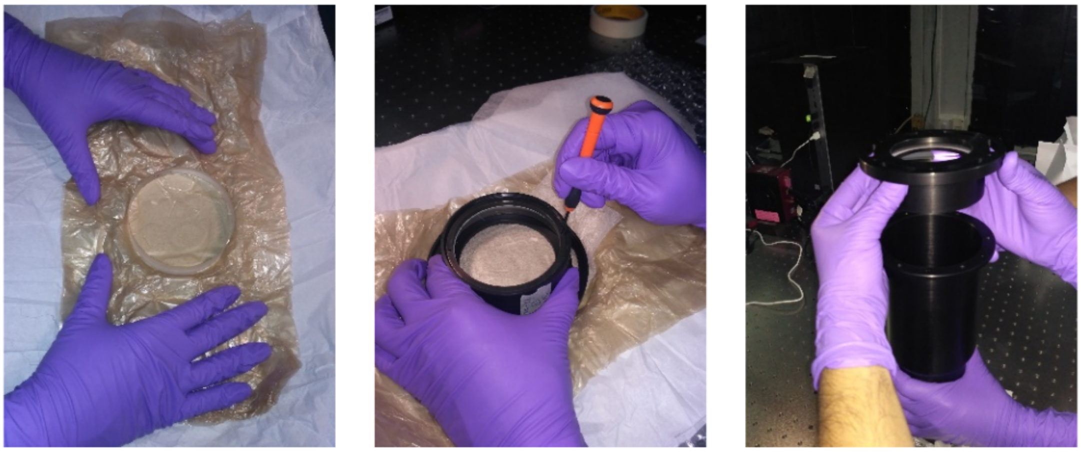

Figure 2.1: The figure shows the development of lens mounts and barrels.

Before the fabrication of the barrels, the primary optics specifications (e.g., focal length) and lens quality of each of the lenses were checked by designing an individual test bench setup for each of the lenses (or, in some cases, for lens sub-assemblies) separately. Different on-axis imaging systems were designed for the test bench around each MFOSC-P lens/lens assembly. Commercial off-the-shelf achromat doublet lenses were used for this purpose. An optical fiber of 10μm core diameter was illuminated with a Neon lamp on one side. The output end of the fiber was imaged using the test setup on a laboratory quality SBIG camera system (Model No. STF-8300M, 5.4μm pixel size) with the pre-determined magnification ratio. Narrow-band Hα filter and a small aperture on the pupil were also used in the setup design to reduce chromatic and geometric aberrations. The image quality was then measured and compared with the expected performance determined with ZEMAX software. Fig. 2.2 shows one such setup to verify the lens specification before its assembly into the barrel. Though such schemes would only provide a good on-axis image quality, they are very useful in verifying the coarse specifications of the lenses without costly wavefront analysis setups like an interferometer.

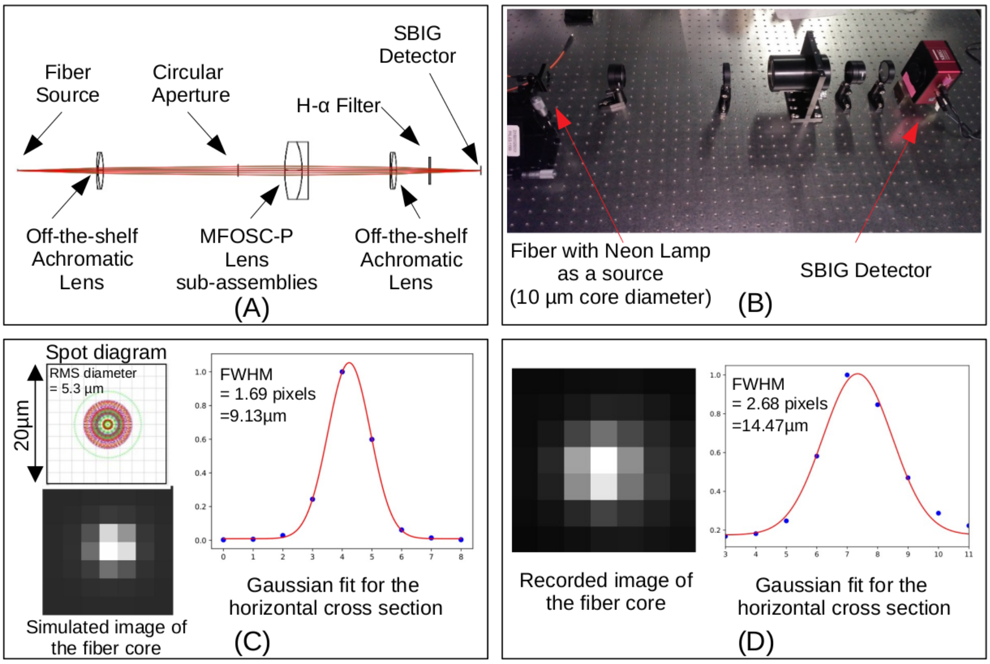

Figure 2.2: The figure shows a test setup designed to verify the basic optical performance of individual lenses and lens assemblies. Panel (A) shows the ZEMAX optical layout of the test setup. This setup was designed to provide magnification of ×0.8 so that a fiber core diameter of 10μm would fall within 1.5 pixels of the detector. Panel (B) shows the laboratory setup as per the ZEMAX design. The spot diagram, simulated image, and expected profile of the fiber core are shown in panel (C). The recorded image of the fiber core and resultant profile is shown in panel (D). SIBG camera with 5.4μm pixel size was used. The measured PSF was in good agreement with the predicted ZEMAX performance. Similar setups were designed and verified for each of the lenses and lens assemblies of MFOSC-P.

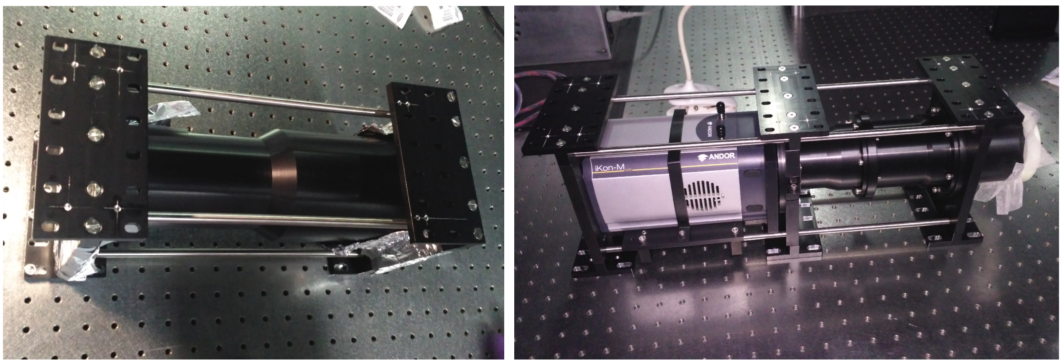

Figure 2.3: The figure shows the lens barrels assemblies, including the optics for the collimator and camera in the left and right panels, respectively.

After the lens quality check of each lens, these lens mounts were assembled into their respective barrels (Right panel of Fig.2.1) using the laser retro-reflection method. The lens alignment into barrels is cross-verified by making a similar optical setup as shown in Fig. 2.2 for each of the lens barrels. Once the barrel alignment is confirmed, these barrels are fixed within a cage-rod system with the help of mounting plates (Fig.2.3). ANDOR camera system was integrated with the camera optics barrel assembly.

2.1.2 Laboratory characterization of MFOSC-P optical system: The test-bench set-up

The optics sub-systems were evaluated for the image quality assessment on the laboratory optical test bench before integrating into the instrument chassis. A laser was first aligned parallel to the optical bench using a retro-reflective flat mirror setup. The collimator and camera cage-rod assemblies (with a CCD detector system) were then aligned on the optical bench using the same laser retro-reflection. A calibration unit optics (to be discussed in Section 2.1.3) with Halogen, Xenon, and Neon lamps were used to simulate the f/13 beam (similar to the 1.2m telescope) on the test bench. A variety of pinholes were used to test the image quality of the MFOSC-P optical chain in this setup. These pinholes were kept at the focal plane of the calibration unit, which coincides with the object plane of the instrument's optics. These pinholes were mounted on a 2-D translational stage to move them over the face of the CCD detector to check the on-axis as well as the off-axis performance of the imaging system. The filter wheel consisting of Bessel's B-V-R-I filters was positioned into the optical path such that the optical axis would pass through the center of the filters (once positioned). This linear setup is shown in the left panel of Fig. 2.4. Test images of the pinholes were recorded at various locations at the detector in different filters.

After verifying the image quality of the imaging system in the linear setup, the system was re-arranged in the spectroscopy modes. The stepper-motor driven rotatable grating module, consisting of a mirror and three gratings (see section 1.3.3), was then aligned with collimator and camera optics barrels. The gratings were rotated appropriately so that their dispersion was along the columns of the CCD detector. A homing sensor was used to set up the zero po-

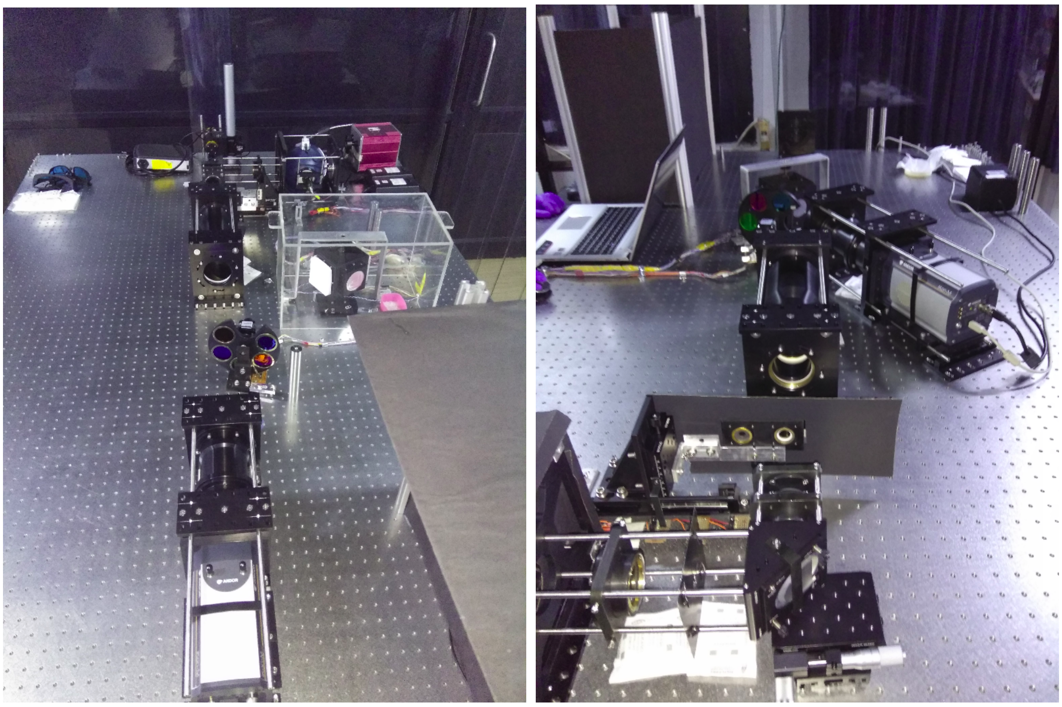

Figure 2.4: The left panel shows the linear setup on the optical bench without the grating box. The right panel shows the 30-degree folded setup on the optical bench with the grating box.

sition of the mirror-grating module. The Camera+Detector section was aligned to make a 30-degrees folded setup with the help of reference images taken during the linear setup. This folded setup is shown in the right panel of Fig. 2.4

The image quality of the MFOSC-P optical chain was characterized on the test bench with off-the-shelf pinholes of various diameters (10, 25, 50 μm, etc.) and resolution test target from M/S Thorlabs Inc[2] in transmission mode (see right panel of Fig. 2.4). As MFOSC-P optics provides magnification of $\times 0.57$, 10μm pinhole is mapped onto 0.44 pixels of the ANDOR camera system. The images of 10μm pinhole at various locations at the detector are shown in Fig. 2.5. Fig. 2.6 shows some of the images obtained to estimate the image quality of MFOSC-P optics. Panels (A) and (B) show the intensity pattern of a 10μm pinhole illuminated by a Neon lamp without filters. A 2-D Gaussian fits this pattern with FWHMs of 1.36 and 1.40 pixels in the X and Y directions. A simple quadrature summation method is used to estimate the Point Spread Function (PSF) of MFOSC-P optics. Thus, the geometrical projection of the

[2] https://www.thorlabs.com; Accessed: 2020-03-20

pinhole is removed from the measured FWHMs. The optics PSF is determined as a Gaussian with FWHM of 1.16 pixels, corresponding to ∼80% encircled energy within 1.5 pixels. This result was consistent with the results of opto-mechanical tolerance analysis, as discussed in section 1.3.2. The PSF was then determined, for each of the B-V-R-I optical filters, by imaging the pinhole at different coordinates on the face of the detector (see Fig. 2.5). The measured PSFs are in good agreement with the predicted performance of the optical design with tolerance analysis. The image quality was also determined by using off-the-shelf resolution and distortion test targets from M/S Thorlabs (Part No. R1L1S1N). The 100μm and 50μm grid patterns, corresponding to the pitch of 4.4 and 2.2 pixels of the CCD, respectively, are well resolved by the MFOSC-P optics chain. The image of the test target is shown in the panel (F) of Fig. 2.6.

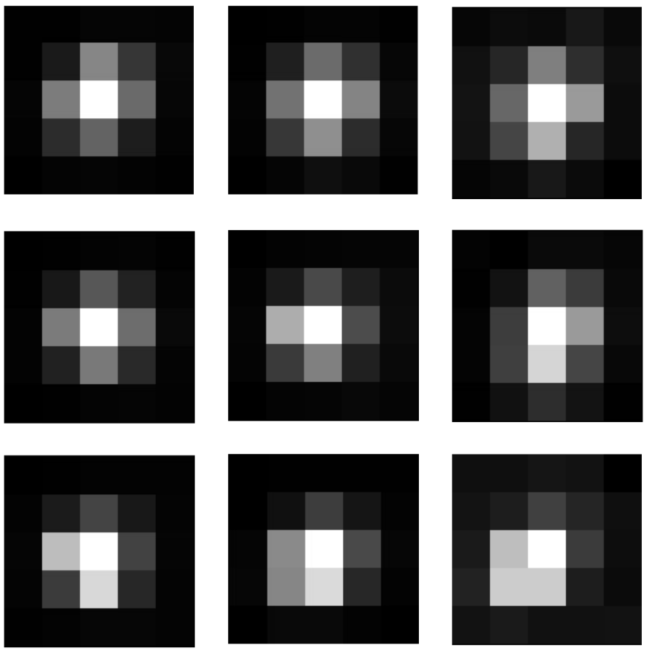

Figure 2.5: The 10μm pin-hole (∼0.44 pixels) images are shown for different locations at the detector from the test-bench set-up. The pin-hole was illuminated by the Neon lamp using the calibration unit at the object plane of MFOSC-P.

MFOSC-P optics was also characterized in all the three spectroscopy modes using lamp spectra with the calibration optics setup. Fig. 2.7 shows the images and reduced spectra of Xenon and Neon spectral lamps using the slit of 75μm width. In all the cases, emission line profiles are well approximated by the Gaussian function with FWHM of ∼3 pixels, which corresponds to 10.9, 5.7, and

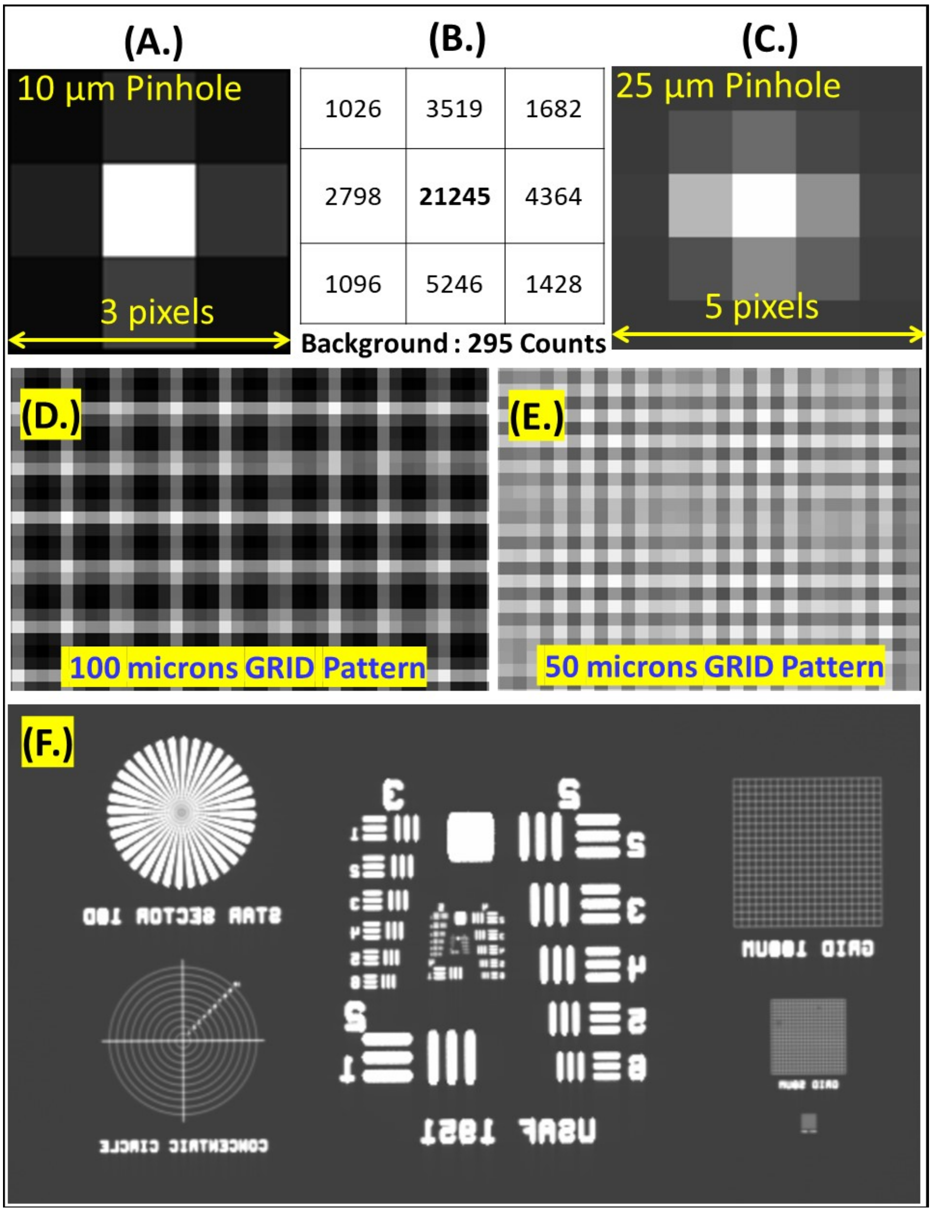

Figure 2.6: Image quality characterization of MFOSC-P. Panel (A) displays the footprint of a 10μm pinhole illuminated with a Neon lamp on the MFOSC-P CCD detector. Panel (B) shows the counts recorded in central 3×3 pixels for the 10μm pinhole. The mean background counts are 295. The FWHM of the PSF is estimated to be $\sim$ 1.16 pixels. Panel (F) shows the standard test and resolution target images. It has grid structures of 100μm and 50μm, which would correspond to the pitch of 4.4 and 2.2 CCD pixels, respectively. Panels (D) and (E) show these grid patterns. MFOSC-P optics well resolve the grid patterns.

3.2Å for R500, R1000, and R2000 grating modes, respectively. Fig. 2.8 shows the profiles of these emission lines for R500, R1000, and R2000 grating modes. Wavelength solutions for all three gratings are determined by using such spectra of the calibration lamps. A third-order polynomial fit is used to determine the wavelength solutions.

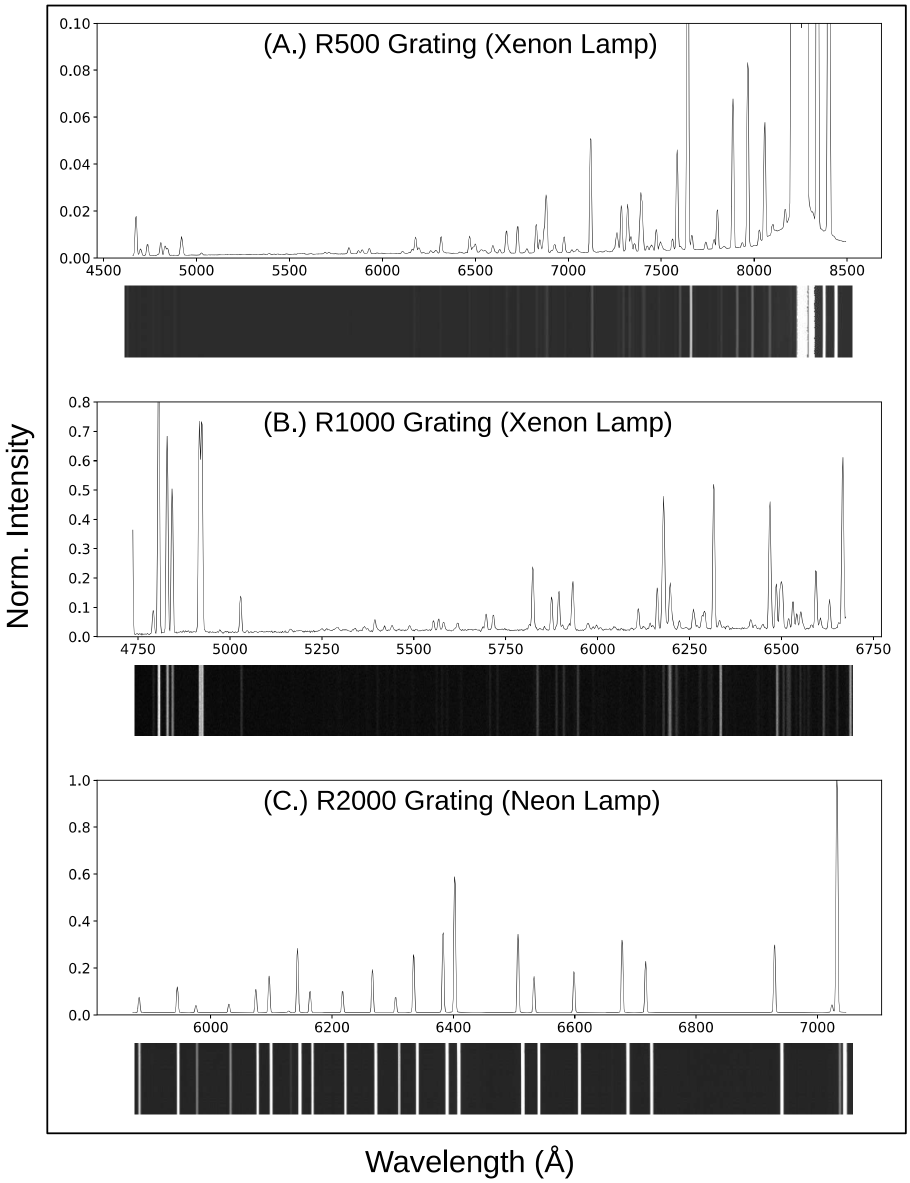

Figure 2.7: Spectra of Xenon and Neon lamps, used for wavelength calibration in different resolution modes of MFOSC-P.

2.1.3 Calibration Unit design

A calibration unit has been designed and integrated with MFOSC-P optics to provide the wavelength solution and flat fielding. It consists of an integrating sphere, two spectral lamps (Neon and Xenon), a halogen lamp, and a re-imaging optical system. The pencil-style spectral (Neon and Xenon) lamps from M/S

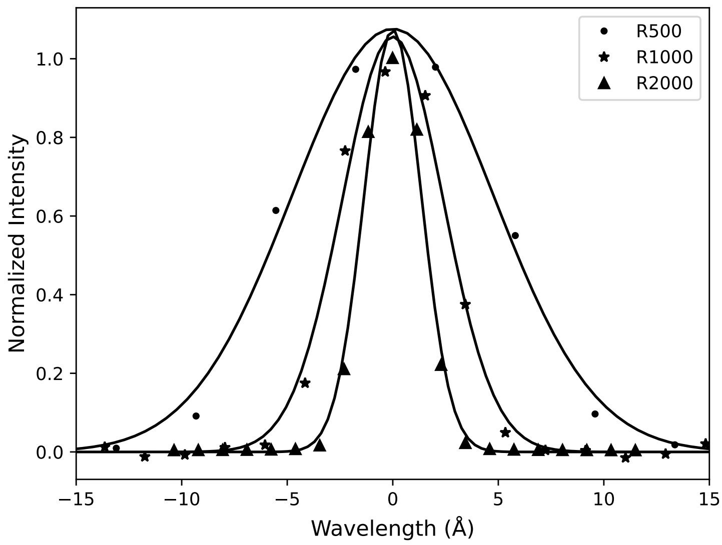

Figure 2.8: Line profiles for Xenon and Neon spectral calibration lamps are shown. The central zero wavelength corresponds to Xenon lamp's 7119Å line using R500 grating (dots), Xenon lamp's 5028Å line using R1000 grating (stars), and Neon lamp's 6506Å line using R2000 grating (triangles). Gaussian fits (solid lines) to these lines result in ∼3 pixels FWHMs which correspond to 10.9Å, 5.7Å, and 3.2Å for R500, R1000, and R2000 modes, respectively.

Newport-Oriel are used for this purpose [3].

The optical layout of the calibration unit is shown in Fig. 2.9. The lamps are coupled to the in-ports of the integrating sphere. The out-port of the integrating sphere is re-imaged on the telescope's focal plane with a magnification of ×2.0. The re-imaging optics is designed using two off-the-shelf achromat lenses (Thorlabs Part No.: AC508-075-A, 75mm focal length, and Edmund Optics Part No.: 49-391, 150mm focal length) and two mirrors to guide the calibration beam into the instrument.

The first fold mirror injects the calibration optics beam into the instrument through a glass window. The second fold mirror is mounted on a stepper motor-driven linear translation stage on the vertical chassis plate, above the linear stage for slit movement (Figure 1.7). This mirror blocks the telescope beam and feeds the calibration beam into the main optics through the slit during the spectral calibration. The second fold mirror is retracted during the science run of the instrument. The telescope pupil is simulated by using a mask

[3] https://www.newport.com/f/pencil-style-calibration-lamps, Accessed: 2020-03-18

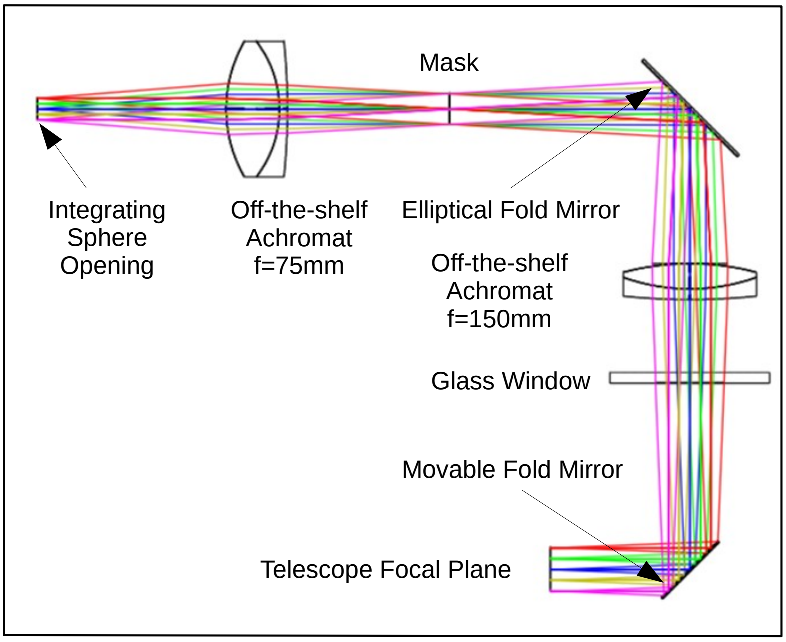

Figure 2.9: The figure shows the optical layout of the MFOSC-P calibration unit. The calibration unit is designed with off-the-shelf optical components to simulate the telescope's f/13 beam. The telescope pupil is simulated by using a mask.

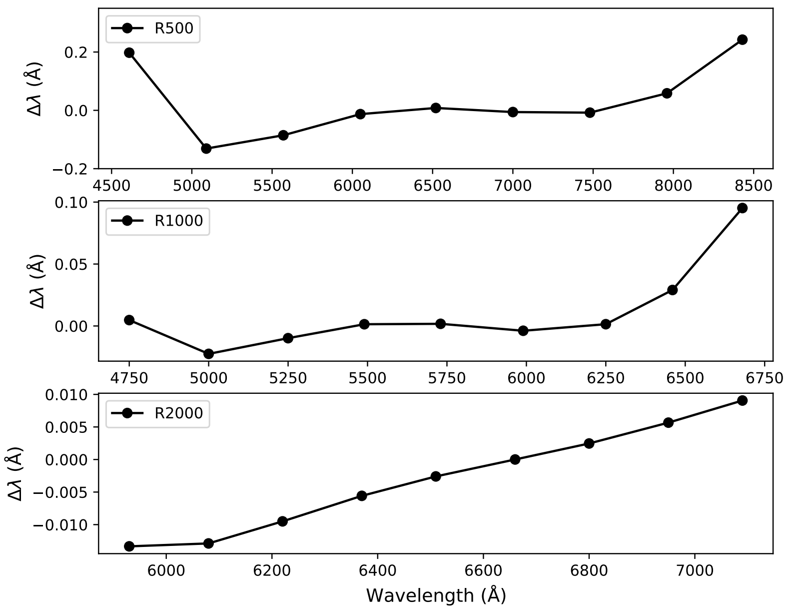

Figure 2.10: The expected errors in wavelength calibration due to the use of calibration unit optics are shown for all three grating modes of MFOSC-P.

(12.0mm clear aperture with a central obscuration of 2.7mm diameter) at the pupil location. Thus, a telecentric $f/13$ beam is generated at the telescope focal plane. The calibration unit optics was simulated with MFOSC-P optical chain in spectroscopy mode to determine the centroid positions for the individual wavelength spots. The centroid positions determined with MFOSC-P + calibration unit optics design are in good agreement with those obtained from MFOSC-P + telescope optics design (within 2-3μm, i.e., $\sim 1/13$ of spectral resolution in higher resolution mode of MFOSC-P). Fig. 2.10 shows the expected wavelength errors for all three modes of gratings. The centroid positions of the emission lines of calibration lamps, obtained with the ZEMAX model of calibration unit + MFOSC-P optical chain, are fitted with a third-order polynomial to obtain wavelength solutions. These wavelength solutions were then compared with the centroid positions of individual wavelengths from the ZEMAX model of telescope + MFOSC-P optical chain to derive the expected wavelength errors.

2.1.4 Repeatability tests of the stepper motors and linear stages

The repeatability of a motor is a measure of positioning and shows the ability to return to its predetermined position. A test set-up was made in the laboratory to check the repeatability and accuracy of the stepper motors (positioning of the slit, calibration fold mirror, filter wheel, and the grating module) with respect to the designed values. The Neon lamp spectrum was used to determine the repeatability of the motors/linear stages. Five emission lines were chosen as reference lines, and a Gaussian fit was used to determine the centroid of each of the spectral lines. Each of the motion sub-systems was moved in-out of the set position repeatedly, and spectra were recorded for each configuration. The comparison of the centroid positions was used to determine the performance of the motion system.

The slit is mounted on a stepper motor-driven linear translational stage with 5mm pitch. The motor is driven in $1/8^{th}$ micro-stepping mode with one full step corresponding to 200 pulses. Therefore, 1600 motor pulses correspond to one full rotation or 5mm translation, thereby giving the resolution of 3.1μm per micro-step on the slit plane. On the detector plane, this maps on to 1.77μm or

0.14 pixels. Through repeated tests in the laboratory as well as on the telescope, the positioning of the slit was found within these values. Similarly, the other motion sub-systems were also evaluated and were found within the designed specifications.

2.2 Instrument Assembly and Integration

After verifying the imaging and spectroscopic performance of the optical chain on the test-bench set-up, the sub-systems were aligned and assembled within the instrument chassis body and enclosure. First, the collimator section was mounted on the vertical chassis plate along with two motorized linear stages for the slit holder and calibration fold mirror (see left panel of Fig. 2.11). All the limit switches were tested before mounting these motors on the chassis plate. Now the grating module was mounted on its predefined position on the chassis base-plate and aligned using the laser retro-reflection by positioning the imaging fold mirror on the module (see middle panel of Fig. 2.11). A collimator fold mirror was then aligned and fixed on the base plate to fold the vertical collimated beam into the horizontal plane towards the grating box, making an angle of 30 degrees with the camera optical axis. A temporary flat mirror was kept at the top of the collimator for the laser retro-reflection purposes (see right panel of Fig. 2.11). The filter wheel was mounted on the chassis base plate at its predefined position.

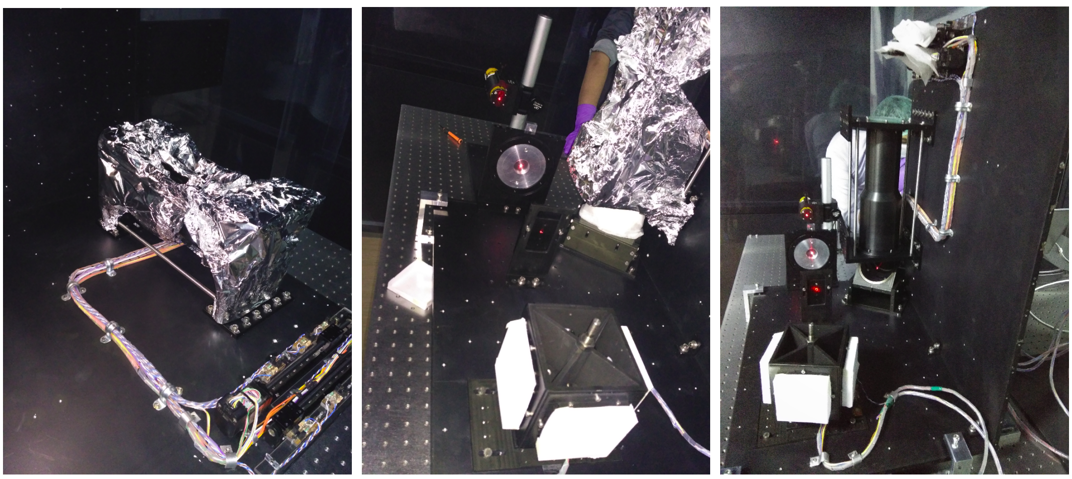

Figure 2.11: The left panel shows the collimator section mounted on the chassis plate , the middle panel shows the alignment of the grating module using laser retro-reflection, and the right panel shows the collimator fold mirror alignment.

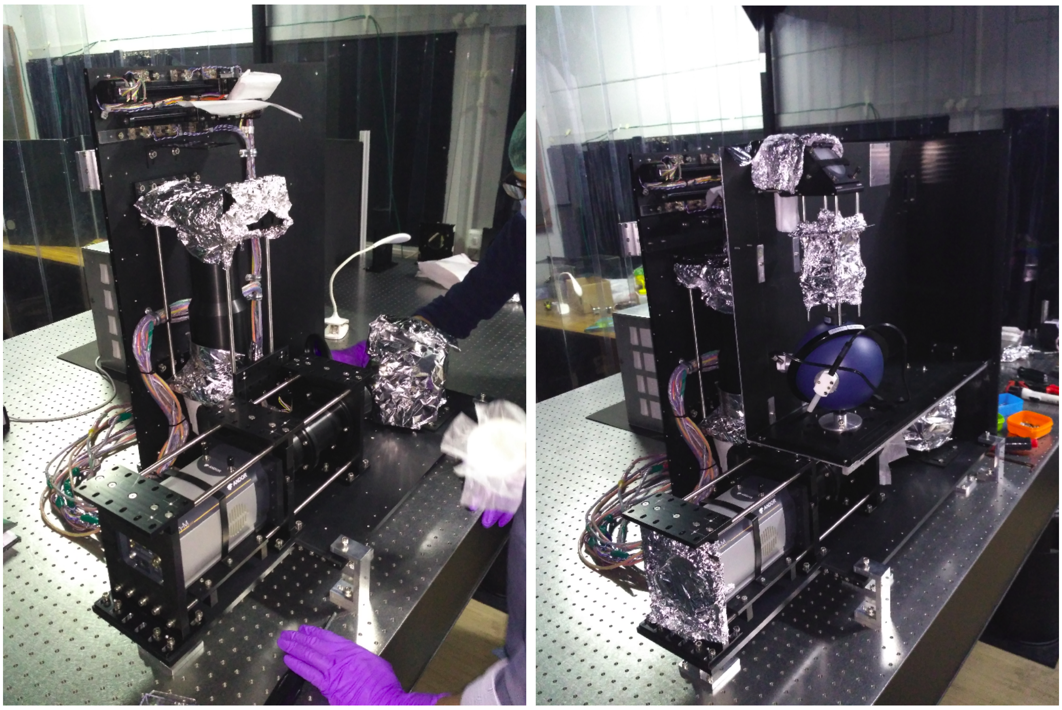

Figure 2.12: The left and right panels show the instrument image without and with the calibration unit, respectively.

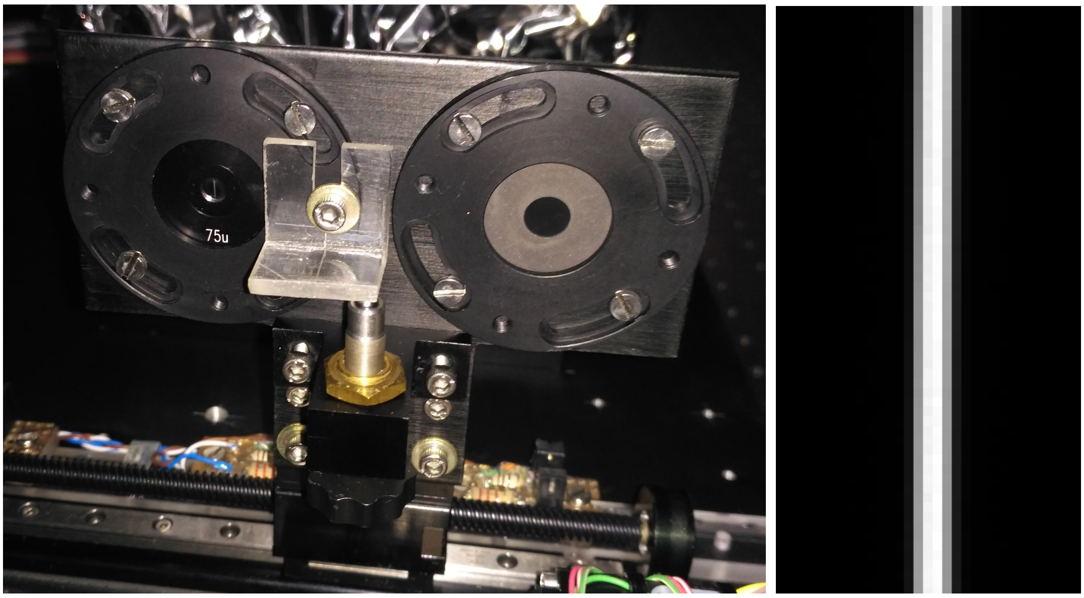

Figure 2.13: The left panel shows the slit alignment tool designed to orient the slit with precision. The right panel shows the vertically aligned slit image with the Xenon lamp.

All the motors and linear stages were then calibrated with respect to their home sensor positions. After calibrating the motor positions, the camera+detector unit was mounted on the base plate (see left panel of Fig. 2.12). A field stop is then mounted between the slit unit and the collimator section. The calibration unit was mounted on an L-shape plate and was fixed to the cage-rod assembly of the collimator and camera units. The slit was aligned parallel to CCD columns within 1 pixel across the slit length (∼130 pixels) by a purpose-designed slit alignment tool (see Fig.2.13). Subsequently, the gratings were aligned so that spectra were recorded parallel to rows of CCD (within one pixel across 1024 pixels) by rotating gratings on the grating module (see Fig.2.14). Finally, The instrument was enclosed from all the sides using outer plates (see right panel of Fig. 2.12).

Figure 2.14: The figure shows a horizontally aligned spectrum of the halogen lamp with 500 lp/mm grating.

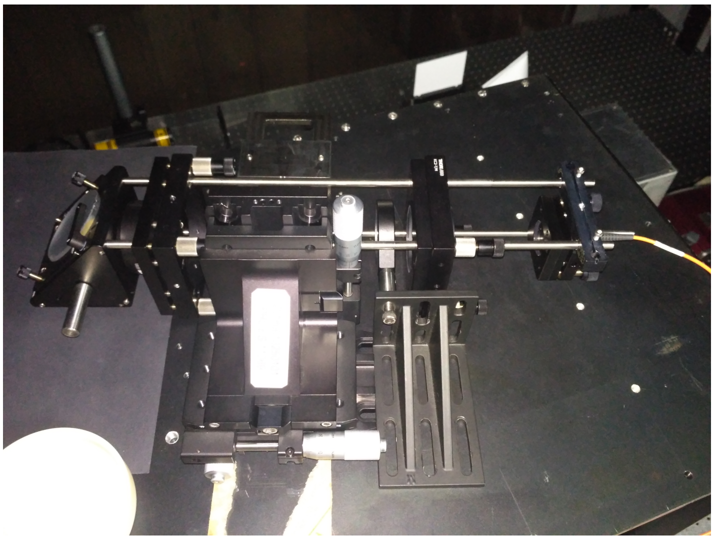

Figure 2.15: The figure shows a setup to simulate the telescope's f/13 beam.

The final performance of the instrument in the laboratory was verified by making another setup to simulate the telescope's f/13 beam (see Fig.2.15). Images of back-illuminated fiber cores were recorded to check the imaging performance (Fig.2.17), and spectral lamp's spectra were recorded to verify the spectral performance (Fig.2.18).

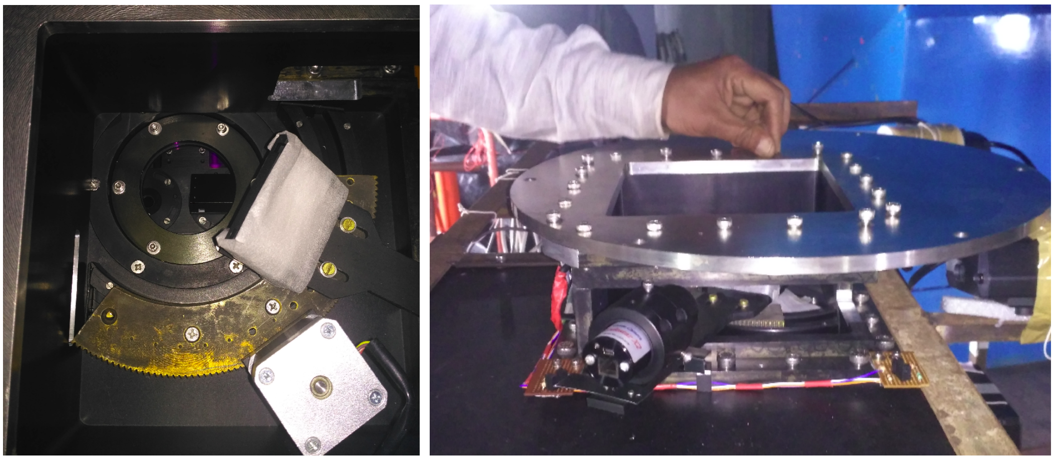

Figure 2.16: The left panel shows the top view of the Auto-Guider system (Telescope beam entrance window, fold mirror, motor for auto-guider). The right panel shows the side view of the Auto-Guider system (Cassegrain plate, auto-guider CCD).

MFOSC-P also has the auto-guider system to guide the telescope with off-axis field stars. The 45-degree flat mirror and the Lodestar camera were mounted on a motorized stage. It allows movement of the auto-guider system around 90 degrees around the periphery of the MFOSC-P field-of-view to scan the off-axis field stars. This was also assembled on top of the instrument assembly. This setup is shown in Fig. 2.16.

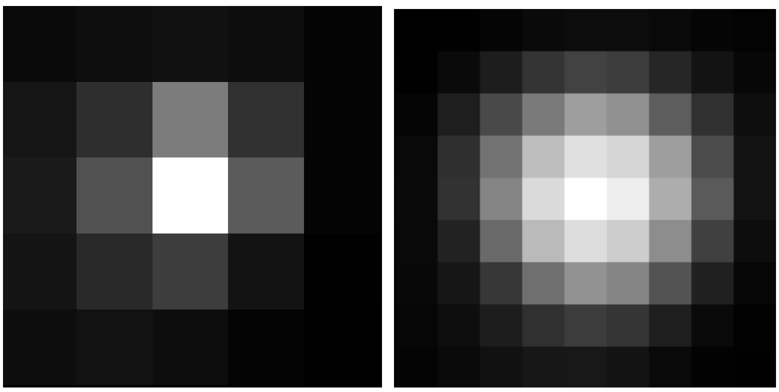

Figure 2.17: Images of 10μm and 50μm fiber-cores using telescope simulator setup. Magnification of the telescope simulator was $\times 2$. The image of the 10 μm core diameter fiber (20 μm at slit position) was found to be $\sim$1.2 pixels FWHM at detector plane (pixel size=13μm). The image of 50 μm core diameter fiber (100 μm at slit position) was found to be $\sim$4.5 pixels FWHM at the detector plane.

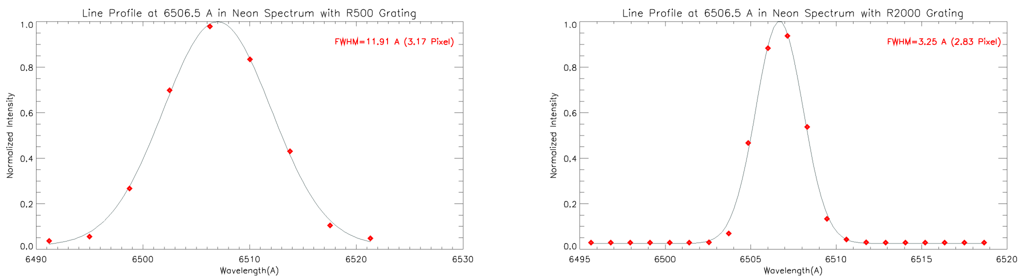

Figure 2.18: The figure shows the spectroscopic performance of the assembled instrument for R500 and R2000 grating modes. The spectra of the Neon lamp with 75 μm slit width are recorded with three gratings. An emission line near the center of each spectrum is chosen, and a 1-D Gaussian fit is made. The resolution of each grating mode was thus verified by determining the FWHM of the lines. The recorded FWHMs are mentioned in each of the panels.

2.3 MFOSC-P On-Sky Characterization

After instrument assembly and performance verification in the laboratory, MFOSC-P was commissioned on the telescope on $5th$ February 2019. Several commissioning and science observations were made with MFOSC-P from February to June 2019; till the onset of the monsoon season, during which the observatory is closed. Various targets were observed over these five months and later after the monsoon season to ensure and confirm the performance of spectroscopy and imaging modes. Fig. 2.19 shows the final mounting configuration of the MFOSC-P instrument on the PRL 1.2m Telescope.

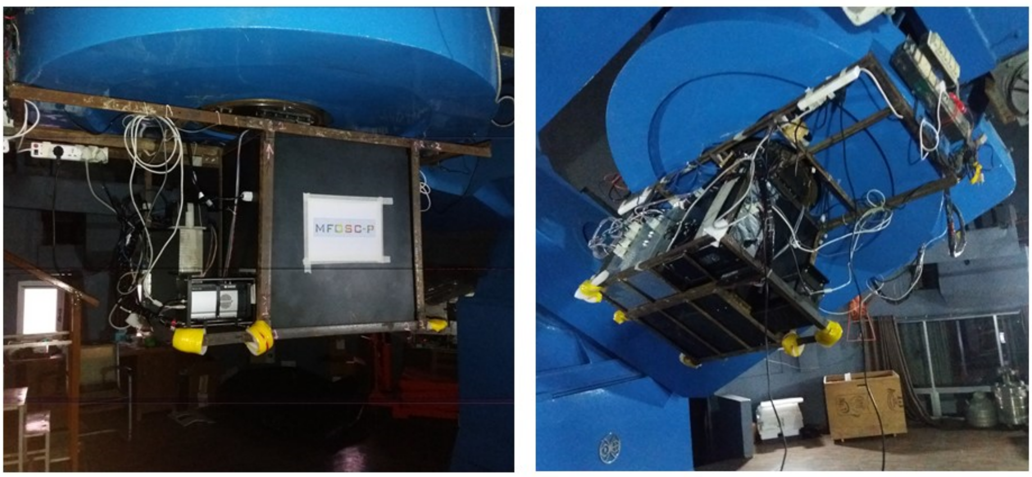

Figure 2.19: Commissioning images of MFOSC-P instrument on the PRL 1.2m telescope.

2.3.1 Photometry

The imaging PSF of MFOSC-P is heavily dominated by telescope optics along with the seeing profile of the site. On a typical night, the PSF had FWHM of $\sim$ 2.3 arc-seconds measured using a separate ATIK CCD (Pixel size: 5.4 μm, used in 5X5 pixel binning). The pupil image of the telescope for a central field star was recorded to check for any vignetting in the light and found no vignetting. As the telescope PSF was not good enough to check the instrument's PSF on the telescope, we took the image of the 75μm slit in diffused dome lights (with MFOSC-P mounted on the telescope) without any filter. The slit profile is shown in Fig. 2.20. A Gaussian fit results in an FWHM of 3.3 pixels, which ensures the intrinsic image quality of MFOSC-P on the telescope. Fig.2.21 shows the image of the M21 open cluster in various MFOSC-P filters, and Fig. 2.22 shows the co-ordinate calibrated M21 open cluster image in the V band filter. The magnitude of one of the faint sources (encircled in Fig. 2.22) is determined to be 15.74 with the photometric error of 0.15 magnitude (corresponding to SNR of 7.3) in 40 seconds of integration time.

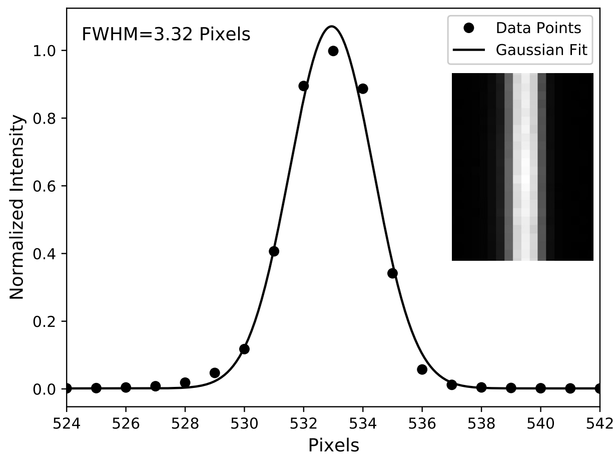

Figure 2.20: The figure shows the slit profile of the 75μm slit recorded with diffused illumination on the telescope dome floor. The instrument was mounted on the telescope. The profile is well approximated by a Gaussian having FWHM of $\sim$3.3 pixels. A section of the slit image is also shown in the inset.

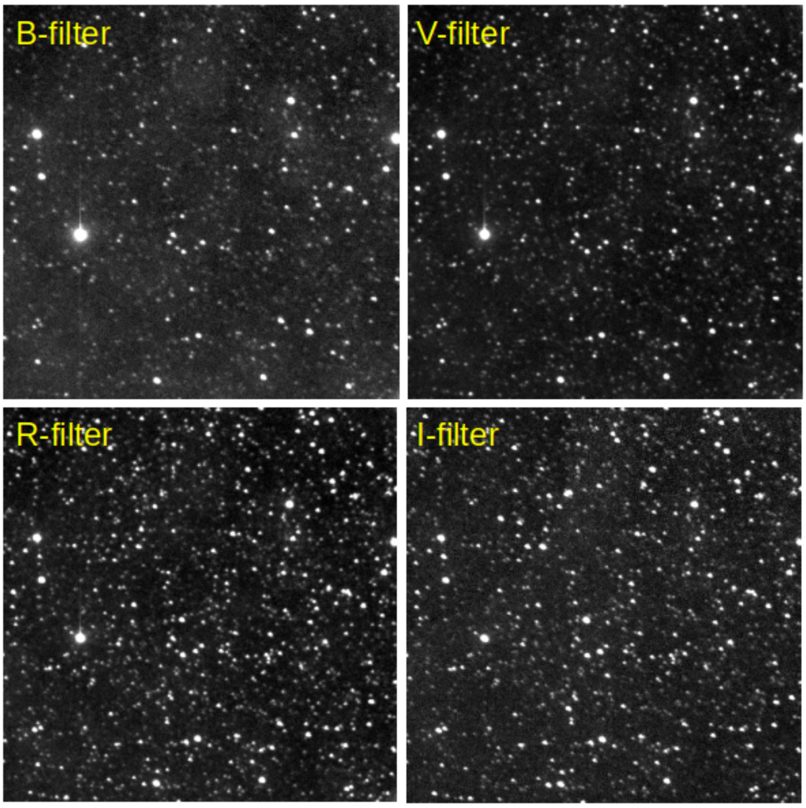

Figure 2.21: The figure shows the image of a field containing star AS281 (RA: 18 10 43.86 , DEC: -27 57 50.10) in B, V, R, and I filters of MFOSC-P.

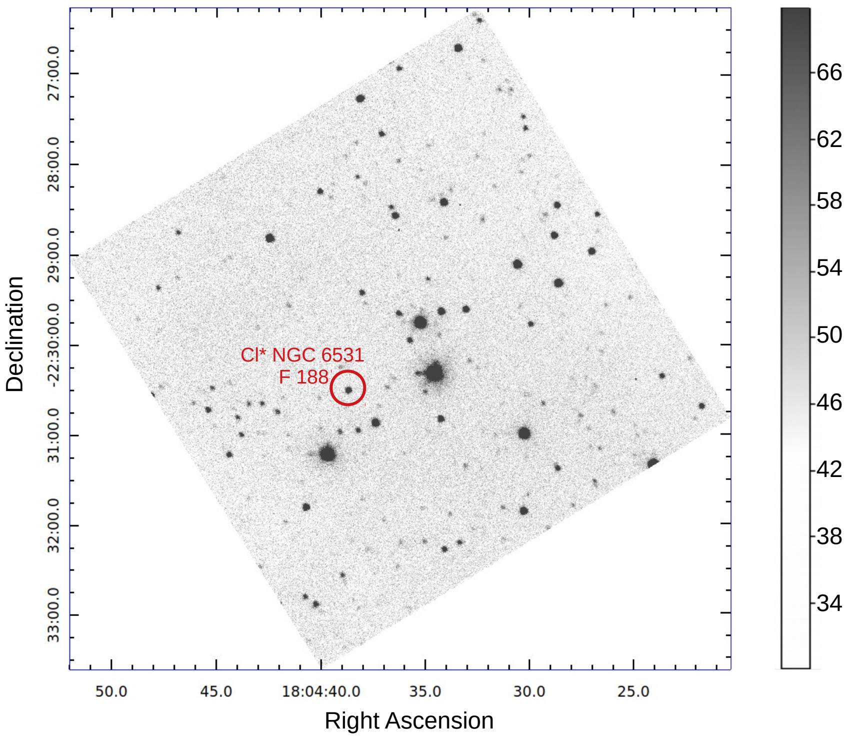

Figure 2.22: Image of a region of M21 open cluster obtained by MFOSC-P in V filter. A source of V magnitude ∼15.74 (encircled) was observed with an error of 0.15 magnitude (SNR∼7.3) in 40 seconds of integration time.

2.3.2 Spectroscopy Performance

Various objects, e.g., symbiotic systems, novae, M dwarfs, etc., were observed with MFOSC-P since the commissioning of MFOSC-P. These are described later in this section. The instrument's sensitivity was verified by comparing SNR obtained with the MFOSC-P spectra of these sources with a theoretical simulation model. The theoretical model assumes a seeing of 2.0 arc-seconds FWHM, slit width of 1.0 arc-second, and the optics PSF as a Gaussian of 1-pixel FWHM. Then, a flat V band spectrum was simulated, incorporating the total instrument efficiency (see Fig. 1.6). The spectrum was convolved with the slit profile function and then digitized using the gain of the CCD. The spectrum was finally recorded against a laboratory recorded bias frame, including the read-out noise, dark noise, etc. This simulated spectrum was then extracted using the same aperture and algorithm as in the case of MFOSC-P observed spectra. The SNRs were determined for each pixel after binning the data along the cross-dispersion direction within the aperture. Fig. 2.23 shows the SNR per pixel achieved with all the three modes of MFOSC-P against their predicted values for sources of various magnitudes and exposure times. The achieved SNRs are in good agreement with the predicted values. In cases where the achieved SNR differs from the expected values, we expect varying seeing conditions and the grating efficiency to be the main reasons for the difference. The efficiency curves used in these simulations were obtained from the manufacturer's datasheet. The curves were generated for the littrow configuration, which differs from those used within MFOSC-P. After the instrument was commissioned, the instrument's stability was verified by undertaking a long-term science observing program of M Dwarfs. Various sub-types of M Dwarf covering a range of magnitudes were observed between February-June 2019. The spectra obtained were then compared with their respective template spectra and later analyzed for their expected outcomes. This program is discussed later in this section.

The on-sky throughput of MFOSC-P, including telescope optics and seeing, is estimated by observing the objects from the list of spectro-photometric

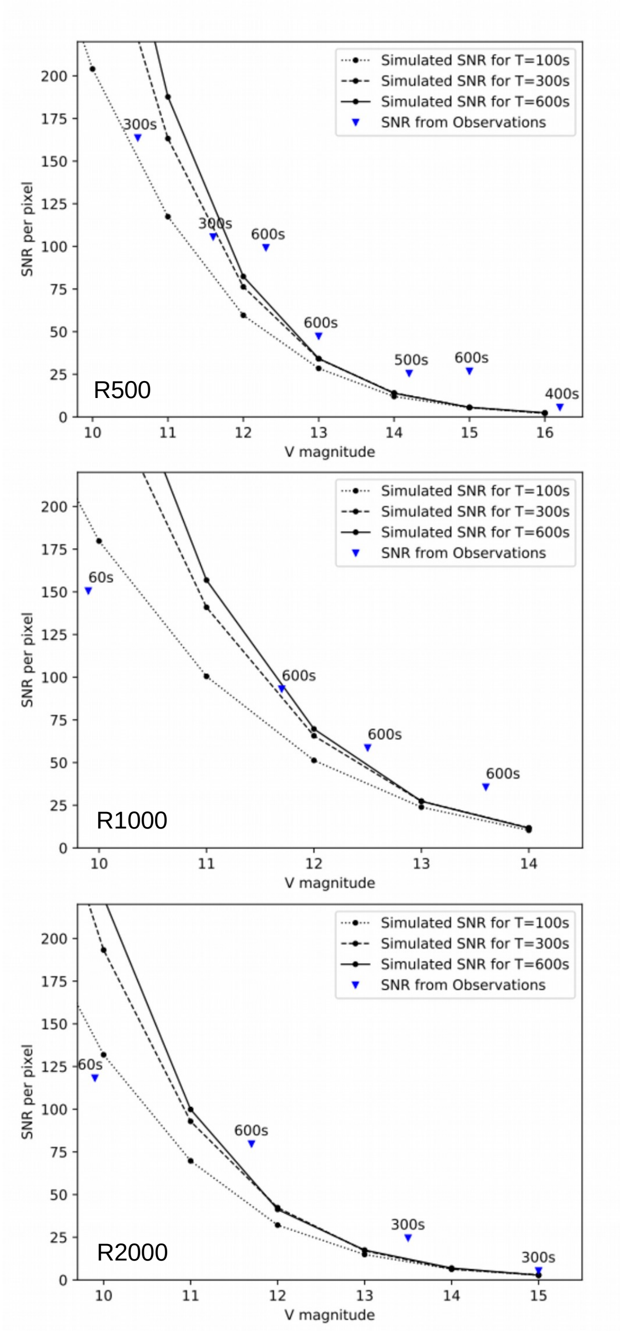

Figure 2.23: The plots show the expected SNRs from MFOSC-P for various V band magnitudes for all three spectroscopy modes. The expected SNR (solid circles) are obtained from a theoretical simulation model for 100 seconds (dotted line), 300 seconds (dashed line), and 600 seconds (solid line) of the simulated observations. The achieved SNR from MFOSC-P observations for varying integration times and various magnitudes are also shown in the solid triangles. The corresponding integration times for each of the observations are also mentioned, along with the data points. The achieved SNRs are in good agreement with the predicted SNR values. See section 2.3.2 for details.

standard stars[4]. In addition to the instrument's intrinsic efficiency, several other factors govern the final throughput. As discussed above, the PSF at the telescope's focal plane is dominated by the telescope optics and the seeing profile, which causes the slit-loss. The reflectance of the telescope optics (primary and secondary mirror) also degrades over time since their aluminization. The grating efficiency curves provided by the manufacturer are for the littrow configuration, which differs from how gratings are used in MFOSC-P. We have incorporated the combined effects of all these factors into the final "seeing" PSF onto the MFOSC-P slit. Similar to what we have done for comparing the SNR (in the above paragraph), we have simulated the spectra of a standard star HD93521 ($V \sim 7$ magnitude), with the efficiency curves discussed in section 1.3.2 and for the seeing of 2.0 arc-seconds. This simulated spectrum was then compared with the observed MFOSC-P spectrum to deduce the instrument efficiencies. Fig. 2.24 shows the flux calibrated spectrum of HD93521 in panel (a). The observed (solid curve) and simulated spectra (dashed curve)) for R500 mode (for an integration time of 30 seconds) are shown in panel (b) in analog-to-digital units (ADUs) without any corrections. Only the continuum of HD93521 is simulated. The derived and simulated efficiencies for R500 mode (solid and dashed curve, respectively) are shown in panel (c) for comparison. The above process is repeated for R1000 and R2000 modes (for an integration time of 45 and 80 seconds, respectively), and their efficiencies are compared in panel (d). It is seen that the efficiency curve is well matched for the R1000 mode while deviating for the R2000 and R500 modes. This is due to the different nature of the grating efficiency curves provided by the manufacturer (see Table 1.2). The efficiency data used for R1000 grating is absolute for this grating in littrow configuration. This has a peak efficiency of ~62% at 5500Å. However, for R2000 and R500 grating, only relative values are given. Due to this, their peak efficiencies are higher (~87% and ~80% at 6600Å and 6800Å respectively). As these grating efficiency curves are used directly from the manufacturer's datasheets, it causes the simulated efficiencies to be higher for R2000 and R500 modes to generate the simulated performance. The efficiencies of R2000 and R500 modes would

[4]https://www.eso.org/sci/observing/tools/standards/spectra.html, Accessed: 2021-02-21

also be in good agreement with the derived ones if we consider the grating peak efficiencies to be around 60%, similar to R1000 modes.

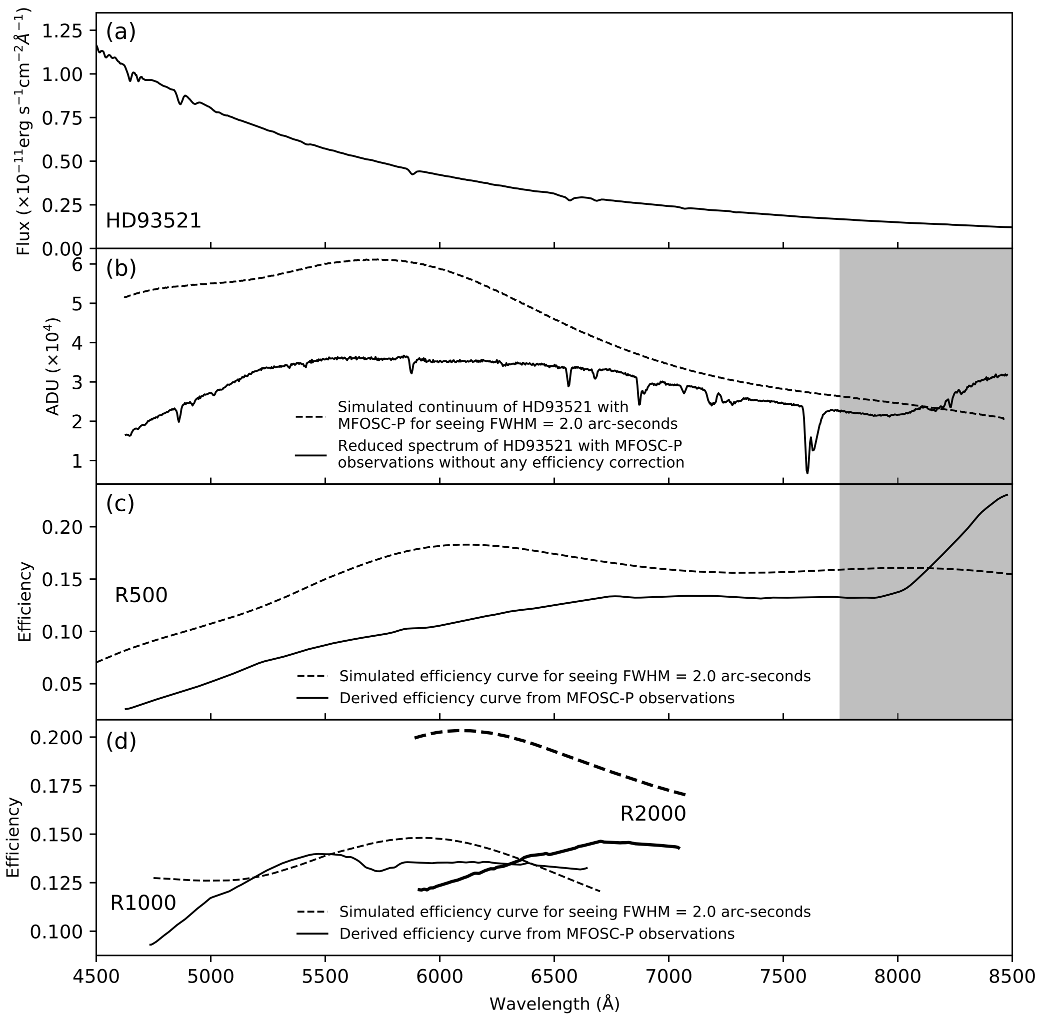

Figure 2.24: The figure shows the on-sky efficiencies of the MFOSC-P derived from the observations. Panel (a) shows the flux calibrated spectrum of a spectrophotometric standard star HD93521. Panel (b) shows the observed spectrum of HD93521 with MFOSC-P R500 mode (solid line). The data is in units of analog to digital units (ADU) as obtained from the CCD detector without any efficiency correction. The dashed curve shows the star's simulated spectrum (only continuum) with MFOSC-P considering seeing two arc seconds. Panel (c) and (d) show the expected efficiency using simulated data (dashed line) and derived efficiency using observations (solid line) of the instrument for given seeing conditions for R500 and R1000/R2000 modes, respectively. The shaded regions in panels (b) and (c) show enhancement due to second-order contamination. See section 2.3.2 for discussion.

As discussed in Section 1.3, three modes of spectroscopy in MFOSC-P were incorporated for varying purposes, viz. (a) to cover a broad spectral range to determine the shape of SED (R500 mode), (b) to study the evolution of emission lines in bluer part of the spectrum covering Hα and Hβ emission in a single frame (R1000 mode), and (c) to check for the profile variability of emission lines, in particular for the variability of Hα profile (R2000 mode). These aspects have been verified using suitable targets during the commissioning of the instrument. Some of the observations are described below.

(1.) Spectroscopy Observations of Symbiotics

Low/medium resolution optical spectroscopy has particularly interested in the studies of transient events like outbursts of symbiotic stars and novae. The profile evolution of emission lines is a diagnostic tool to trace the surrounding environment of a symbiotic system (e.g., Nova Sco 2015 (Srivastava et al., 2015)). The R2000 mode of MFOSC-P would be of particular use for such cases. Two well-known symbiotic stars/novae, T CrB and RS Oph (Anupama & Mikołajewska, 1999) have been observed over the period with MFOSC-P during the on-sky characterization phase.

T CrB was observed between 2019 and 2020. Fig. 2.25 shows the MFOSC-P spectra of T CrB in all the three gratings modes recorded in March 2020. The spectra for 2019 and 2020 appear similar and show the same features as observed during its 2015 super-active state (Munari et al., 2016). Strong emission lines of high ionization species are seen on the top of a nebular continuum with several M giant spectra absorption features. MFOSC-P spectra of T CrB for 2019 and 2020 also show several emission lines like He II 4686Å, Hβ , He I 4922Å, He I 5016Å (blended with [O III] 5007Å), He I 5876Å, Hα , He I 6678Å, and He I 7065Å, etc. FWHMs of Hα emissions are measured using R2000 spectra and found to be 7.1Å and 5.3Å for 2019 and 2020, respectively, including the instrumental profile. The Equivalent widths (EW) of Hα and Hβ were estimated after applying the reddening corrections of E_{B-V}=0.048 (Munari et al., 2016) to R1000 spectra. The EWs for (Hα ,Hβ) are determined to be (-36.5Å,-19.0 Å) for 2019 and (-49.6Å, -28.1Å) for 2020. These measurements for T CrB are similar to those that were earlier reported by Munari et al. (2016) and Iłkiewicz et al. (2016).

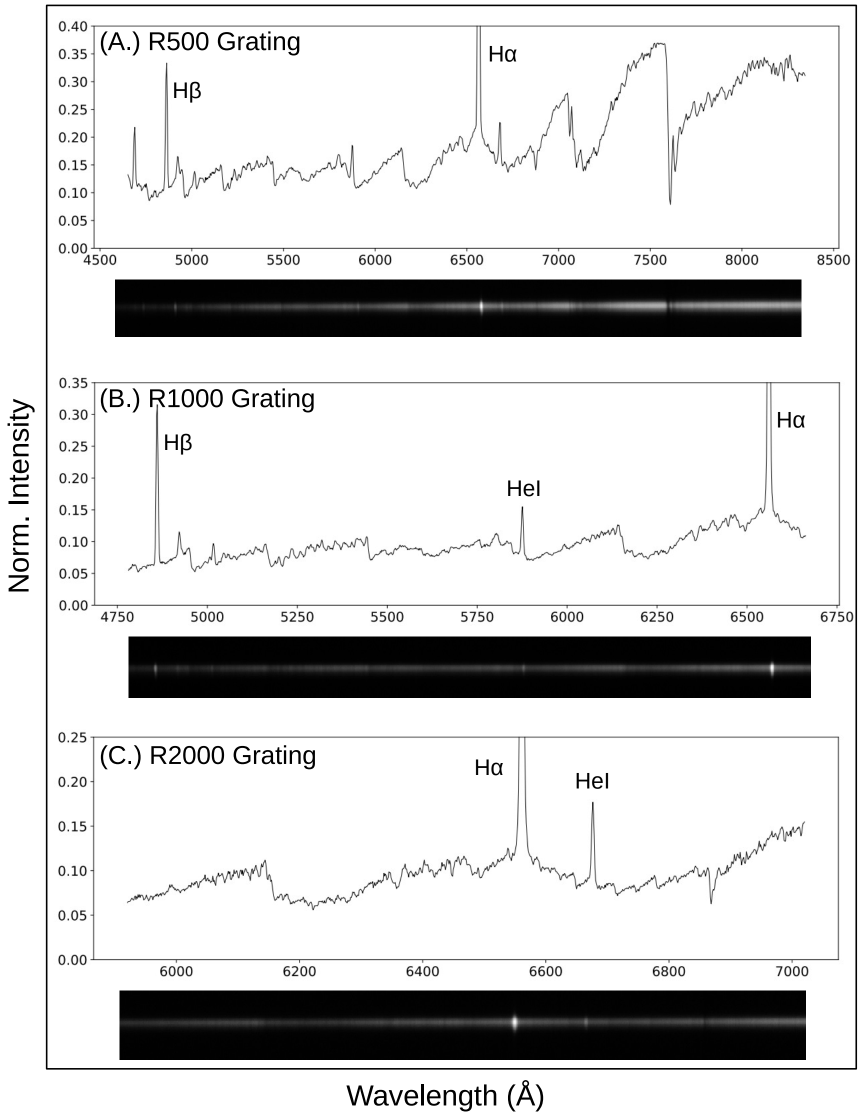

Figure 2.25: The spectra of T CrB, a recurrent nova, using all the three spectroscopy modes of MFOSC-P.

We have monitored the spectral evolution of RS Oph for a few months. Hα emission in RS Oph shows line profile variability over the time scale of a month (Zamanov et al., 2005). MFOSC-P spectra of Rs Oph also show Hα profile variability between April and May 2019. Fig. 2.26 shows line profile variation seen in RS Oph using the R2000 mode of MFOSC-P. The profile shape and its variation are found to be consistent with the spectra of RS Oph available in the public domain, e.g., ARAS (Astronomical Ring for Access to Spectroscopy[5]).

[5]http://www.astrosurf.com/aras/; Accessed: 2020-04-12

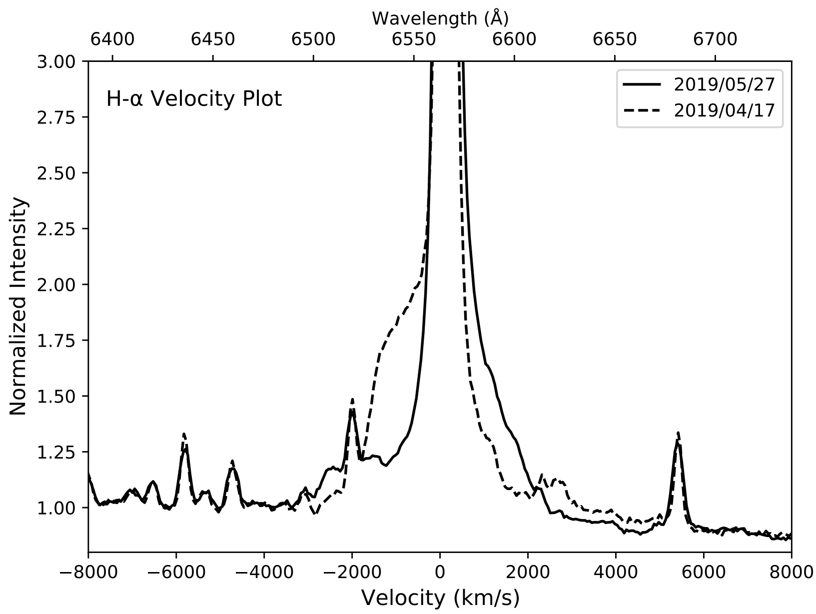

Figure 2.26: Hα variability observed in the spectra of RS Oph.

(2.) Spectroscopy Observations of M dwarfs

Along with the commissioning and characterization run of MFOSC-P, a science program for the characterization of nearby M dwarfs was undertaken in February-June 2019. Bright M dwarfs within 100pc with a V magnitude less than 14 were selected from the all-sky catalog of bright M dwarfs (Lépine & Gaidos, 2011). Selected sources cover the spectral types M0 to M5, derived from the photometry. A total of 80 targets were observed for their low-resolution spectroscopy using the R500 mode of MFOSC-P.

The spectra of these M dwarfs were compared with the SDSS standard M dwarf template spectra for their sub-classification. Fig. 2.27 shows such a comparison for a sample of M dwarf spectra. The derived sub-spectral types of M dwarfs in our sample range from M0-M5 with an error of one spectral subclass. Later the spectral synthesis was performed on these spectra to determine their fundamental stellar parameters, viz., effective temperature, and surface gravity. These stellar parameters of our sample targets were determined by comparing the observed spectra with the synthetic spectra generated by the BT-Settl model (Allard et al., 2013). The derived values of effective temperature and surface gravity ranged from 4000 K to 3000 K and 4.5 to 5.5 dex, respectively. This work shall be discussed in more detail in chapter 3.

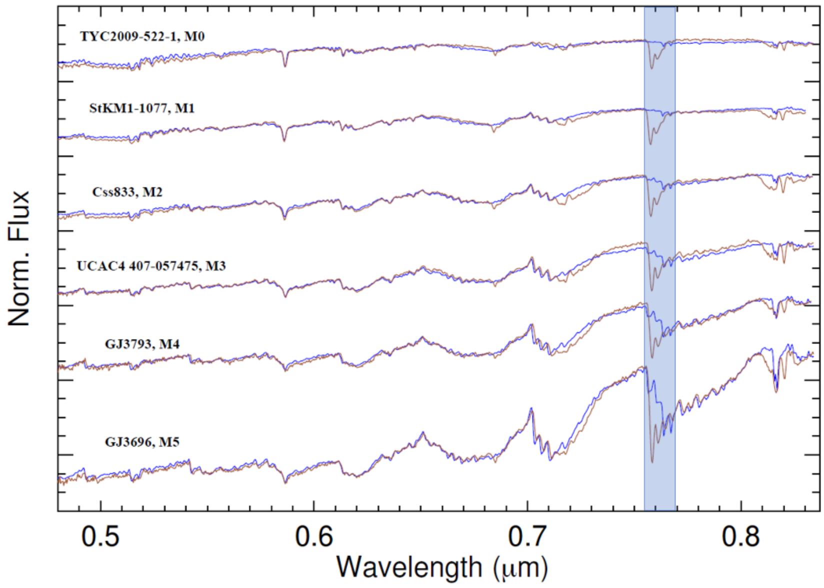

Figure 2.27: SDSS template spectra (blue) from Bochanski et al. (2007) is compared with observed spectral sequence of M dwarf using MFOSC-P (red). The blue-shaded region shows the telluric absorption at 7605 Å.

(3.) Spectroscopy of Nova V2891 Cyg

Nova V2891 Cyg was discovered by De et al. (2019) in a regular survey operation of Palomar Gattini-IR (Moore & Kasliwal, 2019) on UT 2019-09-17.25. The nova was found to be highly reddened, and early spectroscopy (Lee et al., 2019) determined the FWHM of the Hα line to be 840 kms^{-1}. Optical spectroscopy of this nova using MFOSC-P was first done on UT 2019-11-01.71. The spectra were recorded in the R500 and R2000 modes. The low-resolution spectrum showed a highly reddened continuum with prominent Hα emission and OI lines at 7773Å and 8446Å. The OI 7773Å line showed a P-Cygni profile with $\sim$14Å separation between emission maximum and absorption minimum. FWHM and FWZI (full width at zero intensity) of the Hα line were determined to be $\sim$340 kms^{-1}, and 2000 kms^{-1}, respectively, from the spectrum, obtained using the R2000 mode of MFOSC-P. Using the instrumental FWHM of 150 kms^{-1} and quadrature summation method, the intrinsic line-width was found to be $\sim$300 kms^{-1}. Fig. 2.28 shows the spectrum of the nova on UT 2019-11-01.71 obtained with the R500 mode of MFOSC-P with 300 seconds of integration time.

The velocity plot for Hα (as shown in the inset) was derived from the spectrum obtained using R2000 mode. It is to be noted that nova was

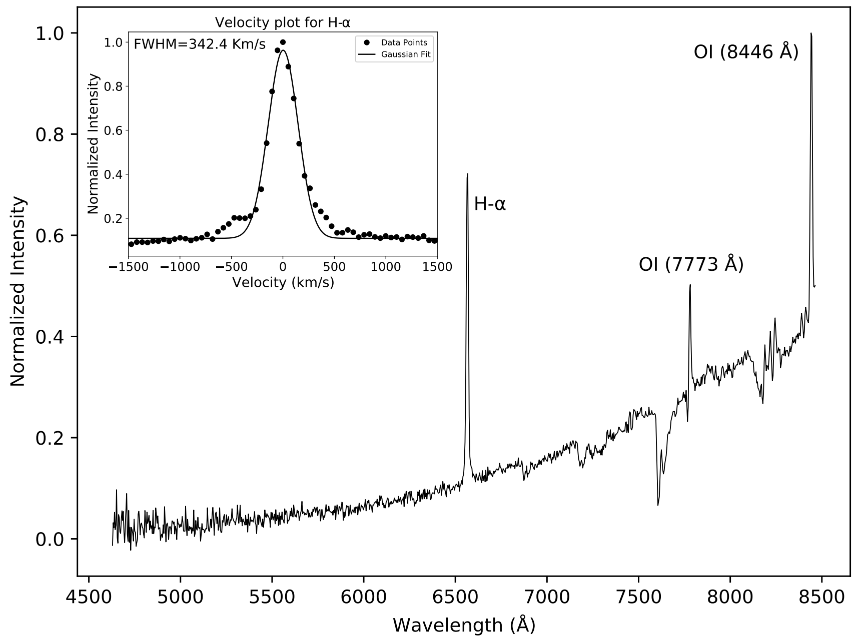

Figure 2.28: The figure shows the low-resolution spectrum of Nova V2891 Cyg, recorded with MFOSC-P. R500 grating mode was used with an integration time of 300 seconds. The nova was ∼16 magnitude in the V band. Inset: Velocity plot showing Hα profile of Nova AT2019QWF. This was observed with the R2000 mode of MFOSC-P.

of ∼16 magnitude in the V band on the day of observations, as determined from the AAVSO light curve (AAVSO - American Association of Variable Star Observers[6]). The above has been reported to the Astronomical Telegrams (Srivastava et al., 2019). This work shall be discussed in more detail in chapter 4.

2.4 Development of MFOSC-P Spectroscopy Data Reduction Pipeline

An automated spectroscopy data reduction pipeline was developed to reduce and analyze the raw observational data from MFOSC-P. The pipeline is a series of tasks (codes) to be applied to the raw data in pre-determined sequences. It has been developed in PYTHON using open-source image processing libraries (e.g., ASTROPY, etc.). This pipeline consists of various spectroscopy data reduction steps like bias subtraction, cosmic ray removal, tracing and extracting the spectra, sky background subtraction, wavelength calibration, instrument

[6]https://www.aavso.org/; Accessed: 2020-03-20

response correction, etc. A graphical user interface was developed by the MFOSC-P engineering team (see APPENDIX-C), which provides the front end of the data reduction software. Several routines have been written to perform each standard data reduction procedure step. Below, we discuss each of these steps. As an example, the data reduction procedure for T CrB, a well-known recurrent nova, in R2000 mode is discussed:

Master Bias Creation: A master bias frame is created by taking the median of several bias frames. This is done to remove the unwanted signal offset due to the electronics (see left panel of Fig. 2.29).

Spectrum Extraction: The master bias frame is subtracted from all science data frames and flat frames, and then the cosmic ray correction is performed. This correction is done by the ASTROSCRAPPY package (a publicly available routine) in PYTHON (see middle panel of Fig. 2.29). We then trace & collect the spectrum choosing a finite aperture width. For tracing purposes, the data is summed up along the rows of pixels in a fits file and find the slit profile position. Using this slit profile, one can choose the range of aperture manually, or the routine can automatically decide the aperture range considering those pixels having a flux greater than 90% of maximum flux in the slit profile. After deciding the aperture range, the data counts are summed up in the cross dispersed direction within the aperture. The same aperture width is used to determine the sky background on either side of the star spectrum. The sky background is subtracted from the star spectrum (see right panel of Fig. 2.29). These counts were converted to electrons using the gain conversion factor (G).

Noise is also calculated associated with each data point of the spectrum with the following equation:

$$N = \sqrt{(N_S * G) + n_{pix}((N_{bg} * G) + N_R^2)}$$

Where N_S is the total counts in ADU within the aperture in cross disperser direction, N_{bg} is the mean sky background counts (ADU) per pixel in

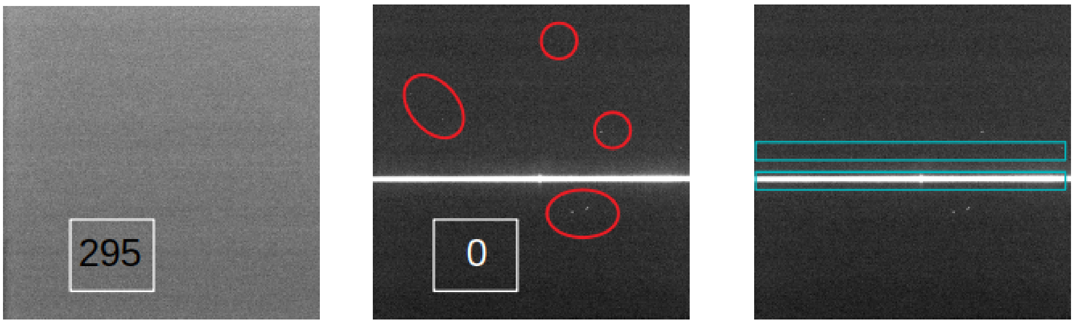

Figure 2.29: The left panel shows the master bias frame, the middle panel shows the bias subtracted science frame, and the right panel shows the cosmic ray corrected science frame. The spectral extraction is done on these frames.

the same aperture, G is gain in electron per ADU, N_R is RMS read out noise in electron.

Flats are also collected using halogen lamps in the calibration unit to correct the pixel-to-pixel variations. The same aperture range used in spectrum extraction is used here. A polynomial of 7 degrees is used to fit the flat spectrum and then divided by the polynomial to find pixel by pixel variation. This variation is $\sim$1%. A provision is provided in the pipeline for flat-field correction.

Wavelength Calibration: Wavelength calibration is done with the help of Neon/Xenon spectral lamps, whose spectra are recorded immediately before or after the science observations in the identical settings of the telescope and instrument. The lamp spectrum is reduced, and a known spectral line is identified. The Gaussian fit gives the centroid of this known line. After that, the shift of this line is estimated with respect to the template calibration spectrum. Once the offset shift is known, positions of several other predefined lines (five to seven) are identified in the lamp spectrum. We then fit a 3rd-degree polynomial between the positions (centroid of each line in the unit of pixels) of these lines and the corresponding wavelengths. This polynomial is applied to the science spectrum to get the wavelength calibrated spectrum (see Fig. 2.30).

Instrument Response Correction: The instrument response correction is done by observing a standard spectro-photometric star. First, the spectrum is reduced with the previously described steps, and a wavelength calibrated

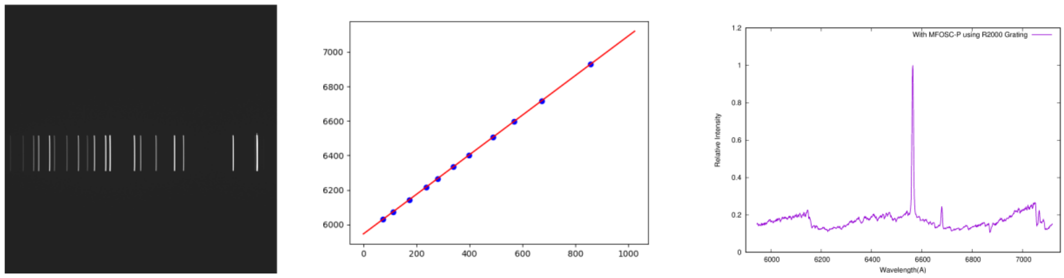

Figure 2.30: The left panel shows the calibration lamp (Neon for R2000 grating) frame, the middle panel shows a 3-degree polynomial fit between pixel and wavelength, and the right panel shows the wavelength calibrated T CrB spectrum.

spectrum is obtained. The known absorption features were then removed from this spectrum, and a $5th$-degree polynomial (say S_{ins}) is fitted to the continuum (see Fig. 2.31). The same process of polynomial fitting is done with the archival spectrum of the same standard star (say S_{true}). The archival spectrum is taken from the ESO list of spectro-photometric standard stars[7]. The response function can be estimated by $R = S_{ins} / S_{true}$. We then divide the wavelength calibrated spectrum of any source by response function R to get the final reduced spectrum (see Fig. 2.32).

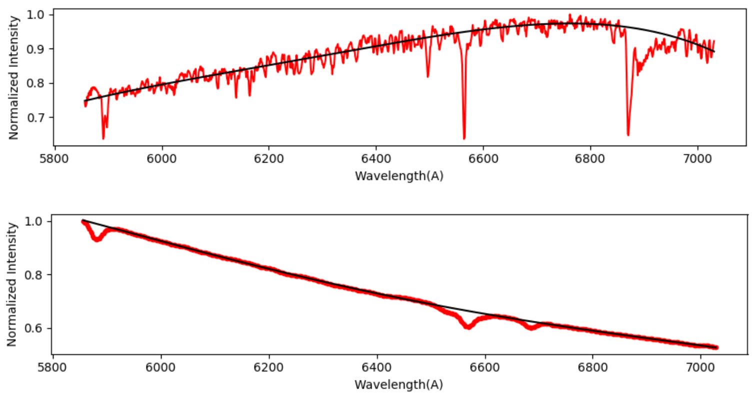

Figure 2.31: The top panel shows the observed standard star with $5th$-degree polynomial fitting after removing absorption features. The bottom panel shows spectrum of the same standard star (from the archives of ESO list of spectro-photometric standard stars) with $5th$-degree polynomial fitting after removing absorption features.

Fig. 2.33 shows the comparison of the low resolution (R500 mode) spectrum of a suspected symbiotic star - SU Lyn, with the spectrum obtained from

[7]http://www.eso.org/sci/observing/tools/standards/spectra/stanlis.html

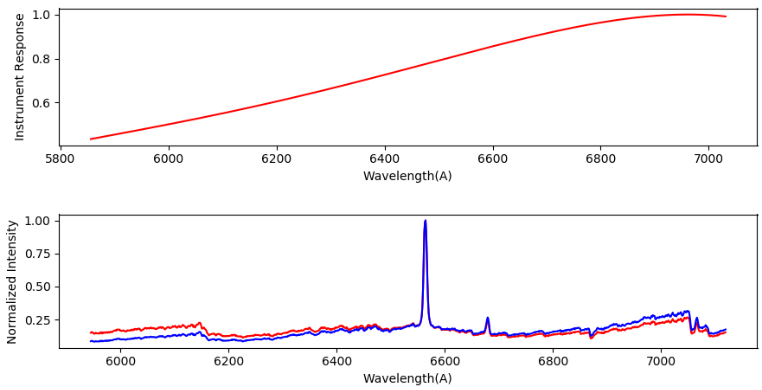

Figure 2.32: The top panel shows the instrument response function (R) of the instrument, and the bottom panel shows the spectrum before (blue line) and after (red line) applying the response function to the science spectrum.

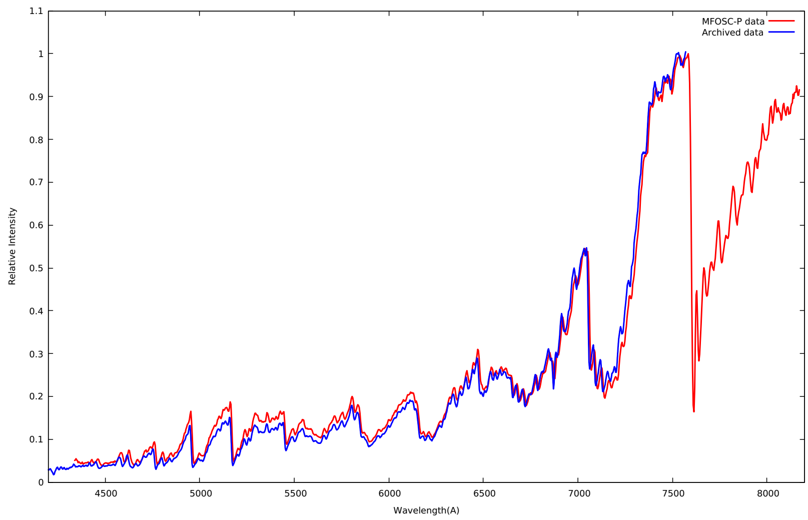

Figure 2.33: The figure shows the comparison of the spectrum of SU Lyn (a suspected symbiotic system) obtained with MFOSC-P (on 18th April 2019) and reduced with MFOSC-P data reduction pipeline, with the spectrum recorded on a nearby date (20th April 2019) obtained from another open database.

an open spectral database on nearby dates. The SU Lyn was observed with MFOSC-P on 18th April 2019, and the archive data was taken from Astronomical Ring for Access to Spectroscopy[8] (ARAS) database, observed with N200mmF telescope on 20th April 2019. The spectrum from MFOSC-P was reduced with the MFOSC-P spectroscopy data reduction pipeline. The spectral features and the continuum are well-matched, thus showing the performance of the data reduction pipeline.

[8]http://www.astrosurf.com/aras/Aras_DataBase/Symbiotics.htm

2.5 Chapter Conclusion

This chapter describes the development of MFOSC-P on the PRL 1.2m optical-NIR telescope at Mt. Abu in detail. The instrument's optical chain was first characterized on a test bench setup using various pinholes and test targets and was later integrated and assembled into the instrument's enclosure. MFOSC-P was commissioned on the PRL 1.2m telescope in February 2019. A series of commissioning and science observations were carried out from February 2019 to June 2019. The instrument has been used for various science observations, e.g., spectroscopy of M dwarfs, novae, symbiotic systems, Hα detection in star-forming regions, etc. An automated data reduction pipeline for MFOSC-P has also been developed during the science observation period, and the data reduction procedure was successfully cross-verified with the spectra obtained from other archival databases.

MFOSC-P has provided much-needed spectroscopy and multi-filter imaging capability in the visible bands to the PRL 1.2m telescope. As PRL is gearing up towards establishing another 2.5m optical-NIR telescope at Mt. Abu, lessons learned from MFOSC-P are most valuable for the development of the next FOSC instrument for the 2.5m telescope. The design and development approach adopted here is well suited for any small aperture telescope/observatory, which often requires a simple yet versatile instrument within a short development period. As the instrument has been successfully used for a range of astronomical observations, the MFOSC-P presents a successful FOSC design, which could be adapted with minimal modifications to similar telescopes worldwide.

The content of this chapter has been published as follows:

- *Mudit K. Srivastava, **Vipin Kumar**, Vaibhav Dixit, Ankita Patel, Mohanlal Jangra, A.S. Rajpurohit, and S. N. Mathur, "Design and Development of Mt. Abu Faint Object Spectrograph and Camera - Pathfinder (MFOSC-P) for PRL 1.2m Mt. Abu Telescope" (Experimental Astronomy, 51, 345-382 (2021); doi:10.1007/s10686-021-09753-5)*

Chapter 3

Performance verification of MFOSC-P with the statistical samples of M dwarfs

The performance verification (PV) observations were initiated as soon as MFOSC-P was commissioned on the telescope, after the successful Assembly-Integration-Test (AIT) process of the instrument in the laboratory. These PV observations were aimed at establishing and characterizing the instrument's performance in various observing conditions, with sources of varying magnitudes, etc. These initials observational data from the PV phase were also used to develop and optimize the MFOSC-P data reduction pipeline. During the PV observations, a sequence and nomenclature of various science and calibration observations were devised in order to automate the data reduction process. These observations were later used to determine the on-sky efficiencies, SNR, etc., of MFOSC-P and later compare them with underlying theoretical estimates.

M dwarfs were found to be suitable targets for the PV phase of MFOSC-P. They are among the most abundant stellar species of our Galaxy, and, therefore, a good number of them would be available for observations at any given time of the year. Their spectra are rich in absorption features, and subtle differences are seen in M dwarfs of different spectral types. Further, a good number of M dwarfs could be found, for each sub-spectral class, in the magnitude range suitable to be observed with the 1.2m aperture PRL telescope. Thus, an early PV observation program of MFOSC-P was conceived for the spectroscopy characterization of a sample of M dwarfs during the commissioning run of MFOSC-P in February-June 2019. In this study, 80 bright M dwarfs (J<10) were selected from a photometric catalog (their spectroscopy data were not available) and were observed with low resolution (R$\sim$500) mode of MFOSC-P for their spectroscopy classification. These first scientific data from MFOSC-P were then used to perform spectral synthesis analysis to determine their fundamental parameters, viz., effective temperature and surface gravity - by comparing the observed spectra with their model synthetic spectra. This work has been done in close collaboration with Dr. Arvind Singh Rajpurohit (a faculty member in Astronomy & Astrophysics division, PRL). The observational campaign of M dwarfs was carried out together as a part of the performance verification of the instrument. In this work, I have reduced the raw spectroscopic data to science-ready data while developing and updating the data reduction pipeline for MFOSC-P. The spectroscopic classification and determination of fundamental parameters were performed by Dr. Arvind Singh Rajpurohit.

Out of 80 sources of the M dwarf sample of the PV observations, Hα emissions were detected in 10 sources, making them the probable candidates of active M dwarfs. In recent times, active M dwarfs have been explored in great detail to understand the underlying causes for their activities (West et al., 2008; Kowalski et al., 2010; Newton et al., 2017; Yang et al., 2017). However, it was realized that very few studies had been done (Lee et al., 2010) to explore the nature of short-term Hα / Hβ variability in M dwarfs. It was realized that R1000 mode (Resolution$\sim$1000, with 300 line-pair/mm grating) of MFOSC-P, covering both Hα and Hβ wavelengths, would be a suitable observing set-up for such studies. Thus, another observing program was conceived to study the statistics of short-term variability in Hα / Hβ emissions in another sample of 83 M dwarfs, including 10 Hα emitters from the previous sample. Time-series spectra over the time scales varying from $\sim$0.7 to 2.3 hours and the cadence in the range of $\sim$3-10 minutes were recorded for each of the sources. These observational data from MFOSC-P were then coupled with the available data in the literature/various

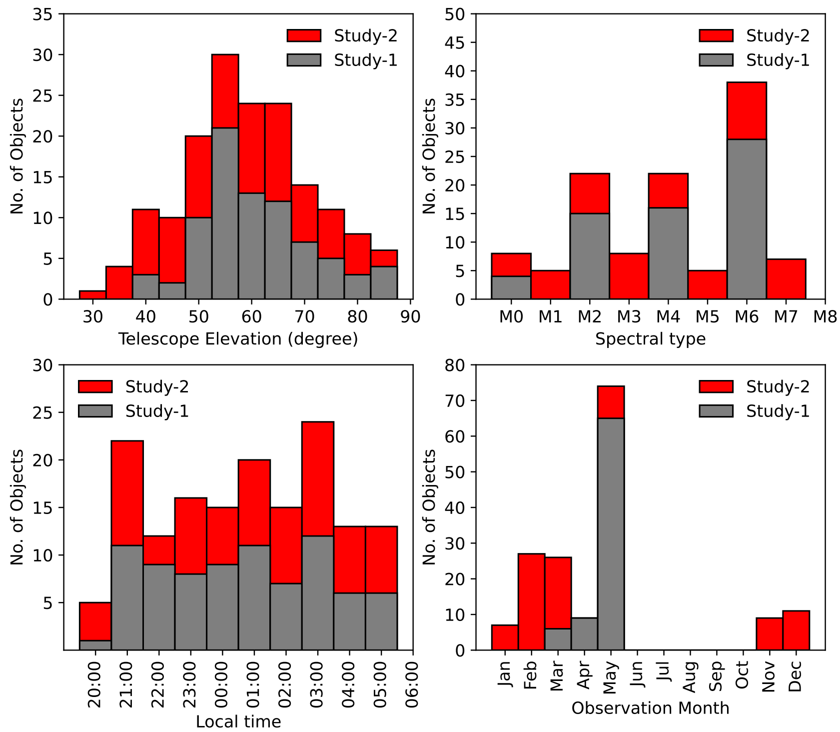

Figure 3.1: Histogram shows the distribution of sources (M dwarfs) observed for the PV of MFOSC-P. The distribution are shown with respect to the telescope's elevation (top-left), spectral type of M dwarf (top-right), local observing time (bottom left), and month of observation (bottom-right).

astronomical data archives to form a complete sample of 126 sources, covering M0 to M8.5 sub-spectral classes. Various statistical variability indicators are used to trace the activity strengths with respect to sub-spectral type, rotation periods, star-spot filling factor, etc.

This chapter describes both the studies on the M dwarfs characterization program. Total 153 sources were observed in these two studies (80 sources in study-1 and 83 sources in study-2 with 10 common sources). Their distribution with respect to the telescope's elevation, spectral type of M dwarf, local observing time, and month of observation are shown in Fig. 3.1. A brief introduction to M dwarfs and the feasibility of the M dwarf characterization program with MFOSC-P are discussed in section 3.1 and 3.2 respectively. The first PV observations of M dwarfs with MFOSC-P, and the derived results are discussed in section 3.3. The next observing program for short-term Hα / Hβ variability in active M dwarfs is described in section 3.4. Finally, we conclude our results in section 3.5.

The studies presented in this chapter were designed to be statistical in nature, wherein a sample consisting of a good number of similar kinds of sources would be observed to study their statistical properties. A separate science observing program to explore the physics of a suitable target (in our case, a nova) with long-term MFOSC-P observations was also undertaken after the first PV observations. Those results will be discussed in chapter 4.

3.1 Introduction: M dwarfs

M dwarfs are the major stellar constituents of the Galaxy. Their population is estimated to be nearly ∼70 % of the total stellar content in our Galaxy, and they contribute ∼40% of its total stellar mass (Henry et al., 1997; Chabrier, 2003). M dwarfs are less massive (0.6-0.075 $M_\odot$) and comparatively cool stars with effective temperature ($T_{\rm eff}$) in the range of 2500-4000 K. As their mean lifetimes on the main sequence path are comparatively much longer, they are a good tracer of the Galactic history (Green & Margon, 1994; Cool et al., 1996; Renzini et al., 1996). M dwarfs are found in any population, from young metal-rich in the open cluster to billion-year-old metal-poor in the galactic halo. A variety of them are expected to host sub-stellar objects, e.g., brown dwarfs and exoplanets, (Bonfils et al., 2012; Gillon et al., 2017; Mercer & Stamatellos, 2020; Baroch et al., 2021), therefore they have been an important topic of attention in recent times. However, the determination of atmospheric parameters using the spectra of M dwarfs is a challenging task due to the presence of several molecular absorption bands. The formation of these molecules is complex, and the corresponding molecular bands consist of several poorly known lines. TiO and VO absorption bands mostly govern their Spectral Energy Distribution (SED) in the optical and CO and H2O in the Near Infra-red regime. The typical M dwarf spectrum in optical can be seen in Fig. 3.2.

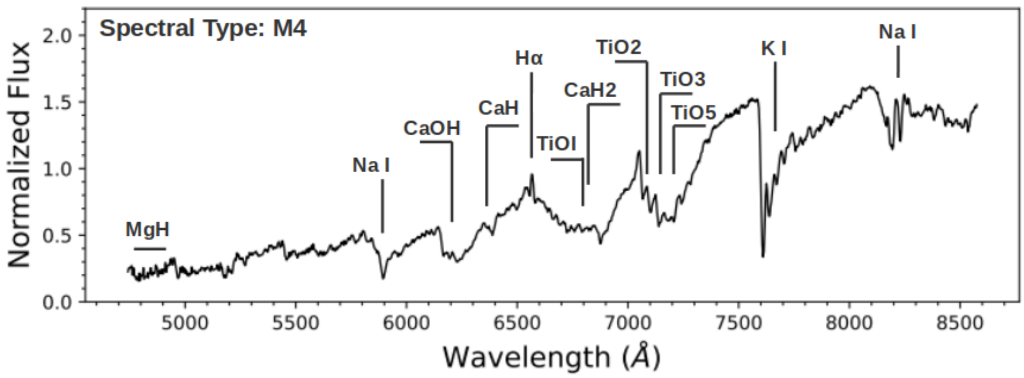

Figure 3.2: M3 dwarf optical spectrum showing several characterstics absorption features of TiO bands.

3.2 Feasibility of M dwarf characterization program with MFOSC-P

Small aperture (1-2m class) telescopes, when equipped with suitable instrumentation, can broaden and diversify the scope of various science programs that could be done with such facilities. The development of the MFOSC-P instrument offers one such opportunity. Though MFOSC-P has been conceived as a general user facility instrument for a variety of astrophysical science programs, it can also be utilized for dedicated long-term observational programs e.g., understanding the Exo-planet host star's properties. As discussed above, M dwarfs were found to be suitable candidates for PV of MFOSC-P for various reasons. However, in general, M dwarfs are of particular interest to explore planet search in the habitable zone as they offer suitable conditions in the solar neighborhood with shorter orbital periods. Though their high-resolution spectroscopy are indeed useful for the detections and characterization of host stars, their intrinsic low luminosities make them difficult targets for such high-resolution spectroscopy programs on small aperture telescopes. On the other hand, low-resolution spectrographs like MFOSC-P can target fainter objects and provide very useful insights regarding the host star properties. Thus the feasibility of M dwarf characterization program using low-resolution spectra from MFOSC-P was taken as the first dedicated science program during the PV phase of the instrument.

3.3 Optical Spectroscopy of M dwarfs: First Results from MFOSC-P

In the recent past, various space-based as well as ground-based surveys (e.g., Wide-field Infrared Survey Explorer - WISE (Wright et al., 2010), Sloan Digital Sky Survey - SDSS (York et al., 2000), Two Micron All Sky Survey - 2MASS (Skrutskie et al., 2006), etc.) have been extremely useful to provide the unprecedented photometric and spectroscopic data of cool M dwarfs. Being suitable targets for various exoplanet search programs, a good number of bright M dwarfs candidates in the solar neighborhood has been surveyed for their photometry (Lépine & Gaidos, 2011) and spectroscopy (Reid et al., 1995a; Hawley et al., 1996; Lépine et al., 2013; Frith et al., 2013). Survey such as Palomar/Michigan State University (Palomar-MSU) Nearby-Star Spectroscopic Survey (Reid et al., 1995a; Hawley et al., 1996) covers a sample of M dwarfs in both northern and southern sky beyond the 25 pc limit with radial velocities accuracy of $\pm$ 10 kms^{-1}. This survey was used to determine spectral types, absolute magnitudes, and distances of their targets, to identify chromospherically active M dwarfs with Hα emission and to determine the luminosity function (Reid et al., 1995a; Hawley et al., 1996). Palomar-MSU survey was further used by Hawley et al. (1996) and Gizis et al. (2002) to study the relation between chromospheric activity and age among early (M0–M2.5) and mid (M3–M6) dwarfs. Later, Lépine et al. (2013) and Frith et al. (2013) performed the spectroscopic observations of bright M dwarfs magnitude J $<$ 9 and K $<$ 9, respectively) in the northern sky, as selected from the SUPERBLINK proper motion catalog and Position and Proper Motion Extended-L (PPMXL) catalog. Such surveys and programs provided an insight into the age, metallicity, and evolution of M dwarfs along with local star formation history.

Determination of fundamental parameters (e.g., effective temperature, metallicity, surface gravity, etc.) and atmospheric properties of M dwarfs from their spectra are also of much significance. However, the atmospheric properties of M dwarfs changes significantly from early M dwarfs to late M dwarfs (M0 to M9). The presence of complex molecular bands (e.g., Titanium oxide (TiO), Vanadium oxide (VO) in the optical and hydrides such as CaH, FeH in the Near-Infrared (NIR) spectra of M dwarfs, etc.) make access to M dwarfs true continuum very difficult and cause uncertainties in the determination of their atmospheric properties and fundamental parameters. Recently, Rajpurohit et al. (2013, 2014, 2016, 2018a,b) and Passegger et al. (2016, 2019) compared observed optical and NIR spectra of M dwarfs with their synthetic spectra to determine their atmospheric properties and fundamental parameters. Model atmosphere such as BT-Settl, which account for recent advancement in various line list by (Plez, 1998) and (Barber et al., 2006) along with dust formation (Allard et al., 2003, 2012, 2013) is now able to reproduce the shape of the spectral energy distribution (SED) down to late M dwarfs (M9) and have improved the previous estimates significantly from earlier studies (Allard & Hauschildt, 1995; Rajpurohit et al., 2012).

The principal aim of this work is to perform the spectroscopic observations to classify and determine the atmospheric properties and fundamental parameters of a sample of M dwarfs, thereby showing the importance of suitable instrumentation on small aperture telescopes for M Dwarfs studies and the usefulness of MFOSC-P for such programs in particular. Our sample of M dwarfs, along with observations and data reduction are described in Section 3.3.1. Section 3.3.2 describes the spectroscopic classification based on the comparison with the template spectra. The determination of fundamental parameters of M dwarfs in our sample is described in Section 3.3.3.

3.3.1 Spectroscopic Observations and Data Reduction

The observations were performed during the commissioning run of MFOSC-P instrument on PRL 1.2m, f/13 Telescope. We had selected bright M dwarf sources from the all sky catalog of bright M dwarfs (Lépine & Gaidos, 2011),

Table 3.1: Properties of M dwarfs sample used in this study along with their coordinates. Optical and Near-infrared photometry is compiled from Ochsenbein et al. (2000) and Lépine & Gaidos (2011). The parallaxes of M dwarfs in our sample is taken from GAIA DR-2 database (Luri et al., 2018). The complete table is given in the APPENDIX-B.1

Source Name	RA	Dec	V (mag)	R (mag)	I (mag)	J (mag)	H (mag)	K (mag)	GAIA parallex (mas)	Distance (parsec)
Css833	13h48m34.02s	+31d59m56.89s	12.34	11.91	-	9.02	8.43	8.22	34.083	29.34
G123-74	12h57m32.41s	+40d57m00.89s	13.23	12.43	10.20	9.22	8.57	8.38	24.400	40.98
G138-64	16h46m13.76s	+16d28m41.08s	11.65	10.60	9.27	7.95	7.29	7.09	63.407	15.77
G138-7	16h11m28.10s	+07d03m59.98s	14.08	13.41	10.60	9.77	9.28	9.02	36.411	27.46
- - - - -	- - - - -	- - - - -	- - - - -	- - - - -	- - - - -	- - - - -	- - - - -	- - - - -	- - - - -	- - - - -
- - - - -	- - - - -	- - - - -	- - - - -	- - - - -	- - - - -	- - - - -	- - - - -	- - - - -	- - - - -	- - - - -

typically with V magnitude brighter than 14 and covering a wide sub-spectral types. A total of 80 suitable targets were observed between February-June 2019. The authors refer to (Lépine & Gaidos, 2011) for more detail of the brightest M dwarfs candidates with magnitude $J < 10$. The details of these targets are summarized in Table 3.1. Parallax for these sources are obtained from GAIA DR-2 archive (Luri et al., 2018) are given as reference. These parallaxes are converted to the distance (pc) as per the method and tool given in Luri et al. (2018). All of these sources are within the distance of 100 pc.

The target M dwarfs in our sample were observed using R500 mode covering the spectral range of 4800-8300 Å with a slit width of 1 arc-second. The sources were observed for integration time in range of 500-1500 seconds per object. Wavelength calibration spectra were recorded immediately after each of the science spectra in the same settings of the instrument and orientation of the telescope. MFOSC-P instrument is equipped with Halogen and spectral calibration lamps. Neon and Xenon calibration lamps are used for wavelength calibration. Spectro-photometric standard stars from ESO catalog [1] were also observed for the instrument response correction.

These early science observations were used to develop the data reduction process and pipeline of MFOSC-P. The observed raw data were reduced using a self-developed data reduction pipeline in PYTHON using astronomical image processing libraries (e.g. ASTROPY etc.) available in the public domain. Wavelength solution was determined from the spectral lamps spectra recorded

[1]https://www.eso.org/sci/observing/tools/standards/spectra/stanlis.html

immediately after the science observations. The detailed steps of the data reduction process and pipeline development are discussed in section 2.4.

Though second-order contamination from the blue part is expected to be there at the redder part of the spectrum, the targets like M dwarfs are redder in the spectrum and typically have U to I band flux ratio of nearly 1:100. Thus, given the spectral throughput of the instrument along with the telescope in blue part, blaze function of the grating and Spectral Energy Distribution (SED) of the objects second order spectral contamination are minimal. Nevertheless, even though the observed spectral range are up to 8300Å, we have restricted our analysis within the wavelength range of 4800-8100 Å (see sections 3.3.2 and 3.3.3).

3.3.2 Follow-up Spectroscopic classification

Over the last few decades, several schemes have been proposed for M dwarfs classification. These schemes, mostly based on spectral shape and features of the M dwarf spectra, are used to preliminary classify them according to their fundamental parameters and atmospheric properties. The SED and the broad-band colors of M dwarfs are mostly governed by the various molecular opacities e.g. TiO, VO and hydrides bands etc, both in the optical and in the NIR. The strength of these opacities varies from early type M dwarf (M0 type) to late-type (M5 or later); for example, the broad molecular bands such as from TiO are stronger in early M dwarfs while VO and hydrides (CaH) bands are stronger (Allard et al., 2000) in later M dwarfs. The strength of these molecular bands depends on the atmospheric properties and various stellar parameters such as effective temperature (T_{eff}), surface gravity ($\log g$), and metallicity ([M/H]) of the M dwarf. Considering such variation in the M dwarf spectra, Kirkpatrick et al. (1991) used the least-squares minimization technique to classify M dwarfs by comparing the template M dwarf spectra with the target spectrum. Later on, Henry et al. (2002) and Scholz et al. (2005) used a similar technique that compares the low-resolution template spectra of M dwarfs with that of the observed M dwarfs spectrum.

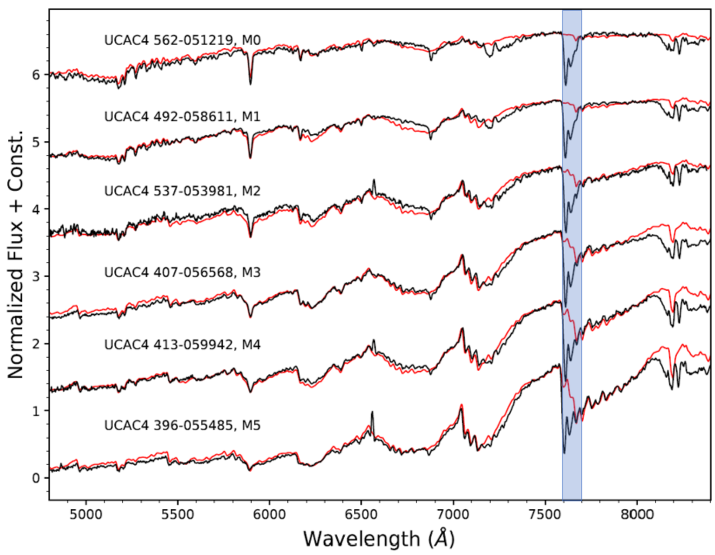

Figure 3.3: SDSS template spectra (red) taken from Bochanski et al. (2007) is compared with observed spectral sequence of M dwarfs (black). Representative spectra of different subclasses from our sample are chosen to show the match. The most prominent spectral features along with the derived spectral type are also labeled. The blue-shaded region shows the telluric absorption at 7605 Å.

Reid et al. (1995a) adopted the classification scheme, which was based on measuring the strength of the most prominent molecular bands called "band indices" such as TiO and CaH. Here the ratio of flux between various bandheads to that of the flux in nearby pseudo-continuum was determined, which was then used to classify early M dwarfs to mid M dwarfs (M0 to M5). These bands get saturated in late M dwarfs (later than M5); thus VO bandheads were used for the classification (Kirkpatrick et al., 1995). Martín et al. (1999) assigns the spectral type to late M dwarfs based on the pseudo-continuum spectral ratios (namely PC3). Gizis (1997) further classified them into the sub-category of M subdwarfs based on the strength and ratio of CaH and TiO molecular bandheads. This work was later expanded by Lépine et al. (2003) and Lépine et al. (2007).

While the above works utilize the high-resolution spectra, Scholz et al. (2005) shows that the comparison of low-resolution spectral templates provides an accurate classification of M dwarfs. In this work, we have utilized the low-resolution spectra of M dwarfs covering the spectral regime 4800-8100 Å for their classification. The template spectra of low-mass M dwarfs are taken from Bochanski et al. (2007) to be used as template spectra of such stars from M0 to L0. These template spectra were derived from 4000 SDSS spectra. Similar to the works of (Kirkpatrick et al., 1995), Scholz et al. (2005), we have adopted the least square minimization techniques to determine the spectral type of the observed M dwarfs in our sample.

Here we first normalized both the template and observed spectra of M dwarfs. The higher resolution (R$\sim$1800) SDSS template spectra were then convolved using a Gaussian kernel at the same resolution as that of the observed spectrum (R$\sim$500). Later, these flux normalized spectra were compared with the template ones for the least square minimization process to obtain the nearest match. The spectral type of this nearest match was then assigned to the observed M dwarf (Table 3.2). We expect the error to be of one spectral class in this method as the template spectra themselves are at the spacing of one spectral class.

Figure 3.3 shows the comparison of a set of observed spectral sequence of M dwarfs in our sample with the SDSS standard M dwarfs template spectra along with the most prominent spectral features. We also tried to classify the M dwarfs in our sample by calculating the spectral indices method developed by Reid et al. (1995a) using the band strengths of TiO and CaH. However, the resolution of our spectra was not good enough to achieve reliable spectral types. APPENDIX-B.2 shows the observed spectra of M dwarfs in our sample along with their spectral type derived from the method described above. Most of the sources show similar spectral sub-classification or within one class of their photometric classification Lépine & Gaidos (2011). In four M dwarfs, the difference is found to be two or three sub-classes.

3.3.3 Fundamental Parameters

Fundamental stellar parameters of our sample targets were determined by comparing the observed spectra with the synthetic spectra generated by the BT-Settl version of PHOENIX (Allard et al., 2011, 2013). The BT-Settl model grid spans the T_{eff} between 300 and 7000 K in the steps of 100 K, $\log g$ ranges from 2.5 to 5.5 at a step of 0.5 dex and metallicity [M/H] ranges from -2.5 to +0.5 at a

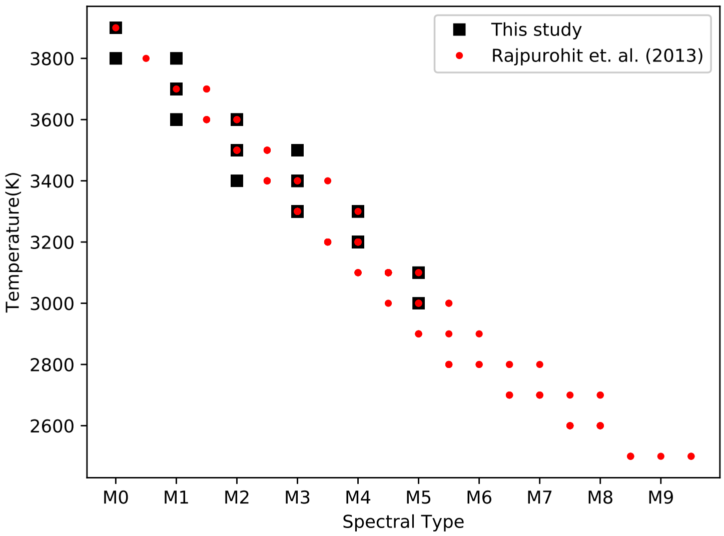

Figure 3.4: Comparison of $T_{\rm eff}$ versus spectral type relation from this study (black filed square) with that of Rajpurohit et al. (2013) (filed red circles).

step of 0.5 dex. These models account for the latest solar abundances by Caffau et al. (2009); Caffau et al. (2010) with updated water vapour opacities (Barber & Tennyson, 2008). Along with the alpha-element enrichment, various microphysical processes as well as dust and cloud formation along with the gravitational settling (Allard et al., 2012) has also been included in these models. Recently, Rajpurohit et al. (2012, 2013, 2014, 2018b,a) have validated the BT-Settl models by comparing the low resolution ($\triangle\lambda$ = 10 Å) as well as the high resolution (R = 20,000 and 90,000) optical and near-infrared spectra (NIR) with the BT-Settl models in the gird range of 2400 $\leq T_{\rm eff} \leq$ 4000 K.

Table 3.2: Stellar parameters of M dwarfs sample determined in this study. The complete table is given in the APPENDIX-B.4

Source Name	Photometric Spectral Type (Lépine & Gaidos, 2011)	Derived Spectral Type (This study)	$T_{\rm eff}$ (K)	$\log g$ (cm/sec^2)	Source Name	Photometric Spectral Type (Lépine & Gaidos, 2011)	Derived Spectral Type (This study)	$T_{\rm eff}$ (K)	$\log g$ (cm/sec^2)
Css833	M2	M2	3500	5	UCAC4 540-054017	M0	M1	3700	5
G123-74	M3	M2	3500	5.5	UCAC4 546-052448	M4	M4	3200	4.5
G138-64	M3	M4	3200	5	UCAC4 548-070636	M2	M2	3500	5
- - - - -	- - - -	- - - -	- - - -	- - - -	- - - -	- - - -	- - - -	- - - -	- - - -
- - - - -	- - - -	- - - -	- - - -	- - - -	- - - -	- - - -	- - - -	- - - -	- - - -

* Hα emission at 6563 Å is detected.

The BT-Settl model grid used in this study for the comparison spans $T_{\rm eff}$ between 3000 to 4000 K in steps of 100 K and $\log g$ ranges from 4.0 to 5.5 in steps of 0.5 dex. Since M dwarfs in our sample lies within 100 pc of the solar neighborhood and belong to the disc population (Lépine & Gaidos, 2011), so we do not expect large deviations from solar metallicity. Thus we have used the models with the solar metallicity ([M/H] = 0.0) for the comparison. The comparison of BT-Settl synthetic spectra with the observed spectra involves the process of degrading the high-resolution synthetic spectra at a resolution of the observed spectra by using a Gaussian convolution. We then employed the χ^2 method as discussed in Rajpurohit et al. (2013) to determine the T_{eff} and $\log g$ of M dwarfs in our sample. The spectral range between 5500 to 8100 Å have been used for the χ^2 calculation. The spectral regions below 5500 Å (due to low SNR) and between 7600 to 7700 Å (which includes the telluric absorption) have not been considered in the χ^2 calculations. During the χ^2 calculations, we have not applied any weights on any spectral region for the determination of T_{eff} and $\log g$. We have retained the models that give the lowest χ^2 as the best-fit parameters. The best fit models have also been inspected visually by comparing them with the observed spectra. With the given resolution of the observed spectra, the error in the derived fundamental parameters are equal to the gird spacing of the synthetic spectrum, which is 100 K for T_{eff} and 0.5 dex for $\log g$. More details about the procedure of determination of the stellar parameters of M dwarfs can be found in Rajpurohit et al. (2013). The BT-Settl model is able to reproduce the shape of SED and the profiles of the strong atomic lines such as Na I D, though no attempt has been made to fit the individual atomic lines, such as the K I and Na I resonance doublets. APPENDIX-B.3 shows the comparison of the entire spectral sequence of M dwarfs (black) with the synthetic spectra (red). The best-fit parameters of M dwarfs in our samples are given in Table 3.2. We have compared T_{eff} and spectral type determined for the individual stars in this study with Rajpurohit et al. (2013) and found a very good agreement between them (Figure 3.4).

3.4 Short-term variabilities of Hα and Hβ emissions in M Dwarfs

As discussed earlier in this chapter, ten sources of the previous study (see the previous section) were found to show Hα emission. This prompted us to conceive another observing program for M dwarfs to study the short-term variability of Hα and Hβ emission in another sample of M dwarfs (including the ten sources of the earlier sample). Such studies are essential to understand and correlate various properties of M dwarfs such as age, activity, or rotation with the observed variability in these emission lines (Hawley et al., 1996; Gizis et al., 2002).

A large fraction of M dwarfs are known to be active (West et al., 2008, 2015), and it is expected that the nature of these activities would affect the evolution of its companion. Therefore, a thorough understanding of the active nature of M dwarfs is essential not only to explore the physics of M dwarfs but also to understand the evolutionary cycle of the associated components. It is well established that magnetic fields play a very crucial role in defining the activity strength of the M dwarfs. Activity is a general term used to describe a wide range of observable phenomena produced in the outer stellar atmosphere (strong stellar winds, flares, coronal mass ejection, spots, etc.). Frequent flaring events are observed in M dwarfs, and they are known to be caused by the strong magnetic field associated with their convective envelopes (Hawley et al., 2014; Chang et al., 2017). Thus, the origin, evolution, and dynamics of the magnetic field in M dwarfs are essential to understand their activities. Further, it has been suggested that these magnetic activities are closely tied with the rotational periods of the underlying M dwarfs (West et al., 2008; Reiners et al., 2012, 2014; Newton et al., 2017; Wright et al., 2018).

While rotation periods of M dwarfs are determined with a variety of well-established methods of spectroscopy (e.g., $v\ sin\ i$ measurements) and photometry (by measuring brightness variations caused by long-lived star-spots) (Kiraga & Stepien, 2007), measuring activity strength relies on some indirect proxies, e.g., coronal and chromospheric emissions and their temporal variations, etc. The atomic lines such as Ca *II*, Mg *II* and K lines along with Hα are commonly used as a proxy of magnetic activity in M dwarfs (West et al., 2004, 2008; Lee et al., 2010), as it is the magnetic heating of the stellar atmosphere that results in such coronal and chromospheric emissions. Out of these, the chromospheric Hα emission line is widely used for activity-related studies, as it is easily observable in M dwarfs, compared to other lines in the faint blue part of the spectrum (Walkowicz & Hawley, 2009). The relation between sub-spectral type (M0-M9), the rotation period, and activity strengths is also an important consideration. West et al. (2008) shows that the chromospheric Hα emission, which is present in approximately 5 % in early M dwarfs (M0-M5), increases dramatically to 80% in M dwarfs with spectral type later than M6 whereas rotation period decrease with later spectral type (Jenkins et al., 2009; Newton et al., 2017). Further, Jenkins et al. (2009) finds that M0 to M5 stars show the change in the rotation period, which is mainly caused due to changing field topology between partially and fully convective M dwarfs.

The magnetic activities in the M dwarf happen at various time scales ranging from a few seconds to several hours (Kowalski et al., 2010; Yang et al., 2017). Doyle et al. (2018, 2019) demonstrated that magnetic activity and energetic flaring events on the stellar surface could vanish in seconds to hours. Such activities would then invariably be seen in the flux variation in Hα (Lee et al., 2010; Hilton et al., 2010; Almeida et al., 2011; Walkowicz et al., 2011; Hawley et al., 2014; Chang et al., 2017). While a good samples of M dwarfs have been studied to characterize the activity at the larger time scales through Hα variability, there are very few studies in the literature that investigate Hα variability at shorter time scales of a few minutes.

In recent times, TESS and Kepler/K2 missions (Caldwell et al., 2010; Koch et al., 2010; Howell et al., 2014; Ricker et al., 2015) have offered another opportunity to study various activity indicators (e.g. star-spots), in addition to determining their photometric periods. The high cadence data from these missions are successfully used to explore the short-duration activities in the photometry light curves (Doyle et al., 2018, 2019). However, we note that a systematic spectroscopy sample of M dwarfs of shorter cadence (5 minutes or below) is scarce in the literature. While several studies have been made on a sample of M dwarfs across spectral type (Lee et al., 2010; Hilton et al., 2010; Kruse et al., 2010; Bell et al., 2012), except Lee et al. (2010), most of these studies had explored the variability in Hα at the cadence greater than 15-20 minutes and/or with a sample of uneven cadence. Thus, shorter duration behavior could not be probed, leading to a gap in the systematic understanding of Hα variabilities on such time scales.

One such sort scale systematic data set was presented by Lee et al. (2010) who had studied 43 sources of M3.5-M8.5 spectral range, at a cadence of $\sim$5 to 10 minutes over a timescale of $\sim$ 0.1-1 hr. Though later Kruse et al. (2010) had expanded this study over a full spectral sequence (M0-M9), they used mostly SDSS survey data of longer exposure time ($\sim$15 minutes). Thus, to the best of our knowledge, Lee et al. (2010) is the only study that explores the activity in M dwarfs at the cadence of $\sim$5 minutes. Therefore, in this work, we have performed a systematic short-term (mostly 5 minutes individual frame exposures over 0.7-2.3 hours) spectroscopy monitoring of a sample of M dwarfs in the spectral range of M0-M6.5, to probe their Hα variabilities. This chosen spectral range was apt as our sample of 83 M dwarfs in M0-M6.5 spectral class complemented the data set provided by Lee et al. (2010) in the range of M3.5-M8.5. We have, thus, constructed a sample of $\sim$ 126 sources (including Lee et al. (2010) sources) in the full spectral range of M0-M8.5. The photometric light curves from TESS and Kepler/K2 missions are used to determine their rotation periods and other activity indicators like star-spot filling factor to study the plausible distribution between rotation periods, activity, and spectral types.

In Section 3.4.1, we describe the sample selection criteria and observations. In section 3.4.2, we have discussed the results from our spectroscopic analysis like the estimation of atmospheric parameters, Hα and Hβ variability indicators, activity strength measurements, etc. In section 3.4.3, we have estimated the rotation periods and star-spot filling factors with the help of photometric light curves and relate these with the variability indicators.

3.4.1 Sample selection & Observations

For this observing campaign, we targeted the M dwarfs in the spectral range M0-M6.5 with MFOSC-P instrument on the PRL 1.2 m, f/13 telescope (Srivastava et al., 2018, 2021; Rajpurohit et al., 2020). The moderate aperture of the telescope and cumulative (telescope + instrument) efficiency compelled us to restrict our sample with V magnitude brighter than 14 typically. This also restricts us from expanding our spectral range beyond M6 as most of the late M dwarf (M7 and beyond) are fainter (V>16) for spectroscopy with MFOSC-P on 1.2m telescope. However, this spectral range would complement the sample of Lee et al. (2010). The distribution of all the sources is shown in Fig. 3.5. The selected sources in this study have typical Hα equivalent widths (EW) < -0.75 Å, which usually corresponds to the detectable Hα line in emission. We, thus, selected 83 suitable targets from the list of Jeffers et al. (2018) and Lépine & Gaidos (2011). They were observed between March 2020 and March 2021. The details of these targets are summarized in Table 3.3.

For this observing program, we have utilized R1000 mode (300 lp mm^{-1}, dispersion ∼1.9Å per pixel) with 1 arc-second (∼3 pixels) slit-width covering a spectral range of 4700-6650Å, i.e., covering both Hβ and Hα wavelengths. The targets were monitored with integration times in the range of 200-600s per frame for ∼0.7-2.3 hours in a single stretch for each of the sources. Thus, each data set typically consists of ∼8-18 frames of the individual spectrum. A lower-resolution spectrum was also recorded for each of the sources in R500 mode (150 lp mm^{-1}, dispersion ∼3.8Å per pixel) to cover a larger wavelength range ∼4500-8500Å for spectral classification purposes. The required data for data reduction and data reduction procedure is the same as discussed in section 3.3.1. The log of the MFOSC-P spectroscopy are given in Table 3.3.

Photometric light curves of 75 of the above sources were obtained from the TESS and Kepler/K2 archival databases through Mikulski Archive for Space

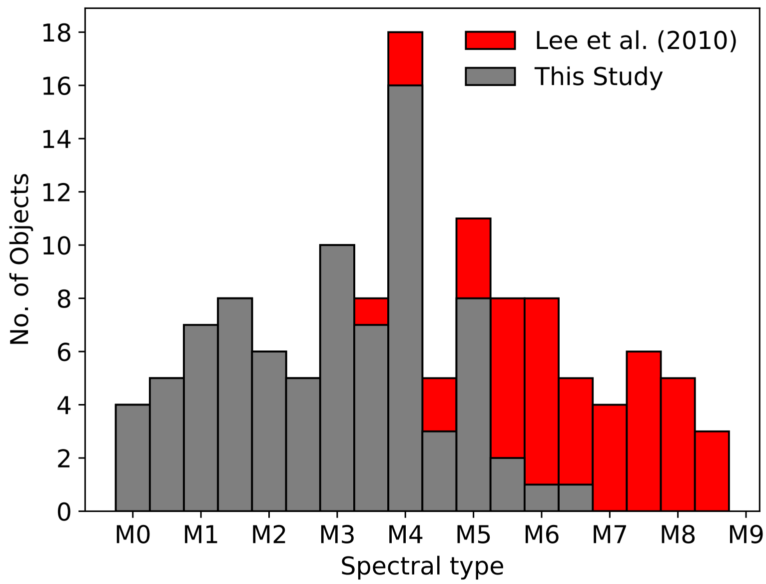

Figure 3.5: Distribution of 83 M dwarfs of this study along with 43 M dwarfs from Lee et al. (2010) with respect to the spectral type.

Telescopes (MAST) portal[2]. The related analysis and derived results are discussed in section 3.4.3.

3.4.2 Analysis and Results from Spectroscopy

3.4.2.1 Determination of Atmospheric Parameters and Spectral Class

Though the spectral classification of the targets is given in Lépine et al. (2013) and Jeffers et al. (2018), we nevertheless choose to re-confirm those with MFOSC-P low resolution (R500 mode) spectra. Even though the second-order contamination (beyond 7600Å) is expected to be minimal given the low U- to I-band flux ratios for M dwarfs (as well as low spectral throughput of the instrument + telescope in the bluer part), we have restricted the spectral range to 4500-7500 Å for this purpose. The spectral classification was derived by comparing the spectra with M dwarf templates from Bochanski et al. (2007) using a similar approach as discussed in section 3.3.2. The derived spectral classes are in good agreement with the spectral classes given by Lépine et al. (2013) and Jeffers et al. (2018) within one sub-spectral class. In this work, however, we shall be using

[2]https://mast.stsci.edu/portal/Mashup/Clients/Mast/Portal.html

Table 3.3: Observation details of the sources of this study along with the derived stellar parameters. V band magnitudes are taken from the SIMBAD database. The spectral types are mostly taken from Lépine et al. (2013), and Jeffers et al. (2018), except for six sources where we have derived the spectral class. These sources are marked with ($\star$). The complete table is given in APPENDIX-B.5

Source ID	Source name	Spectral type	Magnitude (V-band)	Date of observation (UT)	Frame exposure time × No. of frames (s)	log g (cm s^{-2})	T$_{eff}$ (K)
1	PM J03332+4615S	M0.0	13.09	2020-12-29.602	300sx14	5.0	3900
2	PM J03416+5513	M0.0	-	2021-02-01.600	300sx18	5.0	3800
3	PM J07151+1555	M0.0	11.37	2021-01-30.754	300sx18	5.0	4000
4	PM J23083-1524	M0.0	10.87	2020-11-26.563	300sx14	4.5	3900
- - - -	- - - -	- - - -	- - - -	- - - -	- - - -	- - - -	- - - -
- - - -	- - - -	- - - -	- - - -	- - - -	- - - -	- - - -	- - - -

the spectral classes of Lépine et al. (2013) and Jeffers et al. (2018) as they were derived with higher resolution spectra. The spectral classes for 6 sources were not available in these references. Thus, we took their values from our analysis.

To derive the atmospheric parameters viz. $T_{\rm eff}$, surface gravity ($\log g$), the observed spectra were compared with the BT-Sett synthetic spectra (Allard et al., 2011, 2013; Rajpurohit et al., 2012) using a similar approach as discussed in section 3.3.3. The grid for $T_{\rm eff}$ spans between 3000 to 4000 K in steps of 100 K, and $\log g$ ranges from 4.0 to 5.5 in steps of 0.5 dex at solar metallicity. The spectral range between 5000 to 7500 Å has been used for the χ^2 minimization. The spectral regions between 6540-6585 Å and 6840-6920 Å (containing Hα and Hβ emission line and telluric feature, respectively) were excluded for this analysis. The parameters derived would, thus, have errors equal to the grid spacing, i.e., 100 K for $T_{\rm eff}$ and 0.5 dex for $\log g$. The derived atmospheric parameters of all the sources are summarized in Table 3.3 along with the observing log.

3.4.2.2 Hα & Hβ Equivalent Widths (EW) and their variability

The EWs of Hα and Hβ emissions are calculated as,

$$EW = \sum \left(1 - \frac{F(\lambda)}{F_c(\lambda)}\right) \delta\lambda \tag{3.1}$$

where $F(\lambda)$ & $F_c(\lambda)$ are the line and continuum flux at wavelength λ respectively, and $\delta\lambda$ is the pixel size in the unit of wavelength. The errors in EWs include the errors in the line and continuum fluxes and errors in wavelength calibration.

Following Hilton et al. (2010), the spectral wavebands for the Hα nd Hβ are 6557.6-6571.6 Å and 4855.7-4870.0 Å respectively. The corresponding continuum regions are 6500-6550 Å & 6575-6625 Å for Hα and 4810-4850 Å & 4880-4900 Å for Hβ emissions. The average values of the continuum flux in these regions are chosen for the EWs estimations while summing the area under the line.

As discussed in section 3.4.1, each of our sources typically has 8-18 numbers of individual spectral frames with exposure time per frame in the range of 200-600s, depending on source brightness. To quantify the emission line flux variability in this time series, a χ^2 minimization is performed over the EW time series data set (EW light-curve) for each of the sources. The χ^2 values have been estimated by fitting a straight line at a constant EW to Hα and Hβ EW light curves. The confidence of χ^2 fit was determined by calculating p-values for given degrees of freedom, using an open-source numerical library scipy.stats.chi2[3] of Python. A source is termed as a variable if its p-value was determined to be less than 0.05. In our sample of 83 M dwarfs, we find that 30 objects ($\sim 36\%$) show no variation in the Hα emission with the confidence level more than 95% (p-value <0.05). The computed p-value of each of the sources are listed in Table 3.4 for both Hα and Hβ time-series. The summary of the median ($\langle$EW$\rangle$), minimum (Min), maximum (Max), and root-mean-square (RMS) values of the Hα & Hβ EWs are also given in Table 3.4.

We use the same metrics to quantify the variability strength as used by Lee et al. (2010), namely, ΔEW $= Max(EW) - Min(EW)$, RMS(EW)/$\langle$EW$\rangle$ and R(EW) = Max(EW)/Min(EW) for both the Hα and Hβ emission lines. This helps in comparing the variabilities observed in our sample in the range of M0-M6.5 with that of Lee et al. (2010) in M3.5-M8.5 spectral range. Further, these quantities do not require normalization by L_{bol} for comparison across spectral types (Kruse et al., 2010). In Fig. 3.6, we shows the variations of these quantities (ΔEW, RMS/$\langle$EW$\rangle$ and R(EW)) as a function of spectral types (panels a, b, c for Hα and panels e, f, g for Hβ). We notice a clear rising trend as reported earlier by Lee et al. (2010), and Kruse et al. (2010) which signify the higher activity in the later types of M dwarfs. Panels (d) and (h) in Fig. 3.6 show the distribution

[3]https://docs.scipy.org/doc/scipy/reference/generated/scipy.stats.chi2.html

of median normalized RMS values of EWs (RMS(EW) / $\langle$EW$\rangle$) with respect to $\langle$EW$\rangle$, for Hα and Hβ respectively. Here the segregation of our data set (M0-M6.5) and Lee et al. (2010) (M3.5-M8.5) data set is more prominent. The later types of M dwarfs, though having lesser $\langle$EW$\rangle$ tend to be more variable. The values of RMS(EW)/$\langle$EW$\rangle$ for our sources (M0-M6.5) are found to be below $\sim$0.2 for Hα and below $\sim$0.5 for Hβ . These trends are again discussed in section 3.4.4 along with other results.

We attempted to explore the time scales of these variabilities, if any, using a simple construct of the fractional structure function (SF). For a given EW time-series (for Hα and Hβ), the fractional SF at a given time scale (τ) is defined as,

$$SF(\tau) = \left\langle \left[\frac{EW(t+\tau) - EW(t)}{\mathrm{Mean(EW)}} \right]^2 \right\rangle \tag{3.2}$$

where EW(t+τ) and EW(t) are two consecutive measurements of EW at the time interval of τ and Mean(EW) is the mean value of the full time-series. Though the fractional SFs do not clearly show any characteristic time scale of variabilities (especially at lower times of a few minutes), they nevertheless reinforce an interesting trend noticed by Bell et al. (2012).

The sources which are seen to be varied at a longer time-scale (e.g., source ID: 55 in the upper panel of Fig. 3.7) exhibit a fractional SF, which shows an increasing trend, as expected. However, conforming to the results of Bell et al. (2012), the sources whose EWs light curves are seen to be varied at shorter time scales (e.g., source ID: 80 in the lower panel of Fig. 3.7) show a nearly flat distribution of fractional SF at all times. Bell et al. (2012) attributed such behavior of the high variables sources due to the variability time scale shorter than their smallest time-separation bin of $\sim$15 minutes. We also see the same trend even at the cadence of $\sim$5 minutes.

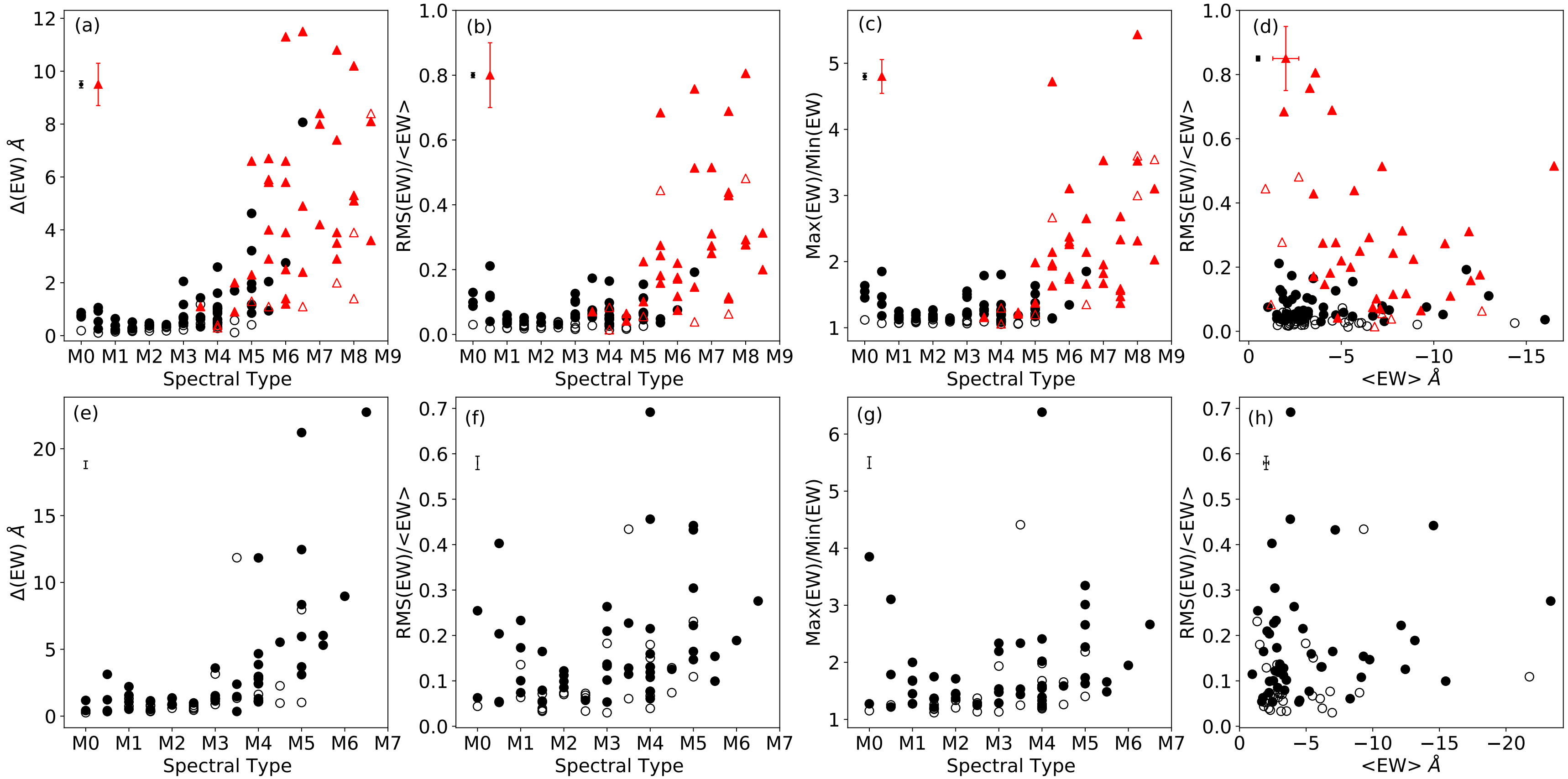

Figure 3.6: Plots showing the variations of various quantities depicting the variabilities of the EWs of Hα and Hβ emissions in M dwarfs. Panels (a), (b), and (c) (in the top row for Hα) and panels (e), (f) and (g) (in the bottom row for Hβ) show the changes in Δ(EW), RMS(EW)/$\langle$EW$\rangle$, and Max(EW)/Min(EW) respectively as the function of spectral type. Panels (d) and (h) show the variation of RMS(EW)/$\langle$EW$\rangle$ with respect to $\langle$EW$\rangle$ for Hα and Hβ respectively. Black circles represent the data points of our sample in this study. Red triangles represent the data points derived from the values given in Table-2 of Lee et al. (2010). Filled and open circles/triangles represent the objects identified with varying and non-varying Hα using the χ^2 criterion ($p < 0.05$ for variable sources). The error bars on the top-left corner show the median errors of the data points. See section 3.4.2.2 for more details.

The spectra, EW light curves, and fractional SFs for Hα and Hβ are shown in Fig. 3.7 for two of the sources of our sample. Similar plots for all the sources of this study are given in Appendix B.6.

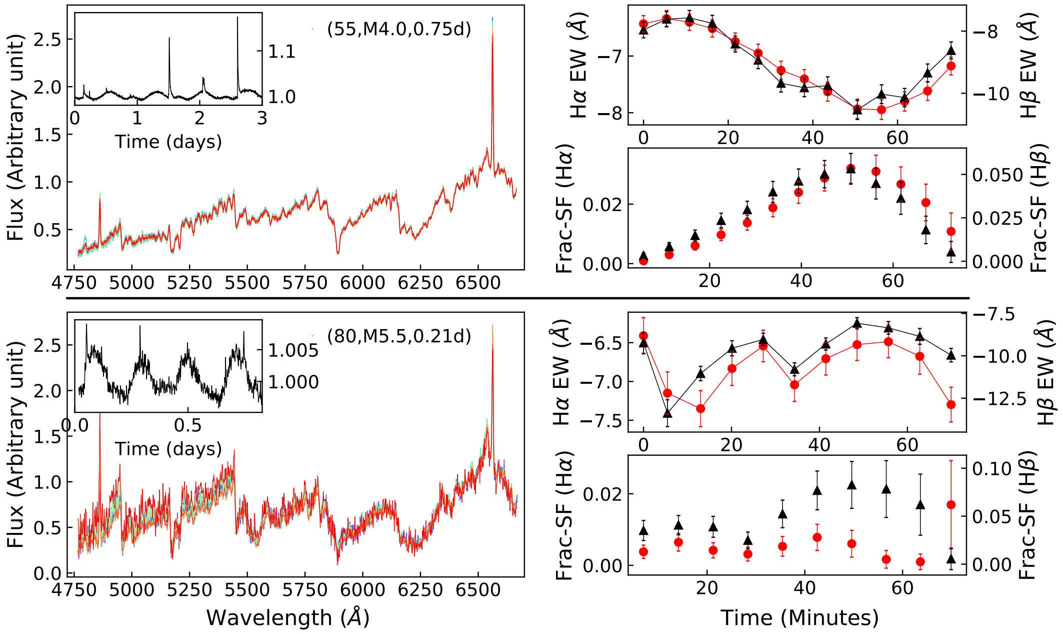

Figure 3.7: The figure shows the time-varying spectra of two sources (source ID: 55 in the top panel and Source ID: 80 in the bottom panel) along with their photometric light curves in the inset. Source ID, spectral type, and rotation period are also mentioned in each of the panels. The corresponding upper and bottom right side panels show the time variations of the EWs of Hα / Hβ and fraction structure function (SF), respectively. Data for Hα and Hβ are shown in red circles and black triangles, respectively. See section 3.4.2.2 for discussion. Similar plots for all the sources of this study are given in the Appendix B.6.

3.4.2.3 Hα and Hβ activity strength and flaring sources

Hα or Hβ activity strength is defined as the ratio of their luminosity to the bolometric luminosity (West et al., 2008; Hilton et al., 2010; Lee et al., 2010; Newton et al., 2017). The activity strength enables a better comparison of activity between stars of different masses than EW alone (Reid et al., 1995b), as it shows the importance of the line flux relative to the entire energy output of the star. We adopted the following relations given by Douglas et al. (2014) to calculate the Hα and Hβ activity strength as,

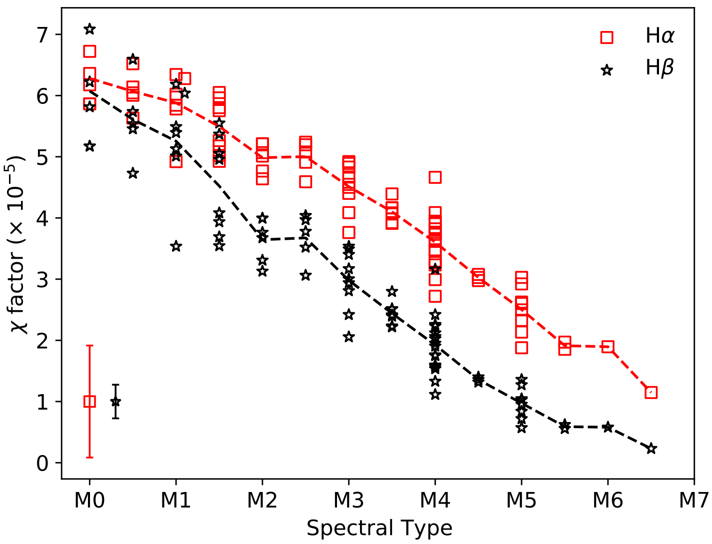

Figure 3.8: The derived χ factors for Hα and Hβ are shown with respect to spectral types. Median error bars are shown in the bottom-left of the plot. The lines joining the mean values of χ factors for a given spectral bin are also shown for Hα and Hβ .

$$\begin{aligned}\frac{L_{H\alpha}}{L_{bol}} &= -\chi_{\mathrm{H}\alpha} \times (EW)_{H\alpha} \\ \frac{L_{H\beta}}{L_{bol}} &= -\chi_{\mathrm{H}\beta} \times (EW)_{H\beta}\end{aligned} \tag{3.3}$$

where $EW_{H\alpha}$ and $EW_{H\beta}$ are the equivalent widths of the Hα and Hβ emission lines respectively, and the χ factor for Hα and Hβ are derived from photometric color $(i - J)$ (Walkowicz et al., 2004; Douglas et al., 2014; West & Hawley, 2008). The χ factor is defined as the ratio of the flux in the continuum near Hα to the bolometric flux (Walkowicz et al., 2004). For the sources where i magnitudes are not available, we adopted the approach of Newton et al. (2017) first to calculate the M_{Earth} magnitudes (Dittmann et al., 2016) and later applied the relation given in section 3.3 in Newton et al. (2017) to calculate the final $i_{48} - J$ color. Similar to Newton et al. (2017), we have not made any additional correction between i_{48} and i as it would be minor. In Fig. 3.8 we show the variation of derived χ factors as a function of the spectral type where a trend similar to Newton et al. (2017) is noticed. They are also consistent with the range of χ factors given in Newton et al. (2017).

The derived values of the means of $L_{\mathrm{H}\alpha}/L_{\mathrm{bol}}$ and $L_{\mathrm{H}\beta}/L_{\mathrm{bol}}$ are shown in

Table 3.4: The derived variability parameters for Hα and Hβ emission lines for the sources of this study, along with the activity strengths ($\log_{10}(L_{H\alpha}/L_{bol})$ and $\log_{10}(L_{H\beta}/L_{bol})$). The p-values are determined from the χ^2 minimization of EW light curves. See section 3.4.2.2 for details. The sources which are characterize as variable are marked with ($\star$). The complete table is given in the APPENDIX-B.7.

Source ID	Source name	emission line	Median Hα EW Hβ EW	Minimum Hα EW Hβ EW	Maximum Hα EW Hβ EW	Δ Hα EW Hβ EW	RMS Hα EW Hβ EW	Mean $\log_{10}(L_{H\alpha}/L_{bol})$ $\log_{10}(L_{H\beta}/L_{bol})$	P-value Hα Hβ
1	PM J03332+4615S*	Hα	-2.333 ± 0.065	-1.717 ± 0.062	-2.492 ± 0.061	0.775 ± 0.087	0.232 ± 0.022	-3.883	0.0000
		Hβ	-1.372 ± 0.085	-0.413 ± 0.091	-1.590 ± 0.086	1.177 ± 0.125	0.349 ± 0.031	-4.199	0.0000
2	PM J03416+5513	Hα	-1.688 ± 0.047	-1.587 ± 0.045	-1.775 ± 0.052	0.188 ± 0.068	0.051 ± 0.012	-3.984	0.2298
		Hβ	-1.818 ± 0.085	-1.690 ± 0.076	-1.947 ± 0.087	0.258 ± 0.116	0.080 ± 0.020	-3.981	0.4134
3	PM J07151+1555*	Hα	-2.094 ± 0.052	-1.372 ± 0.046	-2.246 ± 0.055	0.874 ± 0.072	0.183 ± 0.012	-3.854	0.0000
		Hβ	-1.755 ± 0.076	-1.525 ± 0.077	-1.942 ± 0.081	0.417 ± 0.111	0.110 ± 0.019	-3.905	0.0062
4	PM J23083-1524*	Hα	-1.698 ± 0.110	-1.298 ± 0.061	-2.010 ± 0.117	0.711 ± 0.132	0.220 ± 0.025	-3.980	0.0000
		Hβ	-	-	-	-	-	-	-
- - - -	- - - -	- - - -	- - - -	- - - -	- - - -	- - - -	- - - -	- - - -	- - - -
- - - -	- - - -	- - - -	- - - -	- - - -	- - - -	- - - -	- - - -	- - - -	- - - -

Fig. 3.9 (top-right panel for Hα and bottom-right panel for Hβ) with respect to their spectral type. The ratio of maximum to minimum values of these quantities (for Hα and Hβ) to their mean value is shown in top-left and bottom-left panels of Fig. 3.9. Both of these, $L_{\mathrm{H\alpha}}/L_{\mathrm{bol}}$ and $L_{\mathrm{H\beta}}/L_{\mathrm{bol}}$, represents the activity strength of the M dwarfs. The plots for Hα also include the values from Table-2 of Lee et al. (2010) as well. It is to be noted that Lee et al. (2010) did not provide the values of $L_{\mathrm{H\alpha,min}}/L_{\mathrm{bol}}$. Therefore we have first calculated the χ factor using $L_{\mathrm{H\alpha,max}}/L_{\mathrm{bol}}$, and the corresponding value of maximum EW (using equation 3.3). This χ factor was then used with the corresponding value of minimum EW (from Table-2 of Lee et al. (2010)) to calculate the value of $L_{\mathrm{H\alpha,min}}/L_{\mathrm{bol}}$.

$L_{H\alpha}/L_{bol}$ reaches a constant value of $\sim 10^{-3.8}$ for the M dwarfs with spectral type M0-M4 and then declines for later spectral types (later than M4), indicating the lower activity strengths for the later types. However, the variability, which can be estimated as the ratio of maximum to minimum values (of the Hα and Hβ line flux for a given time series of an M dwarf), is higher for these later spectral types. This again signifies that though the strength of the activity in these later type M dwarfs is low, they are more variable. It should be noted that the plots for Hβ include values from the sources of this study only (M0-M6.5), as Hβ values were not covered in Lee et al. (2010).

Though Hα in M dwarfs are known to show variability up to 30% in the "quiescent" phase (Gizis et al., 2002; Hilton et al., 2010; Lee et al., 2010), flaring events during the observing window could also cause additional variability in Hα

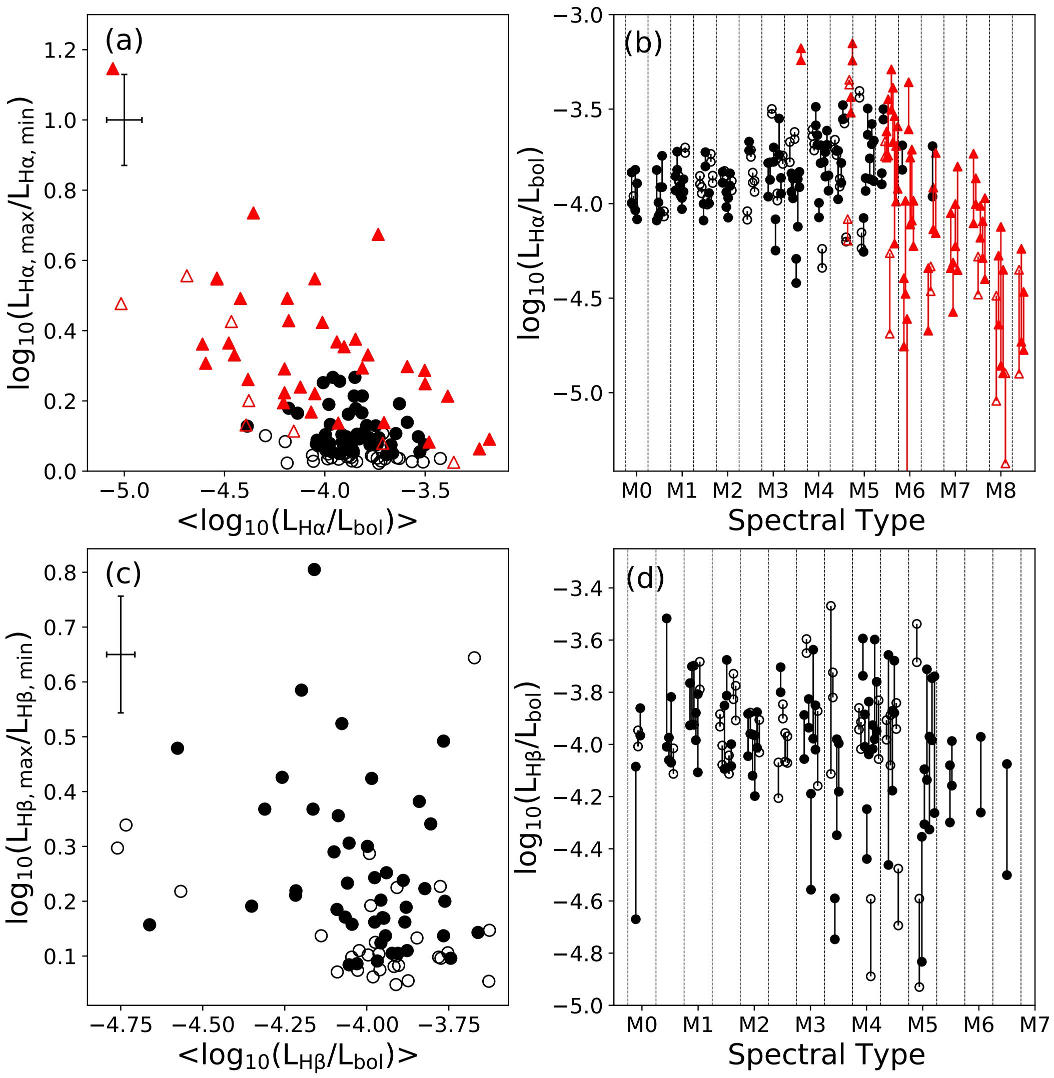

Figure 3.9: The distribution of derived activity strengths ($L_{\mathrm{H}\alpha}/L_{\mathrm{bol}}$ and $L_{\mathrm{H}\beta}/L_{\mathrm{bol}}$) for H$\alpha$ and Hβ (top-right panel for Hα and bottom-right panel for Hβ) with respect to their spectral type. Top-left and bottom-left panels show the variation of the ratio of maximum to minimum values with respect to the mean values of the activity strength for Hα and Hβ , respectively. Symbols have the same meaning as in Fig. 3.6.

and Hβ measurements. We, therefore, also wanted to check the possibility of flaring in our sample. The short exposure spectral time series of the data in this study also allows us to quantify the possibility of flares during our observations. For this purpose, we have utilized the method proposed by Hilton et al. (2010) by determining the "flaring line index" (FLI). FLI for the Hα and Hβ lines are defined as (Hilton et al., 2010),

$$FLI = \bar{l}/\sigma \tag{3.4}$$

where, $\bar{l}$ is the mean value of the continuum subtracted flux in the line region, and σ is the standard deviation of the continuum. FLIs are useful where emission-line strengths are weak and/or continuums are noisy. The statistics of FLIs of a given spectral time series would then be used to decide if a flare occurred in the observing window, based on the following criteria by Hilton et al. (2010):

(1) For strong Hα / Hβ emission sources, where mean FLI values of a time series are > 3. In such a case, if the maximum(FLI) and minimum(FLI) are differed by more than 30%, they are characterized as a flaring source during the time-series observations.

(2) For weak emission line sources (mean FLI values of a time series are < 3), if the maximum(FLI) - minimum(FLI) > 3, they were classified as flaring sources.

(3) If the mean FLI values >3 in Hα but < 3 in Hβ , in these cases, the source was said to be flaring if both the above two conditions were satisfied.

Thus, after applying the above criteria, we found that out of 75 objects that showed both the Hα and Hβ emissions, 53 objects were found to be in a flaring state at the time of observations. Out of these 53 objects, 38 were earlier classified as variable sources based on the χ^2 minimization method as discussed in section 3.4.2.2. Thus, it appears that the flaring events could be a major cause of short-term variabilities seen in the EW light curves. Table 3.5 shows the flaring status of all 75 objects along with their mean FLI values for Hα and Hβ . It has been noticed that the short-term variabilities could very well be caused by low-level flaring events (Hilton et al., 2010). However, there are very few studies that tried to explore the short-term variations in the line fluxes (Lee et al., 2010; Kruse et al., 2010). Thus, a better time resolution could very well be a key to establishing such a hypothesis.

3.4.3 Results from Photometry

In the last decade, TESS and Kepler/K2 missions (Caldwell et al., 2010; Koch et al., 2010; Howell et al., 2014; Ricker et al., 2015) have provided unprecedented cadence and photometric precisions for a variety of stellar sources. Such high cadence data is complementary to our spectroscopy analysis, and thus, we have utilized these photometric light curves to determine the periods of the objects in our sample. While for this study, we wished to explore the period dependence of various activity proxies ($EW_{H\alpha}$, $L_{H\alpha}/L_{bol}$, etc.), such light curves can also be used to determine various activities related parameters such as star-spot filling factors, etc. Some of these findings are discussed below.

70 of the 83 M dwarfs in our sample were observed by TESS in 2014-2021 in various sectors. Data reduction pipelines from the Science Processing Operations Center (SPOC: Jenkins et al. (2016)) and the Quick Look Pipeline (QLP: Huang et al. (2020)) are used to derive the light curves of these sources. For most sources, data with 2 minutes cadence are available and used in this study. In some cases, where this high cadence data were not available, 30 minutes cadence data were used. Of the remaining 13 sources, where TESS light curves were not available, we could find the photometric light curves of 5 of the sources, with 30 minutes cadence, in the Kepler/K2 data archive. The details are given in Table 3.5. TESS and Kepler/K2 light curves are also used to determine the rotation periods of the objects from the Lee et al. (2010). Light curves of 31 (out of total 43) objects were found in these archives. The details are given in Table 3.6.

3.4.3.1 Rotation Period

The rotation periods, P_{rot} are measured by quantifying the periodic brightness variations in the light curve, which are caused by the starspots on the surface of the objects. These have been determined using a periodogram technique such as Lomb-Scargle periodogram (Lomb, 1976; Scargle, 1982; Lightkurve Collaboration et al., 2018; VanderPlas, 2018) in frequency space. The period of the maximum power was further cross-checked with the phase folded light curves by visual inspection. Fig. 3.10 shows a phase folded light curve of one of the sources. Out of 106 sources where the light curves were available, the rotation periods of 82 objects were determined with the above method.

The rotation periods of objects in our sample and from Lee et al. (2010) are listed in Table 3.5 and Table 3.6 respectively. They are found to be in the range of ∼0.2-10 days. These periods are plotted against the spec-

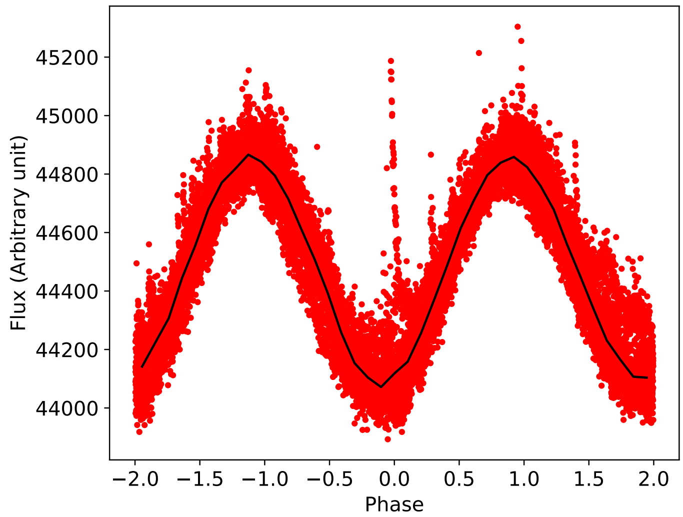

Figure 3.10: The phase-folded light-curve of PM J16170+5516 (Source ID: 30). The black solid curve is the median value of each sub-bin, which is used to determine the star-spot filling factor of the source.

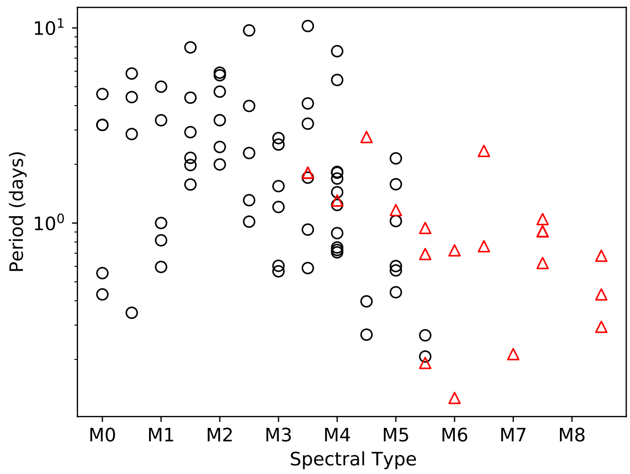

Figure 3.11: Distribution of the derived rotation periods of M dwarfs with the spectral type. Sources of this study and from Lee et al. (2010) are shown in black circles and in red triangles, respectively.

tral type in Fig. 3.11. The derived periods conformed to the general trend seen in the other studies (West et al., 2015; Newton et al., 2017; Jeffers et al., 2018), wherein the periods were found to be shorter for later spectral types. The distribution of the variabilities indicators, namely, ΔEW, RMS(EW)/⟨EW⟩, and Max(EW)/Min(EW) as well as activity strengths ($L_{\mathrm{H}\alpha}/L_{\mathrm{bol}}$ and $L_{\mathrm{H}\beta}/L_{\mathrm{bol}}$) (see sections 3.4.2.2 and 3.4.2.3) with respect to rotation periods are shown in Fig. 3.12.

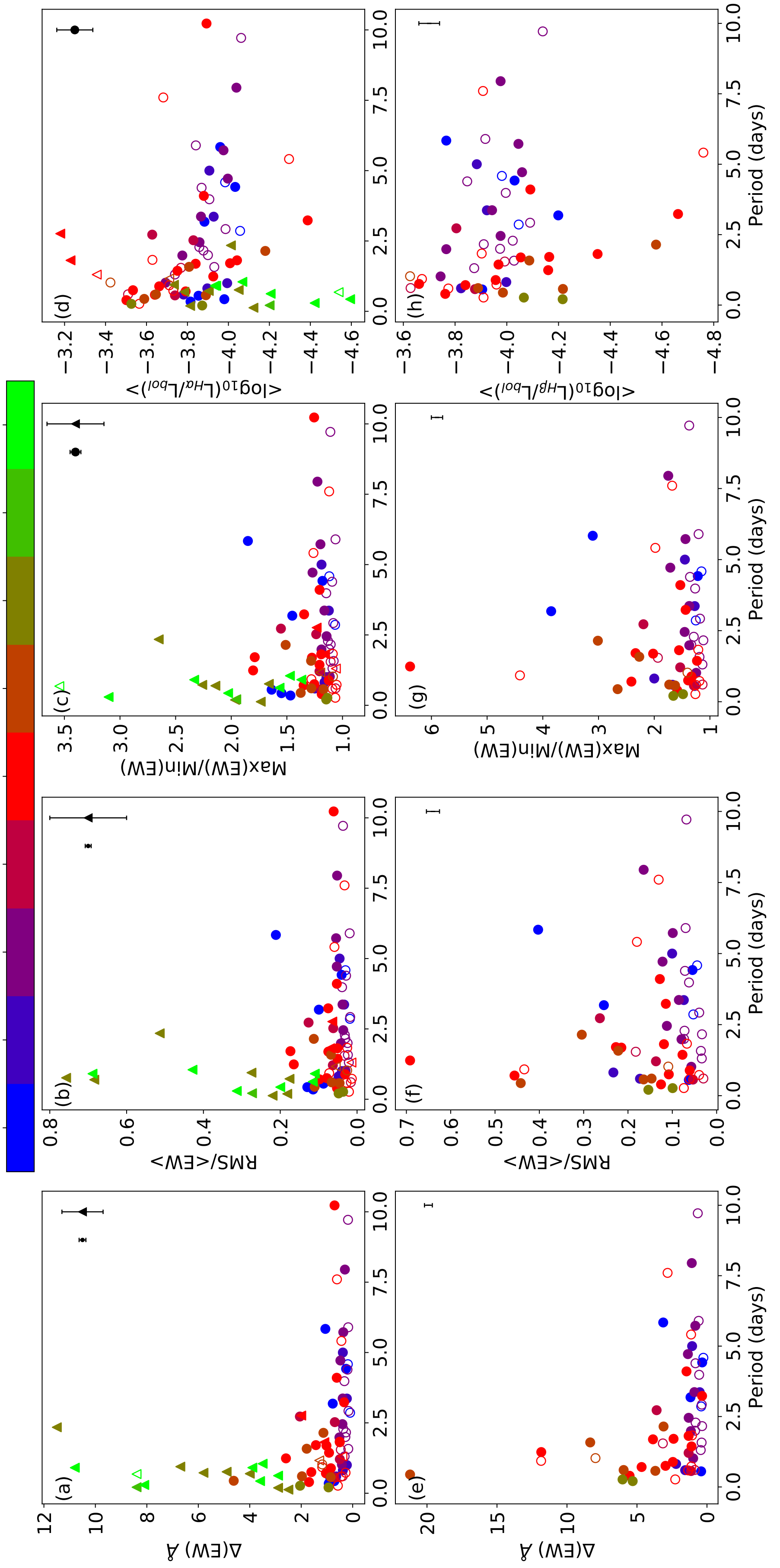

Figure 3.12: Figure shows the distribution of Δ(EW), RMS(EW)/$\langle$EW$\rangle$, R(EW) = Max(EW)/Min(EW) and mean activity strengths with their rotational periods. Top panels are for Hα and bottom panels are for Hβ emission. The median errorbars of the datapoints are shown on the top-right corner. Symbols have the same meaning as in Fig. 3.6

Various magnetic activity indicators have been used in the past to explore the relationship between the magnetic field strength and stellar rotation (Douglas et al., 2014; West et al., 2008, 2015; Newton et al., 2017; Jeffers et al., 2018). Similar to West et al. (2015) and Jeffers et al. (2018), we also find that M dwarfs with longer periods show less variabilities.

It has also been known that in M dwarfs, there is a clear decrease in the strength of activity with increasing rotation period (West et al., 2015; Jeffers et al., 2018). However, an interesting behavior can be noticed in the panels a, b, c (for Hα) and e, f, g (for Hβ), when we consider the spectral types as well. Here, the short-term variability indicators display a very clear increase for the faster rotating M dwarfs with a period $<$ 2 days, and most of these objects belong to the later types (M4-M8). As Fig. 3.11 shows, these later types are, typically, fast rotators; thus, such high variabilities can very well be caused due to coupling of the magnetic field with the rotation-induced dynamics of chromospheric regions. Hα emissions and star-spots are known to be related to magnetic properties of the stars (Newton et al., 2017). Thus such apparent correlations may be plausible and expected.

3.4.3.2 Filling Factor

The light curves from TESS and Kepler/K2 are also used to determine the star-spot filling factors. We have computed these values for the objects in this study as well as from Lee et al. (2010). The star-spots on the photosphere are the regions where the magnetic flux is much stronger, and most of the stellar flares occur. The star-spot filing factor gives the fractional area covered by star-spots (A_{spot}/A_{star}). The filling factors are computed by the following relations (Jackson & Jeffries, 2013; Maehara et al., 2017; Guenther et al., 2021):

$$\frac{A_{spot}}{A_{star}} = \left(\frac{\Delta \mathrm{F}}{\mathrm{F}}\right)_{spot} \left[1 - \left(\frac{T_{spot}}{T_*}\right)^4\right]^{-1} \tag{3.5}$$

where, A_{star} is the area of the stellar disk, A_{spot} is the area of the spots on the stellar disk, and T_* and T_{spot} are the temperature of the star and the star-spot respectively. $\Delta F/F_{spot}$ is the brightness variation amplitude of the rotation

Table 3.5: Derived rotation periods and star-spot filling factors of the objects of this study using TESS and Kepler/K2 light curves. The observing details from TESS and Kepler/K2 archives and computed mean values of FLI for Hα and Hβ emissions from the spectral time series are also mentioned. The flaring sources (as per FLI criteria) during the spectroscopy observations are marked with ($\star$) in the source-name column. See section 3.4.3 for discussion. The complete table is given in the APPENDIX-B.8

Source ID	Source name	Mission/Year/Author	Exposure time (s)	Rotation period (days)	T_{spot} (K)	Filling factor (%)	Mean FLI Hα	Mean FLI Hβ
1	PM J03332+4615S*	T-18/2019/QLP	1800	3.184	3192	36.0	10.40 $\pm$ 1.72	2.65 $\pm$ 0.95
2	PM J03416+5513*	T-19/2019/SPOC	120	4.585	3145	6.2	6.97 $\pm$ 0.62	4.50 $\pm$ 0.45
3	PM J07151+1555*	T-33/2020/SPOC	120	0.554	3239	9.6	12.05 $\pm$ 1.83	4.67 $\pm$ 0.42
4	PM J23083-1524	T-42/2021/SPOC	20	0.431	3192	8.9	6.17 $\pm$ 1.25	-
- - - -	- - - -	- - - -	- - - -	- - - -	- - - -	- - - -	- - - -	- - - -
- - - -	- - - -	- - - -	- - - -	- - - -	- - - -	- - - -	- - - -	- - - -

a : K: K2 compaign; T: TESS sector.

modulation caused by the star-spots.

The temperature difference between the photosphere and starspots is a function of the photospheric temperature of the stars (Berdyugina, 2005). Thus, T_{spot} can be estimated with the following relation (Berdyugina, 2005; Maehara et al., 2017; Notsu et al., 2019; Guenther et al., 2021):

$$T_{spot} = T_* - 3.58 \times 10^{-5} T_*^2 - 0.249 \times T_* + 808[K] \tag{3.6}$$

For the sources in this study, we have used $T_{\rm eff}$ as determined in section 3.4.2 whereas for the sources of Lee et al. (2010) $T_{\rm eff}$ are determined using the spectral type - $T_{\rm eff}$ relation of Rajpurohit et al. (2013) (see Fig.5 therein).

The derived filling factors are given in Table 3.5. We note that these filling factors are the lower limits as many active stars could have polar spots (Guenther et al., 2021). For our samples, the spot temperatures and filling factors are mostly found between ~2700-3200 K and ~0.5-20.0%, respectively. While for the sources of Lee et al. (2010), these values are mostly found to be in the range of ~2460-2800 K and ~0.5-21.8%, respectively.

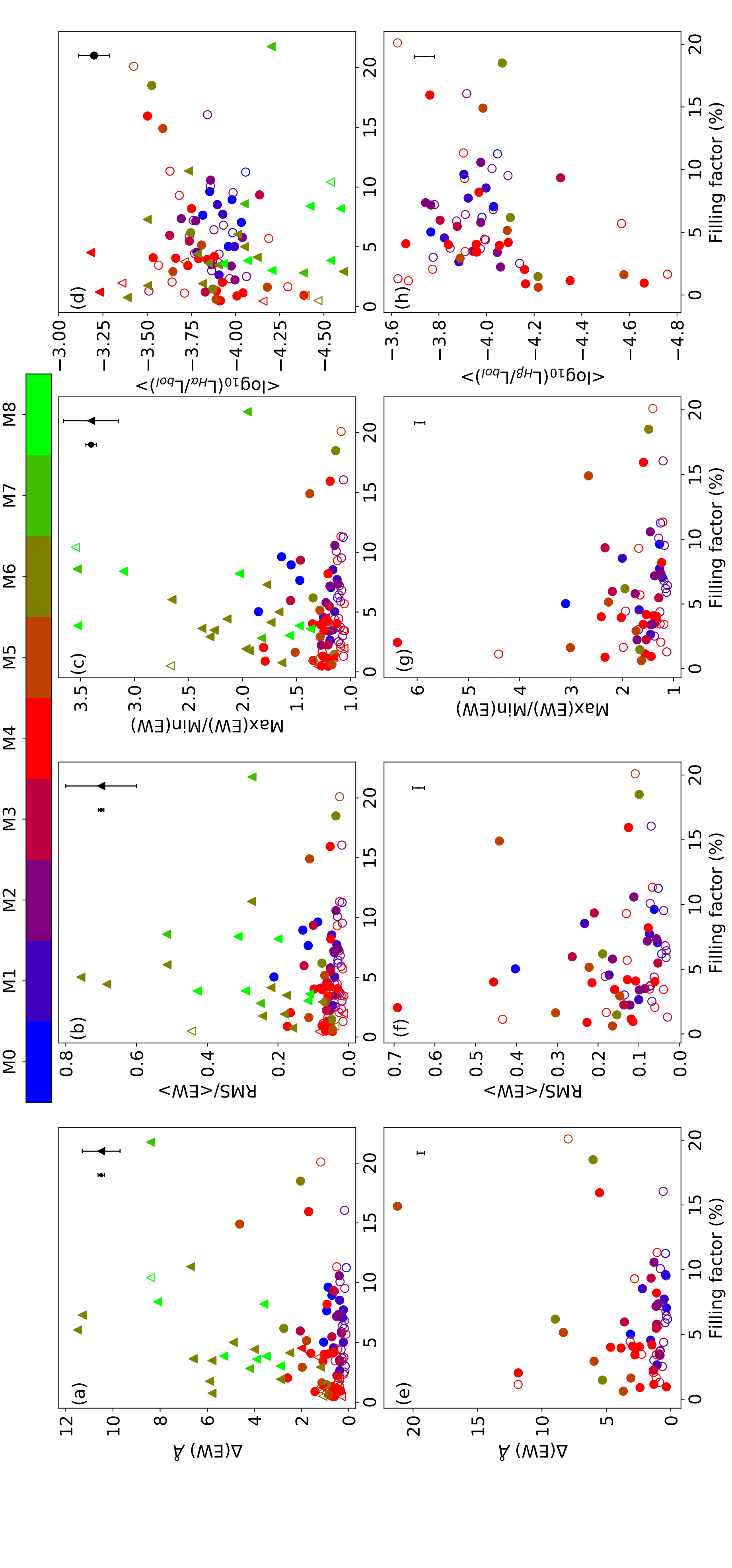

Figure 3.13: Distribution of variability indicators (same as Fig. 3.12) but with respect to star-spot filling factors.

We have also explored the variations in Hα and Hβ variability indicators with respect to the derived filling factors. Fig. 3.13 show these plots similar to Fig.3.12 (for rotations). It is postulated (Bell et al., 2012) that stars having large filling factors would have high activity strength and lesser variability and vice versa. This trend is noticeable in panels (b) and (f) for Hα and Hβ , respectively, i.e. RMS(EW) / <EW> show a downward trend for higher filling factors, i.e., high activity stars (large <EW>) which are less variable (low RMS(EW)) tend to have high filing factors.

Table 3.6: The derived rotation periods and star-spot filling factors for 31 sources of Lee et al. (2010). The $T_{\rm eff}$ values for these sources are estimated from $T_{\rm eff}$ versus spectral type relation given in Rajpurohit et al. (2013). See section 3.4.3 for discussion.

Source name	Mission/Year/ Author	Exposure time (s)	Period (days)	T_{eff} (K)	T_{spot} (K)	Filling factor(%)
G99-049	T-33/2020/SPOC	120	1.812	3100	2792	1.2
LHS1723	T-32/2020/SPOC	20	-	3100	2792	0.5
L449-1	T-32/2020/SPOC	120	1.305	3100	2792	2.0
GL285	T-34/2021/SPOC	120	2.760	3000	2739	4.52
2MASSWJ1013426-275958	T-09/2019/SPOC	120	1.165	2900	2685	3.8
DENIS-PJ213422.2-431610	T-28/2020/SPOC	120	-	2800	2630	0.5
2MASSJ02591181+0046468	T-04/2018/SPOC	120	-	2800	2630	0.8
2MASSJ02534448-7959133	T-39/2021/SPOC	120	-	2800	2630	1.8
2MASSJ00244419-2708242	T-29/2020/SPOC	120	0.944	2800	2630	11.3
2MASSJ00045753-1709369	T-29/2020/SPOC	120	0.192	2800	2630	1.9
2MASSJ20021341-5425558	T-27/2020/SPOC	120	0.694	2800	2630	4.4
LP844-25	T-35/2021/SPOC	120	-	2800	2630	2.9
2MASSJ23373831-1250277	T-42/2021/SPOC	120	-	2800	2630	7.3
2MASSWJ1012065-304926	T-36/2021/SPOC	120	0.725	2800	2630	3.5
LP731-47	T-36/2021/SPOC	120	-	2800	2630	3.6
2MASSJ23155449-0627462	T-42/2021/SPOC	120	0.127	2800	2630	4.1
GJ3622	T-09/2019/SPOC	120	-	2700	2575	0.9
2MASSJ05023867-3227500	T-32/2020/SPOC	120	0.761	2700	2575	5.0
2MASSJ02141251-0357434	T-31/2020/SPOC	120	2.343	2700	2575	6.0
2MASSJ10031918-0105079	T-08/2019/TESS-SPOC	1800	0.213	2700	2575	21.8
2MASSJ13092185-2330350	T-10/2019/SPOC	120	-	2700	2575	2.8
2MASSWJ1420544-361322	T-11/2019/SPOC	120	-	2700	2575	8.6
2MASSJ09522188-1924319	T-35/2021/SPOC	120	0.907	2600	2519	41.6
2MASSJ04291842-3123568	T-32/2020/SPOC	120	0.909	2600	2519	3.6
2MASSJ23062928-0502285	K-19/2018/K2	1800	-	2600	2519	-
2MASSJ03313025-3042383	T-31/2020/SPOC	120	1.048	2600	2519	3.9
2MASSJ04351612-1606574	T-32/2020/SPOC	120	0.624	2600	2519	3.0
2MASSJ02484100-1651216	T-31/2020/SPOC	120	-	2600	2519	3.9
2MASSJ22264440-7503425	T-27/2020/SPOC	120	0.680	2500	2462	10.4
2MASSJ03061159-3647528	T-31/2020/SPOC	120	0.294	2500	2462	8.4
2MASSJ23312174-2749500	T-29/2020/SPOC	120	0.431	2500	2462	8.2

3.4.4 Discusion: EW Variability, Rotation period, and Filling factor

The EW light curves of Hα and Hβ emissions in M dwarfs show a large gradient in the variability amplitudes over the time scale of a few minutes to few 10's of minutes. These short-term variations at various time scales can be related to the magnetic activity and energetic flaring events on the stellar surface, which can vanish in shorter time scales as argued by Lee et al. (2010); Hilton et al. (2010); Almeida et al. (2011); Walkowicz et al. (2011); Hawley et al. (2014); Chang et al. (2017). The derived mean activity strengths ($\langle L_{H\alpha}/L_{bol}\rangle$ and $\langle L_{H\beta}/L_{bol}\rangle$) over this short term time series are also consistent with the trend seen at other time scales (Bell et al., 2012; Lee et al., 2010), where the activity strengths go down for the later spectral types, and the corresponding variabilities were found to be higher. In our dataset of 126 sources, the activity strengths ($\langle \log_{10}(L_{H\alpha}/L_{bol})\rangle$) are determined to be close to $\sim$-3.8 for the spectral types M0-M4 and then decreases to $\sim$-5.0 for mid to late M dwarfs. A noticeable difference in ΔEW (= Max(EW) - Min(EW)) is also seen between early (M0-M3) and the late types. This is very similar to the trend seen in Kruse et al. (2010) and Bell et al. (2012) for larger cadence. These breaks in the activity strength could be explained due to a change in the magnetic dynamo mechanism at the fully convective boundary. While the early types of M dwarfs are known to have a partially convective envelope, the late types (M4 onwards) have a fully convective envelope (Reiners et al., 2012, 2014; Newton et al., 2017; Wright et al., 2018). An additional reason for the variabilities seen in each of the spectral bins could also be the different ages of the objects therein, as young objects typically show strong Hα emissions (Silvestri et al., 2005; Kiman et al., 2021).

High cadence photometric data from TESS and Kepler/K2 missions are of great use to further probe the causes of short-term variabilities and to understand their behavior with their rotation periods. Amplitude variations in the photometric light curves of M dwarfs, caused by large dominant star-spots on the surface of stars (Kiraga & Stepien, 2007), are used to derive the rotation periods and the star-spot covering a fraction of the stellar surface. The derived rotation periods of M dwarfs in this study range between ∼0.2-10 days, and higher variabilities are seen for the stars with the rotation periods $< \sim 2$ days. These are mostly late-type M dwarfs (M6-M8.5). This behavior could be caused by the magnetic heating of the stellar atmosphere, which in turn is a product of the underlying magnetic dynamo having strong dependence on the stellar rotation. Such behavior has been explored in detail in the literature (West et al., 2015; Newton et al., 2017; Wright et al., 2018; Raetz et al., 2020). Thus, the behavior seen in the Hα variability with respect to the rotation period is entirely plausible. The Hα and Hβ variability indicators are further explored with respect to the derived star-spot filling factors, and a similar trend is seen. The sources having smaller filling factors were found to be more variable across the spectral range. However, the late-type sources are more prominent in the variability scale. A large filling factor could give rise to a strong and persistent Hα emission as opposed to the objects having low filling factors. Any minor change (such as the appearance of new small active regions, micro-flare, etc.) on the highly active stars with high filling factors would not be as prominent as for the stars with low filling factors (lower Hα emission). Thus, stars with smaller filling factors are expected to be more variable, as we notice in our analysis. The same inference has also been drawn by Bell et al. (2012).

Variabilities in M dwarfs on the shorter time scales (few minutes) are very significant as they probe the possible link between activity and rotation. Such studies are beneficial for detecting the low-amplitude and short-duration flares, which can further explore our understanding of flare profiles and their rotational phases. The time scales of variabilities in M dwarfs are much dependent on the basic parameters (e.g., rotation, magnetic field strengths, etc.) and dynamics (such as internal dynamos) of the objects. High activity objects with large filling factors are found to be less variable, possibly due to the requirements of more energetic events (such as large flares) to change their observational status in terms of Hα / Hβ strengths. Such energetic events may require larger time scales to build up and/or to evolve. The variabilities of less active stars, on the other hand, would probably be governed by the low energetic events that could occur on the shorter time scales. Such stars would thus be expected to have lesser filling factors. Thus, the measurements of the time scales of the Hα / Hβ variations are of profound significance to understanding the underlying activities on the surface of the star. A larger sample with finer time resolution could very well be the key to unlocking the physical mechanisms responsible for such activities.

3.5 Chapter Conclusions

The PV observations of MFOSC-P were executed with statistical studies of a sample of M dwarfs. 80 Sources were selected from the all-sky photometric catalog of M dwarfs (Lépine & Gaidos, 2011) and were observed with MFOSC-P for their low-resolution spectroscopy. Using the spectra obtained from MFOSC-P (and by comparing them with the template spectra of M dwarfs), these sources were spectroscopically classified to determine their sub-spectral types. The sub-spectral type of M dwarfs in our sample range from M0 to M5. Further, the most recent BT-Settl synthetic spectra (Allard et al., 2013) were used to perform the spectral synthesis analysis in order to determine their atmospheric parameters, viz. $T_{\rm eff}$ and $\log g$. They were determined to be in the range of 4000 K to 3000 K ($T_{\rm eff}$) and 4.5 to 5.5 dex ($\log g$), with an uncertainty of 100 K in $T_{\rm eff}$ and 0.5 dex in $\log g$. This work has been published in the Monthly Notices of the Royal Astronomical Society (2020, MNRAS 492, 5844-5852).

The success of the first PV program and the discovery of Hα emissions in 10 of the sources led us to plan another similar program to statistically study the short-term variability in Hα / Hβ emissions in another sample of M dwarfs. 83 M dwarfs (M0-M6.5 sub-spectral classes) were observed with R1000 mode of MFOSC-P for their time-series spectra. Various variability indicators were derived from this data set and were studied with respect to their sub-spectral classes. Data were also collected for a complementary set of 43 M dwarfs, in the M3.5-M8.5 sub-spectral class, from the earlier published results, Lee et al. (2010), thereby making this a set of 126 sources spanning a full spectral range from M0 to M8.5. The archival photometric data from the TESS and Kepler/K2 missions were also used to relate the derived short-term Hα / Hβ variability with their rotation periods and star-spot filling factors. A manuscript describing this work has been submitted to the Monthly Notices of the Royal Astronomical Society (Manuscript ID: MN-22-0437-MJ) and is currently under revision after the reviewer's report.

The performance verification of MFOSC-P was successfully completed by observing and later characterizing a sample of M dwarfs. It was shown that MFOSC-P could be utilized in various observing conditions, magnitude range, air-mass range, etc. The data collected in this phase was then used to characterize the instrument as well, like determination of SNR, efficiency, etc. Once the first set of observations of the PV phase was completed, an observational science program to study then newly discovered nova V2891 Cyg was commenced. This is discussed in the next chapter.

Content of this chapter has been published/under-review as follow:

1. *A. S. Rajpurohit, **Vipin Kumar**, Mudit K. Srivastava, F. Allard, D. Homeier, Vaibhav Dixit and Ankita Patel, "First results from MFOSC-P: low-resolution optical spectroscopy of a sample of M dwarfs within 100 parsecs" (MNRAS 492, 5844-5852 (2020); doi:10.1093/mnras/staa163)*

2. ***Vipin Kumar**, A. S. Rajpurohit, Mudit K. Srivastava, "Exploring the short term variabilities in Hα and Hβ emissions in a sample of M Dwarfs" (Submitted to MNRAS, Manuscript ID: MN-22-0437-MJ, currently under review)*

Chapter 4

Science verification of MFOSC-P: multi-wavelength studies of Nova V2891 Cyg & Suspected Symbiotic - SU Lyn

As discussed in Chapter 3, the initial performance of MFOSC-P was verified with a sample of M Dwarfs observed in a variety of observing conditions. Another science verification (SV) program was envisaged with MFOSC-P to probe the physics of a suitable astrophysical source. SV program with MFOSC-P was an essential step to establishing the scientific credential of the instrument once the instrument was characterized. Studies of transient objects like novae were one such suitable observational program for MFOSC-P. Novae are the outburst transient and show significant variations in their magnitudes and optical spectrum. During the evolutionary phase of the nova, several emission lines appear and disappear, which helps to understand the various properties of the system in that phase. As novae evolve in many ways since their outbursts and then fade below the detection limits of the instrument towards their quiescence values, their scientific studies with a new instrument were found most suitable to have a good scientific impact and push the instrument close to its observational limits. These long-term observations of a single source would also be required to improve the accuracy and quality of the instrument's scientific calibration and provide further feedback for the development of associated pipeline and reduction tools.

One such opportunity for MFOSC-P occurred in November 2019 as nova V2891 Cyg transient reported. It was immediately after the monsoon season (June-October), during which the instrument was removed from the telescope and packed. Nova 2891 Cyg was discovered in mid-September 2019, and its observations with MFOSC-P were started in November 2019. It turned out to be one of the slowest novae recorded in recent times. It provided a very exciting opportunity to make follow-up observations for nearly 13 months with MFOSC-P, including a gap of one monsoon season. Nova V2891 Cyg was observed with various modes MFOSC-P for its spectroscopy and photometric evolution. Its long evolution also allowed us to explore its physics with a variety of other supportive observations using several national and international observing facilities across a wide wavelength range, e.g. Asiago telescopes in Asiago Novae and Symbiotic stars (ANS) collaboration, Neil Gehrels Swift Observatory using X-Ray Telescope (XRT) and onboard UV instrument, NASA-Infrared Telescope Facility(IRTF), and Aryabhatta Research Institute of Observational Sciences-Devasthal Optical Telescope (ARIES-DOT). A near-infrared (NIR) photometric observation was also conducted with NICS (Near-infrared Camera And Spectrograph) instrument on PRL 1.2m telescope.

In addition to nova V2891 Cyg, another opportunity was found with the timely UV spectroscopy observations of SU Lyn - an ostensibly unremarkable red giant star with ultra-violet imaging telescope (UVIT) aboard AstroSat space mission. While appearing as a normal - not so special - red giant star from ground-based observations, SU Lyn was recently (in 2016) proposed to be a symbiotic star based on its hard X-ray properties, i.e. presence of a hidden white dwarf was speculated along with the red giant. Therefore we started monitoring SU Lyn with MFOSC-P as soon as the instrument was up. Prior to this, SU Lyn was also observed with Mt. Abu observatory using NICS for NIR photometry/spectroscopy, Himalaya Chandra Telescope using Hanle Echelle SPectrograph (HESP)for high-resolution optical spectroscopy, and AstroSat-UVIT (proposal PI: Dr. Mudit K. Srivastava) for its UV photometry and spectroscopy.

As the constituents of a symbiotic system are similar to the novae systems, i.e. a white dwarf in association with the main sequence or red giant star, a short wavelength study of SU Lyn was also undertaken as an auxiliary science program which included MFOSC-P observations as well. The observational studies of SU Lyn - being a probable symbiotic system - were also found in coherence with the study of nova V2891 Cyg, as symbiotic systems are known to erupt as symbiotic novae as well.

In this chapter, the two observational science programs - on nova V2891 Cyg and SU Lyn - are discussed, which form the science verification section of this thesis work. While nova V2891 Cyg was observed primarily with MFOSC-P over 13 months, the studies of SU Lyn were primarily based on the UV observations with UVIT-AstroSat, and MFOSC-P provided the supportive ground-based observations. The first section of this chapter describes the multi-wavelength study of a Nova V2891 Cygni, which showed the presence of several shock-induced processes (including a brief epoch of dust formation) in the nova evolution. The latter section describes the UV-optical-NIR observations of SU Lyn, where based on UV spectrum from UVIT, the presence of accretion disk around a white dwarf was established - thereby confirming SU Lyn to be a rare class of symbiotic system.

4.1 Multi-wavelength studies of Nova V2891 Cygni

4.1.1 Classical Novae

A classical nova explosion is a consequence of a thermonuclear runaway (TNR) on the surface of a white dwarf (WD), which is accreting hydrogen-rich material from a companion star in a close binary system (Sparks et al., 1976). As a result, the material is ejected of the order of $\sim 10^{-8} - 10^{-4} M_{\odot}$ with velocities of thousands of kms^{-1}. All novae follow an evolution path that goes through an optical thick fireball phase, a free-free phase, a nebular phase, and later a coronal phase. During a nova outburst, the brightness of the object increases around 8-10 magnitudes in optical bands.

A nova classification scheme was proposed by Williams (1992) based on non-hydrogen emission lines seen in the early optical spectra. According to this scheme, the nova is classified as He/N class of nova if emission lines of He and N are present or Fe II class of nova if emission lines of Fe II are present. He/N novae show fast evolution, broad lines, and a flat-topped profile with little absorption. On the other hand, the FeII novae evolve slowly, narrow lines, and display P Cygni absorption components. A small fraction of hybrid novae that evolves from initial Fe II to He/N class is also seen (Williams, 1992). An even smaller fraction of reverse hybrid novae that evolve from He/N to Fe II class during its early phase is also seen. Only a few members of reverse hybrid novae are known, e.g., T Pyx, V2944 Ophiuchi, etc.

4.1.2 Nova V2891 Cygni

Nova V2891 Cygni (also known as AT 2019qwf, PGIR 19brv, and ZTF19abyukuy) was discovered at a J band magnitude of 11.3±0.02 on 2019 September 17.25 UT by De et al. (2019) during regular survey operations of the Palomar Gattini-IR telescope. The source was not detected to a five sigma limit of $J = 13.8$ mag on 2019 Sep 14.27 UT, implying a rise of at least $\Delta J \geq 2.5$ mag in ≤3.0 days. It was classified as a Galactic classical nova on the basis of its optical spectrum (De et al., 2019), which showed a reddened continuum and broad emission lines of Hα , Hβ , and O I. It was subsequently pointed out (Lee et al., 2019) that the nova was first detected on 2019 Sep 15 by the Zwicky Transient Factory (ZTF) as ZTF19abyukuy. However, our search of the ZTF archival data[1] shows that the first detection was not on 15 September, but rather on JD 2458740.66 (2019 September 14.16 UT), at $r = 19.34 \pm 0.18$, when the nova had just begun to rise from quiescence. We henceforth use this date as the reference

[1] lasair.roe.ac.uk/object/ZTF19abyukuy/

point for measuring time in all our analyses (t_0 = JD 2458740.66).

Spectroscopy by Lee et al. (2019) on 2019 Sep 21(+7d) showed emission lines of Hα having a full width at half maximum (FWHM) of 820 kms^{-1}, Hβ , O I (at 7774, 8446, and 9266 Å), several Paschen lines between 8500 and 10050 Å; the R magnitude was measured to be 15.1 mag. Optical spectra, recorded by Srivastava et al. (2019) on 2019 November 01.71 UT (+48d), showed a significant narrowing of the Hα emission (FWHM$\sim$300 kms^{-1}) compared to the preceding reports. In addition, the O I 7773 Å line showed a P Cygni profile, even $\sim$48 days after the outburst. The prolonged mass-loss suggested that this would be a slow nova. A Fe II classification of the nova was later made by Munari (2019) with optical spectrum recorded on 2019 November 5.94 UT(+52d). The Fe II classification was confirmed with near-infrared (NIR) spectroscopy (Joshi et al., 2019) on 2019 November 17.85 UT(+64d). Based on the presence of low-excitation Na and Mg lines in the NIR spectrum, it was predicted that the nova is likely to form dust (Das et al., 2008), which did transpire though late in the nova's evolution.

Subsequent evolution of the light curve showed that V2891 Cyg was indeed a slow nova whose brightness fluctuated around maximum for a considerable time (section 4.1.4.1), followed by a slow decline. During this extended phase around maximum, while the photometric variations were minimal, substantial spectroscopic changes were apparent in regular (mostly optical) spectroscopic monitoring. These changes encompassed variations in the FWHMs and equivalent widths of the emission lines, changes and later disappearance of P Cygni profiles, the appearance of time-varying structures in the line profiles, and the emergence of forbidden lines of [O I], etc. (Munari et al., 2019). The nova was also followed at other wavelengths, and spectral changes were reported, e.g. optically thick free-free emission from the expanding nova ejecta (Sokolovsky et al., 2020), fading of carbon lines (a hallmark of the Fe II class of novae), and the emergence of NIR coronal lines (De & Palomar Gattini-IR Collaboration, 2020; Woodward et al., 2020a) etc.

Here we present optical and NIR observations of V2891 Cyg carried out between 2019 November 1 (+48d) to 2020 December 12 (+455d). These observations comprise optical photometry and spectroscopy from the 1.2m Mt. Abu Telescope (India), the Asiago 1.22m and 1.82m telescopes (Italy), the ID0310 telescope from the ANS (Asiago Novae and Symbiotic stars) collaboration (Munari et al., 2012), and NIR spectroscopy from Mt.Abu 1.2m telescope, the 3.6m ARIES-DOT telescope (India), and the 3.2m NASA-IRTF facility.

4.1.3 Observations

4.1.3.1 Optical Observations from Mt. Abu

Optical photometry and spectroscopy of V2891 Cyg were carried out with the Mount-Abu Faint Object Spectrograph and Camera-Pathfinder (MFOSC-P) instrument on the 1.2 m Mount Abu telescope (Srivastava et al., 2018; Rajpurohit et al., 2020; Srivastava et al., 2021). The instrument provides seeing-limited imaging in the Bessell *BVRI* filters over a 5.2 × 5.2 arc-minute^2 field of view, with a sampling of 3.3 pixels per arc-second. MFOSC-P is equipped with three plane reflection gratings that yield resolutions of $R = \Delta\lambda/\lambda = 2000, 1000$ and 500 (referred to as the R2000, R1000, and R500 modes hereafter). The standard spectral coverage of these modes are ∼6000-7000Å, ∼4700-6650Å, and ∼4500-8500Å respectively. In the R500 mode, the spectral region beyond 7400Å is covered by rotating the grating while simultaneously using a Bessel-I blocking filter to avoid second-order contamination. The response corrected spectra for both settings of the grating were co-joined together around 7200Å, after flux matching in the common overlap region to obtain a complete spectrum free from second-order contamination. The spectroscopic observations presented here were made with a 75μm slit width (equivalent to 1.0 arc-second on the sky). Wavelength calibration was done using Xenon and Neon calibration lamps. For the purpose of instrument response correction, spectrophotometric standard stars from the ESO catalog [2] were observed, with settings identical to those for the nova observations.

The raw data were reduced using in-house-developed data analysis rou-

[2] https://www.eso.org/sci/observing/tools/standards/spectra/stanlis.html

Table 4.1: Log of the optical photometry and spectroscopy observations from MFOSC-P.

Date of Observation (UT)	Days[a] since outburst	V (mag)	R (mag)	I (mag)	Spectroscopy Exposure time (seconds) (R500,R1000,R2000)	Spectro-photometric standard star[b]
2019-11-01.67	48.51	-	-	-	(840, — , 1200)	HR 718
2019-11-11.66	58.50	-	-	-	(800, — , 1200)	HR 718
2019-11-12.65	59.49	-	-	-	(800, 1200 , 1800)	HR 718
2019-11-19.73	66.57	15.32±0.03	13.50±0.03	11.83±0.05	(600, — , 600)	HR 718
2019-12-01.66	78.50	-	12.46±0.04	10.83±0.04	(1200, — , —)	HR 3454
2019-12-07.63	84.47	-	-	-	(1400, 1800 ,1800)	HR 3454
2019-12-08.57	85.41	16.22±0.03	13.82±0.04	12.10±0.03	—	—
2019-12-09.60	86.44	-	-	12.19±0.03	—	—
2019-12-10.61	87.45	16.13±0.04	-	12.26±0.03	—	—
2019-12-13.63	90.47	-	-	-	(600, 1500 , —)	HR 718
2019-12-14.60	91.44	15.61±0.03	13.74±0.02	12.12±0.02	(—, —, 900)	HR 718
2019-12-15.65	92.49	-	-	-	(1800, 3600 , 900)	HR 718
2019-12-19.61	96.45	15.35±0.02	-	11.77±0.03	(600, —, 900)	HR 718
2020-01-04.60	112.44	15.88±0.02	-	12.34±0.03	(600, —, 900)	HR 1544
2020-01-05.59	113.43	-	-	12.50±0.02	—	—
2020-01-13.57	121.41	-	-	-	(300, —, 600)	HR 1544
2020-01-14.57	122.41	14.71±0.02	12.90±0.02	11.28±0.02	—	—
2020-05-06.99	235.83	16.50±0.06	-	13.09±0.05	(300, —, —)	HR 4468
2020-05-10.98	239.82	17.15±0.12	14.90±0.16	13.26±0.06	(450, —, 1800)	HR 4468
2020-05-20.98	249.82	17.70±0.14	-	13.90±0.04	(600, —, —)	HR 5191
2020-05-22.98	251.82	-	-	-	(600, —, 900)	HR 5191
2020-05-24.95	253.79	-	-	-	(1200, —, 1800)	HR 5191
2020-10-23.69	405.53	18.36±0.03	16.78±0.02	16.10±0.01	(1200, —, —)	HR 718
2020-11-01.68	414.52	18.59±0.14	16.99±0.04	16.50±0.07	(1200, —, —)	HR 1544
2020-11-02.73	415.57	18.48±0.06	-	-	(3600, —, —)	HR 1544
2020-11-03.72	416.56	18.52±0.06	16.96±0.02	16.24±0.03	(900, —, —)	HR 1544
2020-11-16.62	429.46	18.60±0.02	17.17±0.02	16.48±0.04	(3300, —, —)	HR 718
2020-11-17.58	430.42	18.58±0.02	17.16±0.02	16.44±0.02	(3300, —, —)	HR 718
2020-11-19.65	432.49	18.72±0.05	-	-	(1800, —, —)	HR 718
2020-11-27.58	440.42	18.71±0.07	17.32±0.03	16.57±0.03	(1200, —, —)	HR 718
2020-11-29.61	442.45	18.50±0.06	17.36±0.02	16.57±0.03	(2400, —, —)	HR 718
2020-12-01.62	444.46	18.81±0.07	17.45±0.02	16.67±0.04	—	—
2020-12-08.56	451.40	18.83±0.03	17.47±0.02	16.75±0.02	(2700, —, —)	HR 718
2020-12-12.58	455.42	18.78±0.05	17.59±0.07	16.85±0.03	—	—

a: Time of discovery, 2019 September 14.160 UT (JD 2458740.660), is taken as time of outburst. All spectra were recorded and photometry was done using MFOSC-P instrument.

b: Spectrophotometric standard stars were observed on the same, or on contemporaneous nights.

tines in Python[3] using open-source image processing libraries (ASTROPY[4], etc.). Spectroscopy data reduction steps involve bias subtraction, cosmic ray removal, tracing and extracting the spectra, sky background subtraction, etc. Pixel-to-pixel response variation was found to be less than 1% using the halogen lamp, and hence the correction is not applied to the reduced spectra. The reduced spectra were flux calibrated using broadband photometric magnitudes obtained

[3]https://www.python.org/
[4]https://www.astropy.org/

by us on the same night, or when these were not available, by using contemporaneous ANS magnitudes. The log of the MFOSC-P spectroscopic and photometric observations are given in Table 4.1.

4.1.3.2 Optical Spectroscopy from Asiago

Low-resolution spectra of nova V2891 Cyg were recorded in 2019 November and December with the 1.22m telescope with a B&C spectrograph[5]. A 300 line/mm grating, blazed to 5000Å, provided a wavelength coverage from 3300 to 8000 Å at a dispersion of 2.31 Å/pixel, and a resolution of FWHM=1.9 pixel. The spectrograph is equipped with an ANDOR iDus DU440A CCD camera having a back-illuminated E2V 42-10 sensor (2048 × 512 array of 13.5μm pixels). Its high efficiency at ultraviolet (UV) wavelengths, together with the high UV transparency of the whole optical train, allows it to observe down to the limit of the atmospheric transmission for the observing site (∼3100 Å). The very red colour of V2891 Cyg, its faintness, and the relatively short exposure times, limited the usefulness of the recorded spectra to wavelengths ≥4000 Å.

Table 4.2: Log of the spectroscopic observations from the ANS telescopes.

Date of Observation (UT)	Days since outburst (days)	Instrument Name	Wavelength range (Å)	IT[a] (s)
2019-11-05.94	52.78	B&C	4000-7840	480
2019-11-13.80	60.64	Echelle	6445-6700	1800
2019-11-13.85	60.69	B&C	4000-7840	600
2019-11-27.77	74.61	B&C	4000-7840	120
2019-12-06.79	83.63	B&C	4000-7840	360
2019-12-07.86	84.70	B&C	4000-7840	1080
2019-12-08.74	85.58	Echelle	6445-6700	1800
2019-12-09.72	86.56	Echelle	6445-6700	1800
2019-12-14.81	91.65	B&C	4000-7840	1980
2019-12-14.82	91.66	Echelle	6445-6700	1800

a: IT = Integration Time

High resolution ($R \sim 20000$) profiles of the Hα emission line in V2891 Cyg were recorded in 2019 November and December 2019 with the REOSC

[5]This is operated in Asiago by the Department of Physics and Astronomy of the University of Padova

Echelle spectrograph mounted on the 1.82 m telescope operated in Asiago by the National Institute of Astrophysics of Italy (INAF). All spectroscopic reductions were carried out in IRAF (Tody, 1986), following the data reduction recipes discussed in Zwitter & Munari (2000). The spectrophotometric standards have been taken from the internal Asiago spectrophotometric database (Moro & Munari, 2000; Sordo & Munari, 2006). A log of the spectroscopic observations at the Asiago telescopes is provided in Table 4.2.

4.1.3.3 BVRIz'Y photometry with ANS Collaboration telescopes

The photometric evolution of V2891 Cyg from day $t = +67$d to $t = +230$d was monitored with the ANS Collaboration telescope ID 0310, which is a 30 cm f/10 instrument located in Cembra (on the Italian Alps). The telescope is equipped with an SBIG-10 CCD camera and photometric filters from Custom Scientific ($UBVRI$) and the Baader Planetarium ($g'r'i'z'Y$). We have measured the transmission profiles of all the filters in the laboratory (Munari & Moretti, 2012); in particular, to exclude that any red-leak up to 1.1 μm had no detrimental effect, given the very red spectral energy distribution of V2891 Cyg.

As is the case for all telescopes operated by the ANS Collaboration (Munari et al., 2012), the collected photometry is transformed from the instantaneous local photometric system to a standard one via color-equations extending over a wide range of stellar colours. The reference standard systems are those of Landolt (1992) for the $UBVRI$ bands (as realized locally by APASS All Sky Survey (Henden & Munari, 2014) in its DR8 data release (Munari et al., 2014)) and PanSTARSS PS1 (Chambers et al., 2016) for the $g'r'i'z'Y$ bands.

4.1.3.4 NIR observations

A single epoch of NIR photometry and spectroscopy from Mt. Abu was obtained with the Near-Infrared Camera and Spectrometer (NICS) on 2019 November 17 (+64d). NICS is equipped with a 1024×1024 HgCdTe Hawaii array, and operates in the 0.85–2.45μm wavelength range with a resolution of $R \sim 1000$. The spectra were recorded in three settings of the grating that cover the IJ, JH, and

HK regions. A standard star HD 209932 (spectral type A0V) was also observed at a similar airmass and in similar conditions to remove the telluric lines. The spectra were recorded at two dithered positions of the object along the slit; these were subtracted, one from the other, to remove sky and dark contributions. The data reduction was done using the procedures described in Joshi et al. (2014); Srivastava et al. (2016). The wavelength calibration was done using OH skylines, and telluric lines that register with the stellar spectra. Hydrogen Paschen and Brackett absorption lines in the J, H and K bands were identified and removed from the standard star's spectra, and subsequently, the nova spectra were ratioed with these spectra to remove telluric features. These telluric-corrected spectra were then multiplied by a blackbody at the standard star's effective temperature to obtain the resultant spectra. Photometric observations in J, H and K_s bands were also obtained, along with the photometric standard stars; the nova's magnitudes were obtained using aperture photometry.

Four spectra of nova V2891 Cyg were obtained using SpeX (Rayner et al., 2003) on the 3.2m IRTF telescope between 2020 May 20 (+249d) and September 19 (+371d). The SpeX data were reduced and calibrated using Spextool (Cushing et al., 2004), and the IDL tool xtellcor (Vacca et al., 2003) was used for the corrections for telluric absorptions. The spectra were flux calibrated using AO-standard HD199217 observed at a comparable airmass. Observations used either 0.5" × 15.0" or a 0.8" × 15.0" slit, and both short-crossed dispersed (SXD) and long-cross dispersed (LXD) spectrograph modes.

A single epoch of the NIR spectrum was obtained on 2020 Oct 26 (+408d) from the TANSPEC instrument on 3.6m ARIES-DOT telescope (Ojha et al., 2018) with open observing proposal system (observing proposal no. DOT-2020-C2-P12 during observing cycle DOT-2020-C2). The data have been reduced using in-house-developed data analysis routines in Python. Details of the NIR observations are given in Table 4.3.

4.1.4 Parameters from the light curve and a possible progenitor

4.1.4.1 Light curve

The light curve (LC) and colour plots of the nova V2891 Cyg using data from Mt. Abu and the ANS telescopes are presented in Fig. 4.1. The g and r band light curves from the ZTF are presented separately, for clarity, in Fig. 4.2. The distinctive features of the LCs include the recording of the nova's fast climb from quiescence to maximum, the presence of a fairly long pre-maximum halt, and three pronounced large-amplitude "jitters" around the maximum. There is also a phase of dust formation centered around +273d that is marked by dotted lines in Fig. 4.2. The LC is of a slightly distinctive nature, which does not easily belong to any known LC classes (Strope et al., 2010).

Within the grouping scheme of nova LC proposed by Strope et al. (2010), V2891 Cyg shows partial resemblance to both the F (flat-topped) and J (Jitters) classes. The LC of nova V 2891 Cyg shows a slow rise of duration $\sim$ 120 days, including several episodes of re-brightening with δmagnitude$\sim$1.2, before it begins its decline. There is also a reasonably "flat" phase, of duration $\sim$180 days, between 30-210 days after the outburst, during which the nova stays at a mean value of $V \sim 16$ mag, accompanied by modulations with amplitude ranging up to $\pm$1.2 mags.

Defining a t_2 (the time interval in days for the LC to decline 2 magnitudes from the peak) for an LC of this nature is difficult, so the V band data were smoothed with 5 point running averages to annul the smaller amplitude jitters (Munari et al. (2017) and references therein). From the resultant smoothed curves, we find that if the first peak is considered as the principal maximum, then t_2 is $\sim$ 150 days. If the second peak is taken as the maximum, then $\mathrm{t}_2 \sim 100$ days. A similar estimate of t_2 is also obtained from ZTF g band light curve. For our analysis, an exact value of t_2 is not essential. It is sufficient to note that t_2 is large, and a range of 100 to 150 days may be considered appropriate – we will use this approximation in the distance estimation that follows. Similarly, t_3 (the time interval in days for the LC to decline 3 mags from the peak) is constrained

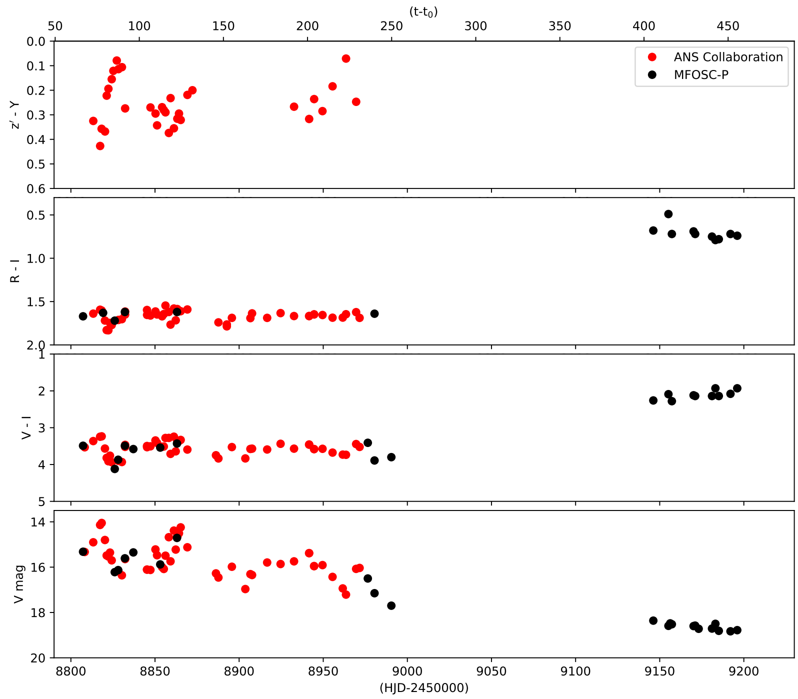

.

Figure 4.1: Photometric evolution of Nova V2891 Cyg in the $VRIz'Y$ bands. The time of discovery, 2019 September 14.160 UT (JD 2458740.660), is taken as t_0 on the abscissae at the top panel. Black and red colors refer to MFOSC-P and ANS Collaboration data, respectively

Table 4.3: Log of the NIR photometric/spectroscopic observations.

Date of Observation (UT)	Days since outburst (days)	Instrument Name	Wavelength range (μm) /Magnitudes	Spectral Resolution	Integration time (s)
2019-11-17.85	64.69	NICS - Spec	0.85-2.4	1000	450
2019-11-17.91	64.75	NICS[a] - Phot	$J = 9.98 \pm 0.02$	-	(250,90,56)
			$H = 8.87 \pm 0.03$		
			$K_s = 7.66 \pm 0.02$		
2020-05-20.25	249.43	SpeX - Spec	0.7-2.55	1200	1434.53
2020-06-07.62	267.46	SpeX - Spec	0.7-4.2	1200	SXD[b] = 637.570
					LXD = 667.224
2020-06-30.53	290.37	SpeX - Spec	0.7-2.55	1200	478.180
2020-09-19.26	371.10	SpeX - Spec	0.7-2.55	750	1438.24
2020-10-26.59	408.43	TANSPEC-Spec	0.86-2.5	2750	2947.348

(a) : NICS- Near infrared Camera Spectrograph, Mt Abu. Phot: indicates photometry; Spec: Spectroscopy (b) SXD and LXD: Short (0.7-2.5 microns) and long wavelength (1.7-4.2 microns) spectral regions covered by SpeX (at IRTF) in the cross-dispersed mode.

to be in the range 180–230 days. Again, the exact value of t_3 is not critical for any of the subsequent analyses.

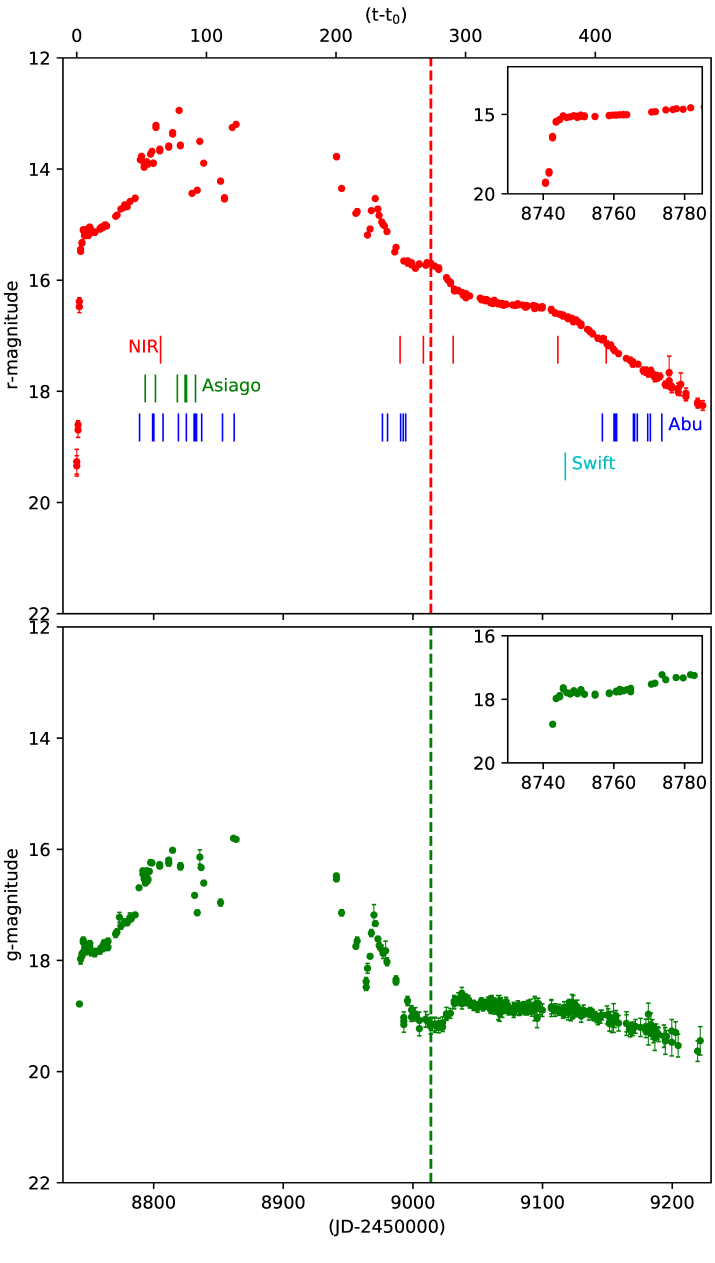

Figure 4.2: The ZTF light curve of Nova V2891 Cyg in the g and r bands. The insets show the well-documented rise from quiescence towards maximum and also the prolonged pre-maximum halt, lasting for $\sim$ 35 days. The epochs of our spectroscopy observations, as well as a Swift target of opportunity observation, are marked in the top panel by vertical lines. The dotted vertical lines show a phase of dust formation in the nova, characterized by a drop in the g band flux accompanied by a simultaneous increment in the r band flux.

4.1.4.2 Extinction and distance estimates

The nova lies in a direction of high extinction, with the total extinction along the entire line-of-sight being estimated as $A_v = 11.224$ from Schlafly & Finkbeiner (2011), and 13.051 from Schlegel et al. (1998). The intrinsic colour of novae at peak, following van den Bergh & Younger (1987), is $+0.23(\pm 0.06)$. Both maxima attained by V2891 Cyg have been covered in our observations, as shown in Fig. 4.1, averaging $(B - V) = 2.47$ (± 0.021 as error of the mean), leading to $E(B - V) = 2.24$. We also estimated the reddening following the empirical law determined by Munari (2014), by using the equivalent width (EW) of the Diffuse Interstellar Band (DIB) at 6614Å in our spectra ($E(B-V) = 4.40 \times EW(\AA)$). In the echelle spectra, the measured EWs on the different days are rather dispersed, given the low signal-to-noise ratio (SNR). The average equivalent width is 0.492Å, leading to $E(B - V) = 2.16$. The MFOSC-P spectrum at $R = 2000$, obtained on 2019 Nov 1 (+48d), gives a closely similar value. Averaging over the two independent estimates gives $E(B - V) = 2.20 \pm 0.03$, or $A_v = 6.82$ (for a value of the total-to-selective extinction R_v=3.1) which is the value we adopt for the rest of our analysis. It was not possible to use the O I 0.8446 μm and 1.2187μm line ratios to estimate the reddening because the spectra recording these lines (observed between 2020 May and September) are affected to varying degrees by nova dust, which clearly causes additional extinction.

Following Das et al. (2015) and Banerjee et al. (2018a), we also use an independent approach with the additional benefit that it allows the simultaneous estimates of the the extinction and distance, by using the distance-dependence of the extinction towards the nova, and the absolute magnitude derived from the Maximum Magnitude Rate of Decline (MMRD) relationship (Cohen, 1985, and references therein). The extinction towards the nova, over a 5 arc-minute field (Marshall et al., 2006), is plotted in Fig. 4.3 for the two closest lines of sight available. We also plot the extinction versus distance as derived from the distance modulus equation using $m_V(\max) = 14.05$ from observations, and $M_V = (-6.86 \text{ to } -6.91) \pm 0.20$ from the MMRD relation of della Valle & Livio (1995); we use $t_2 = 100$d to 150d as derived earlier. The intersection of this curve (solid black in Fig. 4.3) with the two extinction curves (dashed lines) allows us simultaneously to determine the distance and extinction for the nova. The two different intersections (for red and green lines) yield $A_{ks} = 0.67 \pm 0.02$ and $A_{ks} = 0.61 \pm 0.02$ respectively. The corresponding distances are $d = 4.90 \pm 0.15$ kpc, and $d = 6.45 \pm 0.14$ kpc respectively. The average values from this method are $A_{ks} = 0.64 \pm 0.02$ and $d = 5.68 \pm 0.78$ kpc. A recent MMRD relation of Selvelli & Gilmozzi (2019), based on revised distances from Gaia (Gaia Collaboration et al., 2016), uses t_3 values. For t_3 in the range 180 to 230 days, we find $M_v = -6.30 \pm 0.56$ to -6.07 ± 0.58. Following the same method as above, this corresponds to an average $A_{ks} = 0.59 \pm 0.05$ and distance $d = 5.32 \pm 0.37$ kpc. We choose the average of the values derived from these two

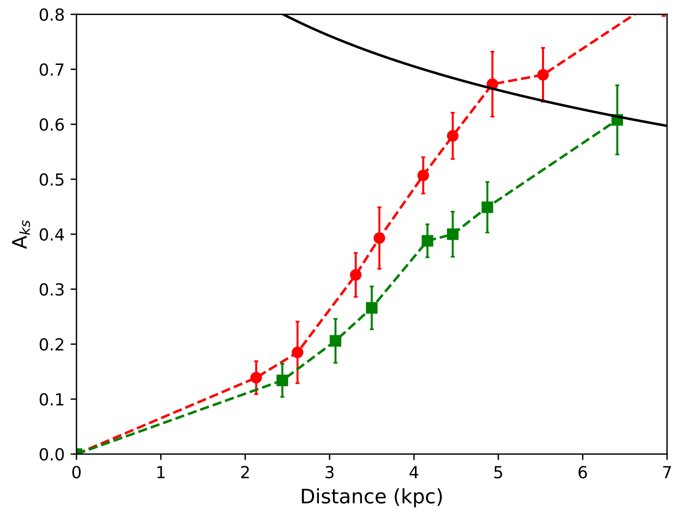

Figure 4.3: The dashed lines connecting the data points (red circles and green squares) show the extinction towards nova V2891 Cyg based on the results of Marshall et al. (2006) along two nearest lines-of-sight (Galactic coordinates $l = 89.5, b = +0.25$ for red and $l = 89.75, b = +0.25$ for green). V2891 Cyg's Galactic coordinates are $l = 89.59686$, $b = +0.21382$. The continuous black curve is a plot of extinction A_{ks} versus distance d (kpc) from the equation $m_V - M_V = 5 \log d - 5 + A_V$, where m_V is known from observations. and M_V is estimated from the MMRD relation (della Valle & Livio, 1995). A relation $A_{ks}/A_V = 0.089$ is used for the necessary conversion (Glass, 1999; Marshall et al., 2006). The intersection of the two curves permits simultaneous estimation of the extinction and distance to the nova. See text for details.

MMRD relations for A_{ks} $(= 0.61 \pm 0.04)$ and d $(= 5.50 \pm 0.86)$ kpc. This implies $A_v = \mathrm{A}_{ks}/0.089 = 6.85 \pm 0.45$ (or $E(B-V) = 2.21 \pm 0.15$) which is a good match with the value $A_v = 6.82$ derived above. We shall use these values for further analysis.

4.1.4.3 Identification of a possible progenitor

A possible progenitor could be a faint star, detected both in the optical and in the NIR in the Pan-STARRS (Chambers & Pan-STARRS Team, 2016) and UKIDSS (UKIDSS Consortium, 2012) surveys, respectively, which shows a good positional match with the nova. The Gattini discovery coordinates of the nova are RA J2000: 21:09:25.52, Dec J2000: +48:10:51.9 (De et al., 2019). These coordinates were refined to the end figures of 25.524, 52.248 after Gaia detected the source on 2019 Nov 4 (+51d) and designated it as Gaia19ext. The UKIDSS-DR6 Galactic Plane Survey (UKIDSS Consortium, 2012) shows a source, just 0".1 away from the Gaia coordinates, with end figures of 25.5278, 52.309 and NIR magnitudes of $J = 18.41 \pm 0.04$, $H = 17.66 \pm 0.04$, $K = 17.25 \pm 0.09$. Similarly, the Pan-STARRS release 1 (PS1) Survey – DR1 (Chambers & Pan-STARRS Team, 2016) identifies the same source with end figures of 25.5343, 52.227, just 0".2 from the nova's position, with $z = 20.80 \pm 0.13$ mag and $i = 21.65 \pm 0.02$. Nothing is seen at the nova's position in the WISE W1, W2, W3, and W4 bands (Wright et al., 2010). After de-reddening the Pan-STARRS and UKIDSS magnitudes (using $E(B-V) = 2.20$), a blackbody fit (see Fig. 4.4) yields a temperature of $T = 6068 \pm 98$ K for the potential progenitor. The luminosity and radius of the donor star are determined to be $2.76 \pm 0.31\, L_{\odot}$ and $1.50 \pm 0.07\ R_{\odot}$, respectively. Although these values may correspond to the spectral type of F9V for the potential progenitor, we also note that an overall temperature of 6000–7000 K is also suitable for an accretion disc. Pre-novae in quiescence can also be disc-dominated systems (Selvelli & Gilmozzi, 2013). Therefore, we are cautious about drawing any conclusion about the nature of the donor. Extrapolating this black-body curve gives an r band magnitude of ~ 22, which, when compared to the peak value of $r = 12.95$ recorded by the ZTF, indicates an outburst amplitude $\mathcal{A}$ of approximately 10 magnitudes. This is consistent with the amplitude expected for a slow nova (see, e.g., the $\mathcal{A}$ versus t_2 correlation plot in Warner, 1995). The close positional coincidence, the

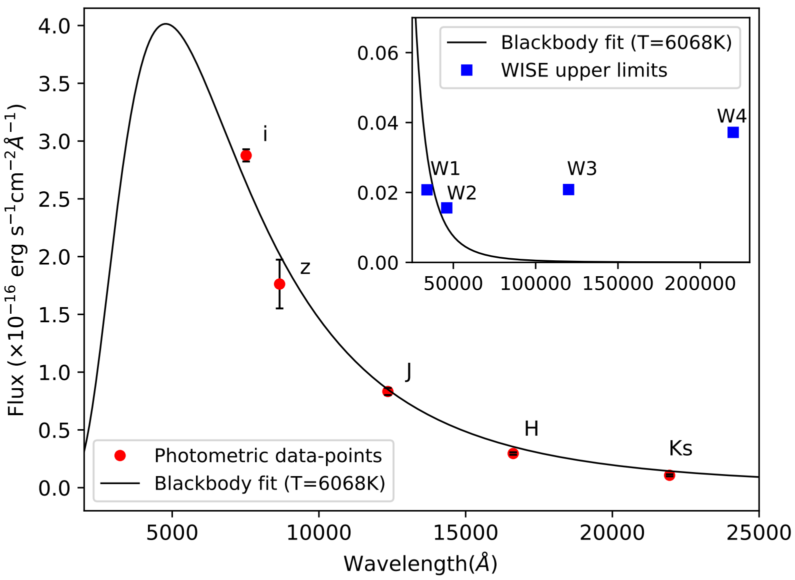

Figure 4.4: The blackbody fit with the temperature of 6068±97K. Filled circles (red) shows the dereddened flux corresponding to the Pan-STARRS-i,z and UKIDSS-DR6-J,H,K magnitudes. Inset shows the WISE 5-σ detection limits (Wright et al., 2010).

estimated $\mathcal{A}$ value and the spectral type of the UKIDSS/Pan-STARRS source are all consistent with that expected of a nova progenitor.

4.1.5 Results from optical spectroscopy

Nova V2891 Cyg presents a good case study for those nova systems that show multiple outbursts and the interactions between ejected material. The claim that the current outburst of nova V2891 Cyg had undergone multiple episodes of mass ejection can be seen in the evolution of the Hα and O I 7773Å lines. NIR spectroscopy offers further clues for the interactions of ejecta from these multiple outbursts in the form of the occurrence and evolution of coronal lines, a brief epoch of dust formation, etc. We present the results from the optical and NIR spectroscopy separately for ease of readability, although there are areas of overlap. Optical spectroscopy is presented here, and NIR spectroscopy is presented later in section 4.1.6.3.

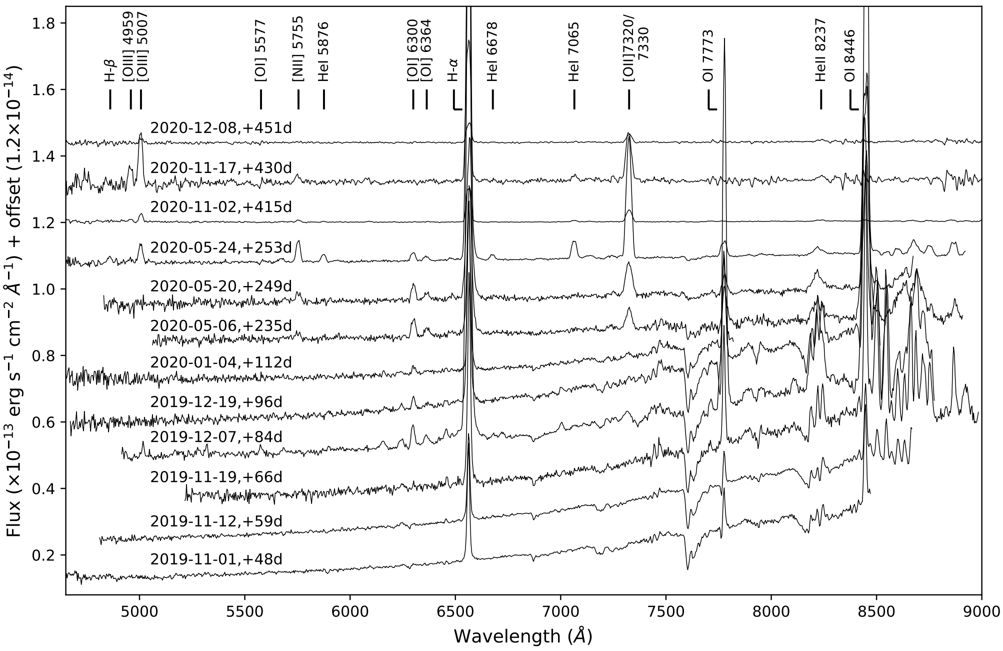

Figure 4.5: Evolution of the optical spectrum of nova V2891 Cyg as seen with the MFOSC-P instrument. The spectra are not reddening corrected. See section 4.1.5.1 for discussion.

4.1.5.1 Evolution of optical spectra

Fig. 4.5 shows the evolution of the low-resolution optical spectra of V2891 Cyg from MFOSC-P. Our first optical spectrum was recorded on 2019 Nov 1 (+48d) with MFOSC-P in R500 and R2000 modes, when the nova was still rising. The spectrum showed a steeply rising continuum towards longer wavelengths, signifying a large amount of reddening, which was also clear from the photometry. Prominent emission lines of Hα , O I 7773Å, and 8446Å were present. The O I 7773Å line exhibited a P cygni profile (Srivastava et al., 2019).

The continuum normalized spectra recorded with the B&C spectrograph are shown in Fig. 4.6. The Hβ and other emission features can be seen on the blue side of the spectra, which aided in the nova classification. Fe II emission at 4924Å(42[6]), 5018Å(42), 5169Å(42), 5198Å(49), 5235Å(49), 5276Å(49), 5317Å(49,48) and 6456Å(74) are clearly present. Later optical spectra, recorded on 2019 Nov 11(+58d), 12(+59d), 19(+66d), and Dec 1(+78d) also show the same features. A noticeable change was the disappearance of the P Cygni profile

[6] Fe II multiplet number

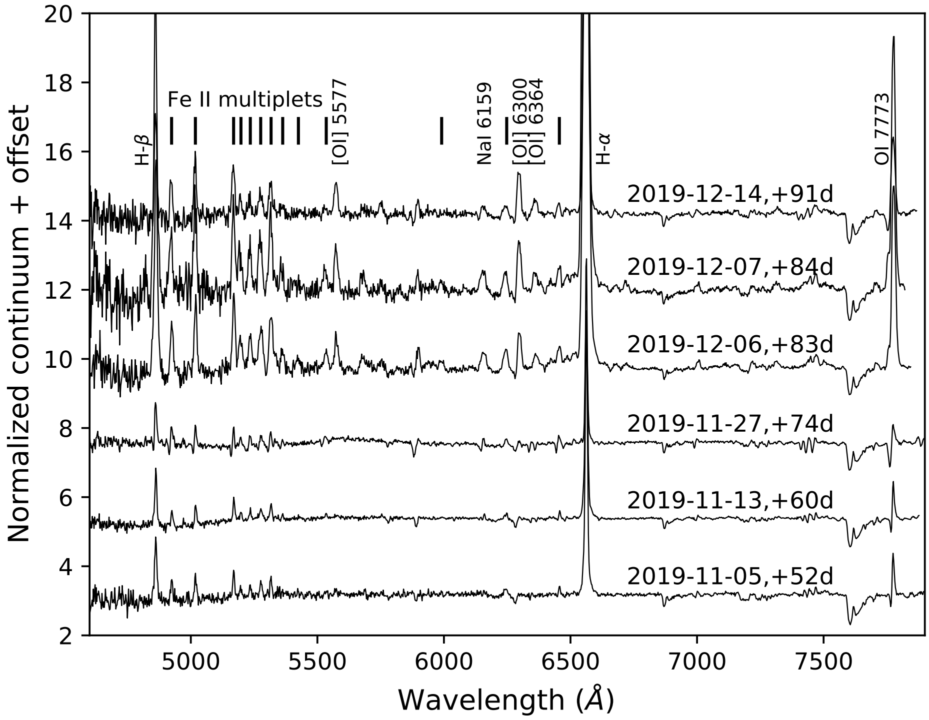

Figure 4.6: The continuum normalised spectra of nova V2891 Cyg from the B&C spectrograph. The Fe II multiplets on the blue end are prominent here.

in O I 7773Å between 2019 Nov 12 (+59d) and Nov 19 (+66d). This will be discussed later in section 4.1.5.3.

The nova spectra in 2019 December to 2020 January (+84d to +122d) show the emergence of [O I] 5577, 6300, 6364Å emission. As the object entered solar conjunction in 2020 January, and due to subsequent COVID-19 lock-down restrictions, our next observations of the nova were not obtained until 2020 May. During the period between 2020 January and 2020 May, as the light curve shows, the nova largely remained at $V \sim 16.5$ mag, varying irregularly within ∼1.5 mag. However, a decline had begun towards quiescence.

The optical spectra of 2020 May (+235d to +253d) showed the onset of the nebular phase, as typically characterised by the presence of [N II] 5755Å, [O I] 6300, 6364Å, and [O II] 7320Å emission. The appearance of these new lines is highlighted in Fig. 4.7 which shows the spectral changes between 2020 May 20 (+251d) and 24 (+253d). Several new lines have appeared, e.g. [O III] 5007Å, neutral helium lines at 5876Å, 6678Å and 7065Å etc. The Hα /Hβ ratio, from

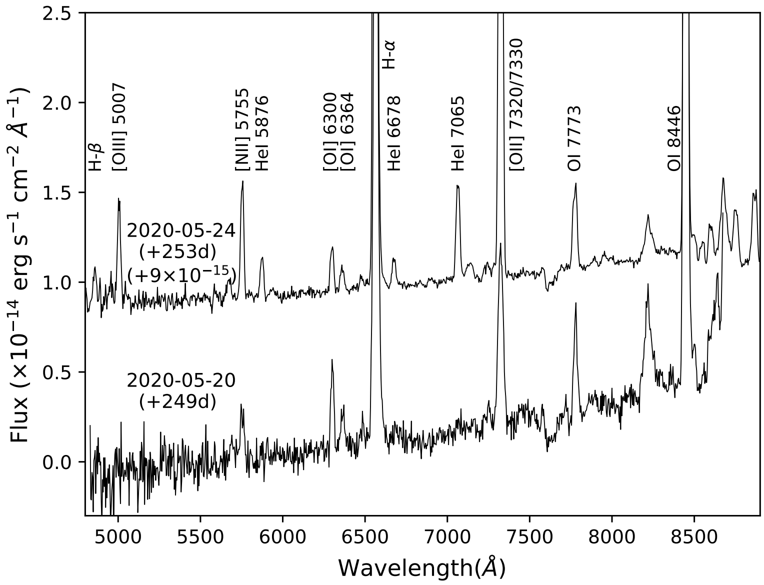

Figure 4.7: Change in spectra between 2020 May 20 (+249d) and May 24(+253d). The emergence of [O III] 5007Å, [N II] 5755Å, He I 5876, 6678, 7065Å is evident. The spectra are not reddening corrected.

the de-reddened spectrum on May 24 (+253d), is $\sim$ 7.2, which is significantly greater than the value 2.7 as deduced from recombination theory (Osterbrock, 1989) for optically thin conditions. As the critical densities for [O III] and [N II] are in the range of $\sim 10^5 - 10^6 cm^{-3}$ (Osterbrock, 1989), this shows that the hydrogen emission lines probably arise in the high-density clumps embedded in lower density surroundings.

Few low-resolution spectra were recorded in 2020 Oct-Dec (+405d to +451d), when nova was around ~18.5, 17, and 16.5 mags in the V, R and I bands, respectively. Given the moderate aperture of the PRL 1.2m telescope and the efficiency on the blue side of the MFOSC-P spectral range, the spectra are noisy on the bluer side. Nevertheless, the emission features of [O III] 4959, 5007Å, [N II] 5755Å, O I 8446Å are evident. [O II] $\lambda\lambda$ 7320,7330 Å are strong and distinguishable, along with Hα . He I 6678Å had by then weakened, and He I 7065Å is noticeable. He II 8237Å is still present, as in the spectra of 2020 May.

4.1.5.2 Evolution of the Hα : The absorption systems

The absorption systems in novae have long been known. McLaughlin (1964) noted four classes: (a) pre-maximum, seen during the rise to the maximum until just after maximum light, (b) the principal component, which replaces the pre-maximum component a few days after the maximum; (c) the diffuse-enhanced component, which appears later than the pre-maximum and (d) the Orion component, which appears when the diffuse enhanced component is strongest. We notice the presence of such systems in nova V2891 Cyg, superimposed on the Hα profile (Fig. 4.8). We decomposed the Hα profiles of the high-resolution echelle spectra recorded on 2019 Nov 13(+60d), Dec 8(+85d), 9(+86d), and 14(+91d) for these superimposed absorption components, as shown in Fig. 4.9 in the velocity space of Hα . While Hα can be blended with [N II] 6548, 6584 Å, the first instance of [N II] emission was not noted until 2020 May 22-24 (+251d,+253d), with the appearance of the [N II 5755Å line. Thus, the Hα emission on these earlier epochs is not expected to be blended with [N II]. The absorption and emission profiles were fitted with symmetric Gaussian functions. The derived heliocentric velocity (HV), velocity width at half maximum (VHM), equivalent width (EW), and integrated flux are given in Table 4.4.

The Hα emission profile of 2019 Nov 13 (+60d) can be reconstructed with two additional absorption components at -194 and -305 kms^{-1}. We identify these as pre-maximum and principal components. The main emission component (e1) had a velocity width of 406 kms^{-1}. Another faint emission component (e2) is also seen on the red wing, at a velocity of +282 kms^{-1}. Subsequent profiles can also be approximated by the same emissions (e1 and e2) and, together with pre-maximum and principal absorption components. On 2019 Dec 8 (+85d), the pre-maximum component was seen at –280 kms^{-1}, while the principal absorption system now had two components (p1 and p2), at –411 and –622 kms^{-1}. The profile of Dec 9 (+86d) is similar to that of Dec 8. In the decomposed profile on Dec 14 (+91d), the pre-maximum absorption is at –282kms^{-1}. The p2 component of the principal absorption is not seen, while the p1 component persists at –393kms^{-1}.

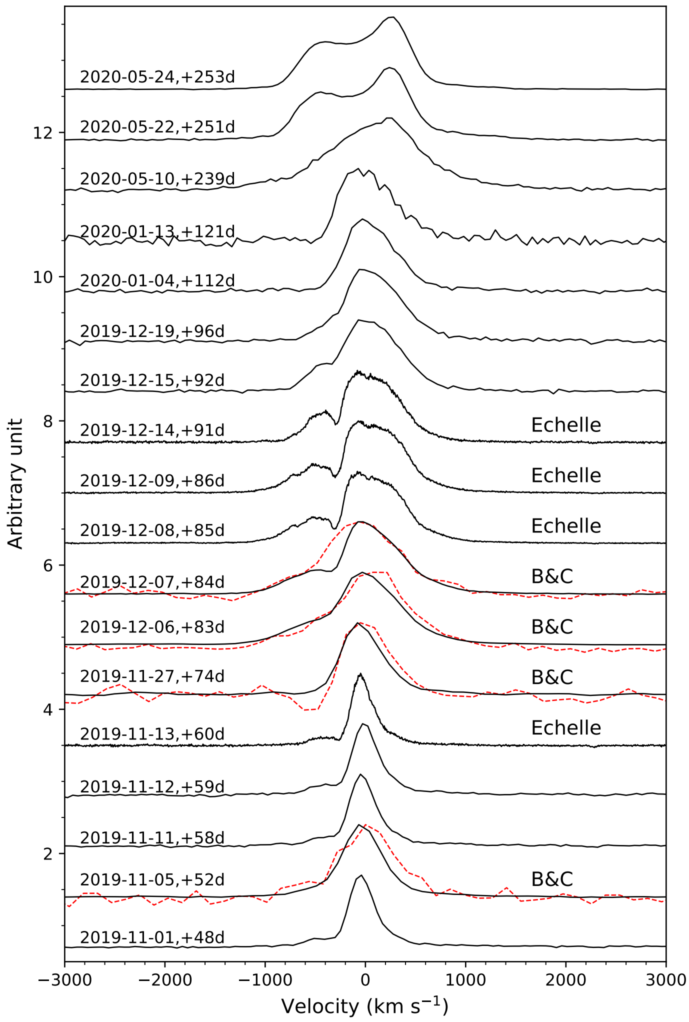

Figure 4.8: Hα emission profile variations in V2891 Cyg. Profiles from R$\sim$2000 resolution MFOSC-P and B&C spectrographs, and high resolution echelle spectrograph data, are presented. Hβ profiles, obtained with the B&C spectrograph, are shown as dashed red lines.

The origin of absorption components in novae have been explored in recent studies (see, e.g., Williams et al., 2008; Williams & Mason, 2010; Arai et al., 2016, and references therein) in the context of *Transient Heavy Element Absorption* (THEA) systems, where the presence of “principal” and “diffuse enhanced” systems was seen as an indication of the presence of multiple envelopes/shells in the nova ejecta. In nova V2891 Cyg, these absorption components were evident until 2019 mid-December, i.e. around 13 weeks after the outburst. The MFOSC-P (R$\sim$ 2000) spectrum of Dec 19 (+96d) also shows the presence of these components. However, these absorption components are not present in the

Table 4.4: Details of the decomposed emission and absorption components of H-α from the echelle spectra. The decomposed profiles are shown in Fig. 4.9 for emission (e1 and e2), pre-maximum (pm) and principal absorption (p1 and p2) components. The listed values are not corrected for instrumental resolution. Errors are derived from the numerical fit.

Component	HV[a] (km s^{-1})	VHM[b] (km s^{-1})	Equivalent Width (Å)	Flux[c]
2019-11-13	(+60d)			
e1	-160±7	406±7	-145.1±5.6	16.77±0.65
pm	-194±7	177±11	34.0±12.2	3.93±1.41
p1	-305±33	234±33	37.7±12.0	4.35±1.39
e2	282±43	471±52	-12.1±1.8	1.39±0.21
2019-12-08	(+85d)			
e1	-69±2	924±2	-855.3±2.4	118.77±0.33
pm	-280±3	136±5	66.9±7.2	9.29±1.00
p1	-411±17	208±32	55.8±7.8	7.75±1.09
p2	-622±7	116±15	8.0±1.2	1.11±0.17
e2	293±3	231±8	-29.4±1.1	4.08±0.15
2019-12-09	(+86d)			
e1	-68±2	913±2	-731.8±2.6	120.63±0.43
pm	-274±3	139±4	60.3±4.8	9.95±0.79
p1	-407±12	185±20	40.8±4.9	6.73±0.81
p2	-616±6	111±13	6.1±0.9	1.01±0.14
e2	301±2	266±7	-36.0±1.3	5.93±0.21
2019-12-14	(+91d)			
e1	-46±3	779±4	-308.3±2.2	44.72±0.31
pm	-282±3	119±5	22.8±1.1	3.30±0.15
p1	-393±14	106±21	3.9±1.0	0.57±0.15
e2	293±5	316±18	-18.5±1.6	2.68±0.23

(a) Heliocentric velocity (HV), (b) The velocity width at half maximum (VHM), (c) Integrated flux (reddening corrected) for emission (e1), pre-maximum (pm), principal (p), and one red-shifted emission (e2) systems are given. Fluxes are in units of 10^{-11} erg s^{-1} cm^{-2}.

MFOSC-P spectrum ($R \sim 2000$) recorded on 2020 Jan 4(+112d), i.e. around 16 weeks after the outburst detection. If we consider the velocity difference of ~700 kms^{-1} between the ejecta and such absorption system, the distance of these systems from the central source is estimated as ~43 au. This is consistent with the projection of Williams et al. (2008), who postulated that the disappearance is due to the collision between the two gaseous components.

The emission component e1 shows the evolution of its heliocentric velocity, as well as a spread in its velocity profile (Table 4.4), while the red-shifted e2 emission remains almost constant. The e2 component is weak in the spectrum of Nov 13 (+60d) but strengthens by Dec 8 (+85d). This could be due to a change in the optical depth of the gas between +60 and +85 days, so that receding material (positive velocity) – previously not visible – has now gained in strength. This e2 component again becomes weaker by Dec 14 (+91d). It is interesting to note that the flux of the e1 and e2 components dropped by factors of ∼2.7 and ∼2.2, respectively, in a 5-day interval (between +86d and +91d). Such speedy recombination rates point to very high electron densities. However, at the time of these Hα observations, the light curve of the nova was undergoing the largest and most rapid up-and-down changes, and the flux of the e1 component evolved in parallel with the V band flux of the nova. Therefore, evidently, the nebular material responsible for the emission in the V band was at high density and capable of recombining in a matter of very few days and rapidly following the changing photo-ionizing input from the central star. This behavior is mirrored by that of the e1 Hα component, being emitted by the same gas as that responsible for the continuum emission at optical wavelengths.

The optical depth and line of sight effects, the complex geometry of the ejecta (e.g. bipolar flow), interaction with surrounding pre-existing material around the nova etc., can give rise to the asymmetry in line profiles, as also seen in other novae, e.g. Nova Sco 2015 (Srivastava et al., 2015), Nova Del 339 (De Gennaro Aquino et al., 2015) etc. As the nova attained its first maximum on 2019 Nov 30(+77d), the relatively narrower width, and larger blue-shifted velocity of the e1 component (on +60d) may possibly be due to the emission coming from a very thin outer layer of the optically thick ejecta. Whereas its evolution between +84d to +91d corresponds to the optically thinning of the ejecta as a larger volume is now available for the emission profile. This could also explain why the fluxes (or equivalent widths) of both emission components e1 and e2 were not in synchronization between +60d and +84d, whereas between +84d and +91d, e2 followed the behavior of e1.

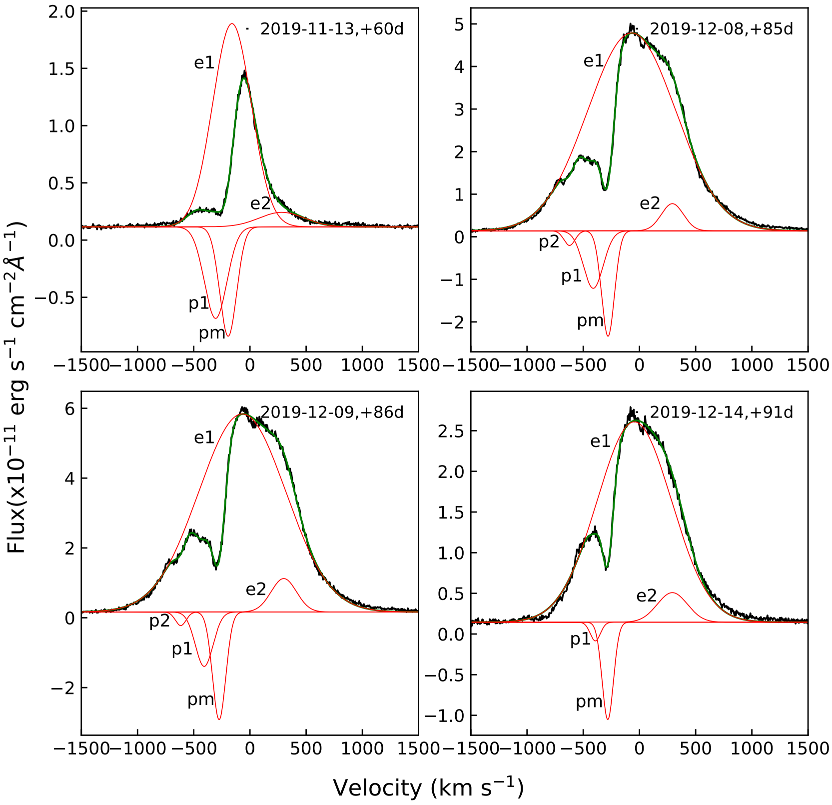

Figure 4.9: The absorption systems superimposed on the (dereddened) Hα profiles from the echelle spectra. The profiles for 2019 Nov 13, Dec 8, Dec 9 and Dec 14 are shown. The constituents profiles are in red, while the combined profiles are in green, superimposed on the observed profiles (black). See section 4.1.5.2 for discussion.

4.1.5.3 Behaviour of O I lines: variability of P Cygni profile of O I 7773Å line

V2891 Cyg showed prominent oxygen lines at various stages of its evolution, from initial fireball to coronal phase, for a period of 15 months. We determined the flux ratios of various optical and NIR lines (e.g., O I 0.8446μm, 1.1287μm, and 1.3164μm), which suggested the action of Ly-β fluorescence. The [O I] lines (5577, 6300, 6364 Å) are used to determine the electron temperature T_e of the neutral gas, and the mass M_{OI} of the neutral O I, following the prescription of Williams (1994). These lines were detected in the spectra of 2019 Dec 7(+83d) and Dec 15(+92d). The mass of neutral oxygen is estimated to be $\sim 8.6[\pm 1.3] \times 10^{-6} M_{\odot}$, which is consistent with the typical mass of oxygen in a nova eruption ($\sim 1.1 \times 10^{-4} - 5.3 \times 10^{-8} M_{\odot}$; Williams, 1994). The corresponding electron temperature was determined to be ∼5600 K.

An interesting development was the variability in the line profile of the O I 7773Å during its early evolution from 2019 Nov–2020 Jan. The velocity profiles of O I 7773Å are shown in Fig. 4.10, from 2019 Nov to 2020 May. A P Cygni profile in the O I 7773Å line was seen in our first optical spectrum, taken on 2019 Nov 1(+48d), and on the spectrum taken on 2019 Nov 12(+59d). It had disappeared by Nov 19(+66d). The absorption feature was at ∼500 kms^{-1} on Nov 1(+48d), while on Nov 12(+59d), it was at ∼300 kms^{-1}. The subsequent change in the O I 7773Å line profile was found to be correlated with its re-brightening. It can be seen from the LC (Fig. 4.1) that the first instance of brightening had begun around 2019 Nov 25(+72d). The nova attained its first maximum on Nov 30(+77d) (m_V ∼14.05), faded to a minimum on Dec 7(+84d), and brightened on Dec 17(+94d). Correspondingly, the O I 7773Å profile of Nov 27(+74d) shows deep P Cygni absorption (absorption component at ∼450 kms^{-1}), which disappeared by Dec 13(+90d).

The P Cygni feature in O I 7773Å had again re-appeared in the spectra taken on Dec 15(+92d) and Dec 19(+96d) (absorption feature at ∼700-750 kms^{-1}). Another re-brightening occurred on 2020 Jan 12(+120d), whose imprint can be seen in the re-appearance of a deep P Cygni profile of the O I 7773Å line on 2020 Jan 13(+121d), with absorption feature at ∼600 kms^{-1}. It is of further interest to note that the Hα profile of Jan 13(+121d) also shows the P Cygni feature. In both cases, the blue-shifted absorption occurred at a velocity of ∼500-600kms^{-1}, indicating that the blue absorptions in Hα /O I 7773Å are likely to be due to the outburst.

The disappearance and later re-appearance of P Cygni profiles also fit the pattern seen in other novae (Tanaka et al., 2011). Tanaka et al. (2011) have studied six slow/moderate fast novae, which showed re-brightening in the early phase after maximum. However, these novae showed a similar re-appearance of P Cygni profiles in multiple emission lines, e.g. Hα , Hβ , He I, Na I, Fe II, O I etc. The typical blue-shifted velocity separation of absorption components was found to be in the range $\sim 750 - 2500$ kms^{-1}.

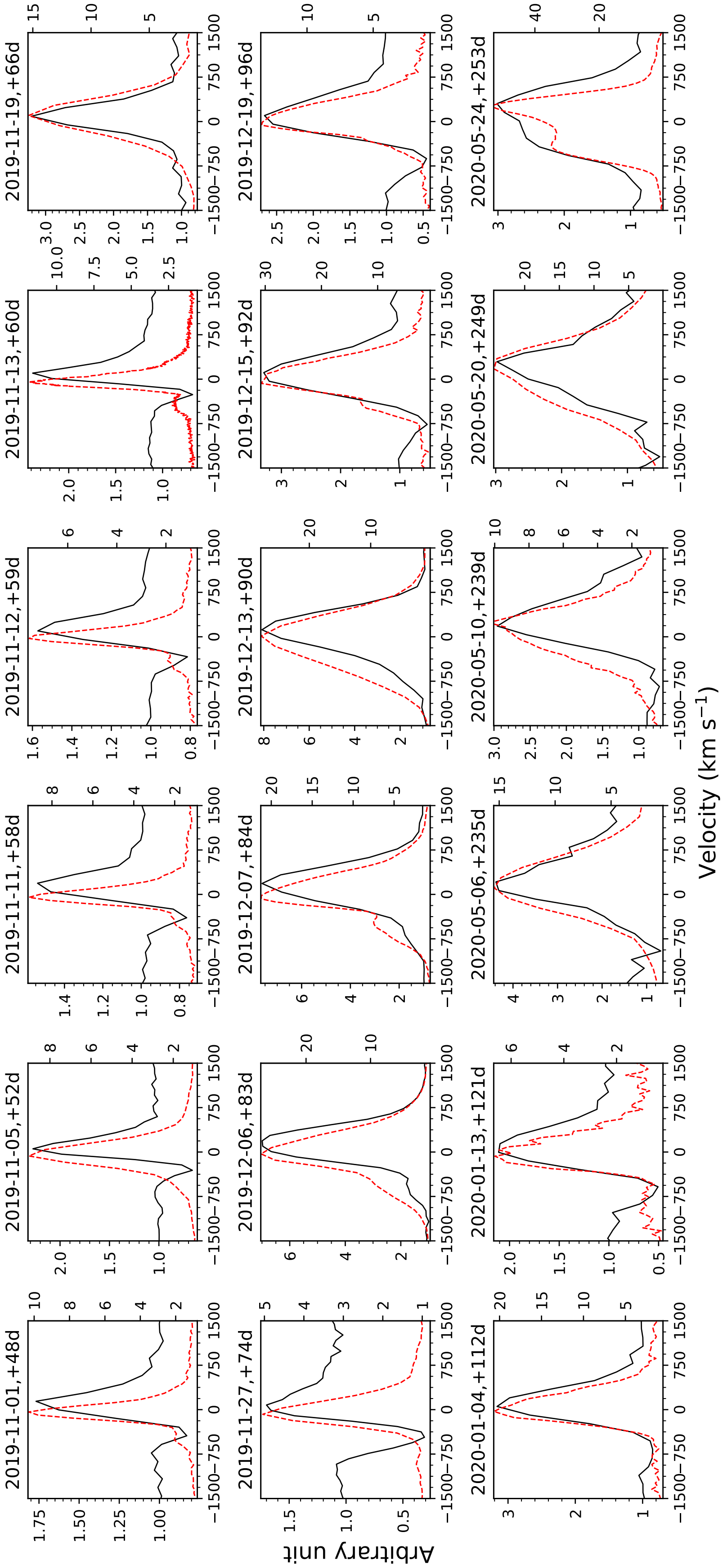

Figure 4.10: The line profile variation seen in the O I 7773Å (solid black) and Hα (dashed red) lines during 2019 Nov - 2020 May. The relative flux for O I 7773Å and Hα are given on the left and right axes for each of the sub-plots respectively. The appearance and disappearance of P Cygni features is evident. Profiles for Nov 5, Nov 13, Nov 27 and Dec 6 are from the B&C spectrograph; the remainder all are from MFOSC-P. See section 4.1.5.3 for discussion

Several consistent reasons for re-brightening, and the re-appearance of P cygni features, in novae have been suggested, such as hydrogen-burning instabilities (Pejcha, 2009), re-expansion of the photosphere (Tanaka et al., 2011), mass ejection at the re-brightening (Csák et al., 2005) etc. The re-appearance of P Cygni absorption at different epochs, around the re-brightening episodes, and at higher velocities confirm the scenario that periodic mass loss is happening during the re-brightening phase. Similar behavior was also seen during the epoch of re-brightening, for example, in nova V4745 Sgr (Tanaka et al., 2011), in which the P Cygni profiles appeared after the second brightness peak.

4.1.6 Results from NIR Spectoscopy

4.1.6.1 NIR Spectroscopy: the pre-maximum phase

Our earliest NIR spectrum of V2891 Cyg, obtained on 2019 Nov 17 (+64d) from Mt. Abu, is shown in Fig. 4.11 with prominent lines marked in the inset. The spectrum displays emission lines of H, C, N, and O, typically seen in the spectra of the Fe II class of novae, several of which are shown in Banerjee & Ashok (2012). The He I 1.083, 2.059μm lines are present but weak. The lines are narrow (Paβ has an FWHM of $\sim$640 kms^{-1}), with no P Cygni features. Although no first overtone CO emission is seen in the K band, lines of Na and Mg are present, which suggest (Das et al., 2008) the presence of cool, low-excitation regions or clumpy material, conducive for molecules and dust to form later in the evolution; dust did indeed condense subsequently. The NIR photometric observations yielded $J = 9.98 \pm 0.02$, $H = 8.87 \pm 0.03$ and $Ks = 7.66 \pm 0.02$.

A recombination Case B analysis of the de-reddened hydrogen Brackett (Br) lines shows that they are optically thick. Fig. 4.12 shows the Br line strengths normalized to Br-12 (the typical error is $\sim$ 10% in the line flux measurements). The Case B emissivities at T_e = 10000 K, and various electron densities from Storey & Hummer (1995), are also shown. A significant deviation is seen in the Br-7 (Brγ) line strength, which is expected, under optically thin conditions, to be of higher intensity compared to the higher Br series (Storey & Hummer, 1995). Such optical depth effects are expected in the early epoch spectra of novae

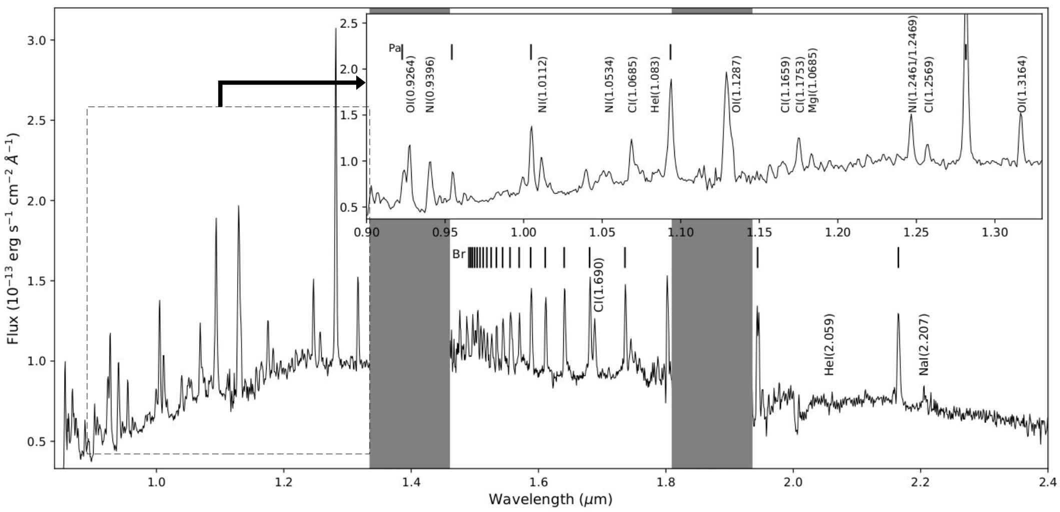

Figure 4.11: The NIR spectrum of Nova V2891 Cyg covering 0.84–2.4 μm obtained from Mount Abu on 2019 Nov 17 (+64d). The region between 0.90–1.35μm is shown in the inset, with features identified. The H band (∼1.4-1.8μm) region shows numerous emission lines of the hydrogen Brackett series, which are marked by vertical ticks. Regions of poor atmospheric transmission are shaded. The spectrum is not corrected for reddening.

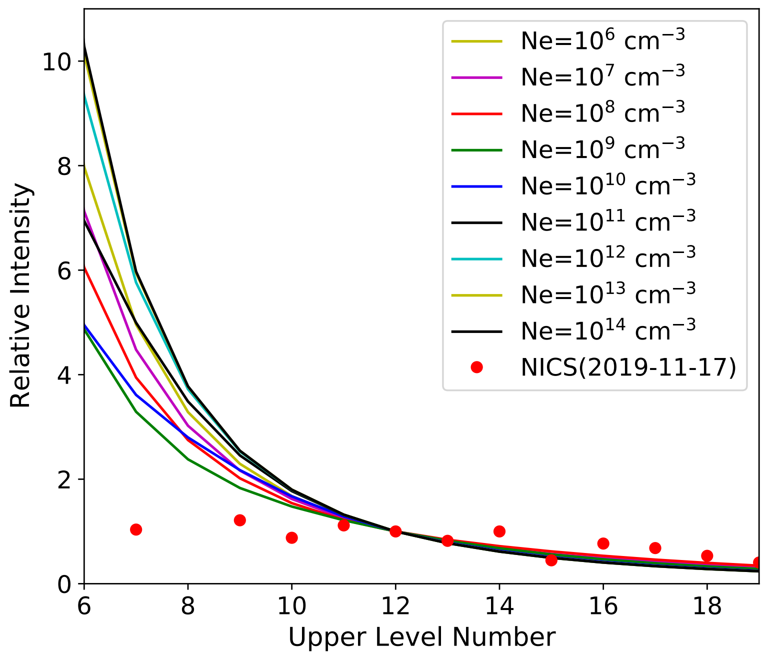

Figure 4.12: Recombination Case B analysis for the Brackett lines on ∼+64d. The abscissa gives the upper level of the line transition. The line intensities are normalized with respect to Br12. The model Case B predictions are also shown for temperature = 10000 K and electron number densities of 10^6-10^{14} cm^{-3}.

(e.g., Nova Cep 2014, and Nova Sco 2015; Srivastava et al., 2015). During these epochs, V2891 Cyg was undergoing episodes of re-brightenings (Fig. 4.1), so such optical depth effects are plausible.

Since the Brγ line is optically thick, only constraints on the electron density and emission measure are possible. The optical depth at the line-center, $\tau_{n,n'}$, is given by $\tau = n_e n_i \Omega(n,n')D$, where n_e, n_i, D and $\Omega(n,n')$ are the electron and ion number densities, path length, and opacity corresponding to the transition from upper level n to lower level n' respectively (Hummer & Storey, 1987; Storey & Hummer, 1995). Using opacities from Storey & Hummer (1995), the condition that the optical depth in the Br-γ line, τ, be > 1, and using the same procedure as in Srivastava et al. (2015), the emission measure $n_e^2 D$ can be constrained to lie between between 1.34×10^{33} and 3.83×10^{34}cm^{-5}. Further, the electron density can be constrained by taking $D = v\times$t as the kinematical distance traveled by the ejecta, where v is the ejecta velocity, and t is the time after outburst. Considering half of the Full Width at Zero Intensity (FWZI) of the Hα line ($\sim$ 1000 kms^{-1}) as the expansion velocity, and t as $\sim$ 60 days after the outburst, this puts a lower limit on electron density in the ejecta in the range of 1.14×10^9-6.08×10^9 cm^{-3}.

The four other NIR epochs of observation between May – October 2020 could be mildly affected by a dust formation event that occurred during that period. The formation of dust affects the line strengths through additional reddening, and hence the dust event is discussed first, followed by a Case B analysis of these May – October 2020 NIR observations.

4.1.6.2 Dust formation

The evolution of the $g - r$ colour from the ZTF lightcurves (bottom panel of Fig. 4.13; also Fig. 4.2 of the ZTF LC's presented initially) clearly shows a reddening of the nova over a period of $\pm$ 50 days, centered around JD 2459013 (2020 June 13 or $\sim$ +273d after outburst). We believe this behavior indicates a short episode of dust formation and destruction. This assertion is supported by a dip in the $g - r$ colour at around this time, indicating reddening by dust. The epochs of our NIR spectroscopy, relative to the dust event, are shown by vertical ticks in the lower panel of Fig. 4.13. The top panel of Fig. 4.13 shows the change in the slope of the K band continuum for 2020 May 20(+249d), when the dust had just started to form, relative to the spectrum of 2020 June 7(+267d). The latter shows a significant flattening with respect to the former, indicating the development of a clearly discernible IR excess due to dust. To estimate the dust mass, we fit a black-body curve (green curve; middle panel) to the excess IR emission of June 7(+267d) relative to the blue-dashed continuum of May 20(+249d). A blackbody temperature of 1400 ± 200 K is estimated.

We estimate the dust mass following Evans et al. (2017) and Banerjee et al. (2018a), assuming that the grains are spherical, and that the dust is composed of carbonaceous material. It has been shown (Evans et al., 2017) that the dust masses for amorphous carbon (AC) and graphitic (GR) grains, assuming optically thin emission, are given by:

$$\frac{M_{\rm dust(AC)}}{M_\odot} \simeq 5.63 \times 10^{17} \left(\frac{d}{5.5\ \rm kpc}\right)^2 \frac{(\lambda f_\lambda)_{\rm max}}{T_{dust}^{4.754}} \tag{4.1}$$

$$\frac{M_{\rm dust(GR)}}{M_\odot} \simeq 5.01 \times 10^{19} \left(\frac{d}{5.5\ \rm kpc}\right)^2 \frac{(\lambda f_\lambda)_{\rm max}}{T_{dust}^{5.315}} \tag{4.2}$$

where a value of $d = 5.5$ kpc has been used for the distance, $\rho = 2.25$ gm cm^{-3} has been taken for the density of the carbon grains and $(\lambda f_\lambda)_{\rm max}$ is obtained from the blackbody fit, and measured in units of W/m^2. The dust mass, which is independent of grain size (Evans et al., 2017), is estimated to be $\sim 0.83 \times 10^{-10}$ M$_\odot$, and 1.25×10^{-10} M$_\odot$, for AC and GR grains, respectively; these are very modest amounts.

Classical novae, especially of the Fe II class, commonly show evidence of rapid dust formation within months of the outburst. In this particular case, we propose a specific origin for dust condensation. Following Derdzinski et al. (2017), we propose that dust formation occurred within the cool, dense shell behind shocks that had formed in the ejecta. We offer proof in the coming subsection that strong shocks were likely present at this stage in time, and that the nebular and coronal lines that were seen between 2020 May to September arose due to shock-heating of the gas rather than due to the presence of a hot

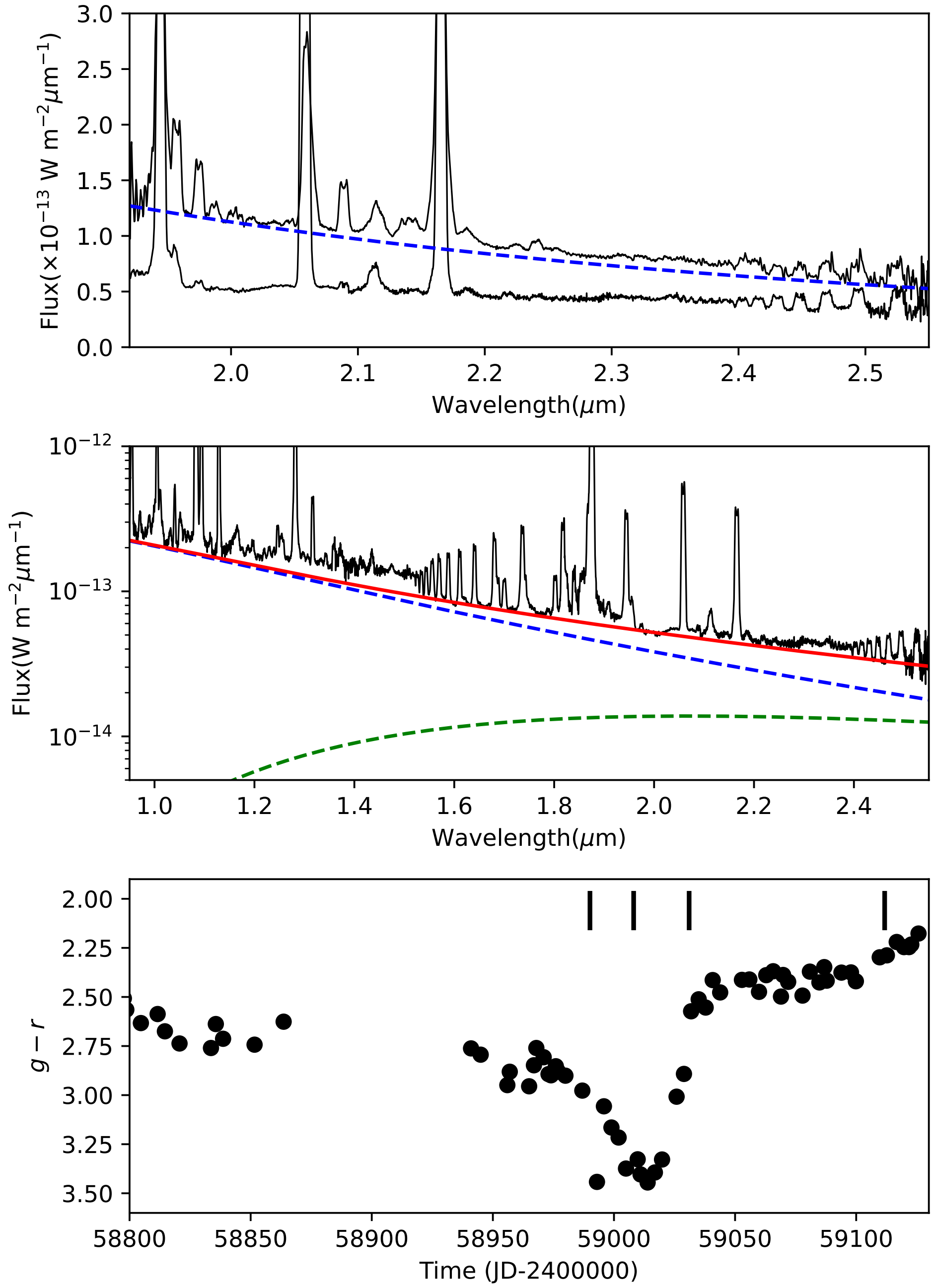

Figure 4.13: Top panel: how the slope of the spectral continuum flattened out between May 20(+249d) (represented by the spectrum whose continuum is fitted by the blue dashed line) and the spectrum of June 7(+267d) just below, thereby indicating the development of an IR excess. The four vertical ticks on the lower panel are the days marking the spectra of May 20(+249d), June 7(+267d), June 30(+290d) and September 19(+371d), respectively. Middle panel: 1400K black-body curve (green), whose contribution needs to be added to the blue-dashed continuum, to reproduce the observed continuum of June 7 (shown in red). Details are given in Section 4.1.6.2. The spectra are dereddened.

central photoionizing source.

4.1.6.3 NIR spectroscopy at late stages between ∼ 250 to 370 days

Near and mid-IR observations in 2020 May (De & Palomar Gattini-IR Collaboration, 2020; Woodward et al., 2020a) showed that the carbon lines (a hallmark of the Fe II class of novae) that had initially been present, had faded. The spectra were rich in the emission lines of H, He, O, N, Fe etc., along with prominent lines of the Paschen and Brackett series. The Paschen and Brackett lines now showed a double-peaked structure having a separation of $\sim 480 - 540$ kms^{-1}, with the red peak stronger than the blue. Subsequent monitoring further showed the emergence of the coronal lines [Si VI] 1.962μm, [Ca VIII] 2.322μm, and [Si VII] 2.483μm in June-September (Woodward et al., 2020b); we discuss these later in this section.

4.1.6.4 Estimate of the ejecta mass

The NIR spectra during the late stages (2020 May - October) are shown in Fig. 4.14, with the prominent lines identified. The lines of the Pa, Br, Pf, and Hu series dominate, while several coronal lines are also detected (Woodward et al., 2020b); these are listed in Table 4.6 and discussed below. A Case B analysis for these late epochs, now shows good conformity with model predictions (Fig. 4.15) over the gamut of lines from each of the Pa, Br, Pf, and Hu series. This indicates that the H lines, at this stage, are optically thin. The compliance with Case B, with only the ISM reddening of $E(B-V) = 2.20$ being applied, also suggests that the dust event has not influenced the strengths of the lines significantly via additional reddening. This is consistent with the earlier inference that the amount of dust formed is modest. Under these circumstances, the ejecta mass M_{ej} (approximated by the mass in the form of ionized hydrogen) can be estimated from

$$M_{ej} = \frac{4\pi d^2 F(\text{line}) m_p}{n_e \epsilon(\text{line})} \quad , \tag{4.3}$$

where d is the distance, F(line) is the observed flux in a H line, ϵ(line) is the emissivity in the line as given in Storey & Hummer (1995), n_e is the electron density, and m_p is the proton mass.

Table 4.5: Mass of the ionised hydrogen in the ejecta as determined from H lines. H line fluxes are estimated from the spectrum of 2020 June 07 (+267d). See section 4.1.6.4 for details.

Wavelength (micron)	Upper level of transition	Line Flux ($\times 10^{-13}$ erg/s/cm^2)	Mass ($\times 10^{-5} M_\odot$) (for $n_e = 10^{7.5}$ cm^{-3})
Brackett			
4.0500	5 (Brα)	73.60	8.35
2.1650	7 (Brγ)	27.40	8.09
Pfund			
3.7385	8	10.10	8.18
3.2950	9	7.42	8.35
3.0376	10	5.80	8.68
2.8714	11	4.42	8.52
2.4940	17	1.68	9.02
2.4686	18	1.45	8.94
2.4470	19	1.21	8.52
2.4300	20	1.02	8.18
2.4150	21	0.72	6.60
2.4023	22	0.55	5.59
Humphreys			
3.9054	15	1.34	9.27
3.8170	16	1.00	8.02
3.6910	18	0.87	9.19
3.6440	19	0.65	7.85
3.6050	20	0.56	7.77
3.5720	21	0.56	8.67
3.5200	23	0.48	9.44

Table 4.5 gives ejecta mass in $M_\odot$. Of these, the most reliable estimates are for the lines at longer wavelengths (viz., the Pf and Hu lines, and Brα) because their strengths are least affected by any extra reddening due to the dust (for example, beyond 3.5 μm, the extinction is only $\sim$ 5% of any additional A_V generated due to the dust in contrast to $\sim$ 25% at Paβ). We have assumed an electron density of $n_e = 10^{7.5}$ cm^{-3} in the mass estimation for two reasons. First, the smallest critical density of the ions seen during the coronal phase (Table 4.6, discussed below) suggests this. Second, geometric dilution of the ejecta with time ($n_e \propto t^{-2}$) suggests that the lower limit on the electron density of 1.14×10^9-6.08×10^9 cm^{-3} at +64d would have decreased to about $\sim 10^8$ cm^{-3} during the coronal phase ($\sim$ 300-360d). A homologous flow would create a faster decline in

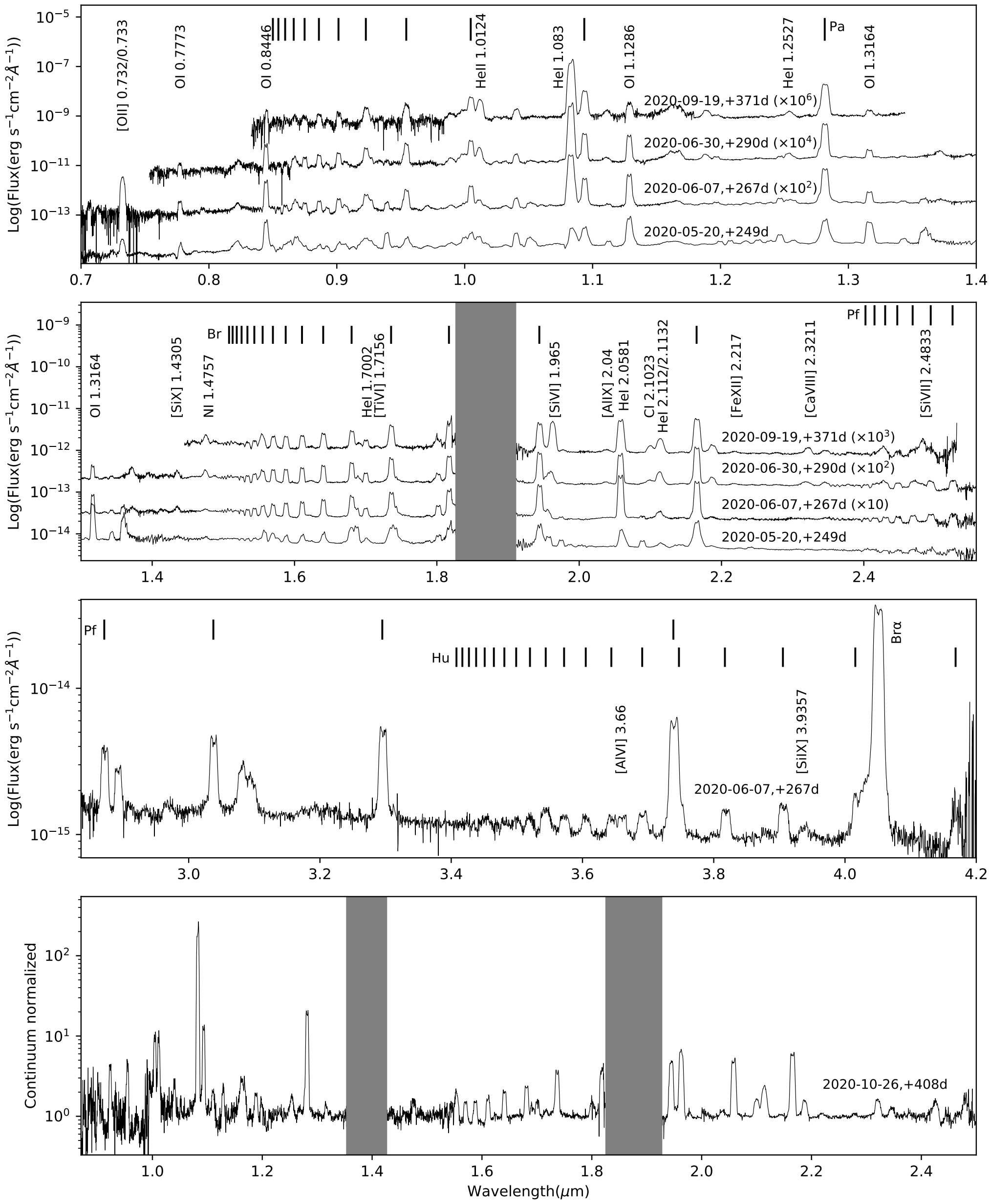

Figure 4.14: The IRTF spectrum (without dereddening) of Nova V2891 Cyg covering 0.67–4.2μm are shown in top three panels. These were obtained on 2020 May 20, June 07, June 30 and 2020 Sep 19. Lowest panel shows TANSPEC spectrum covering 0.86–2.5 μm, obtained on 2020 Oct 26. This spectrum is normalised with respect to the continuum.

the density. The mass, for any other choice of n_e, should be scaled accordingly. Based on this analysis and using the Humphreys lines for arriving at a formal estimate, we obtain the mass of the ejecta to be $M_{ej} = (8.60{\pm}1.73){\times}10^{-5}\ M_{\odot}$.

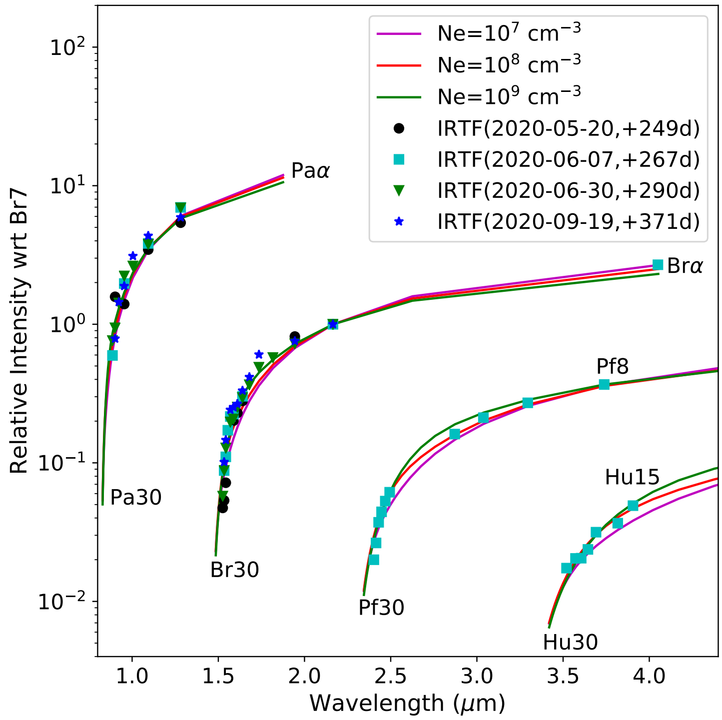

Figure 4.15: Recombination Case B analysis for the Pa, Br, Pf and Hu lines, with the line intensities normalised to Br12. The model Case B predictions are also shown for temperature of 10000 K, and electron densities of 10^7-10^9 cm^{-3}, expected at the epochs under consideration (shown in the inset).

4.1.6.5 Coronal lines

By 2020 June, coronal lines had begun to appear in the NIR spectra; these are most clearly seen in the spectrum of 2020 Sep 19, i.e. after 371 days (Woodward et al., 2020b). Table 4.6 gives the details of the detected NIR lines. It is first necessary to assess whether the coronal lines are truly coronal (in that they are generated by collisional ionization, followed by collisional excitation) or whether photo-ionization due to a hot central source is responsible. Which of these two mechanisms is operating has been debated in the literature (Evans et al., 2003; Benjamin & Dinerstein, 1990; Greenhouse et al., 1990). In this case, the evidence suggests – for several independent reasons – that collisional ionization is the mechanism responsible for the coronal lines, and photoionization plays a negligible role. Greenhouse et al. (1990) define nova coronal lines as arising from ground-state fine-structure transitions in species with ionisation potential (IP) > 100 eV. Considering that the nova pseudo-photosphere collapses at constant bolometric luminosity, the effective temperature $T_\star$ of the stellar remnant is empirically expected to vary as, $T_\star \simeq T_0 \exp[0.921(t/t_3)]$ (Evans et al., 2003; Bath & Shaviv, 1976; Bath & Harkness, 1989), where $T_0 = 15,280K$ and t_3 is the time to fall three magnitudes below the the maximum. However, as novae at maximum show temperature values closer to 8000 K (see discussion in Evans et al. (2005)), we adopt $T_0 = 8000K$ to estimate $T_\star$. However, we note that this formula is mostly applicable for a linear (in mag) LC decline from maximum, and our attempt here is to place limits on the temperature of the central ionizing source. A similar approach had been adopted by Evans et al. (2003) for nova V723 Cas, which showed similar erratic LC like nova V2891 Cyg.

As discussed above, for $t = 371$ days (when the coronal lines were seen) and for t_3 in the range 180-230d days (from section 4.1.4.1), the temperature of the pseudo-photosphere is estimated to be in the range $\sim$ 35000-54000K. For this temperature range, there is a negligible number of photons with energies greater than 100eV (a blackbody at 50000K emits only $\sim 9 \times 10^{-6}$% flux above 100 eV (Cox, 2000)). This makes it difficult to explain the presence of ions like Si VI and Al IX, which are clearly detected. These (and all coronals lines) need IPs > 150 eV. However, in the supersoft X-ray phase of novae, due to shell burning, the temperature of the hot central source can be > 10^5K, (see Schwarz et al., 2011), however we did not find evidence of such hot source with the X-ray observations.

A Target of Opportunity (ToO) observation on 2020 September 25(+377d), using the XRT instrument on the Neil Gehrels Swift Observatory (Gehrels et al., 2004) did not detect X-ray emission in an exposure time of ~1000 seconds (Target ID 12868[7]), with a count rate less than 8.0×10^{-3} counts per second. In addition, the UV instrument onboard Swift did not detect any emission in the UV, with the three filters (centered on 190, 220, and 260 nm) all giving

[7]https://www.swift.psu.edu/toop/summary.php

limits of > 19.4 mags. The Swift non-detection argues against the presence of a sufficiently hot central photoionizing source.

In a rather similar case, Evans et al. (2003) explained the early onset of the coronal phase in nova V723 Cas in terms of the presence of collision ionisation caused by the interaction of ejecta parcels at different velocities. In the present case as well, the multiple re-brightenings in the LC are likely caused by the periodic episodes of material ejection – a premise supported by the re-appearance of P-Cygni profiles in the O I 7773Å line at different epochs (see Section 4.1.5.3). For the gas temperature of $\sim 10^4$K, the speed of sound is $\sim 13 kms^{-1}$. If the relative velocity is in the range of 150-200kms^{-1} the Mach number turns out to be $\sim$12, indicating a strong shock. In this case, the post-shock temperature $T_s(K)$ is related to the single-particle forward shock velocity v_s as

$$v_s = \left(\frac{16kT_s}{3\mu m_H} \right)^{1/2} \tag{4.4}$$

where k is the Boltzmann constant, and μm_H is the mean particle mass (Shu, 1992; Tatischeff & Hernanz, 2007). Thus for the shock-heated gas, which is generated by collisions between parcels of ejecta having a relative velocity difference in the range $\sim$ 150-200 kms^{-1}, the temperatures would be $4.8 - 9.1 \times 10^5$ K. The presence of coronal also lines implies a gas temperature in the same range.

The correlation between optical re-brightenings and strong shocks (manifested through γ-ray emission) has been established in the case of nova V906 Car (ASASSN-18fv). In that nova, the optical and γ-ray flares were seen to occur simultaneously, implying a common origin in shocks (Aydi et al., 2020). As discussed in Section 4.1.5, as well as in this section, the observational evidence for multiple ejections is strong in the nova V2891 Cyg. Thus, we expect physical conditions to be conducive for shock-induced collisional ionization. In the case of collisional ionization, the ion temperatures and abundances can be determined in the following manner.

Table 4.6: NIR Coronal lines

Species	Wavelength (μm)	log(T_{max}) [a]	log(n_{crit}) [b]	I.P. [c] (eV)	Flux [d] (07 June)	Flux [d] (30 June)	Flux [d] (19 Sept.)	Remarks
[S IX]	1.2523	6.0	9.2	379.60	-	-	-	unable to deblend from He I 1.2528μm
[Si X]	1.4305	6.2	8.8	401.40	6.91±0.13	6.86±0.26	-	
[Ti VI]	1.7156			119.53	-	0.80±0.08	0.98±0.04	
[Si VI]	1.9650	5.6	8.8	205.27	10.97±0.18	16.51±0.19	31.76±0.92	Deblended from Br 8-4
[Al IX]	2.0400	6.1	8.2	330.10	-	1.94±0.16	1.74±0.03	
[Fe XII]	2.2170	6.2	8.6	331.00	1.72±0.12	1.60±0.12	1.50±0.21	
[Ca VIII]	2.3211	5.7	7.4 [e]	147.24	-	4.17±0.07	4.18±0.16	
[Si VII]	2.4833	5.8	8.2	246.49	-	5.01±0.06	11.20±0.40	Deblended from Pf 18-5, 17-5
[Al VI]	3.6600	5.7	7.6	190.49	4.33±0.06	-	-	Deblended from Hu 19-6
[Si IX]	3.9357	6.1	7.5	351.10	3.36±0.52	-	-	

(a) : The equilibrium temperature of the maximum concentration of the ion ($n(X^{+i})/n(X_{tot})$) i n a collisionally ionized plasma (Greenhouse et al. 1993)

(b) : Critical densities at $T = T_{\rm max}$ for collisional de-excitation (from Greenhouse et al. 1993, their figure 3a). Somewhat lower values of $n_{\rm crit}$ are expected in cooler photoionised regions as listed, for example, in Spinoglio & Malkan (1992) and Ferguson et al. (1997) since $n_{\rm crit} \propto T^{1/2}$; equation (1) of Greenhouse et al. (1993)).

(c): Ionisation Potential

(d): Observed undereddened line fluxes (in units of $\times 10^{-14}$erg $s^{-1} cm^{-2}$), after deblending with the contaminating lines mentioned in the Remarks column. Where reliable deblending was not possible, or the line was not detected, flux values are not given.

(e) : Estimated from Fig. 2, Greenhouse et al. (1993)

The line flux from a region of volume V, electron temperature T and distance d is given by Greenhouse et al. (1988); Lang (1980); Chandrasekhar et al. (1993),

$$\mathrm{I}_{\mathrm{x}^{+i}} = \frac{(8.629 \times 10^{-6})\mathrm{n}_{\mathrm{x}^{+i}}\mathrm{n}_e V \mathrm{h}\nu\Omega}{4\pi \mathrm{d}^2\mathrm{T}^{1/2} g_u} \mathrm{erg.s}^{-1}.\mathrm{cm}^{-2} \tag{4.5}$$

where, $\mathrm{n}_{\mathrm{x}^{+\mathrm{i}}}$ is the number density of the x^{+i} ion; hν is the transition energy of the line under consideration, Ω is the collisional strength, and g_u is the statistical weight of its upper level. For two distinct ion species, or for different ionization stages of the same ion, this may be recast as:

$$\frac{I_x^{+i}}{I_y^{+j}} = \frac{n_x^{+i}}{n_y^{+j}} \frac{\nu_x}{\nu_y} \frac{\Omega_x}{\Omega_y} \frac{g_y}{g_x} \tag{4.6}$$

where I, n, ν, Ω and g are the measured fluxes, total numbers of ionised atoms, frequency of the transition, collision strength of the transition and statistical weights of the lower level, respectively.

These are defined for species x in its i^{th} ionisation state, and species y in its j^{th} ionisation state. If T_e is known, the ratio of total relative abundances of the neutral element n_x^0/n_y^0 can be determined, provided the ionisation fraction n^i/n^0 for both the elements are known at T_e. The fractional ionisation values of an ion, as a function of temperature, and the collision strengths for the different transitions have been taken from various sources in the literature (see Blaha, 1969; Jain & Narain, 1978; Jordan, 1969; Greenhouse et al., 1988; Zhang et al., 1994; Berrington et al., 1998; Shull & van Steenberg, 1982). Using the [Si VI 1.96μm and the [Si VII] 2.48μm lines, the temperature is estimated to be 4.77[$\pm$0.04] $\times$ 10^5 K, and 4.54[$\pm$0.04] $\times$ 10^5 K respectively, using values of the fractional ionisation ratio n_{Si}^{+5}/n_{Si}^{+6} from Jordan (1969) (Table XVII) and Shull & van Steenberg (1982) respectively. For the [Al VI] 3.06μm and the [Al IX] 2.04μm lines, the temperature is estimated to be 4.33[$\pm$0.04] $\times$ 10^5 K using values of the fractional ionisation for Al from Jain & Narain (1978). These ion temperatures lie in between the values of 3.2 $\times$ 10^5 K estimated for the coronal zone in V723 Cas (Evans et al., 2003), and 6.3 $\times$ 10^5 K for Nova Vulpeculae 1984 (Greenhouse et al., 1988).

The Al/Si abundance n(Al)/n(Si) can be estimated by using Equation (4.6), where in the left hand side one can use different combinations of the line intensities choosing from the [Si VI] 1.96 μm, [Si VII] 2.48 μm, [Al IX] 2.04 μm, and [Al VI] 3.06 μm lines. On the right hand side of the equation, the term $n^i_{\rm Al}/n^j_{\rm Si}$ can be recast as below to allow $(n_{\rm Al}/n_{\rm Si})$ to be determined:

$$n^i_{\rm Al}/n^j_{\rm Si} = (n^i_{\rm Al}/n_{\rm Al}) \times (n_{Al}/n_{Si}) \times (n_{Si}/n^i_{Si})$$

A mean value of $(n_{\rm Al}/n_{\rm Si}) = 1.53 \pm 0.15$ is found, which implies the ratio $[n_{\rm Al}/n_{\rm Si}]$(nova)$/[n_{\rm Al}/n_{\rm Si}](\odot)$= 18.4, where we have used the solar abundances of Lodders (2021). This over-abundance with respect to solar is plausible: novae of both the CO and ONe types are known to overproduce Al (José & Hernanz, 1998; Starrfield et al., 1997).

Using Equation (4.5), the volume of the coronal gas, derived using the coronal lines of [Si VI] and [Si VII] in the spectrum of September 19, is in the range of $9.95 \times 10^{42} - 1.01 \times 10^{44}$cm^{-3}, and the corresponding mass of the coronal gas is in the range $\sim 8.37 \times 10^{-7} - 8.42 \times 10^{-7}$ M$_\odot$. The volume of the coronal gas is almost a factor of 100–1000 smaller than the maximum volume that the ejecta can attain kinematically, (i.e. $4/3\pi R^3 \sim 10^{45} - 10^{46}$cm^{-3}, with $R = v \times t$; for the velocity v in the range 200–500 kms^{-1}, and $t \sim 371$d for 2020 Sep 19). This suggests the ejecta are in the form of a thin shell with a very small filling factor. This small volume of the coronal gas (compared with the total volume of the ejecta) is also consistent with the non-detection of the UV/X-ray emission, as well as the modest amount of shock-induced dust mass estimated earlier.

4.1.6.6 Velocity shifts of the coronal lines

A rather curious phenomenon is seen where the coronal lines “migrate” from bluer to redder velocities with the passage of time. This is demonstrated in Fig. 4.16 for the [Si VI] 1.96μm and [Ca VIII] 2.32 μm lines, shown in velocity space. For the [Si VI] line, the line shift is significantly large, exceeding 1000 kms^{-1}, between 2020 June to September. On the other hand, a similar shift

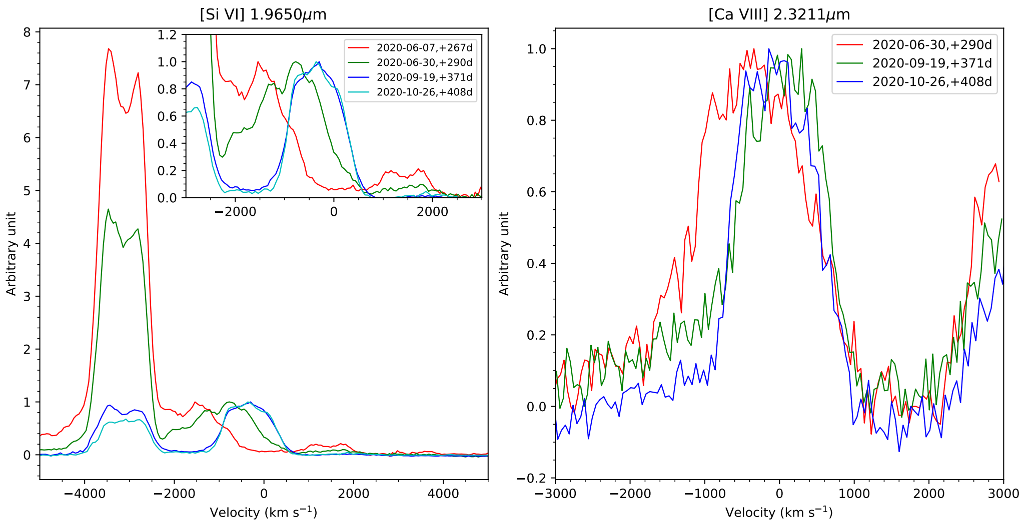

Figure 4.16: The left and right panels show the velocity shifts seen in the coronal lines as the obscuring dust behind the shocked gas, which is the site of the coronal line emission, dissipates or changes its optical depth with time. In contrast to the coronal lines, the H lines remain fixed in velocity, as seen for example, from the Brδ line at 1.944 μm (at ~ -3000 km s^{-1} in the upper panel). Inset in the upper panel shows the shift of the [Si VI] 1.9650μm line. 2020-10-26 epoch data are from TANSPEC, the remainder are from SpeX. Details are given in section 4.1.6.6.

is not seen in the H lines (Brδ 1.944 μm at ~ -3000 kms^{-1} is shown here to demonstrate this), or in the He lines (e.g. the He I 2.059 μm line). Clearly, there is a spatial stratification of the species. But the more interesting implication of this behavior is related to the dust event. As per the model proposed by Derdzinski et al. (2017) (see Fig. 1 in that paper), a cool, possibly clumpy, dust shell is expected to form behind the forward shock for both the approaching and receding parts of the nova shell. Thus a plausible interpretation of the coronal line shifts is that in the June 7 (+267d) observation, the dust is dense and completely blocks the emission from the receding part of the shell. Hence the line profile is blue-shifted to the maximum. As the dust dissipates with time, more emission from the receding red component reaches the observer (as in the profiles of June 30 (+290d) and September 19(+371d)). This is a simplified interpretation because the dust geometry could be more complex, and dust clumps could drift in and out of the line of sight, causing time-varying obscuration of the red shell (and hence evolving profile shapes as seen between the June 7(+267d), June 30(+290d), Sep 19(+371d) and Oct 26(+408d) profiles shown here). The line shift in the [Si VI] 1.96 μm line is also seen in the [Ca VIII] 2.32 μm line. This behavior may thus be confirmation that dust formation can be triggered by a radiative shock, as proposed by Derdzinski et al. (2017), wherein as gas behind the radiative shock cools, it compresses, reaching high densities. The shocked ejecta is expected to collect in a geometrically thin, clumpy shell. If the formation of the dust in V2891 Cyg is indeed shock-induced, then this observation is likely the first time that dust formation via this route is being witnessed in a nova. Interestingly, Harvey et al. (2018) (following Derdzinski et al. (2017) and references therein) had further suggested that dust formed in the forward shock zone can subsequently be destroyed as the shock passes through this small amount of dust. However, this process retains the seed nuclei responsible for dust formation. Thus, this process of shock-induced dust formation and destruction may be repeated over the successive shock cycles. For the case of nova V339 Del, Evans et al. (2017) and Gehrz et al. (2015) considered grain shattering by electrostatic stress due to charging of grains by UV/X-ray emission; however, as we did not notice any UV-X-ray emission in the case of nova V2891 Cyg so this mechanism is unlikely to be important.

4.1.7 Summary: Nova V2891 Cyg

In this study, we have explored the optical and NIR spectroscopic evolution of the nova V2891 Cyg, one of the slowest novae recorded in recent times. Our optical and NIR spectroscopy campaign lasted around 13 months (2019 Nov – 2020 Dec) and utilized several facilities worldwide. The nova's light curve is of the "jitter" class, having a couple of episodes of re-brightening, which we propose is due to periodic mass ejection, as manifested in the line profile of the O I 7773Å line. The temperature and mass of the gas containing the O I are consistent with values typically seen in a similar class of novae. The absorption components of the Hα are studied, and their evolution is found most likely to be due to interaction between gaseous components associated with separate episodes of previous mass ejection. A brief period of dust formation occurred during the evolution, along with the production of coronal line emission in the NIR. The analysis presented here shows that the coronal emission, most likely, is due to shock heating rather than photoionization, and the episode of dust formation is shock-induced. These phenomena are rare in the evolution of novae. Thus, the present data set and our associated analysis would be of interest to the community to explore the physics of the nova phenomenon.

4.2 Exploring the symbiotic nature of SU Lyn

4.2.1 Symbiotic stars

Symbiotic stars are interacting binary systems having a red giant or a supergiant star that transfers matter to a companion, usually a white dwarf (WD), which can also be a neutron star. A schematic diagram of a symbiotic star is shown in Fig. 4.17. In the case of a WD as a primary, the secondary can be a red giant or an asymptotic giant branch (AGB) star, and they are known as WD symbiotics. Whereas, in the case of a neutron star as a primary, the secondary can be a giant, AGB star, or a supergiant, and they are known as symbiotic X-ray binaries (Masetti, N. et al., 2006; Bozzo et al., 2018).

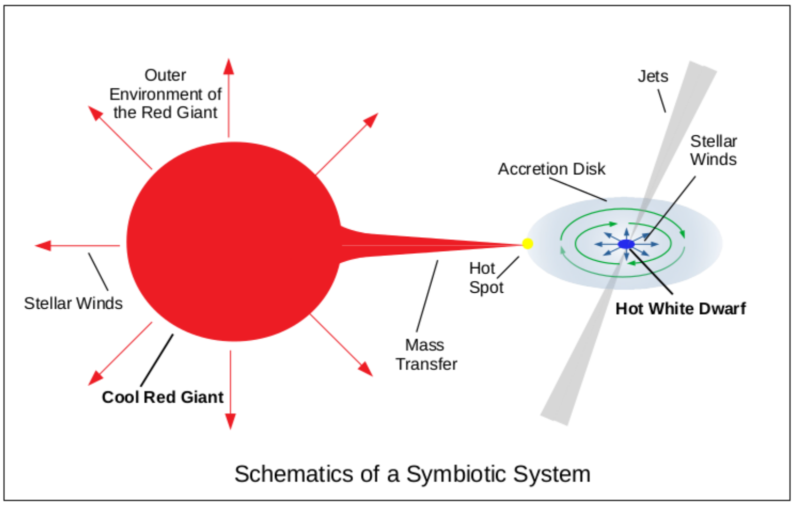

Figure 4.17: Schematics of a symbiotic system.

Symbiotic systems have traditionally been identified by the presence of strong emission lines of high excitation species (e.g., He II, [Fe VII], etc.) on the top of the continuum, with absorption features of TiO, VO, and CN, associated with the cool companion's photosphere, in their optical spectra (e.g. Kenyon (1986)). In addition, they often show two rather "exotic" lines at 6825Å and 7082Å, which have been identified due to Raman scattering of the OVI 1032Å, 1038Å resonance lines by neutral hydrogen (Schmid, 1989). The presence of the aforementioned emission lines has thus always been the conventional route for identifying such systems.

4.2.2 SU Lyn: A suspected symbiotic star

SU Lyn is an infrared-bright (K_s = 1.618) unremarkable M-type star from ground-based observation. Based on its X-ray observations, it has recently been proposed to be a symbiotic star despite showing no obvious emission lines in its low-resolution optical spectra. SU Lyn was discovered in hard X-rays in the Swift/BAT hard X-ray all-sky survey by Mukai et al. (2016). These observations, coupled with a NuSTAR spectrum obtained by Lopes de Oliveira et al. (2018), showed that the X-ray emission could be modeled to arise from hot ionized plasma at $T \sim 2\text{x}10^8$K, which was proposed to be originated from a boundary layer between an accretion disk (AD) and a hot component. Thus, the discovery of the hard X-ray emission indicated that SU Lyn had a hot component that was accreting matter. Mukai et al. (2016) have tried to match the low-resolution optical spectrum with an M6III type star and found that the spectrum matched well in the red part of the spectrum, But on the UV side, they found UV excess. They have also found weak emission lines in the optical spectrum using high-resolution spectroscopy. Based on the UV to X-ray flux ratio, the hot component in SU Lyn was inferred to be a WD rather than a neutron star. The distance to the system was estimated to be 640 ± 100 pc, and the spectral type of the secondary was determined as M5.8III (Mukai et al., 2016). Thus, the X-ray and the high-resolution optical spectrum together implied that SU Lyn had the necessary properties of a symbiotic star.

While the WD in symbiotic systems are known to be a primary source of UV radiation, it has also been realized that the accretion disks can also be a dominant source of UV emissions. Based on their relative intensities, the symbiotics are also classified as shell burning and non-shell burning systems (Luna et al. (2013); Mukai et al. (2016) and references therein). In the case of the shell-burning systems, the accreting matter from the giant star burns in a shell on the white dwarf's surface. Thus, the white dwarf is hot and luminous. So the optical emission is dominated by light from the red giant and ionized nebula. These symbiotic systems were revealed through high excitation lines in the optical spectrum. On the other hand, non-burning symbiotics are without shell burning. They are proposed to be dominated by accretion disk luminosity, as the white dwarf does not produce enough flux through shell burning. They typically have no or weak emission lines in the optical spectrum. These symbiotic systems can be revealed through their X-ray emission, UV excess, and UV variability. The weakness of the visible emission lines and the rapid variability in the UV (Mukai et al., 2016; Lopes de Oliveira et al., 2018) suggested SU Lyn as a non-burning system powered purely by accretion process. The lack of shell burning leads SU Lyn to have very weak symbiotic signatures in the optical and the observed UV luminosity predominantly originating from the accretion disc.

Given the lack of signatures in the optical and predominance of UV radiation in non-burning systems, it is expected that UV spectroscopy could be a powerful tool to probe the dynamics of such systems. The UV/optical spectra of well-established symbiotic stars show a complex blend of lines, e.g. forbidden, permitted and intercombination lines excited through a variety of atomic processes (Meier et al., 1994). These lines are suggested to originate from different regions of the symbiotic system. The lines of high ionization potential (IP) species, e.g. [Ne V], [Fe VI], etc. clearly demonstrate the existence of low-density regions of thin plasma heated and ionized from the UV radiation of the hot components. These lines presumably originate from the winds of WD and AD. The lines of lower IPs (e.g. N II, O I, O II, O III etc.) are most likely formed in the upper atmosphere of the red giant or in the extended surrounding nebula (see Kenyon & Webbink (1984); Mikolajewska et al. (1989); Nussbaumer & Vogel (1989) and references therein).

The UV emission lines (e.g [C IV] 1907,1909Å, [N III] 1749Å, [N IV]

1485Å, [O IV] 1401Å, Si III 1883,1892Å) were found to be extremely helpful for emission-line diagnostics. Di-electric recombination lines from C II, C III, C IV, N III, N IV, N V, O III, O IV, Si III, Si IV etc. were found useful to estimate the electron temperature and densities of the nebula (Hayes & Nussbaumer, 1986; Nussbaumer & Storey, 1987). The UV spectra were also useful to determine the individual element abundances, their locations from the hot source and the temperature of the hot source (Nussbaumer & Vogel, 1989). However, the scenario is complex and detailed models (e.g. Vogel & Nussbaumer (1994)), which depend on many input parameters, are needed to reproduce the strengths of the emission lines as well as the underlying continuum.

We have studied SU Lyn through ground-based observations for its optical-NIR spectroscopy and space-based UV observation from Ultra-Violet Imaging Telescope (UVIT) on the AstroSat space mission. While UVIT is primarily an imaging telescope, it also provides a very low-resolution slit-less UV spectrum using transmission grating. We have utilized the UV spectrum to robustly entrench SU Lyn as a symbiotic system. In addition to low-resolution spectroscopy data from MFOSC-P and NICS, a high-resolution (R∼30,000) optical spectrum from the HESP instrument on the IIA-HCT telescope was also utilized in this study.

4.2.3 Observations and Data Analysis

4.2.3.1 UV observations

The UV observations were done with the Ultra-Violet Imaging Telescope (UVIT) on the AstroSat satellite, which consists of two telescopes of 38 cm diameter, one optimized for the Far UV (FUV, 1300-1800 Å) and the other for the Near-UV (NUV, 2000-3000 Å). The details can be found in Subramaniam et al. (2016); Tandon et al. (2017a,b, 2020).

The UV data presented here were obtained against proposals IDs AO4-026, and AO5-144 (observation IDs $A04\_026T01\_9000001712$ and $A05\_144T02\_9000003176$) wherein photometry was proposed to cover both the FUV and NUV filter bands. However, for certain technical reasons, observations

Table 4.7: Log of SU Lyn Observations using various facility

Instrument & Mode (Facility)	Date (UT)	Wavelength range (Å)	Integration Time (sec)
UV			
UVIT-Photometry[a] (Astrosat)	2017-11-22.26	2000-3000	1385,509, 1853[b]
UVIT-Spectroscopy[c] (Astrosat)	2019-09-21.66	1300-1800	9542
Optical			
HESP-Spectroscopy R∼30000, (HCT)[d]	2018-01-09.81	3750-10500	5400
MFOSC-P Spectroscopy R∼500-R2000	2019-12-13.77[e]	4500-8500	Various
Near-Infrared			
NICS[f]-Spectroscopy R∼1000, (Mt. Abu)	2017-12-25.78	8400-24000	380

(a): The NUV telescope has 4 narrow band filters viz. NUVB15(λ_{centre} 2196Å, width 270Å), NUVB13 (2447Å, 280Å), NUVB4(2632Å, 275Å), NUVN2(2792Å, 90Å) and two broad band Silica (2418Å, 785Å) filters. (b): In the NUVB15, NUVB4 and Silica filters respectively (c) : UVIT is equipped with low resolution grisms (400 line pairs/mm) which provide a low resolution spectrum in slitless mode viz. ∼17Å in second order for the FUV (which was used here). (d) : Hanle echelle spectrograph of the Himalaya Chandra Telescope (e) : Several spectra were collected between 2019-2020. The one listed in this Table is used in this work and other observation log using MFOSC-P are given in Table 4.8. (f) : Near-IR Camera Spectrograph

were executed only in the NUV bands in the NUVB15, NUVB4, and Silica filters (see table-note of Table 4.7). The slit-less FUV grism spectra were obtained in AO5 proposal cycle. The science-ready level-2 data was provided by the UVIT payload operation centre (POC) team through the ASTROSAT data archive. The reconstructed images and spectra are corrected for distortion, flat-field illumination, spacecraft drift and other effects as discussed in Tandon et al. (2017b, 2020). Aperture photometry, reduction of the spectra, wavelength and flux calibrations were done following prescribed procedures given in Tandon et al. (2017a, 2020).

4.2.3.2 Optical and NIR (OIR) observations

OIR spectroscopic observations were done with the PRL 1.2m Mt. Abu Telescope using the Near-Infrared Camera and Spectrometer (NICS) for the NIR 0.8-2.4 μm region and the Mt. Abu Faint Object Spectrograph and Camera (MFOSC-P) for the optical region (Srivastava et al., 2018).

Table 4.8: Log of SU Lyn Observations using MFOSC-P

Mode	Date (UT)	Wavelength range (Å)	Integration Time (sec)
R500	2019-03-28.69	4400-8400	20
	2019-04-18.61		30
	2019-12-13.79		100
	2020-05-05.64		50
	2020-05-06.63		50
R1000	2019-04-13.63	4700-6600	40
	2019-04-18.64		120
	2019-12-13.78		100
	2020-05-05.64		80
R2000	2019-03-28.71	6900-7100	100
	2019-04-13.64		240
	2019-04-18.65		450
	2019-12-13.77		190
	2020-05-05.63		200

The details of the observations are presented in Table 4.7 and Table 4.8. Spectra from MFOSC-P were reduced using the data-reduction process/pipeline as discussed in Chapter 2. Spectra from NICS were reduced as per standard procedures described in several studies done earlier, e.g. Banerjee et al. (2018b); Srivastava et al. (2016). A high-resolution echelle spectrum covering 3750-10500Å in 61 orders at R$\sim$30000, was also obtained using the Hanle Echelle Spectrograph (HESP) on the 2m Himalayan Chandra Telescope (HCT). The pipeline reduced data was used for the analysis; further details of HESP can be found at https://www.iiap.res.in/hesp/.

4.2.4 Results and Discussion

4.2.4.1 UV Spectroscopy, Modeling of FUV Continuum, and photometry

The FUV spectrum of SU Lyn is shown in Fig. 4.18 with the lines marked. It shows the characteristic spectra of symbiotic stars, many of which are observed by the International Ultraviolet Explorer (IUE) and reproduced, for example in Michalitsianos et al. (1982) and in the catalog of Meier et al. (1994). For com-

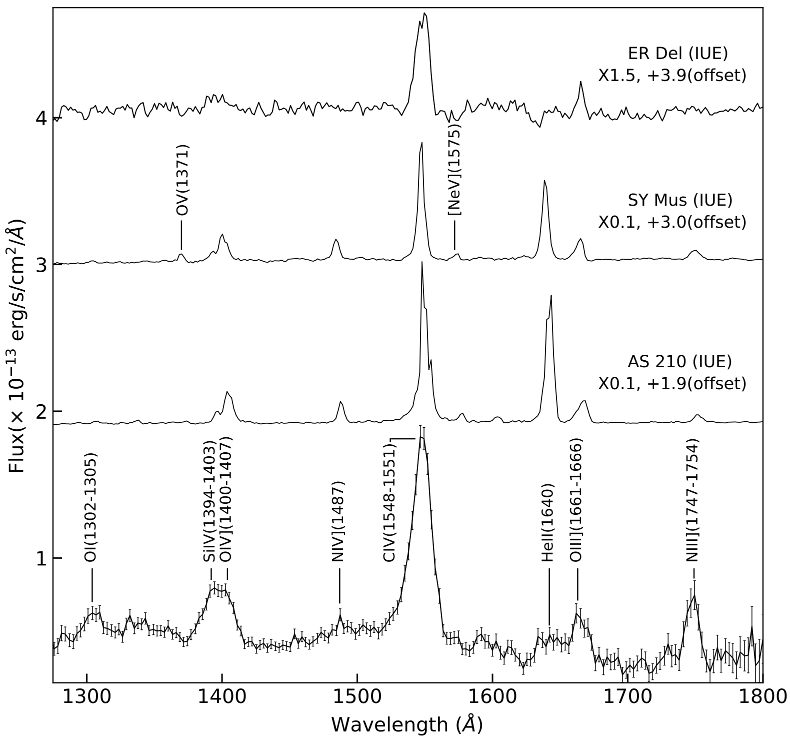

Figure 4.18: The UVIT spectrum of SU Lyn with the lines identified. Archival IUE spectra of three symbiotics ER Del, SY Mus, and AS 210, are also shown for comparison.

parison, we also present in Fig. 4.18, the spectra of three symbiotics viz. SY Mus, AS 210, and ER Del which are discussed shortly. To paraphrase Meier et al. (1994), the UV spectrum of a symbiotic usually consists of a great range of excitation lines ranging from relatively low-temperature species (e.g., O I 1302-1305Å, C II 1334, 1335Å); strong resonance emission lines (e.g. N V 1238Å, 1242Å, C IV 1548, 1551Å) and other high-ionization lines like He II 1640Å. Diagnostic lines for studying the ambient nebular conditions is principally through the inter-combination lines (e.g. O IV] 1397-1407Å, N IV] 1487Å etc.).

The lower spectral resolution of UVIT (∼17Å), as compared to other UV probes like IUE (∼6Å) or high-resolution GHRS/HST spectra, does not allow us to resolve components of some of the inter-combination lines to allow estimating density and temperature parameters (e.g. Keenan et al. (2002)), as discussed in Section 4.2.2. However, what we do see for certain is that He II 1640Å (the highest excitation line seen in our spectrum) is weak which likely implies that the temperature of the photo-ionizing source is not too high. In comparison, SY Mus is a shell-burning type of symbiotic system consisting of a hot $T = 105000K$ WD with a total luminosity $L = 1600L_{\odot}$. He II 1640Å line is among the brightest lines in its IUE spectrum, while emissions of [Ne V] 1575Å emission (IP=97.12 eV) and O V 1371Å (IP=77.41eV) have also been detected (Pereira et al. (1995) and reference therein). The optical and UV spectra of AS 210 are rich in emission features and display high ionization lines, e.g. [Ne V] 3426Å (Gutierrez-Moreno & Moreno, 1996; Munari & Zwitter, 2002). We wish to draw the reader's attention toward the symbiotic system ER Del, which has been classified as a δ-type system showing evidence of boundary layer X-ray emission (Luna et al., 2013). Its optical spectrum (Munari & Zwitter, 2002) show only prominent Hα emission and IUE UV spectrum is devoid of high-ionization lines (even HeII 1640Å is very weak or absent). These features make ER Del a system closely resembling the characteristics of SU Lyn, a non-burning system.

The weakness of He II 1640Å, in conjunction with the results from X-ray studies that strongly suggest that SU Lyn is a disk-dominated system, makes us propose that the central WD (which lacks shell-burning) is not the dominant source of the hard ionizing radiation in SU Lyn. Rather, photo-ionization likely occurs predominantly through the UV flux emitted by an AD which we propose is present (the presence of an AD is similarly proposed by Mukai et al. (2016) and Lopes de Oliveira et al. (2018)). We thus explored whether the observed FUV continuum can be simulated with a simple model consisting of a WD and a steady-state, time-independent AD.

The modeling of the FUV continuum has been done assuming the system consists of a White dwarf (WD) and a steady-state, time-independent Accretion Disk (AD). A multi-colour black body approximates the AD with a radial temperature profile given by the standard disk model (Pringle, 1981), while the WD is considered to be a black body source. This simple model has been developed in PYTHON and consists of the following steps:

1. Mass (M_{WD}) and temperature (T_{WD}) of the WD, as well as accretion rate, were chosen as free parameters.

2. The radius (R_{WD}) of WD was calculated from the mass-radius relation for WD (Nauenberg, 1972) as following:

$$\frac{R_{WD}}{R_\odot} = \frac{0.0225}{\mu} \frac{[1 - (M/M_\star)^{4/3}]^{1/2}}{(M_{WD}/M_\star)^{1/3}} \tag{4.7}$$

   where, μ is mean molecular weight per electron, M_{WD} is mass of the white dwarf, and $M_\star$ is Chandrasekhar mass limit, which can be estimated by,

$$\frac{M_\star}{M_\odot} = \frac{5.816}{\mu^2} \tag{4.8}$$

3. The continuum flux from WD was estimated using Stefan-Boltzmann relation for black-body, i.e. the total luminosity $L_{WD} = 4\pi R_{WD}^2 \sigma T_{WD}^4$ and flux $= L_{WD}/(4\pi D^2)$, where D is the distance of the WD from earth.

4. The continuum flux of the accretion disk (AD) is estimated with a multi-colour black-body model, wherein the AD comprises several thin annular disks of varying temperatures. The temperature profile of the AD at a distance R from the center of the WD is given by (Godon et al., 2017):

$$T_{\rm eff}(R) = \left\{ \frac{3GM_{\rm WD}\dot{M}}{8\pi\sigma R^3} \left[1 - \sqrt{\frac{R_0}{R}}\right] \right\}^{1/4}, \tag{4.9}$$

   where, $M_{\rm WD}$ is the mass of the WD, $\dot{M}$ is the accretion rate, and R_0 is the radius of the inner part of the AD. For convenience, this expression can be written as,

$$T_{\rm eff}(x) = T_0 x^{-3/4}(1 - x^{-1/2})^{1/4}, \tag{4.10}$$

with

$$T_0 = 64,800K \times \left[\left(\frac{M_{\rm WD}}{1M_\odot} \right) \left(\frac{\dot{M}}{10^{-9} M_\odot/yr} \right) \left(\frac{R_0}{10^9 cm} \right)^{-3} \right]^{1/4} \tag{4.11}$$

where $x = R/R_0$.

5. Thus, the continuum flux from AD can be estimated by summing up all the Blackbody flux coming from individual thin annular disks of area $= 2\pi R dR$.

6. Total flux of the continuum at any given wavelength is thus estimated by summing up the contributions from AD and WD.

The results of the simulations are shown in Fig. 4.19 against our UVIT spectrum and NUV photometry points. GALEX photometry points for 2006 and 2007 are also shown as given in Mukai et al. (2016). All the photometry data and spectrum have been dereddened using the Cardelli et al. (1989) extinction law with $E(B-V) = 0.07$ as estimated by Mukai et al. (2016).

Our UVIT photometry yielded magnitudes of 16.02±0.02 and 15.19±0.01 in the NUVB15 and NUVB4 filters with corresponding fluxes of 9.44×10^{-15} and 1.28×10^{-14} ergs/s/cm^{-2}/Å respectively, before reddening correction. In the broadband NUV silica filter, we estimate a magnitude of 16.25±0.01, but this observation may be affected by saturation effects as discussed in Srivastava et al. (2009), and hence is not being used in our analysis. It may also be noted that significant fluctuation in the UV flux is seen between the GALEX and UVIT observations. SU Lyn is known to display considerable UV variability, both at sub-minute scale (Mukai et al., 2016) and also on a longer time-scale. Lopes de Oliveira et al. (2018) interpreted the UV variation between 2015 and 2016 to be a consequence of a large drop by almost 90% in the accretion rate. This aspect is discussed again in the next sub-section.

We attempted to reproduce the UV continuum through visual inspection of the simulated continuum. The mass of WD and the accretion rate were varied in the range of $0.7-1.0\ M_\odot$ and $1.0-9.0\times10^{-10} M_\odot$ per year respectively, as per the estimates suggested by Mukai et al. (2016) and Lopes de Oliveira et al.

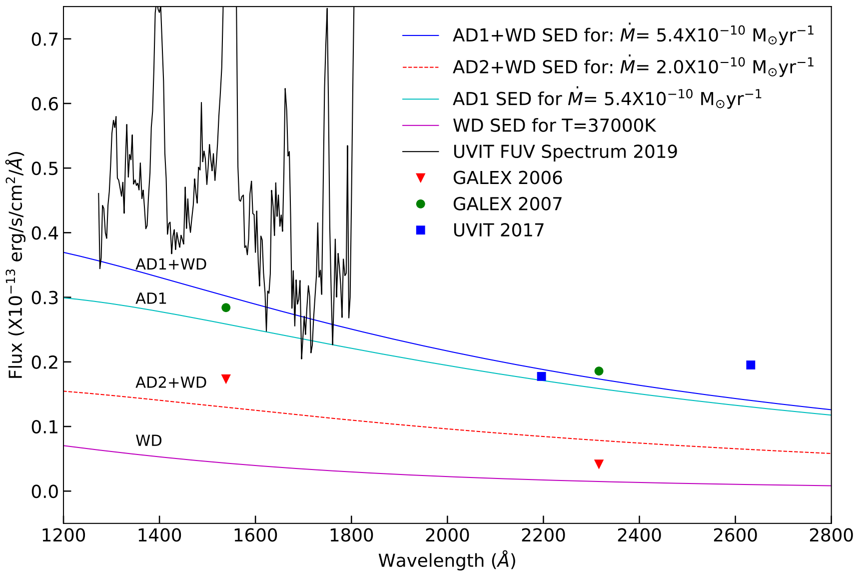

Figure 4.19: Model fits to the UV spectrum and photometry using the combined spectral energy distribution (SED) of a WD of mass 0.85M$_\odot$ at 37,000K and an AD accreting mass at different rates as indicated in the inset. Most of the GALEX and UVIT data are reasonably reproduced using mass accretion rates of $\sim 10^{-10} M_\odot$ per year. The GALEX magnitudes in the NUV and FUV filters are 17.42±0.02 and 16.64±0.03 for Dec 2006 respectively; and 15.8±0.02 and 16.11±0.03 for Jan 2007 respectively. UVIT magnitudes/fluxes are given in the texts.

(2018). The choice of these ranges then constrained the allowed temperature values of the WD. In order to reproduce the appropriate UV continuum for SU Lyn UVIT spectrum and NUV photometry points, we tried WD temperature value in the range of $\sim 30000 - 45000K$. Through visual inspection, we found a suitable fit for the WD mass of $0.85M_\odot$ and temperature of $37000K$. A wider range of temperatures may be allowed by the data and also be scientifically reasonable. However, our aim here is to provide a simple model till a higher-resolution UV spectrum is collected which we intend to obtain. As shown in Fig. 4.19, the continuum of the observed FUV spectrum is reasonably well reproduced using an accretion rate of $5.4 \times 10^{-10} M_\odot$ per year. The GALEX data of both the 2006 and 2007 epochs are fairly well fitted by using mass accretion rates of $5.4 \times 10^{-10} M_\odot$ per year and $2.0 \times 10^{-10} M_\odot$ per year, respectively. The necessity of having to use different accretion rates to fit the UV fluxes at different epochs, strongly suggests that it is the AD that predominantly powers the UV part of the spectrum and which is responsible for the variability seen in UV bands. It may also be pointed out that a very high flux ($\sim 10^{-13}$ ergs/s/cm^2/Å was observed by Swift-UVOT in 2015 in the UVM2 band (Mukai et al., 2016)). These data are not plotted in Fig. 4.19 since the numerical values of the Swift fluxes are not given in Mukai et al. (2016). However, our simulations indicate that such a level of the NUV continuum can be reproduced with a mass accretion rate of $\sim 6.5 \times 10^{-9} M_{\odot}$ per year. This is not entirely inconsistent with the estimate of $1.6 \times 10^{-9} M_{\odot}$ per year, adopted by Mukai et al. (2016) to explain their observed UV luminosity with 1 $M_{\odot}$ WD.

In the simulations, the WD luminosity is estimated to be $0.16 L_{\odot}$ while the disk luminosity is significantly higher at $0.66 L_{\odot}$ with its flux peaking at $\sim$ 1100Å. It thus suggests that the WD lacks the flux, in contrast to shell-burning symbiotics, to photo-ionize the wind of the red giant, thereby giving rise to the characteristic intense emission line spectra of symbiotics. On the other hand, the more luminous AD could be the dominant photo-ionizing source. Further, the combined SED of the WD and the AD shows that the flux drops to insignificantly low levels by $\sim$ 220Å which corresponds to $\sim$ 56.4 eV. This could explain why no emission lines are observed with associated ionization potentials larger than 54 eV. However, we caution that our model is simplistic and we plan to obtain a higher resolution UV spectrum to enable more rigorous modelling (e.g. Nussbaumer & Vogel (1989); Proga et al. (1996); Mikołajewska et al. (2006)) to account for the strengths of both the observed UV emission lines and the faint lines seen in the high-resolution optical spectra.

The absence of O V 1371Å line in the FUV spectrum also rules out the possibility of O VI being present. The O V 1371Å line is predominantly produced by dielectronic recombination from O VI (Espey et al., 1995). This is consistent with the absence of 6825Å and 7082Å features, as they are caused by the Raman scattering of O VI 1032, 1038Å resonance transitions. It is worth noting that it is mostly symbiotic stars of the burning type that are known to show these Raman scattered lines (Munari, 2019).

4.2.4.2 Optical and Infrared spectroscopy

Low-resolution optical spectra of SU Lyn from MFOSC-P instrument on PRL 1.2m telescope are shown in Fig. 4.20 and Fig. 4.21.

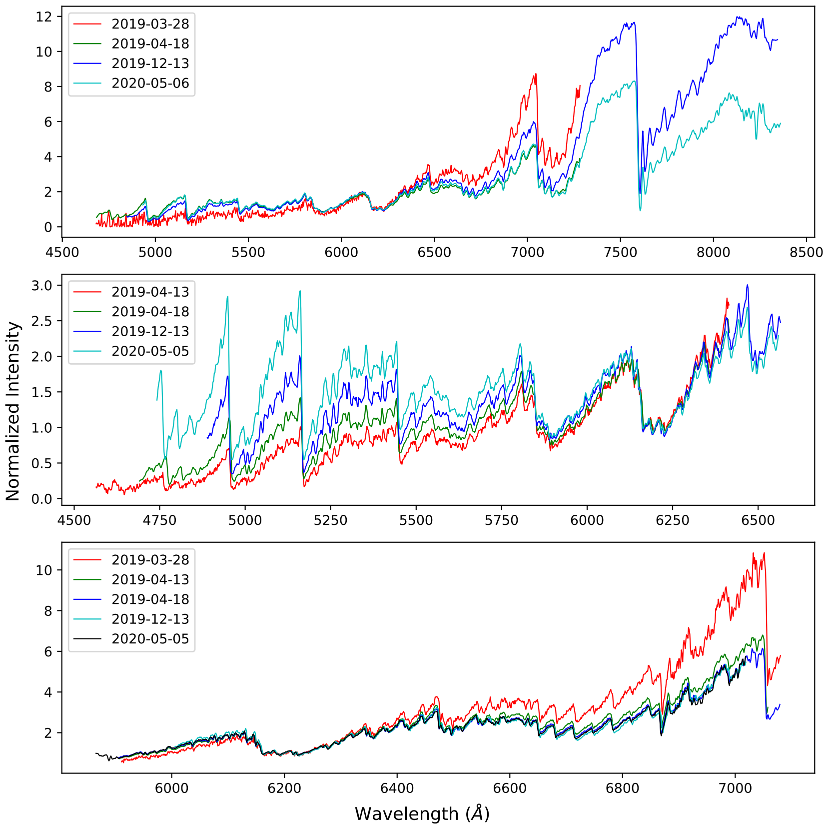

Figure 4.20: Low-resolution optical spectra of SU Lyn at R∼500, 1000 and 2000 are shown in top, middle and bottom panels respectively. The epochs of observations are mentioned in the panels (in the top-left corner). The emission lines are too faint to be seen at low resolution. The spectra are de-reddened and normalized at 6200Å wavelength.

The spectra of different epochs show considerable variability in the visible bands. This variability in the blue continuum is expected as symbiotic stars show variability and flickering in U, B, V bands, etc., at a few minutes to several months of timescales due to various reasons. The short-term flickering may originate from the bright spot (Stoyanov et al., 2018), and the variations are seen in the B band light curve of ∼0.5 magnitude within a timescale of hours. Other causes of the variability are eclipses of the hot spot, variation in the nebular emission due to orbital inclination, etc. (Skopal, 2008), which may reflect in the B-band variability of ∼1-2 magnitude.

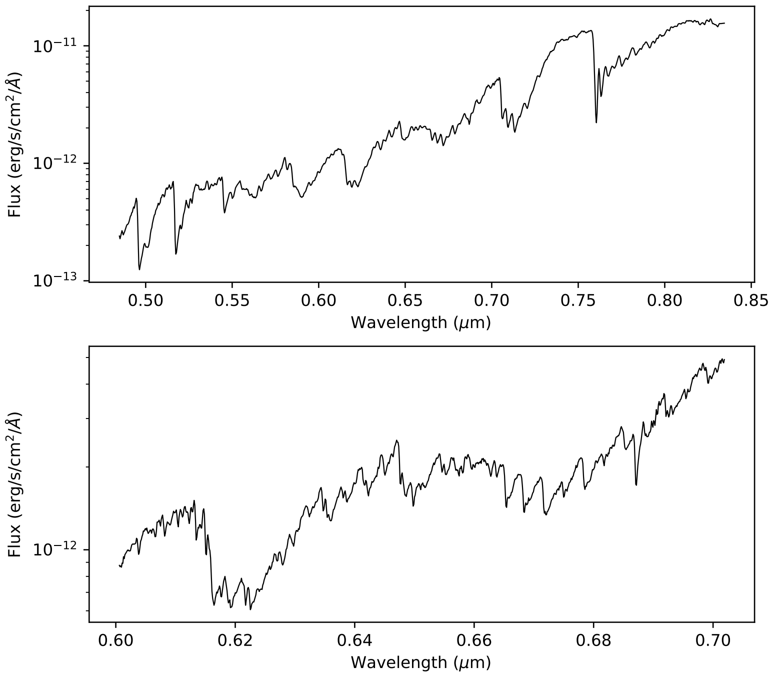

Figure 4.21: Top and bottom panel show low-resolution optical spectra of SU Lyn at R∼500 and 2000 respectively for epoch 2019 December 13, showing that emission lines are too faint to be seen at low resolution. The spectra have been flux-calibrated by matching their flux levels with the NIR spectrum at their common end regions (at ∼8400-8500Å) of the same epoch. The spectra are de-reddened.

Although low-resolution optical spectra of SU Lyn do not show any emission line, however in the echelle spectra, several emission lines are detected. Some are shown in Fig. 4.22, including Balmer Hα to Hϵ. For reasons that are unclear, He I lines are absent. We are also unsure whether He II 4686Å is present; there is a faint feature at that position.

We also observe a feature at the position of [Fe V] 3969.4Å (IP = 54.8 eV), but we consider it more likely to be H-ϵ 3970Å because of a better wavelength match of the line centers. Thus, He II 1640Å (IP = 54.4 eV) represents the highest stages of ionization associated with the lines observed here. The higher critical densities of $\sim 10^9 - 10^{10} cm^{-3}$ for some of the intercombination lines (N III] 1747,1754Å; O III] 1661,1666Å) versus the relatively lower critical densities of $\sim 10^5 - 10^7 cm^{-3}$ for the forbidden lines (such as [OIII] 4959Å, 5007Å and [Ne III] 3868Å) in SU Lyn spectra, suggests (after Mikolajewska et al. (1989)) that the intercombination lines are formed closer to the hot component, while most of the forbidden lines occur in the extended nebula.

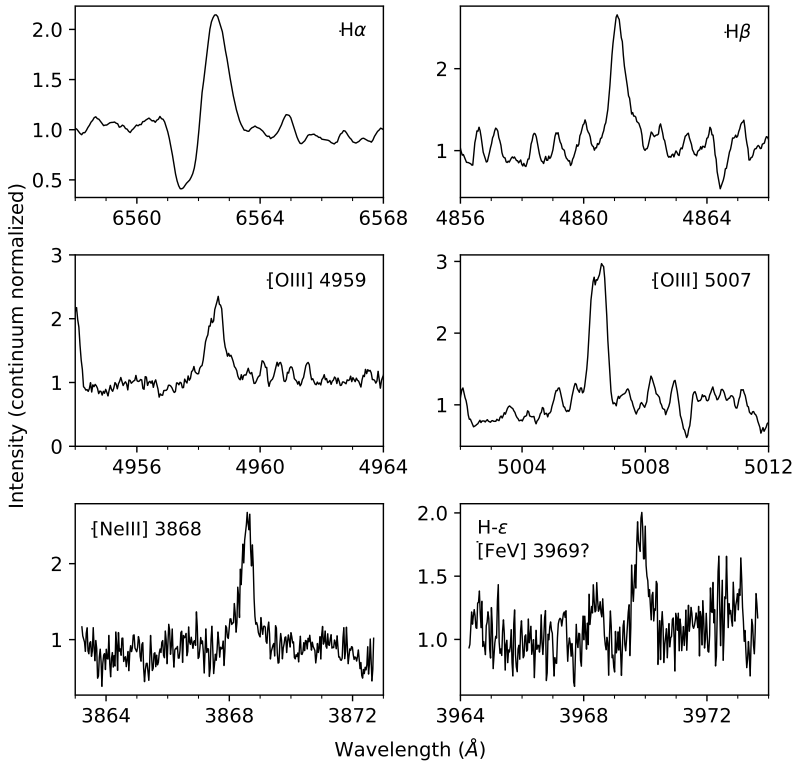

Figure 4.22: Emission lines seen in the high resolution spectrum of SU Lyn.

The Hα line shows a P Cygni profile which is relatively rare in symbiotics. Ivison et al. (1994) have presented multi-epoch high-resolution echelle spectroscopy of 35 symbiotics, of which 27 have double-peaked Hα profiles. Only in TX CVn, a deep P Cygni profile has been observed. They propose that the predominance of reversed profiles with the blue component stronger, which supports the idea that the majority of the structured Balmer lines arise from self-absorption by neutral gas in the cool companion's wind. Munari (2019) has shown six high-resolution Hα profiles of SU Lyn between October 2015 to December 2017 of which P Cygni profiles are seen on two epochs. Since P Cygni profiles arise in an accelerated region of the wind and also need large absorption column densities, we propose that there may be episodic phases of enhanced mass loss from the cool companion which manifest in P Cygni profiles. A consequence of the enhanced mass loss episodes would be corresponding increases in the accretion rate, causing enhancements in the UV luminosity. This speculative interpretation could explain the large UV variability seen in the star.

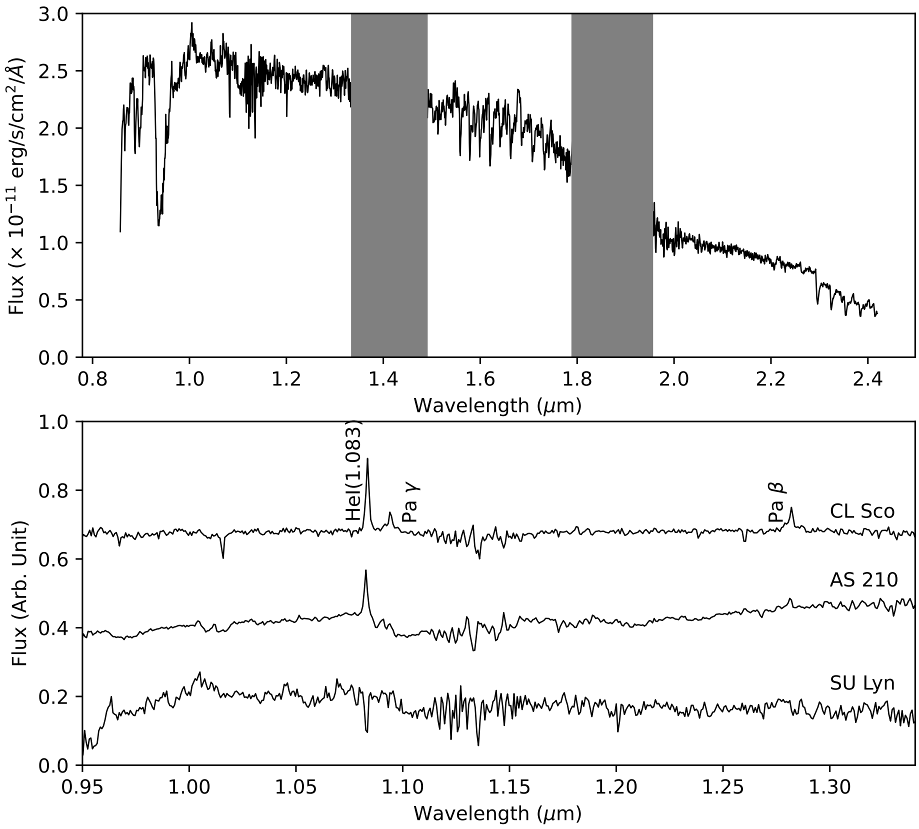

Figure 4.23: Top panel shows the NIR spectrum, which is devoid of emission lines but HeI 1.083 μm is seen in absorption. The bottom panel presents an expanded view of the J band, which shows no emission lines in contrast to two other symbiotic stars CL Sco and AS210 whose spectra were obtained at the same resolution. The spectrum has been anchored using the 2MASS H band flux (H = 1.92 magnitudes). The spectra are de-reddened.

The NIR spectrum showed in Fig. 4.23 (top panel) is dominated by the red giant; the spectrum is typical of a late M type star. Both first and second overtone bands of CO are strongly prominent in the H and K bands, respectively. No evidence of dust is seen in our data, consistent with the lack of an IR excess in its SED plotted using WISE, AKARI and IRAS data.

No evidence of emission lines is seen, consistent with the findings of the low-resolution optical spectra. For comparison, the new, unpublished spectra of two symbiotics CL Sco and AS 210, obtained from Mt. Abu, are plotted (bottom panel), showing the lines that may be expected to be seen. A puzzling feature is that HeI 1.083μm is seen in absorption. The fact that HeII lines are seen in emission (1640Å and perhaps 4686Å) whereas HeI is in absorption indicates a different site of origin for these lines. CL Sco has been classified as a low ionization symbiotic system (Kenyon & Webbink, 1984). Though its optical spectrum in outburst (Munari & Zwitter, 2002) shows a bright emission line typical of a symbiotic system, the IUE UV spectrum showed a very weak He II 1640Å, absence of N V 1239Å, and a modest C IV emission. Moreover, the He II 4686Å was not present in the optical spectrum recorded close to the epoch of IUE observations (Michalitsianos et al., 1982).

4.2.5 Summary: SU Lyn

To summarize, the UV spectrum presented here, complemented by optical and NIR spectra, provides direct and robust evidence that SU Lyn is a non-burning symbiotic star. The presence of emission lines in low-resolution optical spectra has been the traditional way to identify and discover symbiotics. But such a technique will fail in the case of SU Lyn-type of objects thereby underestimating the census of symbiotic systems in the galaxy. The number of known symbiotics stands at ∼400 at present but is rapidly expanding as a consequence of surveys of the Galactic Bulge and Plane (Munari (2019) and references therein). It is estimated that the total Galactic population of symbiotic stars is approximately a factor of 1000 more than the known number (Munari & Renzini, 1992). But this number may need to be substantially revised if SU Lyn type systems are included.

4.3 Chapter Conclusions

This chapter presents the observational studies of nova V 2891 Cyg and a suspected symbiotic system -SU Lyn, to establish the utility of MFOSC-P on PRL 1.2m telescope for various science programs of the observatory. These two studies form the science verification program of the newly developed MFOSC-P instrument. Nova V2891 Cyg has been studied for its long spectroscopic evolution from outburst phase to coronal phase. The observations were done in all modes of MFPSC-P of spectroscopy (R500, R1000, and R2000) and photometry (B, V, R, and I bands). The nova was observed for 13 months with MFOSC-P, in which Nova V-band magnitude varies between 15.3-18.8. During this period, we are able to even trace the faint continuum in R500 mode spectroscopy mode of MFOSC-P in late 2020 when its V-band magnitude was around ∼18 (with 3-5 SNR in 60 minutes of integration time). Nova V2891 Cyg was proved to be an extremely suitable astrophysical object for MFOSC-P as it turned out to be one of the slowest novae of recent times and traced its long evolution through multiple phases (e.g. fireball, nebular, coronal etc.) any nova evolution. Regular observations from MFOSC-P and from various other facilities were able to put together a complete picture of this transient evolution. These various observational signatures proved that this nova presents a rare case to study various shock-induced physical processes during the evolution of the nova, thereby making this study a significant one for the studies of novae.

The second science project was to explore the nature of a red-giant star-SU Lyn, which was suspected of harbouring a white dwarf, thereby making it a symbiotic system. SU Lyn was probed by regular monitoring with MFOSC-P and additional proposal-based observations from AstroSat and Himalayan Chandra (2m) Telescope of the Indian Institute of Astrophysics, Bengaluru. The slitless UV spectra of SU Lyn from the UVIT instrument on AstroSat were proved to be pivotal in firmly establishing the presence of accretion disk around the WD, thereby confirming its symbiotic nature.

Thus, MFOSC-P has been successfully utilized to study the physics of nova V2891 Cyg and suspected symbiotic SU Lyn. It has been regularly used on PRL 1.2m telescope for various other observational programs as well.

Content of this chapter have been published in the following journal:

1. ***Vipin Kumar***, *Mudit K. Srivastava, Dipankar P.K. Banerjee, C. E. Woodward, Ulisse Munari, Nye Evans, Vishal Joshi, Sergio Dallaporta, and Kim Page*, "Optical and near-infrared spectroscopy of Nova V2891 Cygni: evidence for shock-induced dust formation" (MNRAS, 510, 3, 4265-4283 (2022); doi:10.1093/mnras/stab3772)

2. ***Vipin Kumar***, *Mudit K. Srivastava, Dipankar P.K. Banerjee and Vishal Joshi*, "UV spectroscopy confirms SU Lyn to be a symbiotic star" (MNRAS Letters, 500, L12-L16 (2021); doi:10.1093/mnrasl/slaa159)

   Note: It is worth mentioning that this study was the first referred publication from UVIT spectroscopy data and was later selected as *ISRO story of the week*.

Chapter 5

Designs of spectro-polarimeters for PRL telescopes

We have discussed (Chapter-1, section-1.4 and 1.5) the necessity for the instrumentation that would offer observing capabilities beyond the regular "Faint Object Spectrograph and Camera" (FOSC) modes on the upcoming PRL 2.5m telescope. The requirements of various science cases then culminated in the form of the instrument named "Mt.Abu Faint Object Spectrograph and Camera - Echelle Polarimeter (M-FOSC-EP)". M-FOSC-EP was conceived to be a multi-mode two-channel instrument having the capabilities of a normal FOSC instrument like low-resolution spectroscopy and seeing limited imaging, in addition to the option for intermediate-resolution spectro-polarimetry. The FOSC mode of M-FOSC-EP was conceptualized along the lines of the MFOSC-Pathfinder instrument with two major differences 1.) electron-multiplying CCD (EMCCD) based camera was proposed to be used to enable the fast photometry requirements of the science cases that demand faster readout rates and 2.) Grisms were to be used in place of gratings. The spectro-polarimetry mode was conceptualized with a traditional half-wave plate plus Wollaston prism-based polarization measurement set-up in conjunction with an intermediate resolution echelle spectrometer.

While the development modalities of the FOSC module were known, thanks to the successful development of the MFOSC-Pathfinder instrument, a similar effort was planned for the echelle spectro-polarimeter mode as well. It was planned to develop a prototype spectro-polarimeter (later named - ProtoPol) using commercially available off-the-shelf optical elements to expedite its development period and efforts. It was envisaged that ProtoPol should have been developed by 2022. However, due to the COVID pandemic during 2020-2021, significant restrictions (administrative, financial, etc.) were placed, which hampered the original development timeline of ProtoPol development due to delays in the procurement process etc. Therefore, in this thesis, we only describe the design aspects of M-FOSC-EP and ProtoPol. We have successfully completed the optical designs of M-FOSC-EP and ProtoPol. Here we are describing the requirements, system designs, and optical designs of both instruments. We have also developed the preliminary mechanical system design (CAD model) for the ProtoPol. A full-fledged mechanical system was later developed by the engineering team of ProtoPol. At the time of writing this thesis, the mechanical design of ProtoPol was completed, most of the optical components were procured, and its various mechanical parts were being fabricated.

M-FOSC-EP is being developed as a facility instrument and would cater to the general requirements of the Astronomy and Astrophysics (A&A) PRL division for imaging and spectroscopy in visible wavebands. It should be mentioned that the optical design of the M-FOSC-EP instrument, described in this chapter, has been discussed and approved by a national-level Technical Evaluation Committee (TEC) for the M-FOSC-EP instrument (constituted by Director, Physical Research Laboratory, Ahmedabad) for its realization. A manuscript describing the designs of M-FOSC-EP and ProtoPol is currently in preparation to be submitted to an appropriate journal.

In this chapter, the optical design and analyses of M-FOSC-EP and its prototype instrument will be discussed. In the first section, the optical designs of various sub-modules of M-FOSC-EP - the Low-Resolution Arm (LRA), Polarimeter module, and the Echelle spectrograph module, will be discussed, along with their optical performance and various design analyses. Several other aspects of the optical design like efficiency, resolutions, cross-talk of orders in Echelle spectroscopy, etc., will also be discussed for this instrument. In the chapter's second part, the optical design of ProtoPol will be described along with its expected performance. A preliminary opto-mechanical design of ProtoPol will also be discussed.

5.1 Mt.Abu Faint Object Spectrograph and Camera - Echelle Polarimeter (M-FOSC-EP): Instrument requirements & system design

There are several science cases (see section-1.5) for objects like Symbiotics, M-Dwarfs, AGNs, Novae and Super-Novae, etc., that would greatly benefit from having a relatively higher resolution spectroscopy mode (resolutions $\sim$10000-15000) and having a spectro-polarimetry capability on the telescope. The studies of spectral line profile variability to probe symbiotics morphology and kinematics, spectro-polarimetry to trace the surrounding environments of obscure objects (e.g., novae, supernovae, symbiotics, etc.), spectroscopic studies of M-dwarfs, etc. are some of the key science goals that require the intermediate resolution spectroscopy/spectro-polarimetry capabilities as well, in addition to few traditional modes of FOSC instrument (i.e., low-resolution spectroscopy with seeing limited imaging). Some of these goals would also benefit if the choice of detector system also provides fast, low-noise read-out for fast photometric timing studies (time resolution $\sim$ 1 second). These science requirements translate into the following instrument specifications:

1. To investigate the time variability of various types of stars (e.g., symbiotics, white dwarf binaries, M dwarf and associated magnetic structures, etc.) both in their line profile shape as well as in the degree of polarization, the required polarization accuracy (δP) of the instrument is to be around 0.1-0.2%.

2. Full-width-at-half-maximum (FWHM) of prominent emission lines (e.g. Hα) of the above science case are typical $\sim$200 kms^{-1}. Thus to map out any variability in the line shape, the velocity resolution should be around $\sim$20kms^{-1}, i.e., at H alpha wavelength, the required spectral resolution should be $\sim$15000.

3. A lot of science cases (e.g., spectroscopy of novae, supernovae, etc.) demand the traditional FOSC modes of low-resolution spectroscopy (R$\sim$500) over the full visible band ($\sim$3900-9500Å) and seeing limited imaging in various filters.

4. There are special science cases like short-duration flickering observations of symbiotic systems to measure fast-time photometric variations of a few seconds. At high-speed read-out, the read-out noise typically dominates and would be a limiting factor for such fast photometry applications, which should be limited by photon noise only. Thus, the requirement of low noise along with fast read-out would demand the use of an EMCCD detector system.

The first two requirements were combined in the form of an intermediate-resolution Echelle spectrometer, while the other two requirements were coupled in the form of a low-resolution FOSC module equipped with an EMCCD detector system. EMCCDs contain an electron multiplier gain register that enhances received signals without increasing read noise. However, EMCCDs cause additional noise when not in photon counting mode for low-level photon signals, and thus, in such cases, CCD might be a good option compared to EMCCD (see more detail about noise in CCDs and EMCCDs in Coughlin et al. (2019); Tulloch & Dhillon (2011)). However, there are important science cases related to high-precision photometry on shorter timescales (e.g. flickering studies of symbiotic systems or suspected symbiotic candidates as discussed in point (c) of Sec. 1.5.1) where EMCCD-based detector system is highly desirable (Smith et al., 2008; Zamanov et al., 2021).

M-FOSC-EP was, thus, conceptualized by combining the functionalities of these two modules within a single instrument's envelope. A common collimator optics was thought to be used for both of the modules, and a movable fold mirror was to be used to select any of the modules during observations.

5.2 The Optical design of M-FOSC-EP

5.2.1 System Design Overview

FOSC series of instruments are generally designed for low to medium resolution spectroscopy (R $\sim$ $\lambda/\delta\lambda$ $\sim$500 to 3000) along with seeing limited imaging. Additional polarization components were later included in some versions for imaging polarimetry purposes. Inclusion of intermediate resolution (R$\sim$10000-15000) modes and provision for spectro-polarimetry have not been traditionally done in such instruments due to optical design constraints posed by requirements of low/medium resolution modes. Thus, a low-resolution arm (LRA) for the FOSC module was added to the basic optical design of the intermediate resolution spectro-polarimeter to form the complete M-FOSC-EP optical chain. M-FOSC-EP would have the imaging and low resolution (resolution $\sim$500-800) capabilities of a typical FOSC instrument and the functionalities of an intermediate resolution spectro-polarimeter (resolutions $\sim$15000). The low-resolution arm (LRA) would incorporate an EMCCD detector system for fast timing applications. The instrument schematic and baseline specification are shown in Fig. 5.1 and Table 5.1, respectively. The layout has been designed with a modular optical system. A common collimator optics is coupled with two separate optical arms having two separate detector systems (1.) for low-resolution spectroscopy and band-limited imaging and (2.) for intermediate resolution spectro-polarimetric mode. Either of the two modes can be selected by moving a fold mirror into the beam path after the collimator.

The optical design of M-FOSC-EP is thus made up of three major optical modules: (1.) the low-resolution arm (LRA) for the FOSC mode, (2.) a polarimeter section, and (3.) an echelle spectrometer. The first two optical modules use common collimator optics. A motorized fold mirror will be used after the collimator to feed the beam either towards the camera optics of LRA

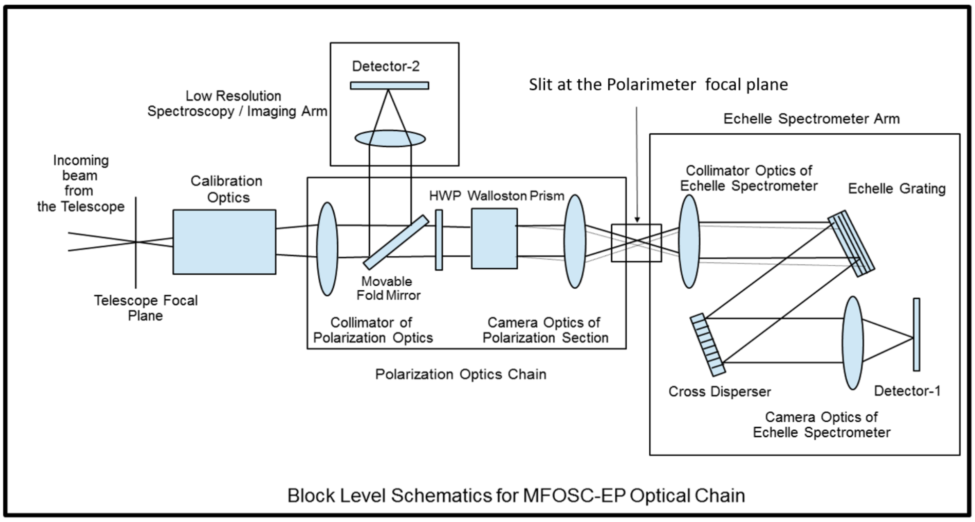

Figure 5.1: Schematics of M-FOSC-EP system design

or into the polarimeter camera optics. The optical design of these individual modules and their performances are discussed below. The optical system has been designed using ZEMAX-optical design software. It is to be noted that the optical design of M-FOSC-EP has been optimized along with the ZEMAX model of the 2.5m PRL telescope.

Table 5.1: Baseline specifications of M-FOSC-EP

Instrument Capabilities	Seeing limited imaging in SDSS standard filters, Low-resolution spectroscopy, Intermediate-resolution Spectro-polarimetry
Working reliability	With upcoming PRL 2.5m, f/8 telescope at Mt. Abu, India
Field of View	$\sim$5.5 $\times$ 5.5 arc-minute square for imaging
Wavelength Range	390-990 nm
Detectors	2K$\times$2K CCD for spectro-polarimetry 1K$\times$1K EMCCD CCD for Low Resolution Arm (LRA)
Resolutions ($\sim \lambda/\delta\lambda$)	$\sim$500-800 for LRA, $\sim$15000 for spectro-polarimetry for 1 arc-second slit width
Polarization Accuracy	$\sim$0.1-0.2% in nearly 4000 seconds of integration for V$\sim$11.5 magnitude

5.2.2 Low Resolution Arm (LRA) of M-FOSC-EP: Optical design, Performance, & Efficiency

5.2.2.1 LRA: The optical design

The instrument's low-resolution arm (LRA) is used for filter-based imaging and spectroscopy in visible waveband (∼390-990 nm) on an off-the-shelf 1024×1024 EM CCD detector. It provides seeing-limited imaging in astronomy standard SDSS filters with ∼5.5 X 5.5 arc-minute square field of view. The spectroscopy mode is achieved with two grisms with resolutions ∼500-800 around 540 and 820 nm with a 1.0 arc-second slit width. The f/8 beam from the telescope is mapped onto a 1K×1K detector (with 13-micron a side pixel size) through collimator optics (designed with four optical elements: two singlet and two achromat doublet lenses) and camera optics (designed with three singlet and two achromat doublet lenses). The camera optics provide an f/3.325 beam onto the detector system, thereby providing a de-magnification of ×0.416. The LRA design layout is shown in Fig. 5.2. Though the optics image quality is optimized for 390-990 nm, the spectral range of one of the grism would start from 380nm. This was done to include a very strong cometary band at 387nm and several others closer to 385nm.

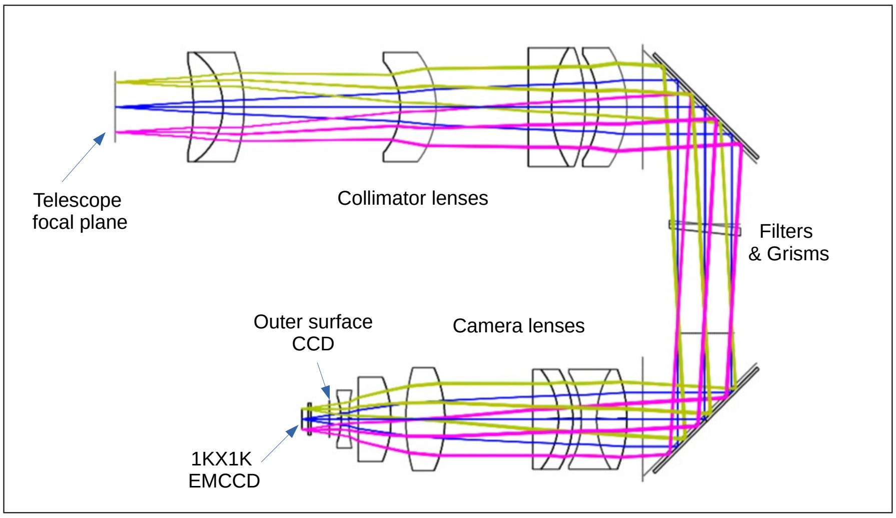

Figure 5.2: Optical design of the low-resolution-arm (diameter of all lenses are oversized by 8mm and more for mounting purposes). Ray configuration are shown for 5.52 × 5.52 arc-minute square field.

Table 5.2: Specification of low resolution arm of M-FOSC-EP

Parameters	**Values**
Imaging Wavelength range	390-990 nm
Imaging field of view	~5.52 × 5.52 arc-minute square
Imaging pixel scale	3.1 pixels/arc-sec
Imaging mode quality requirement	80% EE diameter should be within 1 pixel (13 μm)
Magnification in LRA mode	0.416
Collimator focal length	275.8 mm @500nm
Camera focal length	114.8 mm @500nm
Pupil distance from last lens of Collimator	205mm
Camera f/#	3.325
CCD Detector	1K X 1K EMCCD with 13μm pixel size
Broad-band filters	SDSS's ugirz filters
Narrow-band filters	Hα, Hβ, S II, O III, N II (To be decided)
Spectral coverage of grisms	380-990 nm using two different grisms
Pupil diameter	~ 35mm

The specifications and the optical design parameters of LRA are given in Table 5.2. The optical design criteria were the 80% encircled energy (EE80) diameter was to be preferably within 1 pixel of the EMCCD detector for nominal performance (before tolerance analysis).

The ZEMAX optical design prescription data are given in Table 5.3. The glasses are chosen from the optical glasses from the SCHOTT and OHARA glass catalogs. The physical diameters of the lenses are increased by 8mm for mounting purposes. Two fold mirrors are added to the design, and broad-band filters and grisms would be placed in-between these two mirrors, with pupils forming at the grism's location. A set of narrowband filters are also being considered, and they would be kept in front of the telescope focal plane, in the path of the converging beam.

5.2.2.2 LRA performance: Imaging mode

a) Spot Diagram & RMS spot radius

Different tools and techniques are used to evaluate the optical design performance. One of the tools used to evaluate the performance is the spot diagram,

Table 5.3: ZEMAX lens surface data for LRA collimator and LRA camera design. All dimensions are given in mm. CA: Clear aperture (required for 5.52'X5.52' field), Diameter: designed Lens diameter

Comment	Radius	Thickness	Glass	Catalogue	CA	Diameter
COLLIMATOR						
Doublet1	-120.8	19	S-NBH52V	OHARA	51.65	58
	-42.5	13.5	S-TIL26	OHARA	54.70	70
	-104.7	100			57.85	70
Singlet1	-45.1	23	S-BAL12	OHARA	52.16	58
	-57.3	59.1			61.75	70
Doublet2	Infinity	14.9	PBL6Y	OHARA	62.42	76
	72.2	21.5	S-FPL53	OHARA	62.57	76
	-105.3	8.5			63.19	76
Singlet2	-61.8	18.2	S-BAM4	OHARA	62.29	68
	-68.5	10			67.81	76
CAMERA						
Doublet1	86.2	19.4	S-FPL53	OHARA	55.94	64
	-60.7	9.7	S-FSL5Y	OHARA	55.15	64
	59	5.5			53.83	60
Doublet2	62.1	9.2	N-BASF64	SCHOTT	56.52	64
	50.8	16.5	S-FPL53	OHARA	54.60	64
	Infinity	56.3			54.83	64
Singlet1	82.2	25	S-FPL55	OHARA	57.29	66
	-126.8	9.5			53.91	66
Singlet2	68.9	21	S-LAH58	OHARA	45.64	54
	Infinity	6			35.38	54
Singlet3	-91.8	5	S-LAH60	OHARA	28.96	37
	44.8	7.5			25.53	29.6

showing the performance of the optics pictorially. The spot diagrams show the projected beam points for different fields and wavelengths on an image plane of an imaging system. The spot diagram is simply an image produced by the optical system of a point source at the object plane. The spot diagram helps to understand the aberrations present in the design and thus to optimize the aberrations. The different fields used to optimize the optics are shown in Fig. 5.3.

The spot diagrams for LRA imaging mode are shown in Fig. 5.4 & Fig. 5.5 for 400-850nm & 390-1000nm, respectively. RMS spot radius/diameter of these spot diagrams is the root mean square radius/diameter determined by considering the centroid of the spot diagram as the reference. It gives a measure of the spread of rays from a single field point on the image plane, including the aberrations. The values of spot diameter for various field points for different

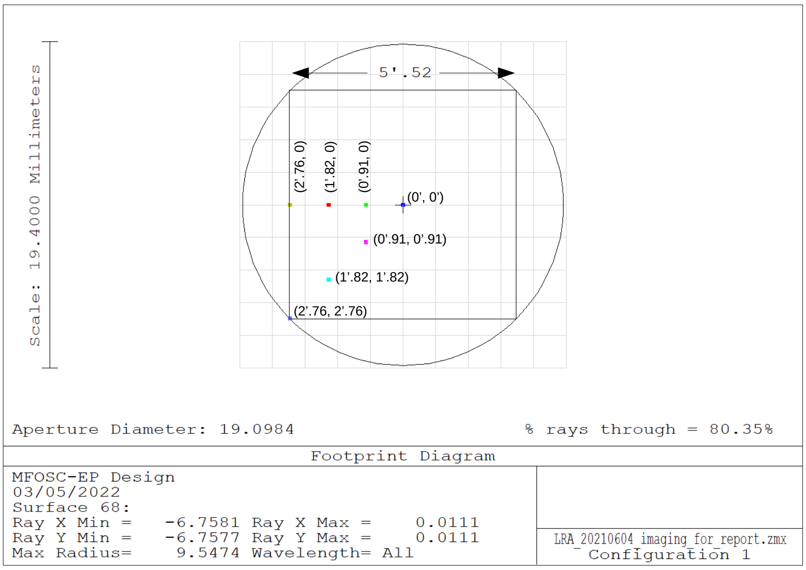

Figure 5.3: The footprint diagram showing all field points covering the field of view of 5.52×5.52 arc-min^2.

wavelengths are given in Table 5.4.

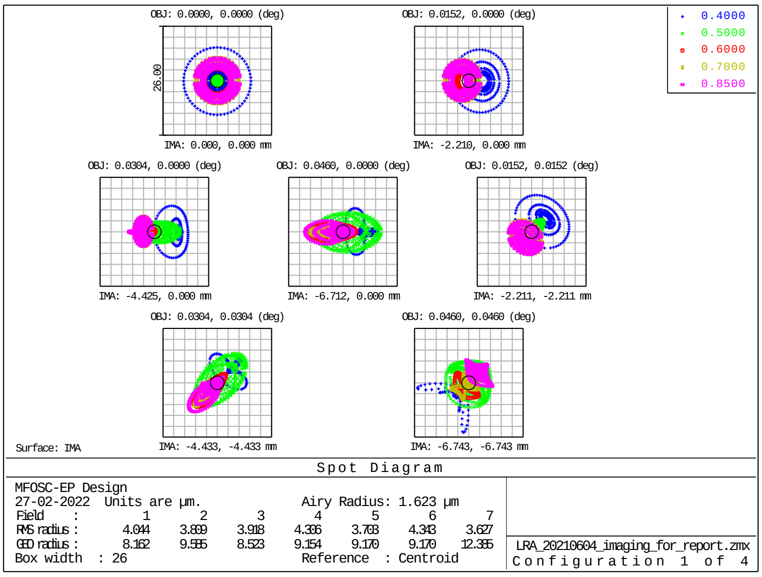

Figure 5.4: Spot diagrams from the LRA imaging modes (0.4-0.85 μm). The box size is 2 pixels (pixel size: 13μm). (0.046,0.046 degrees= 2.76,2.76 arc-minutes).

b) Diffraction Encircled Energy

Encircled energy measures the concentration of energy in an optical image and is also an essential parameter for the characterization of any optical imaging system. It is defined as the fraction of the total integrated flux in the given circle

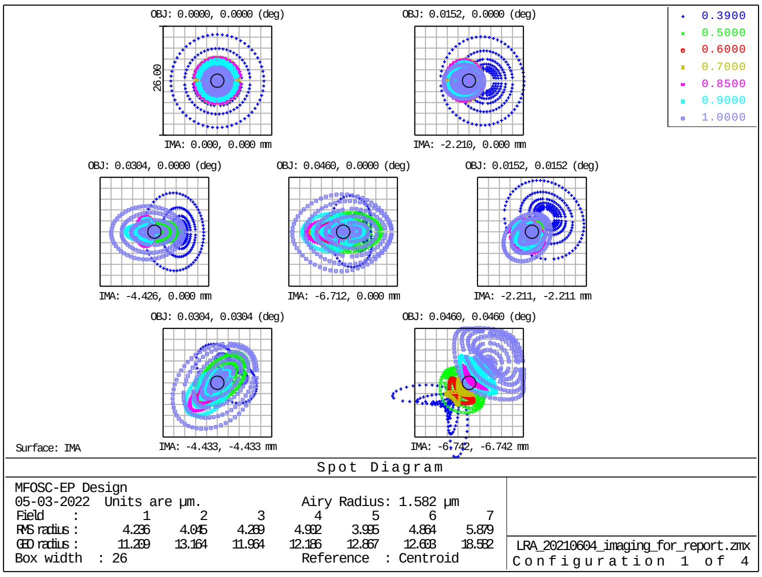

Figure 5.5: Spot diagrams for LRA imaging modes (0.39-1.0 μm). The box size is 2 pixels (pixel size: 13μm). (0.046,0.046 degrees= 2.76,2.76 arc-minutes).

Table 5.4: RMS diameters for imaging mode of LRA (0.39-1.0 μm). Mentioned dimeters are in microns.

Field(deg.,deg.) (arc-min,arc-min)/ Wavelength(μm)	(0,0)	(0.0152,0) (0.91,0)	(0.0304,0) (1.82,0)	(0.046,0) (2.76,0)	(0.0152, 0.0152) (0.91,0.91)	(0.0304, 0.0304) (1.82,1.82)	(0.046, 0.046) (2.76,2.76)
0.39	13.67	12.26	9.16	6.96	10.94	6.96	7.64
0.4	9.40	8.02	5.24	4.58	6.74	4.40	5.02
0.5	1.40	1.58	5.76	10.02	3.08	9.60	8.38
0.6	6.78	5.04	2.71	5.63	3.62	5.26	4.29
0.7	10.22	8.38	4.46	3.87	6.74	3.76	3.56
0.85	8.81	7.04	4.09	5.68	5.59	5.38	4.26
0.9	7.01	5.46	4.42	7.69	4.46	7.25	5.91
1.0	4.73	5.52	9.56	14.39	6.83	13.76	12.39
0.4-0.85	7.98	7.54	7.79	8.52	7.36	8.60	7.14
0.39-0.9	8.90	8.63	8.85	8.85	8.50	9.06	9.23

of specified radius of the point spread function (PSF).

The encircled energy curves for LRA are shown in Fig. 5.6 and Fig. 5.7 for different field points (showing by different colours) and for different wavelength ranges. The black colour curve represents the diffraction-limited performance. The values of 80% encircled energy (EE80) diameters are given in Tables 5.5 for the different fields and wavelengths. The EE80 diameters are close to 1 pixel for all the wavelengths and fields.

c) Field curvature Fig. 5.8 shows the field curvature & distortion aberrations of the LRA optical chain. Field curvature causes the imaging plane to be curved,

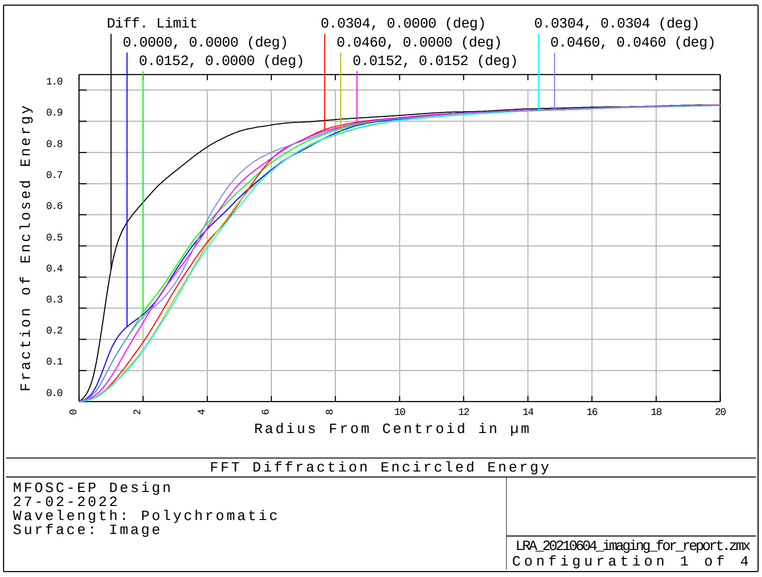

Figure 5.6: Encircled energy diagram for different fields in Imaging mode (For 5.52 X 5.52 arc-minute square field of view and for 0.4-0.85 μm wavelength range).

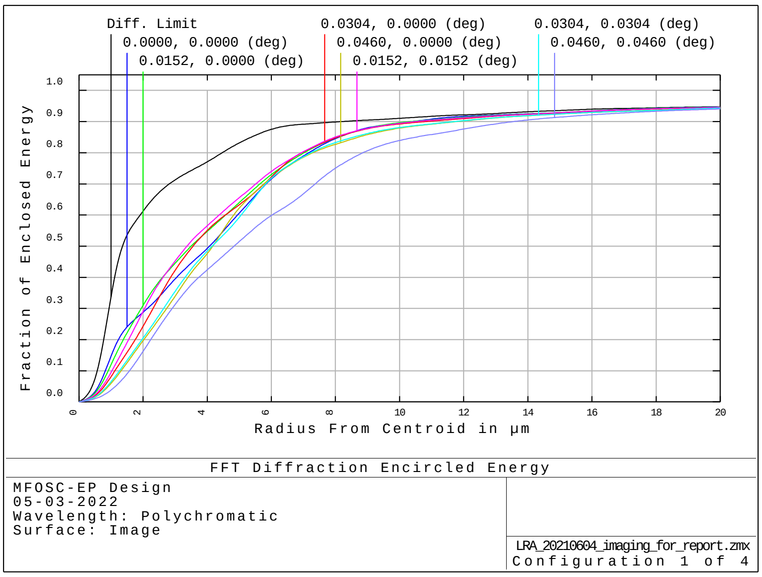

Figure 5.7: Encircled energy diagram for different fields in Imaging mode (For 5.52 X 5.52 arc-minute square field of view and for 0.39-1.0 μm wavelength range).

and thus the sharpest image is formed on a curved surface. It occurs due to the power difference for rays coming from off-axis fields. On the other side, distortion refers to the deformation of an image at the imaging plane. It occurs due to the dependence of linear magnification on distance from the optical axis. In the LRA module, the values of the field curvature and distortion for all the wavelengths and fields of the instrument were found to be within $\sim$0.15 mm and $\sim$1.1%,

Table 5.5: 80% encircled energy diameters for imaging mode of LRA (0.39-1.0 μm). Mentioned dimeters are in microns.

Field(deg.,deg.) (arc-min,arc-min)/ Wavelength(μm)	(0,0)	(0.0152,0) (0.91,0)	(0.0304,0) (1.82,0)	(0.046,0) (2.76,0)	(0.0152, 0.0152) (0.91,0.91)	(0.0304, 0.0304) (1.82,1.82)	(0.046, 0.046) (2.76,2.76)
0.39	15.44	13.78	10.40	7.54	12.28	7.78	9.02
0.4	10.88	9.36	6.08	7.00	7.72	6.80	6.98
0.5	6.06	6.22	9.98	14.74	7.62	14.34	12.94
0.6	11.50	10.52	7.66	10.52	9.44	10.08	9.44
0.7	16.24	13.96	11.30	9.28	12.86	9.06	9.06
0.85	16.14	15.18	11.34	11.74	14.36	11.30	11.00
0.9	15.90	14.90	11.38	14.24	12.78	13.38	12.92
1.0	12.00	11.91	14.58	19.04	12.29	18.28	18.16
0.4-0.85	13.68	12.96	12.48	13.60	12.53	13.56	11.98
0.39-0.9	14.26	13.92	13.42	13.36	13.66	13.40	14.53

respectively.

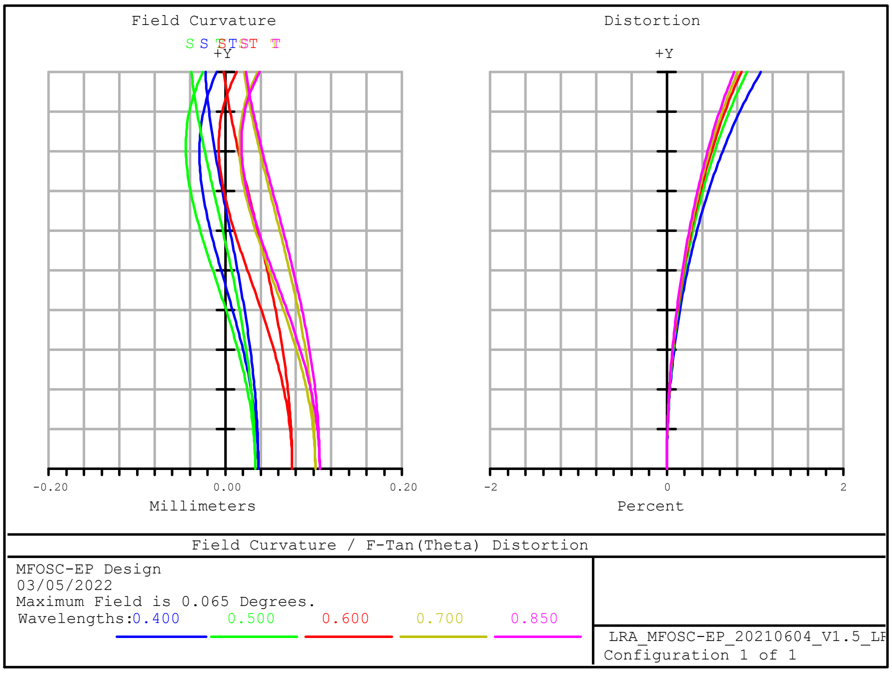

Figure 5.8: Plots showing the field curvature and distortion values for LRA imaging mode.

5.2.2.3 LRA - Spectroscopy modes : Design and performances

LRA employs two grisms to cover the full spectral range of 390-990nm. This is a major departure from MFOSC-Pathfinder instrument, where gratings were used. Below we first discuss the basic theoretical approach for grism design and later, we shall describe the design and performance of the spectroscopy mode of LRA.

Grism: Theoretical perspectives

The grisms are the combination of transmission grating and prism and thus have the dispersive properties of both the dispersive elements. The chosen central wavelength shows no deviation during dispersion. The major advantage of the grisms is that the same camera optics can be used for both imaging and spectroscopy. Dispersive elements are generally kept in the collimated space, and the best place to insert the grism is the pupil location of the optical system.

Basic parameters playing a role in designing the grisms are groove spacing of the grating (d), apex angle ($\theta+\delta$), and refractive index of the prism ($n(\lambda)$), etc. They are shown in Fig. 5.9. The grism equation can be written as (Deen et al., 2017),

$$\frac{m\lambda}{d} = n(\lambda)\sin\left(\theta + \delta - \sin^{-1}\left(\frac{\sin(\alpha)}{n(\lambda)}\right)\right) - \sin\beta \tag{5.1}$$

where m is the working order of the grating, α is the entrance angle of the beam from the front surface normal, β is the exit angle of the beam for a given wavelength λ from the grating surface normal, and $n(\lambda)$ is the refractive index of the prism for wavelength λ. The relation between the apex angle of the grism, the beam entrance, and exit angles for an un-deviated beam is given as follows (using geometry in Fig. 5.9):

$$\beta = \theta + \delta - \alpha \tag{5.2}$$

If the incoming beam is parallel to the prism's base (i.e., $\alpha = \theta$), then for an undeviating beam, $\beta = \delta$. The resolution ($R = \frac{\lambda}{\delta\lambda}$) would be given as (Eversberg

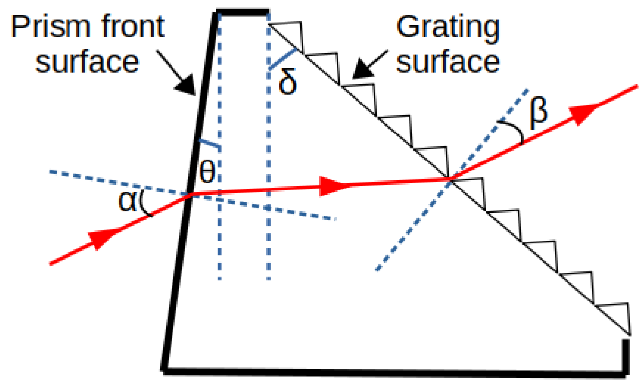

Figure 5.9: Figure shows the grism diagram with various angles. Grooves are in the perpendicular direction to the plane of the paper.

& Vollmann, 2015)):

$$R = \frac{f_{cam}}{d_D} \frac{n\left(\lambda\right)\sin\left(\theta + \delta - \sin^{-1}\left(\frac{\sin\alpha}{n(\lambda)}\right)\right) - \sin\beta}{cos\beta} \tag{5.3}$$

where f_{cam} is the focal length of the camera optics of the spectrograph, and d_D is the slit size at the detector plane. Therefore using the equations 5.1 and 5.3, one can determine the groove density of the grating and the grating tilt (δ) for a given set of other parameters.

LRA Grisms : Spectroscopic performance

Two grisms (named R500 and R800) have been designed within the LRA optical chain to cover the visible waveband of 380-990nm with a pixel scale of ∼3.3Å per pixel. Thus, on a 1K × 1K EMCCD, each grism would cover nearly ∼335nm in a single snapshot. one grism (R500) would span from 380-710nm, while the other grism (R800) would cover the redder part of the spectrum from ∼650-990nm. The initial parameters of a transmission grating and prism apex angle are estimated with the help of equations 5.1 and 5.3. Prism material were chosen from the grism used in another similar instrument (e.g. ALFOSC instrument on Nordic Optical telescope [1]) and gratings parameters were selected based

[1]http://www.not.iac.es/instruments/alfosc/grisms/

on the available gratings from the catalogs of commercial grating manufacturers (e.g. M/S Newport/Richardson Grating catalog[2]). A tilt angle ($\theta = 6°$) is given to the prism front surface to avoid the multiple reflections in the optical system, which may cause the ghost images at the detector plane. An order sorting filter would be required to avoid the second-order contamination in the R800 grism, e.g. SCHOTT RG-610 (M/S Edmund Optics part number#66-094[3] with cut-off wavelength at 610nm).

Table 5.6: Specification of the two grisms in low resolution arm of M-FOSC-EP.

Grism Name	Grating specification (Groove density, Blazed wavelength)	Used prism material (Catalog)	Wavelength coverage	Prism Apex Angle in degree ($\theta + \delta$)
R500	300lp/mm, 490nm	LF5 (SCHOTT)	380-710nm ∼3.2Å/pixel	16 (6+10)
R800	300lp/mm, 725nm	N-SF66(SCHOTT)	650-990nm ∼3.3Å/pixel	15.9 (6+9.9)

The grisms specifications are given in Table 5.6. The spot diagrams for the spectroscopy modes are shown in Fig. 5.10 and 5.11. The corresponding EE80 diameters and RMS diameters are given in Table 5.7. The 80% Encircled Energy (EE80) diameters are found to be close to 1 pixel for all the configurations.

5.2.2.4 LRA: Tolerance analysis

Tolerance analysis is a necessary and the most critical aspect of realizing the optical system. Since the optical components or opto-mechanical sub-assemblies can only be developed within their manufacturing limits, the effects of such error on the performance of the optical system must be evaluated during the design phase. Tolerance analysis is also important to determine if any optical elements require special attention in their mounting, alignment, etc. This, in turn, would impact the instrument budget as well. There are various types of tolerance factors which would be determined by (1.) from the optics manufacturer's perspective such as radius of curvature & thickness of the lens, refractive index & abbe

[2]https://www.newport.com/b/richardson-gratings
[3]https://www.edmundoptics.in/p/rg-610-50mm-dia-longpass-filter/20626/

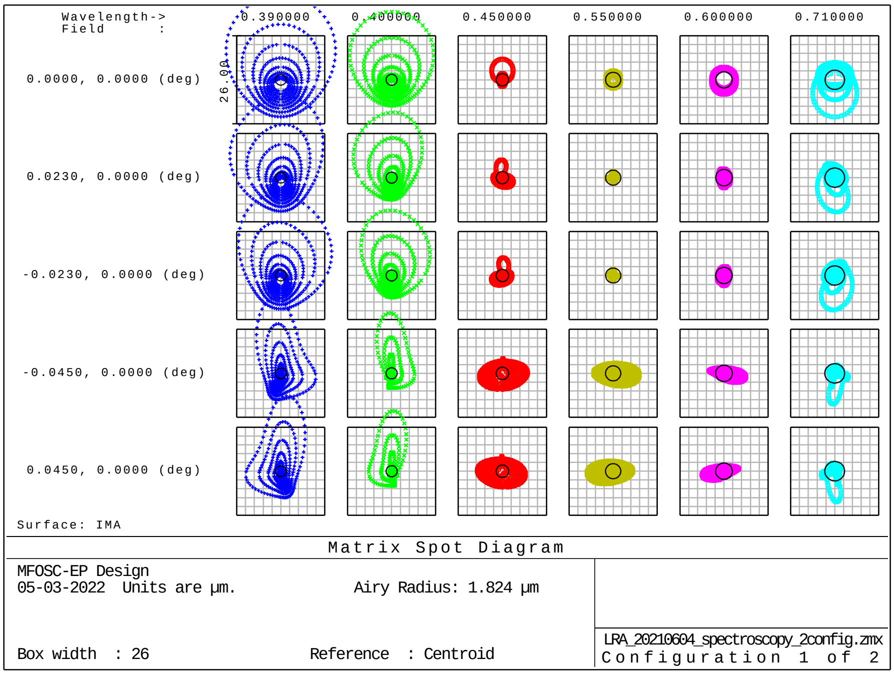

Figure 5.10: Spot diagram of the LRA with R500 grism. On-axis and off-axis ($\pm$2.7 arc-minutes along the slit) points are shown. The box size is 2 pixels (pixel size: 13μm). This mode is not optimized for 0.38μm, though it is covered on the detector.

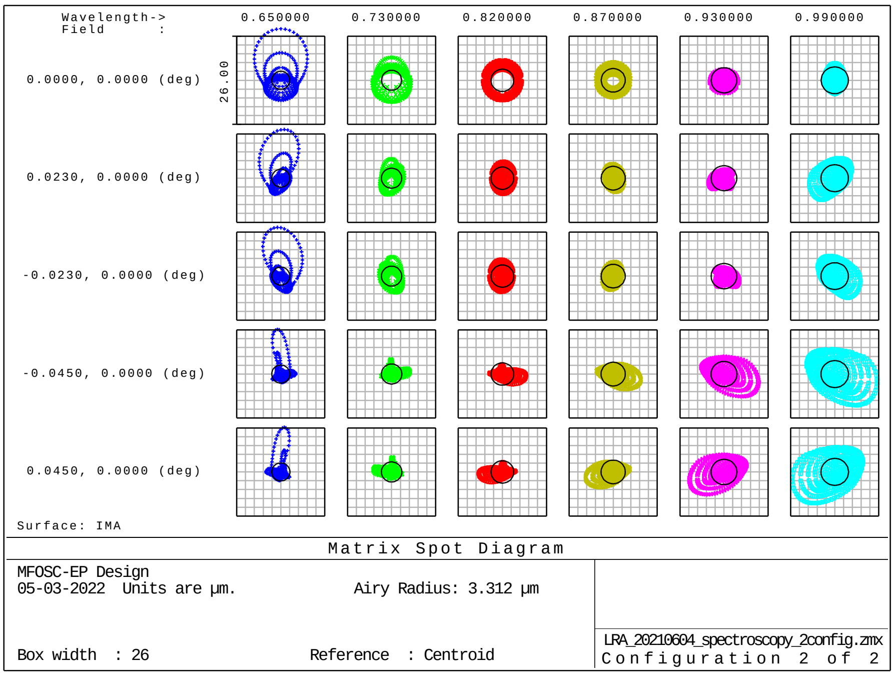

Figure 5.11: Spot diagram of the LRA with R800 grism. On-axis and off-axis ($\pm$2.7 arc-minutes along the slit) points are shown. The box size is 2 pixels (pixel size: 13μm).

number of lens material, de-centering & tilt in surfaces of lenses etc. and, (2.) from the opto-mechanical assembly perspective, e.g., spacing between lenses, de-centering & tilt of lenses with respect to the optical axis etc.

Table 5.7: 80% Encircled Energy & RMS diameters for both spectroscopy modes (R500 and R800) of LRA.

Field(deg.,deg.) (arc-min,arc-min)/ Wavelength(μm)	80% Encircled Energy Diameter (μm)				RMS diameter (μm)			
	(0,0) (0,0)	(0.0152,0) (0.91,0)	(0.0304,0) (1.82,0)	(0.045,0) (2.7,0)	(0,0) (0,0)	(0.0152,0) (0.91,0)	(0.0304,0) (1.82,0)	(0.045,0) (2.7,0)
R500								
0.390	20.52	19.16	16	13	18.14	16.98	14.34	11.66
0.400	14.48	12.86	9.84	7.84	13.04	11.92	9.56	7.74
0.460	5.58	6.9	10.6	14.44	2.04	2.60	6.22	10.06
0.520	7.04	6.28	9.36	14.08	2.30	1.54	5.08	9.42
0.600	11.08	10.18	7.64	10.42	6.38	4.78	2.98	5.68
0.680	13.64	12.4	9.6	8.84	9.06	7.64	5.00	4.40
0.710	14.38	13.1	10.5	9.14	9.73	8.34	5.70	4.66
R800								
0.650	13.34	12.02	9.04	9.04	9.64	8.30	5.92	5.38
0.730	16.36	14.3	11.48	9.82	10.22	8.46	4.92	4.40
0.800	16.86	15.08	12.4	10.72	10.12	8.30	4.78	5.06
0.870	15.56	14.66	11.04	12.9	7.44	5.88	4.30	6.90
0.950	11.88	11.7	14.4	17.2	4.12	4.40	7.30	10.58
0.990	12.74	13.88	17.32	20.08	5.42	6.49	9.89	12.96

ZEMAX (the optical design software) allows the sensitivity and inverse-sensitivity analyses to determine the error limits to be placed on each of the parameters as mentioned earlier to achieve the desired performance - in terms of any quantitative criteria such as RMS spot-diameters etc. ZEMAX also allows, in the form of the Monte-Carlo simulations, random combinations of such error perturbations to be incorporated into the given optical system simultaneously. A number of such random optical systems are then generated, and their statistical performance is then taken as the success criteria of the given optical system.

Table 5.8: Tolerance parameters for LRA imaging and spectroscopy.

Criteria	Tolerance (Imaging)	Tolerance (Spectroscopy)
Surface tolerances		
Thickness(mm)	±0.05	±0.05
Radius (fr)	3	3
Decentre X,Y(mm)	±0.015	±0.015
Tilt X,Y(deg)	±0.0170(1')	±0.0170(1')
Irregularity (fr)	1	1
Index	±0.0001	±0.0001
Abbe No. (%)	±0.5	±0.5
Element tolerances		
Decenter X,Y (mm)	±0.05	±0.05 for Collimator, ±0.03 for Camera
Tilt X,Y (deg)	±0.05(3')	±0.05(3') for Collimator, ±0.03(1.8') for Camera
Distance b/w two lenses (mm)	±0.05	±0.05

Here, we are presenting only the final Monte-Carlo simulation results for the LRA module. In these simulations, the back focal length was chosen as the compensator and RMS spot-radius as the performance evaluation criteria. The tolerance analysis for imaging and spectroscopy modes of LRA is done within the range of precision optics parameters offered by commercial optics manufacturers. These values are given in Table 5.8.

The analysis also included the temperature/pressure[4] variation at Mt Abu throughout the observing season (October-June). The tolerance analysis was done for three cases to explore the effects of temperature variation on the designed performance: (1.) at a fixed temperature value of 20 degrees C, (2.) for a temperature variation from 5-25 degrees C, and (3.) for a temperature variation from 0-30 degrees C. The results (RMS diameters) for 10000 Monte-Carlo simulations are shown in Tables 5.9, 5.10 and 5.11. For all the configurations, the RMS spot diameters were found to be ∼1 pixel with 90% confidence limit

[4] https://keisan.casio.com/exec/system/1224579725

and within ∼1.5 pixels with 98% confidence limit. The tolerance analysis results confirm that the designed performance would be achieved with the appropriate position of the CCD detector as the compensator.

Table 5.9: Tolerance analysis for imaging mode in 390-1000nm wavelength range and for 5.52'X5.52' field. The distance from CCD to the last lens surface is used as compensator.

Wave-length (nm)	Nominal Criterian RMS dia	Temperature: 20°C Pressure: 1 atm Compensator: -0.33/+0.35 mm				Temperature: 5-25°C Pressure: 0.8167-0.8277 atm Compensator: -0.36/+0.28 mm				Temperature: 0-30°C Pressure: 0.8138-0.8302 atm Compensator: -0.36/+0.28 mm			
		98%	90%	Mean	σ	98%	90%	Mean	σ	98%	90%	Mean	σ
390	8.23	21.62	16.86	11.92	3.56	21.05	16.4	11.69	3.46	21.09	16.49	11.68	3.49
400	5.19	19.50	14.82	9.96	3.54	19.36	14.84	9.86	3.55	19.29	14.67	9.85	3.54
500	6.31	20.12	15.37	9.86	3.94	21.05	15.92	10.17	4.1	20.67	16.03	10.17	4.11
600	4.66	17.3	13.32	8.97	3.14	17.53	13.42	9.02	3.19	17.59	13.44	9.05	3.19
700	6.13	17.14	13.51	9.78	2.71	17.27	13.51	9.73	2.74	17.12	13.49	9.74	2.71
800	6.26	17.11	13.49	9.88	2.66	16.82	13.36	9.78	2.62	17.15	13.61	9.87	2.69
900	5.83	17.24	13.54	9.50	2.91	17.70	13.77	9.66	2.97	17.92	13.87	9.68	3.03
950	6.75	18.57	14.37	9.90	3.25	19.46	15	10.25	3.44	19.47	15.07	10.27	3.44
1000	8.94	21.31	16.84	11.47	3.82	21.69	17.44	11.81	3.92	21.61	17.21	11.82	3.86

Table 5.10: Tolerance analysis for spectroscopy in R500 mode (Blue: 380-710nm) for 5.52 arc-min field along the slit. The distance from CCD to the last lens surface is used as a compensator.

Wave-length (nm)	Nominal Criterian RMS dia	Temperature: 20°C Pressure: 1 atm Compensator: -0.33/+0.34 mm				Temperature: 5-25°C Pressure: 0.8167-0.8277 atm Compensator: -0.42/+0.31 mm				Temperature: 0-30°C Pressure: 0.8138-0.8302 atm Compensator: -0.4/+0.37 mm			
		98%	90%	Mean	σ	98%	90%	Mean	σ	98%	90%	Mean	σ
390	13.16	30.14	23.76	15.61	5.84	28.77	22.87	14.93	5.6	29.17	23.08	15.08	5.64
400	8.91	24.17	18.99	12.28	4.69	23.46	18.19	11.89	4.51	23.5	18.14	11.87	4.44
450	6.17	15.77	12.75	9.11	2.59	16.24	13.1	9.41	2.66	15.99	13.18	9.46	2.65
550	5.18	11.54	9.69	7.36	1.72	11.69	9.9	7.61	1.72	11.95	9.97	7.62	1.77
600	4.81	11.72	9.64	7.4	1.67	11.75	9.83	7.54	1.67	11.83	9.9	7.56	1.68
710	5.98	19.81	15.43	10.3	3.64	19.56	15.11	10.21	3.52	19.47	15.02	10.15	3.51

Table 5.11: Tolerance analysis for spectroscopy in R800 (Blue: 650-990nm) for 5.52 arc-min field along the slit. The distance from CCD to the last lens surface is used as a compensator.

Wave-length (nm)	Nominal Criterian RMS dia	Temperature: 20°C Pressure: 1 atm Compensator: -0.36/+0.31 mm				Temperature: 5-25°C Pressure: 0.8167-0.8277 atm Compensator: -0.39/+0.27 mm				Temperature: 0-30°C Pressure: 0.8138-0.8302 atm Compensator: -0.41/+0.40 mm			
		98%	90%	Mean	σ	98%	90%	Mean	σ	98%	90%	Mean	σ
650	6.35	22.59	17.03	11.2	4.21	21.89	16.69	11.05	4.07	22.45	16.83	11.16	4.15
730	6.39	14.58	11.87	9.12	2.03	14.13	11.74	9.08	1.94	14.24	11.78	9.09	1.94
820	6.55	11.62	10.1	8.41	1.26	11.80	10.16	8.48	1.27	11.76	10.14	8.49	1.26
870	6.03	11.75	10.02	8.16	1.4	11.94	10.31	8.32	1.43	11.89	10.17	8.29	1.41
990	9.11	23.27	18.19	11.89	4.46	24.43	19.04	12.45	4.72	24.2	19.09	12.53	4.68

5.2.2.5 Efficiency of LRA module

The efficiency curves for both the grisms are calculated with the grating efficiency equation with peak efficiencies at 60% and the constant prism transmission of 0.96. The efficiency of the grating can be estimated with the help of the following equation for $\alpha > \beta$ (Bottema, 1981):

$$E(\alpha, \beta, m) = \frac{\cos\alpha}{\cos\beta} sinc^2 \left[m\pi \cos\alpha \frac{\sin\{1/2(\alpha+\beta) - \theta_B\}}{\sin\{1/2(\alpha+\beta)\}} \right] \tag{5.4}$$

Where α & β are the angles of incidence and dispersion from the grating normal, m is working order, and θ_B is the blaze angle for the transmission grating. The blaze angles are calculated with the grating equation for the given blazed wavelengths (Table 5.6). The final efficiencies for the grism-modes of LRA are shown in Fig. 5.12 along with their various constituents. The peak efficiencies for both the LRA spectroscopy modes are thus estimated to be around ~30%.

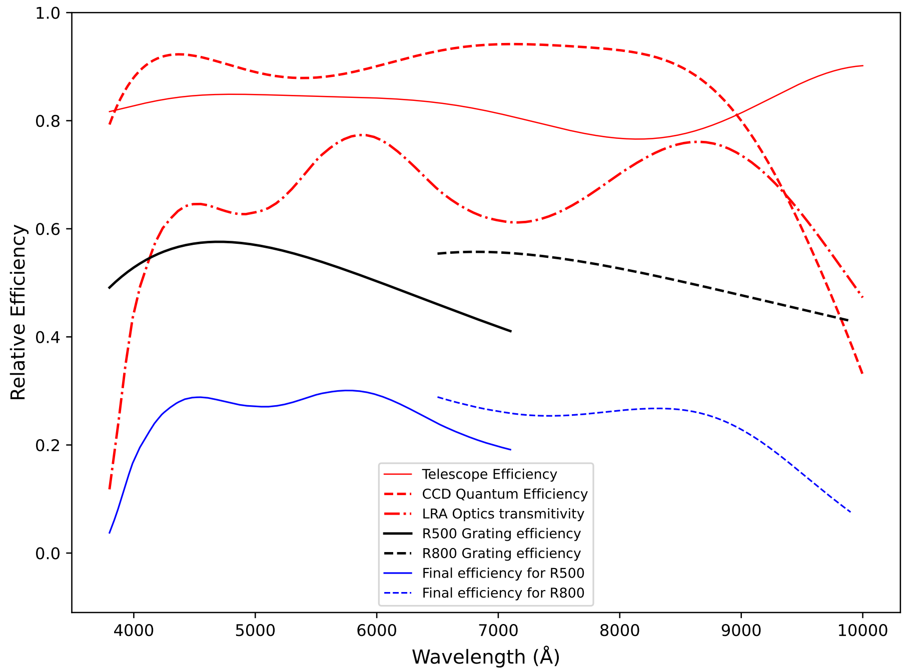

Figure 5.12: Figure shows the efficiency curves for telescope efficiency, CCD quantum efficiency, theoretical grating efficiencies, LRA optical chain transmission efficiency and total efficiency for R500/R800 modes.

5.2.3 Polarimeter Module: Optical design, Performance, & Efficiency

5.2.3.1 Polarimeter module: Optical design

In the spectro-polarimeter arm, the collimated beam from the collimator optics enters the polarization optics. It consists of an MgF_2 Wollaston prism as a polarizing beam splitter and a rotatable Half Wave Plate of PMMA material as a polychromatic modulator. The collimator makes the pupil diameter (∼35mm) within the polarimeter optical chain. The Wollaston prism decomposes the beam in the form of ordinary and extraordinary beams (o- and e-beams), which are focused by the polarimeter camera optics (designed with two achromatic doublets and a singlet lens) onto the entrance of the echelle spectrometer (separated by ∼514 microns) for their simultaneous spectroscopy. The Collimator+Polarimeter optics provides magnification of ×1. Thus, the f/8 beam of the telescope remains intact and enters the spectrometer section. Similar to the collimator section, glasses are chosen from the optical glasses from the SCHOTT and OHARA glass catalogs,

Table 5.12: Specification of polarimeter section of M-FOSC-EP.

Parameters	Values
Input f/# at telescope focal plane	8
Output f/# at Polarimeter focal plane	8
Collimator focal length	275.8 mm @500nm
Polarimeter camera focal length	275.9 mm @500nm
Magnification	1
Pupil diameter	$\sim$ 35 mm
Field of View	$\sim$ 1 X 1 arc-minute square
Half wave plate	Material: PMMA Retardance- 180 degree Required Clear Aperture: 37.4mm (1'X1' field)
Polarizer	Type- Wollaston prism Material: MgF2 Prism Cut angle: 4.5 degree Deviation angle:$\sim$0.106 degree Required CA: 36.8mm X 36.8mm (1'X1' field)
Separation between o-ray and e-ray at polarimeter focal plane	$\sim$ 514 μm

and the physical diameters of the lenses are over-sized by $\sim$8mm for mounting purposes. The field of view for this arm is 1$\times$1 arc-minute square. A slit (1.0-1.5 arc-seconds width) may be kept in the image plane of the polarimeter arm. The polarimeter arm would feed the o- and e-rays into the echelle spectrometer. The ZEMAX optical design prescription data for the polarimeter section are given in Table 5.12 and the ZEMAX layout is shown in Fig. 5.13. The Wollaston prism is custom-designed with a 4.5-degree cut angle. The optical design layout of the polarimeter arm is given in Table 5.13.

Table 5.13: ZEMAX lens surface data for Polarimeter camera design. All dimensions are given in mm. CA: Clear aperture (required for 1'$\times$1' field), Diameter: designed Lens diameter

Comment	Radius	Thickness	Glass	Catalogue	CA	Diameter
Doublet1	74.8	11	S-LAH88	OHARA	35.82	44
	74.6	7	S-FPL55	OHARA	33.19	44
	123.8	71.7			32.09	44
Doublet2	85	9	S-FPL53	OHARA	25.47	36
	-39.9	15	PBL6Y	OHARA	24.60	36
	65.3	89.8			22.87	36
Singlet1	Infinity	18	S-BAM4	OHARA	26.88	36
	-102	150.71			27.40	36

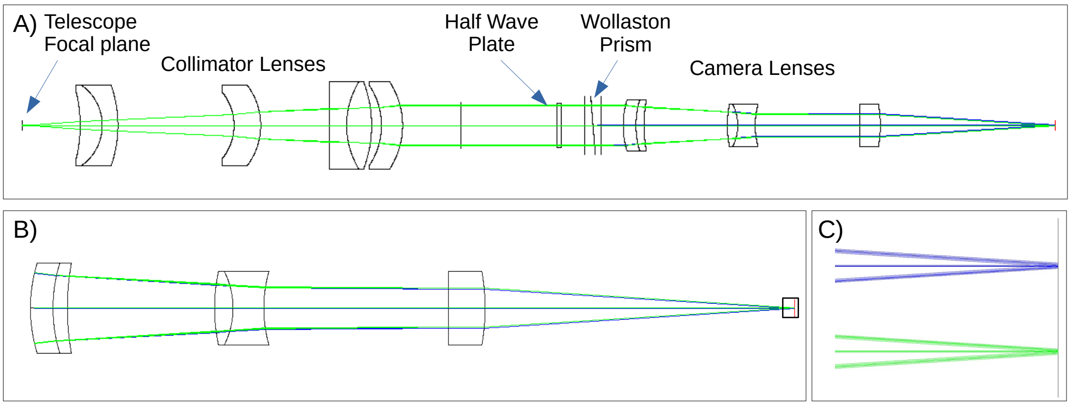

Figure 5.13: (A.) ZEMAX layout of the polarimeter section of M-FOSC-EP along with collimator optical chain. (B.) zoomed-in view of the polarimeter camera optics. (C.) Zoomed in view of separated o-ray and e-ray (separation ∼514μm) at the polarimeter focal plane.

5.2.3.2 Polarimeter module: Performance

The imaging performance of polarimeter arm are given in Tables 5.14 and 5.15 as EE80 and RMS spot diameters respectively. For both o-ray and e-ray, the EE80 diameters are ∼0.33 arc-seconds (∼32 μm at the polarimeter image plane) for various field points. The spot diagrams are shown in Fig. 5.14 and 5.15. The corresponding encircle energy plots are shown in Fig. 5.16 and 5.15.

5.2.3.3 Polarimeter module: Tolerance analysis

The tolerance analysis for the polarimeter optical chain is done along the same lines as for the LRA module (section 5.2.2.4). Tolerance values for the precision optics are considered, and effects of temperature/pressure variation are incorporated. The tolerances for various lens parameters are given in Table 5.16. The results (RMS diameters) for 10000 Monte-Carlo simulations are shown in Tables 5.17 and 5.18.For all the configurations, the RMS spot diameters were

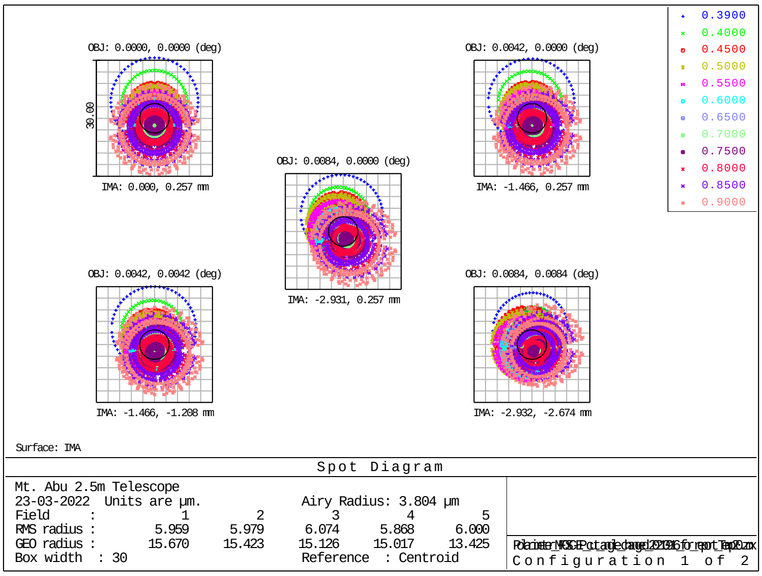

Figure 5.14: Spot diagram for the polarimeter arm at its image plane for o-ray configuration (0.39-0.90 μm). The the box size is 30μm ($\sim$0.3 arc-seconds). Note: 0.0084,0.0084 degrees= 0.5,0.5 arc-minutes.

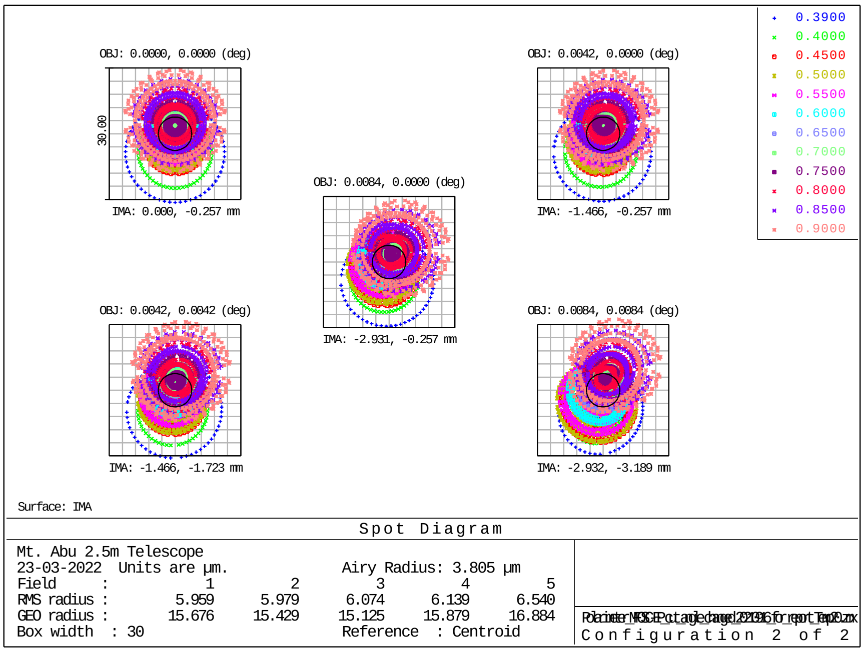

Figure 5.15: Spot diagram for the polarimeter arm at its image plane for e-ray configuration (0.39-0.90 μm). The the box size is 30μm ($\sim$0.3 arc-seconds). Note: 0.0084,0.0084 degrees= 0.5,0.5 arc-minutes.

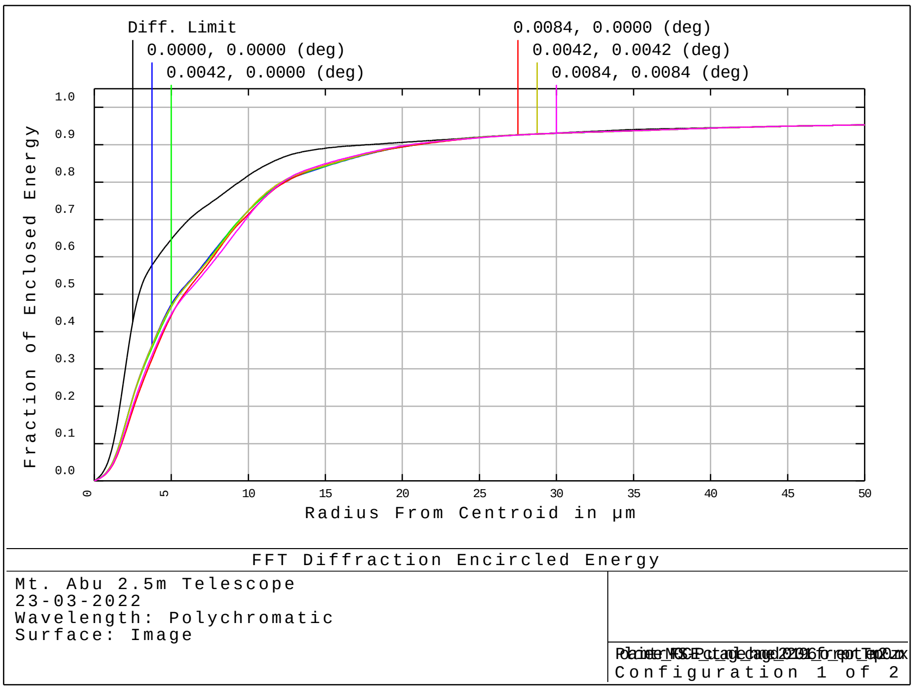

Figure 5.16: Encircled energy diagram for o-ray configuration at the polarimetrer image plane (0.39-0.90 μm). Note: 0.0084,0.0084 degree= 0.5,0.5 arc-minutes.

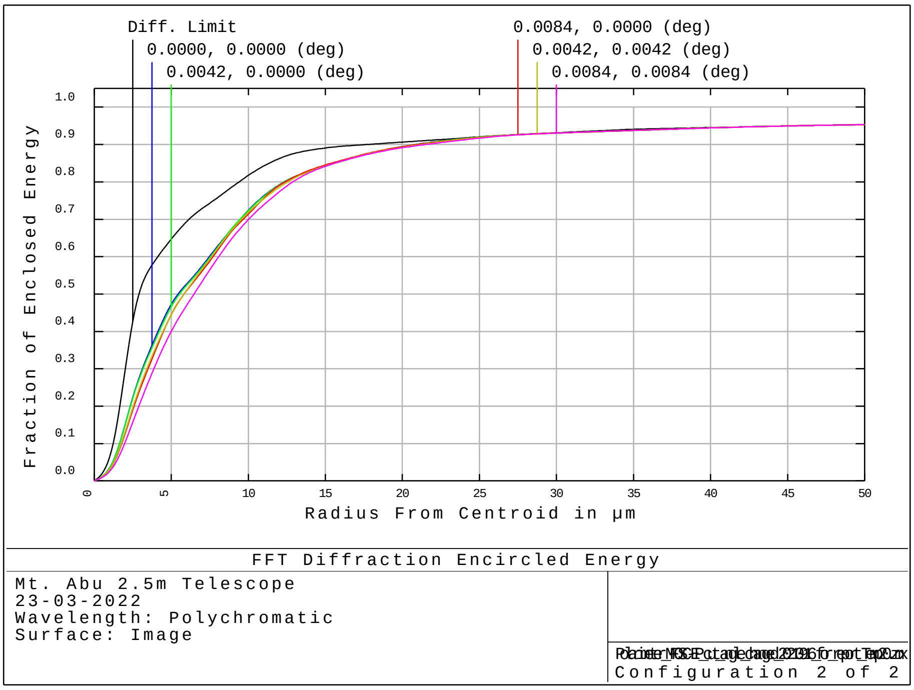

Figure 5.17: Encircled energy diagram for e-ray configuration at the polarimetrer image plane (0.39-0.90 μm). Note: 0.0084,0.0084 degrees= 0.5,0.5 arc-minutes.

Table 5.14: 80% Encircled energy diameters for polarimeter section (0.39-1.0 μm; 1 arc-minute $\times$ 1 arc-minute field of view). Mentioned diameters are in microns.

Field(deg.,arc-sec)/ Wavelength(nm)	390	400	600	800	900	1000	390-900
O-ray							
(0,0) (0,0)	12.70	15.64	19.38	31.04	38.88	46.77	24.63
(0.0042,0) (15,0)	13.12	15.95	19.70	30.72	38.72	46.51	24.67
(0.0084,0) (30,0)	15.33	16.59	20.83	29.51	38.25	45.81	24.77
(0.0042,0.0042) (15,15)	13.78	16.17	20.04	30.37	38.57	46.28	24.26
(0.0084,0.0084) (30,30)	16.21	17.18	22.36	27.44	37.66	45.03	24.45
E-ray							
(0,0) (0,0)	12.69	15.64	19.40	31.02	38.89	46.78	24.63
(0.0042,0) (15,0)	13.12	15.96	19.70	30.71	38.73	46.51	24.67
(0.0084,0) (30,0)	15.34	16.59	20.84	29.50	38.26	45.82	24.77
(0.0042,0.0042) (15,15)	14.11	16.23	20.07	30.32	38.56	46.26	25.12
(0.0084,0.0084) (30,30)	16.32	17.27	22.48	27.26	37.61	45.00	25.77

found to be $< 30\mu$m ($\sim$0.3 arc-second) pixel with a 98% confidence limit.

Table 5.15: RMS diameters for polarimeter section (0.39-1.0 μm; 1 arc-minute $\times$ 1 arc-minute field of view). Mentioned diameters are in microns.

Field(deg.,arc-sec)/ Wavelength(nm)	390	400	600	800	900	1000	390-900
O-ray							
(0,0) (0,0)	10.10	8.38	7.06	11.65	19.72	27.74	11.82
(0.0042,0) (15,0)	9.96	8.40	7.37	11.37	19.41	27.43	11.87
(0.0084,0) (30,0)	9.76	8.63	8.29	10.55	18.52	26.53	12.07
(0.0042,0.0042) (15,15)	9.86	8.42	7.66	11.11	19.13	27.14	11.64
(0.0084,0.0084) (30,30)	9.68	9.11	9.50	9.56	17.40	25.38	11.91
E-ray							
(0,0) (0,0)	10.10	8.38	7.06	11.65	19.72	27.74	11.82
(0.0042,0) (15,0)	9.96	8.40	7.37	11.37	19.41	27.43	11.87
(0.0084,0) (30,0)	9.76	8.63	8.29	10.55	18.52	26.53	12.07
(0.0042,0.0042) (15,15)	9.90	8.49	7.69	11.08	19.11	27.12	12.20
(0.0084,0.0084) (30,30)	9.80	9.28	9.56	9.52	17.36	25.35	13.01

Table 5.16: Tolerance parameters for Polarimeter section.

Criteria	Tolerance
Surface	
Thickness(mm)	±0.05
Radius (fr)	3
Decentre X,Y(mm)	±0.015
Tilt X,Y(deg)	±0.0170(1')
Irregularity (fr)	1fr for Collimator, 0.5fr for Camera
Index	±0.0001
Abbe No. (%)	±0.5
Element	
Decenter X,Y (mm)	±0.05
Tilt X,Y (deg)	±0.05(3')
Distance b/w two lenses (mm)	±0.05

Table 5.17: Tolerance analysis for polarimeter (with common collimator; o-ray configuration) in the 390-1000nm wavelength range for 1 arc-minute X 1 arc-minute field of view. The distance from the polarimeter focal plane (slit) to the last lens surface of POL-CAM is used as a compensator.

Wave-length (nm)	Nominal Criterian RMS dia	Temperature: 20°C Pressure: 1 atm Compensator: -1.21/+1.37 mm				Temperature: 5-25°C Pressure: 0.8167-0.8277 atm Compensator: -1.62/+1.14 mm				Temperature: 0-30°C Pressure: 0.8138-0.8302 atm Compensator: -1.77/+1.00 mm			
		98%	90%	Mean	σ	98%	90%	Mean	σ	98%	90%	Mean	σ
390	7.7	11.54	10.23	8.94	0.96	11.46	10.23	8.88	0.98	11.52	10.2	8.88	0.98
400	8.19	12.02	10.82	9.36	1.07	12.17	10.95	9.5	1.1	12.25	10.97	9.49	1.11
600	9.52	14.22	12.81	10.44	1.84	14.79	13.35	10.99	1.82	14.84	13.39	10.96	1.87
800	9.35	13.87	12.47	10.45	1.48	13.45	12.08	10.18	1.39	13.47	12.08	10.18	1.4
900	16.63	21.71	20.02	17.3	2.06	21.16	19.42	16.85	1.98	21.26	19.51	16.84	2.02
1000	24.1	29.64	27.7	24.57	2.44	28.94	27.13	24.03	2.36	29.05	27.24	24.07	2.39

Table 5.18: Tolerance analysis for polarimeter (with common collimator; e-ray configuration) in the 390-1000nm wavelength range for 1 arc-minute X 1 arc-minute field of view. The distance from the polarimeter focal plane (slit) to the last lens surface of POL-CAM is used as a compensator.

Wave-length (nm)	Nominal Criterian RMS dia	Temperature: 20°C Pressure: 1 atm Compensator: -1.29+1.17 mm				Temperature: 5-25°C Pressure: 0.8167-0.8277 atm Compensator: -1.69/+1.07 mm				Temperature: 0-30°C Pressure: 0.8138-0.8302 atm Compensator: -1.67/+1.11 mm			
		98%	90%	Mean	σ	98%	90%	Mean	σ	98%	90%	Mean	σ
390	7.74	11.58	10.28	8.97	0.96	11.58	10.28	8.94	0.99	11.63	10.29	8.95	0.99
400	8.24	11.99	10.81	9.39	1.06	12.20	11.02	9.54	1.11	12.21	11.06	9.55	1.11
600	9.54	14.3	12.87	10.47	1.83	14.87	13.45	11.01	1.88	14.79	13.44	11.04	1.85
800	9.33	13.87	12.45	10.43	1.5	13.52	12.08	10.18	1.4	13.46	12.12	10.18	1.41
900	16.61	21.68	19.95	17.22	2.09	21.16	19.48	16.82	2.03	21.31	19.52	16.82	2.04
1000	24.09	29.68	27.78	24.55	2.44	29.07	27.25	24.02	2.43	29.16	27.23	24.03	2.44

5.2.4 Echelle Spectrometer: Optical design, Performance, & Efficiency

5.2.4.1 Echelle Spectrometer: Optical design

The echelle spectrometer is designed with the f/8 collimator (designed with two doublets) and f/4.43 camera (designed with two doublets and three singlets) optics. The system provides a magnification of $\times 0.554$ to the slit width. The echelle-collimator makes a pupil of $\sim$51 mm diameter at the echelle grating (52.67 line-pair/mm, 63.5-degree blaze angle). The dispersed beam is then cross-dispersed by the two grating cross-dispersers. Two plane rules reflection gratings (600 lp/mm blazed at 500 nm and 235 lp/mm blazed at 750 nm) are used for two wavelength ranges ~382-570 nm and 564-1000 nm, respectively. The echelle camera optics finally records the cross dispersed multi-order spectra onto a 2K × 2K CCD detector with 13.5 microns pixel size. The geometrical projection of the slit (1 arc-second width) is, thus, 4.1 pixels. The effective projection of the slit is, however, slightly larger (4.5 pixels) due to a slit-tilt factor caused by the out-of-plane tilt of the echelle grating. This effect is later discussed in section 5.2.4.5. The designed slit-limited spectral resolution is, thus, ~15000.

Table 5.19: Specification of Echelle spectrometer of M-FOSC-EP

Pupil size	~50.8mm
Echelle spectrometer input f/#	8
Echelle spectrometer output f/#	4.428
Magnification	0.5535
Collimator focal length	406.5mm
Camera focal length	225mm
Separation between o & e-ray as input	514 μm
1 arcsec at input plane	96.96 μm
Echelle Specification	
Model No. (Richardson grating)	53-*-415E (52.67lp/mm)
Require over-sized size in mm^2	75 X 140
Blaze, Alpha and Beta angles for Echelle	63.5 degree
Gamma angle	6.5 degree
Cross dispersers	
1. Blue cross disperser	
Model No. (Richardson grating)	53-*-260R (600lp/mm,λ_b=500nm)
Require over-sized size in mm^2	120 X 90
Alpha and Beta values	36.75 and 18.25 degree
Order range (Wavelength range)	60-87(382nm-570nm)
1. Red cross disperser	
Model No. (Richardson grating)	53-*-790R (235lp/mm,λ_b=750nm)
Require over-sized size in mm^2	120 X 90
Alpha and Beta values	33.5 and 21.5 degree
Order range (Wavelength range)	34-59 (564nm-1000nm)
Detector	2Kx2K CCD (13.5 μm pixel size)
Detector Model No. (ANDOR)	IKON-L 936
Minimum separation between two order	~41 pixel
Separation between o & e-ray at detector	~ 21 pixels
slit sampling (geometric projection)	4.1 pixels
slit sampling (due to the effect of the tilt of echelle grating)	4.5 pixels
Resolution	~15000

The cross-dispersed footprint of o-ray and e-ray would be recorded on the CCD detector in multiple orders. The separation between the dispersed spectra of o and e rays is 21 pixels (5.1 arc-seconds)) for a given order. The minimum separation between o rays of consecutive orders is 41 pixels for the lowest wavelengths. This separation would keep on increasing with wavelengths. The baseline specifications of the echelle spectrometer module are given in Table 5.2.4.1. The ZEMAX optical design prescription data for the echelle spectrometer are given in Table 5.20. Similar to the other modules, glasses are chosen from the optical glasses of SCHOTT and OHARA glass catalogs, and the physical diameters of the lenses are oversized by 8-15mm for mounting purposes. The ZEMAX model of the spectrometer is shown in Fig. 5.18 for the dimensions and configuration of the system. The echelle-camera optical design is shown in Fig. 5.19. The optical design data is given in Table 5.20.

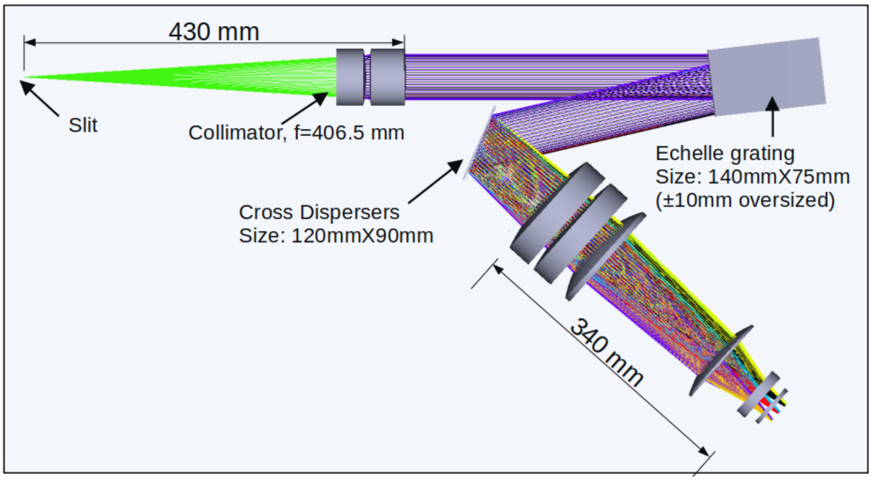

Figure 5.18: ZEMAX shaded model of the echelle spectrometer module of M-FOSC-EP.

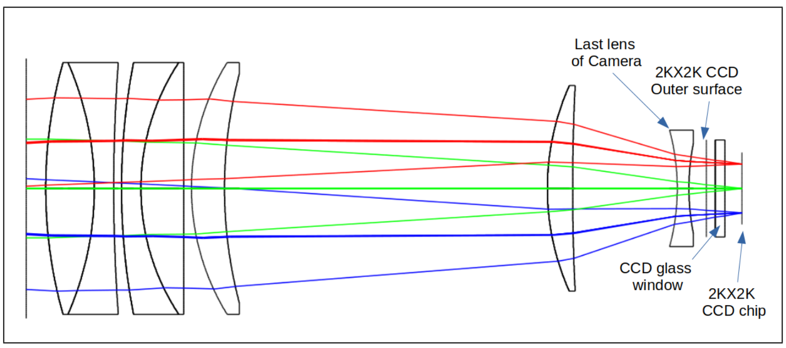

Figure 5.19: ZEMAX model of spectrometer camera consisting of 2 doublet and three singlet lenses.

Table 5.20: ZEMAX lens surface data for both collimator and camera of spectrometer section. All dimensions are given in mm. CA: Clear aperture (required for 30 arc-seconds X 30 arc-seconds field of view; 0.382-1.01 μm), Diameter: designed Lens diameter

Comment	Radius	Thickness	Glass	Catalogue	CA	Diameter
COLLIMATOR						
Doublet1	-233.5	21	S-FPL53	OHARA	48.36	64
	-129	10	S-LAH51	OHARA	51.33	64
	-165.4	3.8			53.44	64
Doublet2	324.5	21	S-FPL53	OHARA	54.16	64
	-95.8	20	S-FSL5Y	OHARA	54.45	64
	-410.6	355			55.33	64
CAMERA						
Doublet1	241.9	25	S-FPL55	OHARA	121.71	130
	-162.1	10	S-FSL5Y	OHARA	121.45	130
	903.4	4			121.05	130
Doublet2	343	10	N-BASF64	SCHOTT	121.37	130
	118.1	22	S-FPL53	OHARA	118.72	130
	Infinity	4			119.21	130
Singlet1	124.1	17	S-FPL55	OHARA	121.55	130
	231.8	166.16			119.24	122
Singlet2	130.2	13	S-LAH88	OHARA	95.90	106
	1102.2	53.84			93.70	106
Singlet3	-116.2	6	S-FPL55	OHARA	50.53	60
	118.6	13.46			46.15	48
Glass Window	Infinity	5	Fused Silica[a]		43.38	50
	Infinity	8.83			42.66	50

a: The glass window is only 8.83 mm away from the detector chip; hence it must not contain any radioactive substances (e.g., potassium in N-BK7 glass, etc.) that could cause a charge particle event to occur on the detector (Smith et al., 2002). Additionally, in order to be sustained in high-pressure differences, it must have a high mechanical strength despite having a small window thickness (to minimize aberration caused by the large distances between the lens and detector). For these purposes, fused silica windows are commonly used.

5.2.4.2 Echelle Spectrometer: Performance

The spot diagrams showing the imaging performance of the echelle-spectrometer are given in Fig. 5.20, for three cross-dispersed orders from blue and another three orders from red cross-dispersers. These spectral orders are chosen from the start, middle, and end of their wavelength span. The spot diagrams are well within a single pixel. The footprints of all the orders on the 2K$\times$2K CCD detector are shown in Fig. 5.21 and 5.22 for both o- and e-rays. EE80 and RMS

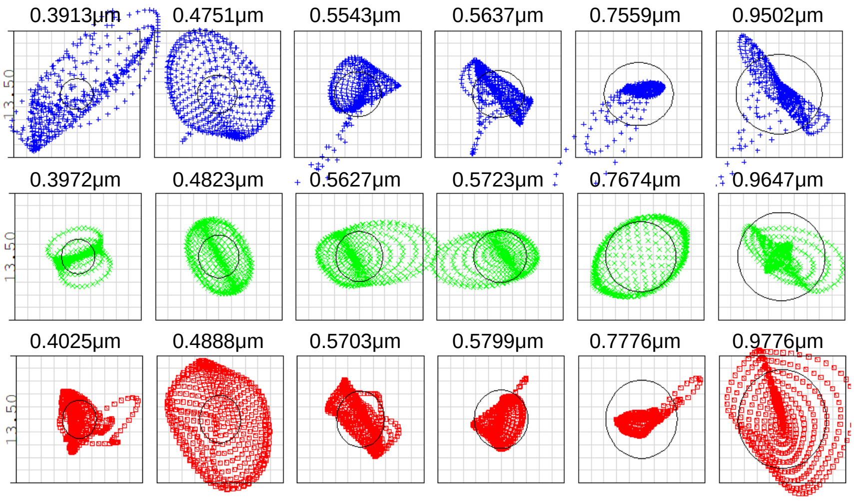

Figure 5.20: Spot diagrams for the echelle-spectrometer (0.39-0.98μm; central field). The box size is 1 pixel (pixel size: 13.5μm). First three columns represents the blue cross disperser orders and last three column represents the red cross disperser orders. Wavelengths in microns are shown at the top of each panel.

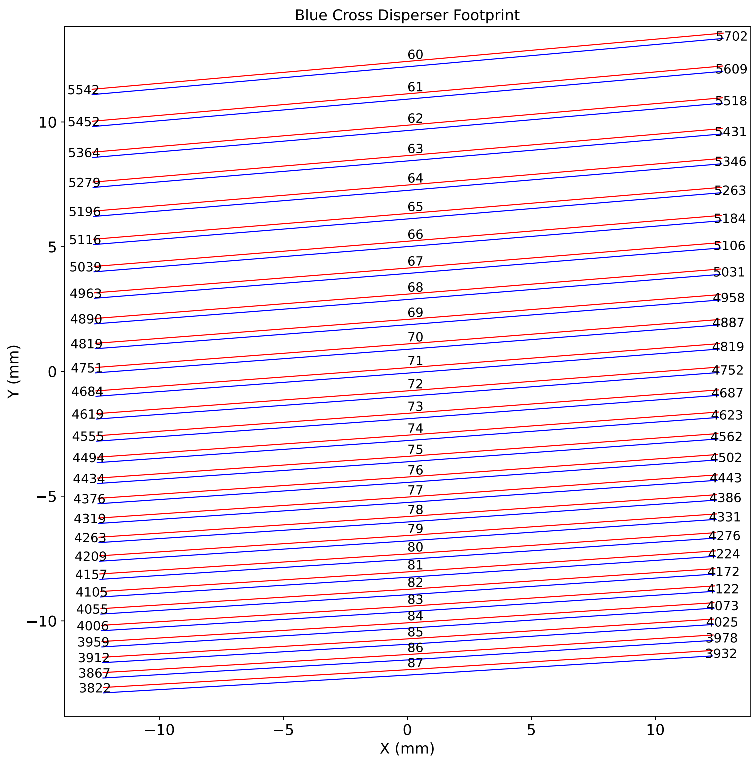

Figure 5.21: Echellogram footprint on 2KX2K detector in Blue cross-disperser mode. Red & blue spectrum shows the same order of o-ray and e-ray respectively. Start and end wavelengths & order numbers are mentioned in the left, right and in the centre of each of the orders respectively.

diameters for some of the orders (covering full wavelength range) are given in Tables 5.21 and 5.22 respectively. These values are well within 1 pixel for most of the orders.

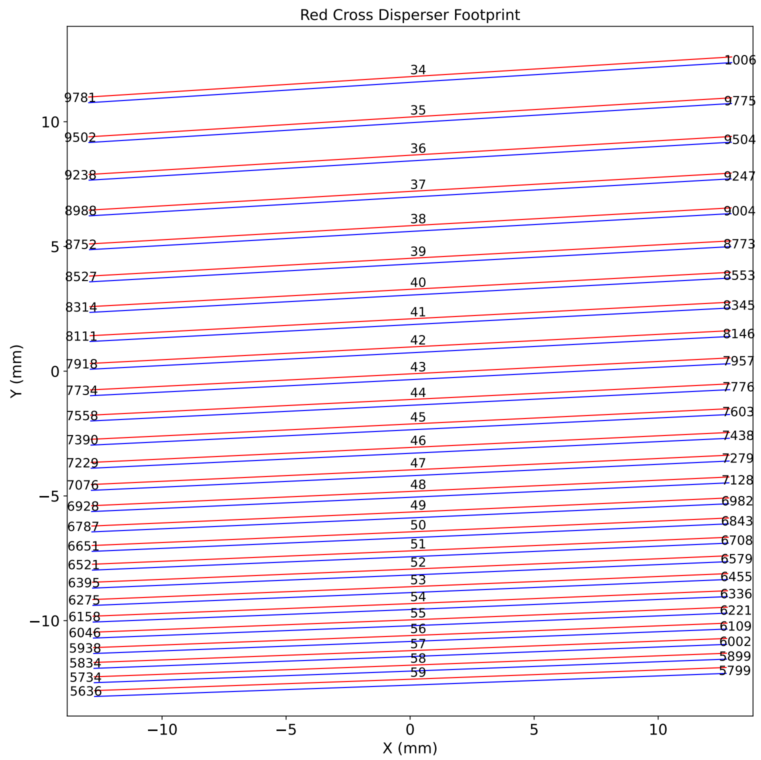

Figure 5.22: Echellogram footprint on 2KX2K detector in the red cross-disperser mode (numbers and color notations are same as in Fig.5.21).

Table 5.21: 80% Encircled energy diameters for spectrometer section only (391-978nm; 30”×30” (∼ ±1.5mm×1.5mm) field). Mentioned dimeters are in microns.

Order No.	Field(mm,mm)/ Wavelength(nm)	(0,0)	(1.5,0)	(1.5,1.5)	Order No.	Field(mm,mm)/ Wavelength(nm)	(0,0)	(1.5,0)	(1.5,1.5)
	Blue CD					Red CD			
85	391.3	16.32	18.98	23.05	59	563.7	7.31	8.2	10.35
85	397.2	6.66	8.99	11.04	59	572.3	8.22	8.21	8.2
85	402.5	6.07	9.45	9.62	59	579.9	7.7	8.46	9.52
70	475.1	11.55	11.05	11.27	44	755.9	8.84	9.46	9.98
70	482.3	8.04	8.39	8.87	44	767.4	14.81	15.36	16.03
70	488.8	12.51	12.72	12.26	44	777.6	9.41	10.02	11.02
60	554.3	8.17	7.84	7.64	35	950.2	9.89	10.44	11.11
60	562.7	9.68	9.78	9.95	35	964.7	9.24	10.88	11.57
60	570.3	7.39	8.2	9.86	35	977.6	13.21	13.18	12.93

Table 5.23: Tolerance parameters for spectrometer section.

Criteria	Tolerance
Surface	
Thickness(mm)	±0.05
Radius (fr)	3
Decentre X,Y(mm)	±0.015
Tilt X,Y(deg)	±0.0170(1')
Irregularity (fr)	1
Index	±0.0001
Abbe No. (%)	±0.5
Element	
Decenter X,Y (mm)	±0.05
Tilt X,Y (deg)	±0.05(3') for Collimator, ±0.03(1.8') for Camera
Distance b/w two lenses (mm)	±0.05

Table 5.22: RMS diameters for spectrometer section only (391-978nm; 30"×30" (∼ ±1.5mm×1.5mm) field). Mentioned dimeters are in microns.

Order No.	Field(mm,mm)/ Wavelength(nm)	(0,0)	(1.5,0)	(1.5,1.5)	Order No.	Field(mm,mm)/ Wavelength(nm)	(0,0)	(1.5,0)	(1.5,1.5)
	Blue CD					Red CD			
85	391.3	11.29	14.15	17.82	59	563.7	5.39	6.66	7.64
85	397.2	3.94	7.36	8.73	59	572.3	5.62	6.50	6.80
85	402.5	4.74	9.35	9.05	59	579.9	3.96	6.74	7.72
70	475.1	9.14	9.15	9.19	44	755.9	5.46	6.75	7.20
70	482.3	5.87	7.20	7.78	44	767.4	8.86	10.23	11.11
70	488.8	9.96	10.90	10.98	44	777.6	4.06	6.68	7.90
60	554.3	6.74	7.36	7.30	35	950.2	6.95	7.39	7.83
60	562.7	6.55	8.07	8.64	35	964.7	4.92	6.46	7.45
60	570.3	5.42	6.87	8.33	35	977.6	9.11	10.02	10.28

5.2.4.3 Echelle Spectrometer: Tolerance Analysis

The tolerance analysis for the echelle-spectrometer module is done, including the effects of temperature variations etc., similar to the LRA and polarimeter modules. The range of various tolerance parameters are given in Table 5.23. The results (RMS diameters) for 10000 Monte-Carlo simulations are shown in Tables 5.24. For all the configurations, the RMS spot diameters were found to be <1.5 pixels (∼0.37 arc-seconds) with a 98% confidence limit.

Table 5.24: Tolerance analysis for spectrometer section in the 391-978nm wavelength range for the on-axis field point. The distance from CCD to the last lens surface is used as a compensator. Mentioned dimeters are in microns.

Order No.	Wave-length (nm)	Nominal Criterian RMS dia	Temperature: 20°C Pressure: 1 atm Compensator: -0.38/+0.37 mm				Temperature: 5-25°C Pressure: 0.817-0.828 atm Compensator: -0.66/+0.23 mm				Temperature: 0-30°C Pressure: 0.814-0.830 atm Compensator: -0.70/+0.27 mm			
			98%	90%	Mean	σ	98%	90%	Mean	σ	98%	90%	Mean	σ
	Blue CD													
85	391.3	10.93	23.39	18.69	13.56	3.76	28.62	23.33	16.68	4.76	29.13	23.54	16.7	4.92
85	397.2	3.78	13.45	10.11	6.13	2.82	19.2	15.35	9.42	4.26	20.07	15.88	9.63	4.43
85	402.5	4.51	14.66	11.58	8	2.63	19.99	15.7	10.28	3.9	20.53	16.59	10.53	4.17
70	475.1	9.08	20.38	16.22	11.33	3.6	18.89	15.54	11.01	3.39	19.66	15.91	11.19	3.55
70	482.3	5.8	13.21	10.36	7.61	2.06	17.01	13.12	8.24	3.44	18.01	13.57	8.43	3.67
70	488.8	9.92	19.56	16.46	11.73	3.53	22.2	18.29	12.65	4.23	22.6	18.69	12.8	4.42
60	554.3	6.02	16.85	13.29	9.51	2.85	20.29	15.87	10.71	3.8	20.9	16.28	10.89	3.89
60	562.7	6.28	16.19	12.32	8.39	2.93	16.54	12.34	7.93	3.25	17.51	13.1	8.2	3.53
60	570.3	5.32	18.56	14.34	9.38	3.64	23.73	18.75	11.75	5.04	24.67	19.13	11.81	5.33
	Red CD													
59	563.7	5.17	18.89	14.22	9.13	3.66	22.47	17.22	10.73	4.67	22.84	17.53	10.86	4.82
59	572.3	5.38	13.39	10.63	7.33	2.45	14.93	11.49	7.24	3.05	15.87	11.99	7.43	3.24
59	579.9	3.84	14.75	11.53	7.44	2.95	18.31	14.18	8.69	3.91	19.02	14.59	8.9	4.08
44	755.9	4.84	18.25	13.8	8.55	3.76	23.61	18.52	11.42	5.07	23.95	18.81	11.53	5.2
44	767.4	8.8	17.47	14.08	10.34	2.8	23.47	19.56	14.16	3.9	24.21	20.12	14.33	4.06
44	777.6	3.79	16.79	12.83	7.9	3.57	22.45	17.76	10.98	4.86	23.35	17.99	11.09	5.02
35	950.2	6.37	19.34	15.22	10.18	3.74	24.3	19.34	12.19	5.07	25.35	19.56	12.31	5.25
35	964.7	4.52	16.96	12.73	8.10	3.33	21.10	16.24	9.55	4.59	21.40	16.05	9.48	4.62
35	977.6	8.67	22.28	18.11	12.06	4.52	25.50	20.00	12.78	5.38	26.16	20.63	13.10	5.56

5.2.4.4 Echelle-Spectrometer: Efficiency

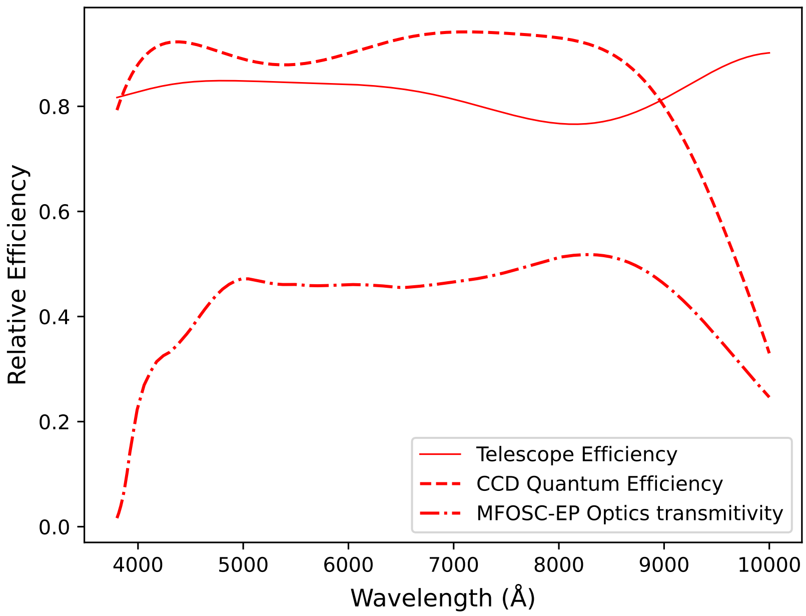

Figure 5.23: Figure shows the efficiency curves for the telescope, CCD quantum efficiency and spectro-polarimeter optical chain's transmission efficiency excluding the grating's contributions.

The efficiency curves for both the gratings (Echelle and cross disperser) are calculated with the grating efficiency equations 1.20 and 1.21 with peak efficiencies at 80%. First, the efficiency of each order has been calculated, and then it is multiplied by the first-order efficiency of the corresponding cross disperser grating. The final efficiency of the echelle spectrometer (including telescope, collimator, polarimeter's efficiencies, and CCD quantum efficiency) is estimated to be around 15-20%. Fig. 5.23 and 5.24 show the efficiency curves for various constituents and the total cumulative efficiencies of various echelle orders, respectively.

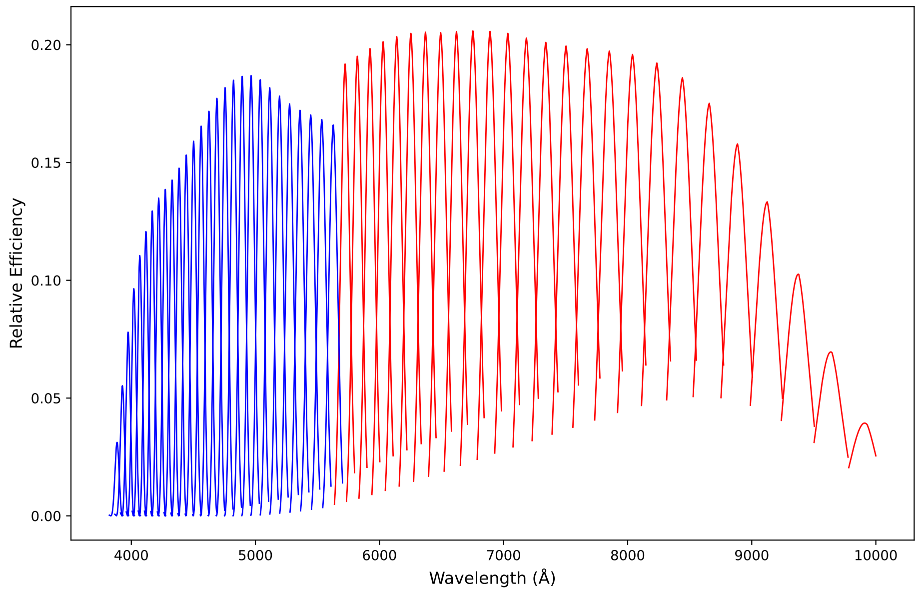

Figure 5.24: Figure shows the cumulative efficiency curves for each of the orders of the echellogram. These efficiency curves include the reflectivity of the telescope, transmission efficiency of spectro-polarimeter module, CCD quantum efficiency, efficiency of the echelle grating and the blaze efficiencies of the cross-disperser.

5.2.4.5 Rotation of the projected slit in echelle spectrometer

As we have discussed in section 1.7.3, echelle gratings are used in the spectrometer with an out-of-plane angle γ, which results in an effect of line-tilt/slit-tilt, which effectively increases the projected slit width and lowers the resolution. In our design, γ=6.5 degrees and the blaze angle Θ_B=63.5 degrees. Therefore, the projected tilt in the slit can be estimated by using equation 1.18 and is determined to be χ=24.6 degrees. This tilt in the projected slit would increase the effective slit width on the CCD plane by a factor of $1/\cos\chi$. However, in the case of the spectro-polarimeter (for on-axis source), the Wollaston prism and slit both can be oriented appropriately to negate such effects.

We have shown this situation with the help of ZEMAX simulations (with M-FOSC-EP optics) in Fig. 5.25 for a rectangular slit of 1.0 arc-second width (along dispersion direction) and height of 2.0 arc-seconds. Various field points on the periphery of the slit are shown in different colours. In the top panel (A), the left figure shows the orientation of the slit at the focal plane of the telescope; the middle figure shows the projected slit for o-ray and e-ray at the polarimeter image plane (input of echelle-spectrometer). The right figure shows the dispersed footprint of the slit on the CCD detector for o and e-rays. The tilt of the slit is clearly seen for both o and e-rays. This tilt will reduce the spectral resolution if the dispersed spectra are summed during the reduction along the cross-dispersion direction. Thus,the original 97 μm slit-width would be having a projected width of 104 μm ($\sim$ 7.7 pixels) as compared to the de-magnified slit-width of $\sim$54μm ($\sim$4.1 pixels).

The effect of slit-tilt on the resolution can be negated by appropriately rotating the Wollanton prism and the slit in the counter-direction. These situations are simulated in panels (B) and (C) of the Fig. 5.25. In panel (B), the Wollaston prism is rotated by an angle of 24.6 degrees; this would “shift” the projected slits for o and e-rays. In panel (C), the slit at the telescope plane is also rotated by 24.6 degrees, causing the intermediate slits at the polarimeter image plane to rotate by this angle as well (middle figure in panel (C)). Finally, at the CCD detector plane, the footprints for slits of o and e-rays would be aligned along the CCD pixels, thereby removing the tilt effect in the projected slit-widths.

While a rectangular slit is chosen above to demonstrate the effect of slit-tilt on the resolution with clarity, the effect of seeing limited point sources (FWHM$\sim$1 arc-second) is depicted in Fig. 5.26. Approximating seeing PSF as a circle of diameter 1 arc-second (97μm) at the telescope’s focal plane, the rotation of the Wollaston prism would cause the o and e-ray to orient at an angle where a

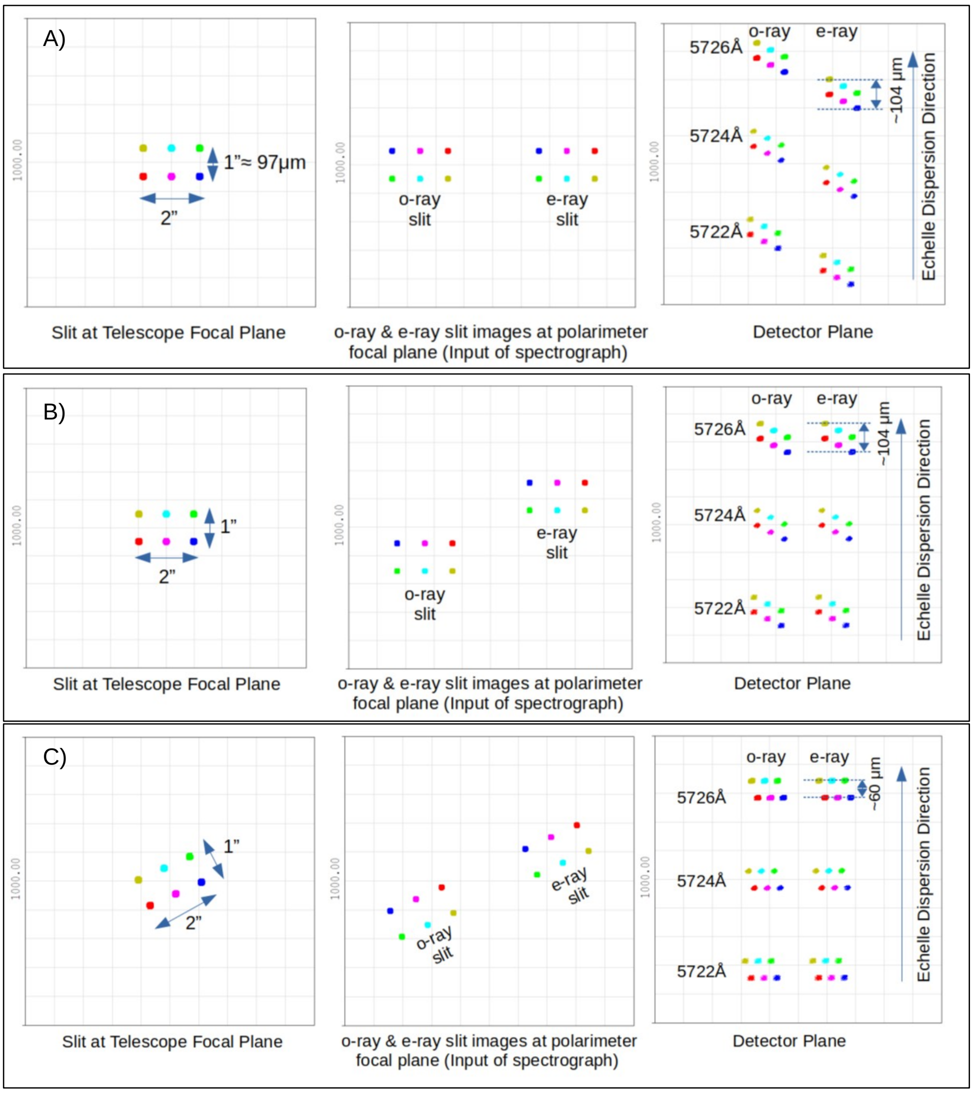

Figure 5.25: Figure shows the ZEMAX-simulations to demonstrate the effects of the rotations of the Wollaston prism and the slit (1"X2" at telescope focal plane) on the resolution elements of o-ray & e-ray on the detector. In each panel, the left figure shows the slit at the telescope focal plane; the middle figure shows the projected slit images for o-ray & e-ray at the polarimeter image plane (input for echelle-spectrograph), and the right figure shows the slits-footprint on the detector of o-ray and e-ray for three wavelengths for order 59 (the starting order of the red cross-disperser). The different colour shows the different field points located at slit edges. The box size is 1mm. Panel (A): The normal configuration of the M-FOSC-EP optical chain without any rotation of slit/Wollaston prism. The effective slit width (ESW) is determined to be 104μm $\sim$ 7.7 pixels as compared to the 4.1 pixels in the absence of the slit-tilt. Panel (B) : when the Wollaston prism is rotated by 24.6 degrees around the optics axis. (ESW: 104μm$\sim$7.7 pixels). Panel (C): When both the slit at the telescope focal plane and the Wollaston prism is rotated by 24.6 degrees, the ESW is estimated to be $\sim$60μm$\sim$4.45 pixels.

physical slit (of 1 arc-second width) may be placed to limit the slit profile along the dispersion direction. 1 arc-seconds slit-width would thus be projecting over ∼4.5 pixels. Further, along the cross-dispersion direction, the spectral traces for o and e-rays would also be aligned.

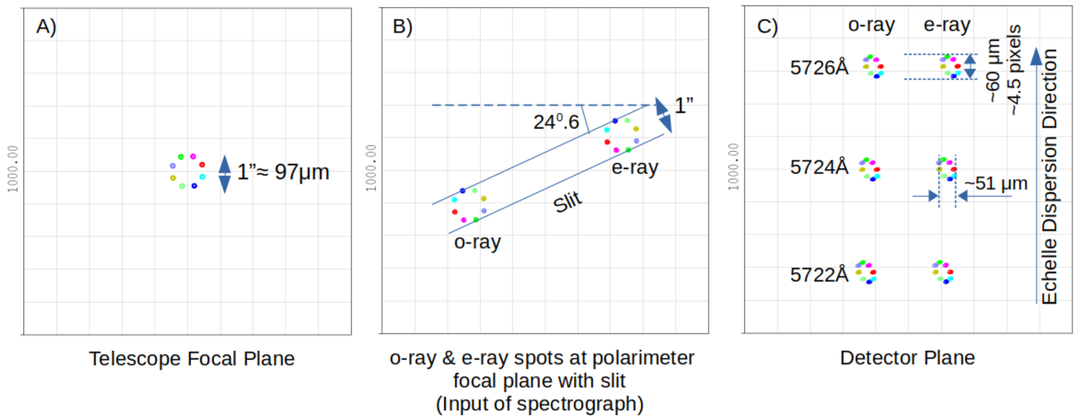

Figure 5.26: Figure shows the ZEMAX simulations to estimate the effects of the rotation of Wollaston prism on resolution element, in the case where a single seeing limited point source is considered as a source. Seeing PSF (FWHM of 1 arc-second) is approximated by a circle of diameter 1 arc-second (97μm) at the telescope focal plane. Panel (A) shows a seeing PSF approximated by a circle of 1 arc-second diameter at the telescope focal plane. Different field points at the perimeter are shown with different colours. Panel (B) shows the projected images of the seeing PSF for o-ray and e-ray at the polarimeter image plane. A physical slit (1 arc-second width) may be kept here with a tilt of 24.6 degrees ($=\chi$). Panel (C) shows the dispersed footprints on the detector of o-ray and e-ray for three wavelengths of order 59. The resolution element is determined to be 60μm (∼seeing PSF/cos(χ);in dispersion direction). Seeing PSF extension in cross dispersion direction is determined to be ∼51 μm (∼seeing disk*cos(χ)).

5.2.4.6 Effect of varying seeing conditions on the cross-talk between o-ray & e-ray seeing

The spectral traces of o and e rays for various orders should be well separated to minimize any cross-talk in the cross-dispersion direction. The extent of spectral traces along the cross-dispersion direction would depend on the seeing profile as well. Fig. 5.27 show the situation for seeing FWHMs of 1.0 and 2.0 arc-seconds. The minimum separation between the traces for o-rays of order m and m+1 is 41 pixels; this will then keep on increasing with wavelength (see Fig. 5.21 and 5.22). The separation between the spectral traces for o and e rays of the same order is fixed at 21 pixels. The figures show that for seeing FWHMs of 1.0 and 2.0 arc-seconds, the o ray of order m is well separated from the e-ray of order m+1 in the cross-dispersion direction. Considering 3σ as a cutoff for the seeing profile in the cross-dispersion direction, there is a gap of 1 pixel even for the relatively poor seeing of 2.0 arc-seconds. It is to be noted that this is the case for the orders containing lower wavelengths. The gap will keep on increasing for the orders containing higher wavelengths. Thus, no cross-talk is expected up to seeing FWHM of 2.0 arc-seconds at the 3σ level.

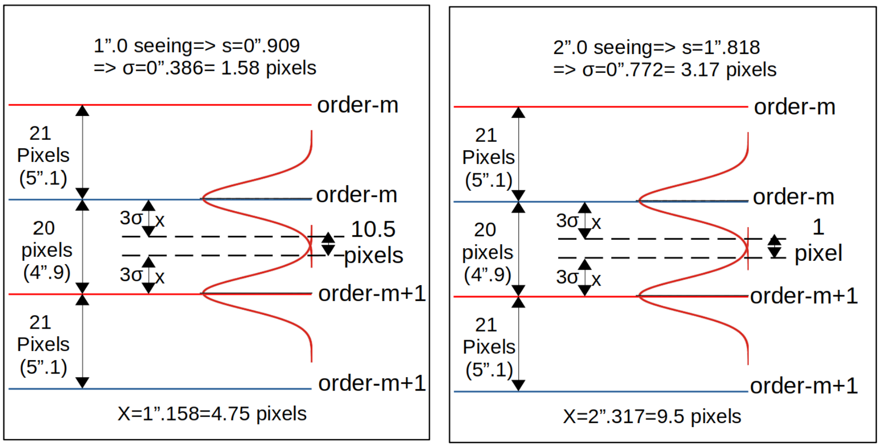

Figure 5.27: Left and right panels show the minimum separation between two adjacent spectral order for 1 arc-second and 2 arc-seconds seeing FWHM respectively. (s is effective seeing disk size in cross-dispersion direction (s = seeing disk*cos(χ))). Blue traces are for o rays and red traces are for e rays.

5.2.5 M-FOSC-EP : Preliminary mechanical design setup

A preliminary idea of the mechanical design setup is required at the final stage of the optical design optimization. Each optical component with its optical mounting arrangement must have sufficient space so that it should not hit any other optical component/mount and should not vignette the light beam. After the preliminary mechanical setup, the optical design has been frozen now. Currently, two mirrors are being used to fold the beam path so that all the components can be accommodated within the available space at the telescope backend. However, the positions of various fold mirrors may be changed for mechanical design optimization. A preliminary mechanical design setup of M-FOSC-EP is shown in Fig. 5.28. The mechanical design is currently underway.

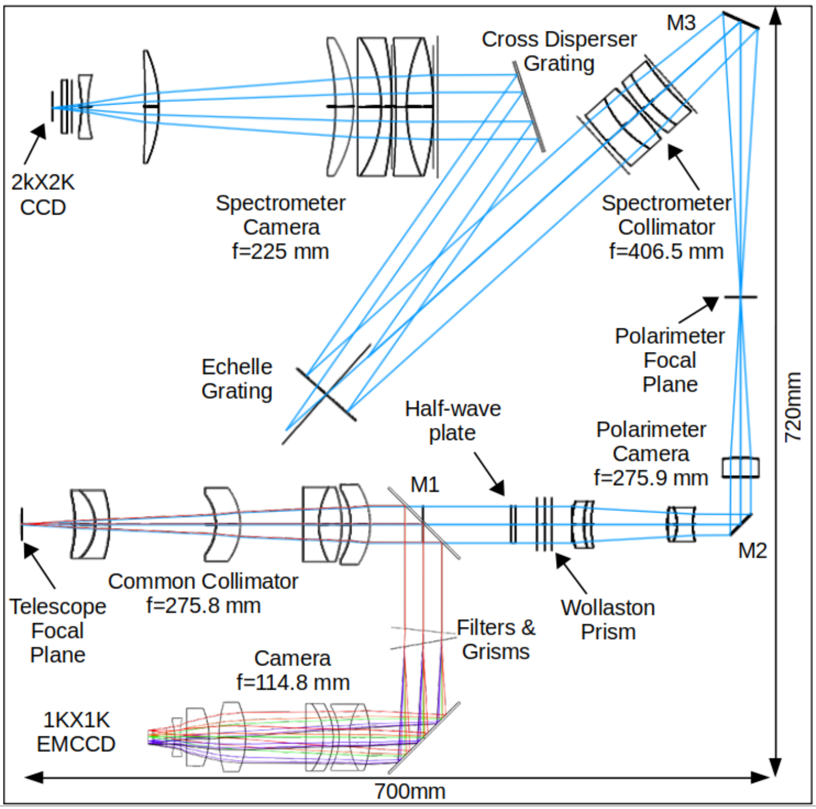

Figure 5.28: Figure shows a preliminary mechanical design model of the M-FOSC-EP optical chain. Fold mirrors are used to fold the design within the constraints of the mechanical dimensions.

5.3 ProtoPol: A prototype instrument with "off-the-shelf" components

As a precursor of the M-FOSC-EP, a prototype spectro-polarimeter (named ProtoPol) was decided to be developed with completely off-the-shelf optical components. ProtoPol has been designed so that it could be mounted on both existing 1.2m as well as upcoming 2.5m PRL telescopes. The prime aim of the development of ProtoPol was to experimentally simulate and test the development methodology of the spectro-polarimeter module of M-FOSC-EP within a short time span prior to its development. ProtoPol has, thus, been designed with off-the-shelf optical and mechanical components, making the design cost-effective and helping in the quick instrument build-up. It covers the optical wavelength range from 381 to 977 nm on off-the-shelf 1024×1024 back-illuminated CCD in cross-dispersed mode, though it is optimized for the range of ∼400-900 nm. For a slit width of 1.0 arc-second, its spectral resolution ($\lambda/\delta\lambda$) is determined to be ∼6000-7000. The system parameters of the ProtoPol instrument are given in Table 5.25. Most of the optical components for ProtoPol have been procured, and the fabrication of its mechanical parts is currently underway.

Table 5.25: Specifications of ProtoPol instrument.

Instrument Capability	Medium resolution (∼6000-7000) spectro-polarimeter
Working reliability	With f/8, PRL 2.5m telescope With f/13, PRL 1.2m telescope
Field of View	1×1 arc-minute^2
Wavelength Range	400-900 nm
Detector	1K×1K CCD detector system with 13 μm pixel size

Despite having a moderate resolution, as compared to M-FOSC-EP, the ProtoPol would be useful for some of the science cases as discussed in section 1.5 e.g., the evolution of ejecta geometry in novae (Kawakita et al., 2019), the spectro-polarimetry of symbiotic stars, spectroscopy of M dwarfs to estimate the physical parameters and spectro-polarimetry of super-novae etc.

5.3.1 Design Overview

ProtoPol has a similar optical layout as used in the spectro-polarimeter module of M-FOSC-EP with some minor differences like a commercial off-axis parabolic mirror is used (instead of lenses) as the echelle-collimator. The schematic diagram of ProtoPol is similar to the M-FOSC-EP as shown in Fig. 5.1, except for the LRA module. The light from the telescope enters the instrument through a protective glass window and forms the focal plane inside the instrument. A slit (150 μm width) is kept at the focal plane at 45° for the slit viewer/on-source guiding purposes. Thus the projected slit width, as seen by the subsequent optical chain, is ∼106 μm (∼1.1 arc-seconds). The polarimeter section contains collimator optics with two commercial off-the-shelf (COTS) achromatic doublets, a half-wave plate, a Wollaston prism, and camera optics with two COTS achromatic doublets. The spectrograph section contains a COTS parabolic mirror as collimator, echelle grating, two cross disperser gratings, a COTS Canon camera/lens system as the camera optics, and a 1K×1K CCD detector system from M/S ANDOR/Oxford Instruments. The ANDOR CCD detector system (Model-IKON-M-934[5]) & off-the-shelf Canon camera (Model-EF 200mm f/2L IS USM[6]) are shown in the Fig.5.29.

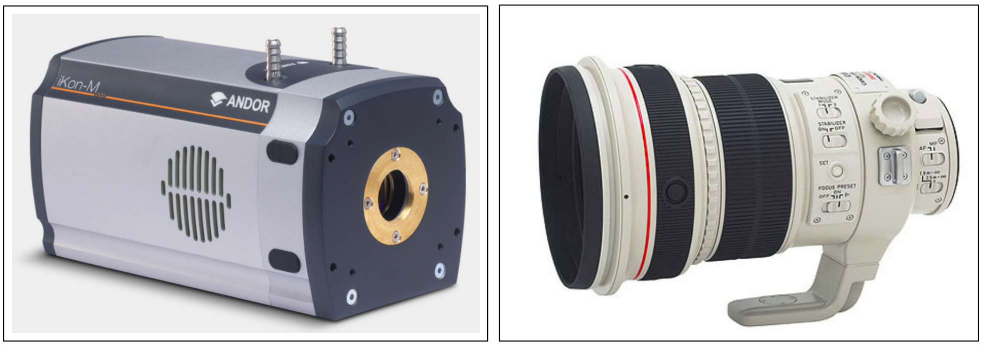

Figure 5.29: Left panel: ANDOR CCD detector system (Model- IKON M-934) is used as a main detector in ProtoPol. Right panel: The Canon camera lens system (Model- EF 200mm f/2L IS USM) would be used as a spectrometer camera.

5.3.2 Polarimeter: Optical design & Performance

5.3.2.1 Polarimeter: Optical Design

The polarimeter optics is designed with the f/8 collimator and f/5.4 camera, and hence, it provides the magnification of 0.67 to the slit width. The collimator makes the pupil diameter of ∼7mm within the polarimeter optics chain. The field of view is 1×1 arc-minute^2. The polarimeter section consists of a COTS quartz Wollaston prism as a polarizing beam splitter and a rotatable COTS half-wave plate of PMMA material as a poly-chromatic modulator.

[5]https://andor.oxinst.com/products/ikon-xl-and-ikon-large-ccd-series/ikon-m-934
[6]https://www.usa.canon.com/internet/portal/us/home/products/details/lenses/ef/telephoto/ef-200mm-f-2l-is-usm

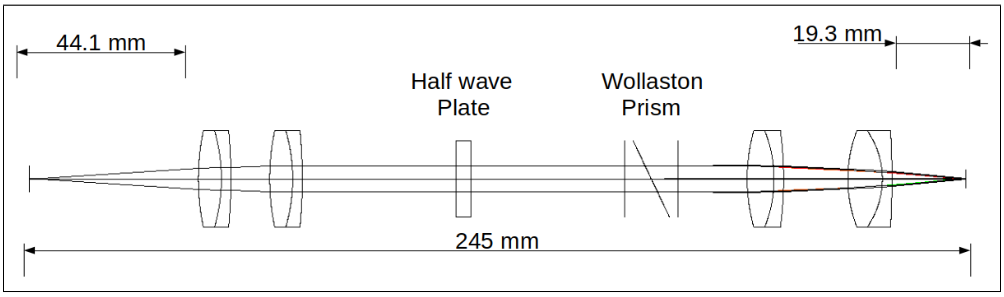

Figure 5.30: ZEMAX 2D layout of Polarimeter section optical design.

Table 5.26: Specification of the polarimeter section of ProtoPol.

Parameters	Values
Input f/# at telescope focal plane	8
Output f/# at polarimeter focal plane	5.355
Collimator focal length	54.23 mm
Polarimeter camera focal length	36.33 mm
Magnification	0.67
Pupil diameter	6.78 mm
Half wave plate specification	Material: Quartz Retardance: 180 degrees
Polarizer	Type: Wollaston prism Material: Quartz
Prism cut angle	25.5 degrees
Deviation angle	0.5 degrees
Separation between o-ray and e-ray at polarimeter focal plane	$\sim$ 324 μm

Table 5.27: Details of various COTS components used in the polarimeter section of ProtoPol

Component	Component Type	Specifications	Part number
Collimator	1. Doublet Lens 2. Doublet Lens	1. Focal length=100mm 2. Focal length=100mm	1. #49-360 2. #49-360 (M/S Edmund Optics[7])
Half Wave plate	Super Achromatic Retarder	Wavelength range:390-920 nm	APSAW-5-Wide[8], 20 mm
Polarizer	Quartz Wollaston Prism	Wavelength range:230-2800nm Ray deviation: 30 arc-minutes	PWQ 30.20 (M/S Bernhard Halle Nachfl[9])
Camera	1. Doublet Lens 2. Doublet Lens	1. Focal length=75mm 2. Focal length=50mm	1. #49-358 2. #49-356 (M/S Edmund Optics)

The Wollaston prism decomposes the beam in o-ray and e-ray, which are focused by the polarimeter camera optics at the entrance of the echelle-spectrometer (separated by $\sim$324 μm) for their simultaneous spectroscopy. The

[7]https://www.edmundoptics.in/
[8]http://astropribor.com/waveplates/
[9]http://www.b-halle.de/products/polarizers/wollaston_polarizers.html

ZEMAX layout of the polarimeter section is shown in Fig. 5.30. The design specification and various COTS component list are given in Table 5.26 and 5.27.

5.3.2.2 Polarimeter: Performance

The projected slit size at the polarimeter focal plane is 71 μm (after magnification of 0.67), and the EE80 diameters are within 29 μm for various field points. The design performances of the o-ray and e-ray are nearly similar. The spot diagram for o-ray is shown in Fig. 5.31, and the corresponding encircled energy plot is shown in Fig. 5.32. The imaging performance of the polarimeter for the different fields is given in Table 5.28 as EE80, RMS, and geometrical spot diameters.

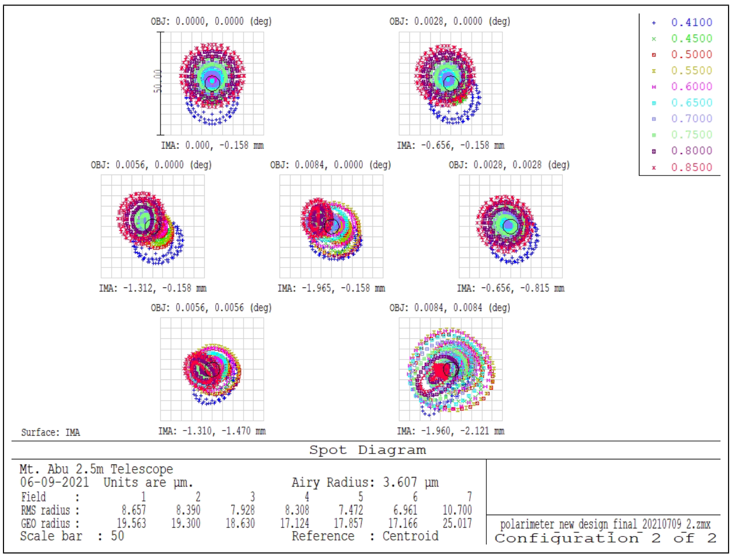

Figure 5.31: Spot diagram for the polarimeter section of ProtoPol at its focal plane for o-ray configuration (0.41-0.85 μm). The the box size is 50μm ($\sim$0.5 arc-seconds).

5.3.3 Echelle Spectrometer: Optical design & performance

5.3.3.1 Echelle Spectrometer: Optical Design

The e-ray and o-ray from the polarimeter section are fed into the spectrometer section of ProtoPol. It is designed with a COTS parabolic mirror as a collimator and a Canon camera lens system as the camera optics. The system provides a magnification of 0.612 to the slit width. Therefore, $\sim$71 μm at the input of the

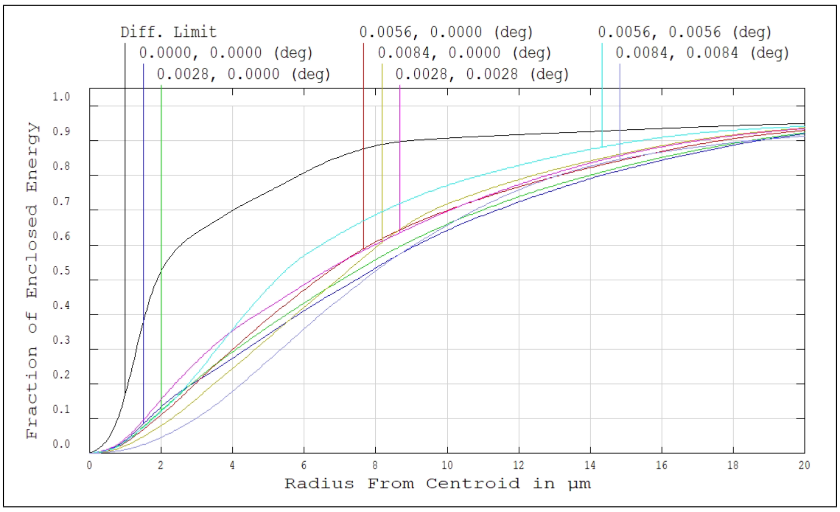

Figure 5.32: Encircled energy diagram for o-ray configuration at the polarimeter focal plane (0.41-0.85 μm) for 1×1 arc-minute^2 field.

Table 5.28: EE80, RMS and geometrical diameters at polarimeter focal plane of ProtoPol for 1X1 arc-minute square field of view (0.0084 degrees = 0.5 arc-minutes).

Field (degrees,degrees)	EE80 Diameter (μm)	RMS Diameter (μm)	Geometrical Diameter (μm)
(0,0)	28.6	17.3	39.1
(0.0028,0)	28	16.8	38.6
(0.0056,0)	26.3	15.8	37.3
(0.0084,0)	24.8	16.6	34.3
(0.0028,0.0028)	25.6	15.0	35.7
(0.0056,0.0056)	22.0	14.0	34.4
(0.0084,0.0084)	26.2	21.4	50.0

spectrometer would fall over 3.3 pixels at the detector. The echelle-collimator makes a pupil of ~61 mm diameter at an echelle grating (54.49 lp/mm, 46 degrees blaze angle). The dispersed beam is then cross-dispersed by the two grating cross-dispersers. The two plane ruled reflection gratings (150 lp/mm blazed at 800 nm and 300 lp/mm blazed at 422 nm) are used for two wavelength ranges ~381-586 nm and 580-977 nm, respectively. The echelle camera optics finally records the cross dispersed multi-order spectra onto a 1K × 1K CCD detector with 13 μm pixel size.

The cross-dispersed footprint of o-ray and e-ray would be recorded on the CCD detector in multiple orders. The separation between the dispersed spectra of o-ray and e-ray is 15 pixels (4.9 arc-seconds)) for a given order. The

Table 5.29: Details of various COTS components used in the echelle-spectrometer section of ProtoPol.

Component	Component Type	Specification	Part number
Collimator	Off-Axis Parabolic Mirror	Focal length=326.7 mm Off-axis angle=30 degrees	#35-584 (M/S Edmund Optics)
Echelle Grating	Echelle	Groove density: 54.49 lp/mm Blaze angle: 46 degrees	53-*-416E Richardson Gratings[10] (M/S Newport Corp.)
Cross Disperser Gratings	Plane Ruled Reflection Gratings 1. Type-1 2. Type-2	1. Groove density:150 lp/mm Blazed at 800nm 2. Groove density: 300 lp/mm Blazed at 422nm	1. 53-*-426R 2. 53-*-091R Richardson Gratings (M/S Newport Corp.)
Camera	Canon Camera Lens System	Focal length:200mm, f/2	Canon EF 200mm f/2L IS USM Lens[11]
Detector System	ANDOR CCD Camera	1K×1K with 13 μm Pixel size	IKON-M-934[12]

minimum separation between o-rays of consecutive orders is 28 pixels for the lowest wavelengths. This separation would keep on increasing with wavelength. The baseline specifications and the COTS component list of the echelle spectrometer module are given in Table 5.30 and 5.29, respectively. The ZEMAX 3D model of the spectrometer is shown in Fig. 5.33 for the dimensions and configuration of the system.

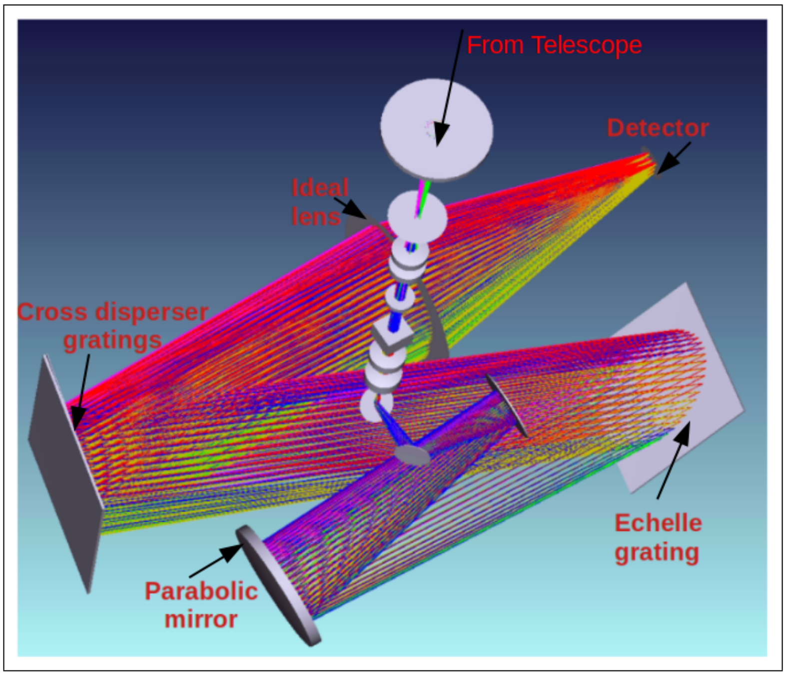

Figure 5.33: The ZEMAX 3D shaded model of ProtoPol instrument.

[10]https://www.newport.com/b/richardson-gratings
[11]https://www.usa.canon.com/internet/portal/us/home/products/details/lenses/ef/telephoto/ef-200mm-f-2l-is-usm
[12]https://andor.oxinst.com/products/ikon-xl-and-ikon-large-ccd-series/ikon-m-934

Table 5.30: Specifications of echelle-spectrometer section of ProtoPol.

Pupil size	∼61mm
Echelle spectrometer input f/#	5.359
Echelle spectrometer output f/#	3.28
Magnification	0.612
Collimator focal length	326.7mm
Camera focal length	200mm
1 arc-second at polarimeter focal plane	65.66 μm
Minimum separation between two orders	∼28 pixel
Separation between o & e-rays at input	324 μm (∼ 15 pixel on detector)
Anamorphic magnification	∼0.95-1.02
Expected Resolution ($\lambda/\delta\lambda$)	∼6000-7000
Echelle Specifications	
Physical Size	102mm × 102mm
Angles of incident (α) and dispersion (β) for central wavelength (Blaze angle)	46 degrees
Out-of-plane tilt angle of the echelle(γ)	10.5 degrees
Cross disperser Gratings	
1. Blue cross disperser	
Physical Size	120mm × 120mm
α and β angles	6.26 and 14.74 degrees
Order range (Wavelength range)	45-67 (381nm-586nm)
1. Red cross disperser	
Physical Size	120mm × 120mm
α and β angles	7.07 and 13.93 degrees
Order range (Wavelength range)	27-44 (580nm-977nm)

5.3.3.2 ProtoPol Performance

The ZEMAX design of the ProtoPol has been done using an ideal lens in place of a Canon camera since its ZEMAX optical design is not available in the public domain. Hence the performance of this module is estimated by using the ideal lens as camera optics in the ZEMAX model. The spot diagrams showing the performance of ProtoPol are given in Fig. 5.34, where three cross-dispersed orders from blue and another three from red are shown. The spot diameters are well within 2 pixels. The footprint of all the orders on 1K×1K CCD is shown in Fig. 5.35 and 5.36 for o-ray and e-ray. EE80, RMS, and geometrical diameters for some orders (covering full wavelength range) are given in Tables 5.31. The 80% encircled energy diameter is well within 2.5 pixels for most of the configurations.

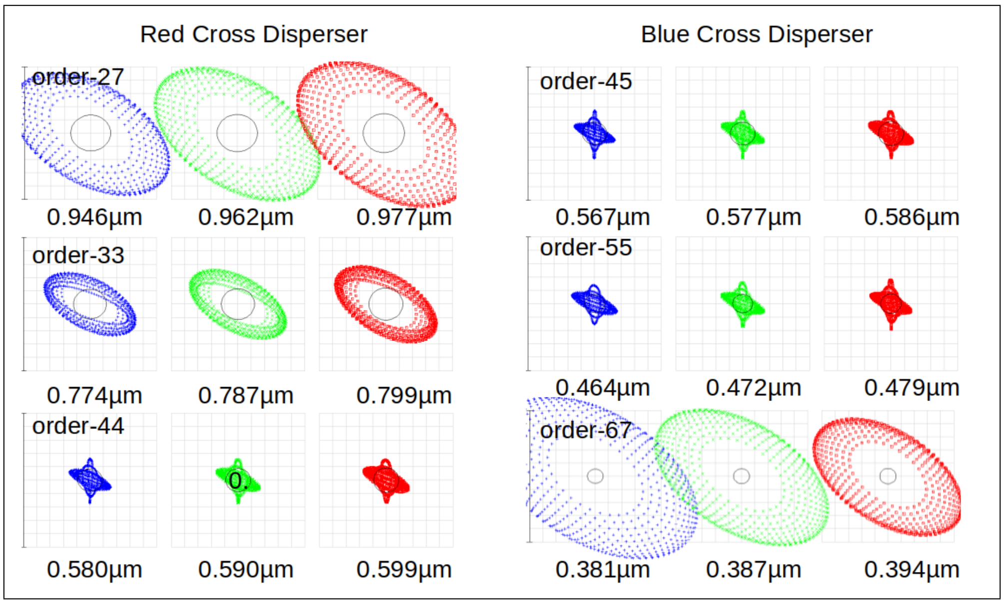

Figure 5.34: RMS, Geometrical and EE80 diameters for the on-axis point at the CCD detector plane of ProtoPol for the o-ray. Performance for selected orders and wavelengths are given (Box size is 26μm= 2 pixels).

Table 5.31: RMS, Geometrical and 80% EE diameters for central field at detector plane (o-ray and e-ray have almost same performance).

Order No.	Central Wavelength (nm)	RMS diameter (μm)	Geometrical diameter (μm)	80% EE diameter (μm)
27	962	27.1	36.7	32.6
33	787	14.7	20.8	20.5
44	590	5.7	9.2	10.1
45	577	5.7	10.0	10.0
55	472	5.7	9.4	9.1
67	387	27.8	38.4	30.2

As the ZEMAX model of the Canon lens system was not available, its optical performance is assumed to be Gaussian in nature (with full width at half maximum- FWHM of 2 pixels). This PSF would convolve with the geometrical projection of the slit and further increase the projected slit width to ∼3.9 pixels. Additionally, the slit would be further tilted/skewed due to the out-of-plane tilt of the echelle grating. Appropriate counter-rotation of the slit at the telescope focal plane and of the Wollaston prism is required to minimize this effect. This slit tilt angle (χ) is determined to be 21°, degrading the resolution with a factor of $1/\cos\chi$. Considering all these effects, the slit-limited spectral resolution of ProtoPol is expected to be in the range of ∼6000-7000.

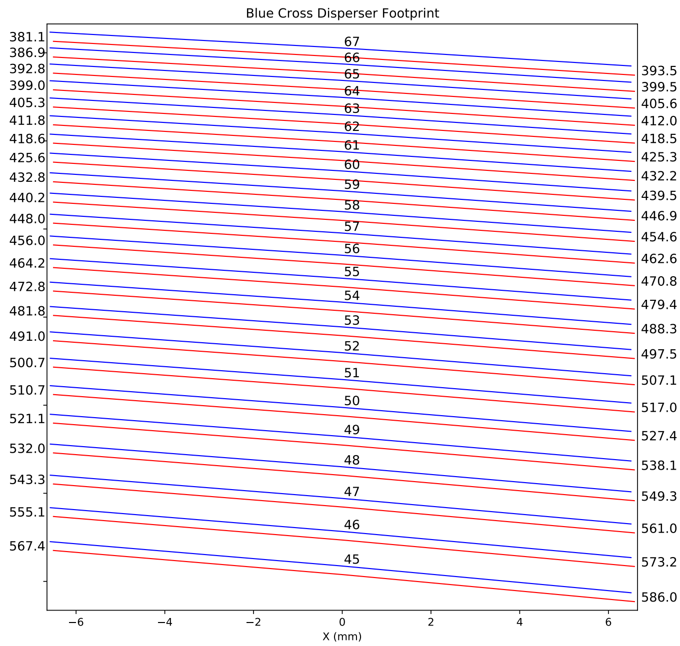

Figure 5.35: Echellogram footprint on 1K×1K detector in the blue cross-disperser mode. Red & blue spectrum shows the same order of o-ray and e-ray respectively. Start and end wavelengths & order numbers are mentioned in the left, right and in the centre of each of the orders respectively.

The efficiency of ProtoPol is estimated by considering 90% reflection efficiency for the telescope’s primary & secondary mirrors. Similarly, 98% transmission efficiency is considered for each of the lens/mirror surfaces in the polarimeter section (which also includes two fold mirrors- a total of 22 surfaces have been considered) and 90% for the off-axis-parabola mirror of the spectrometer-collimator. The echelle and cross-disperser gratings are considered to have a peak efficiency of 60% each, and the Canon lens system camera to have 85%

peak efficiency as given in Harding et al. (2016). The instrument's throughput is, thus, estimated as $(0.90\times0.90\times0.98^{21})\times0.90\times0.6^{2}\times0.85)$ $\sim$15%. With this throughput, it is estimated that the spectroscopy (by combining o- and e-spectra) of an R=13 magnitude source (centered at 6410$\mathring{A}$ & with the zero magnitude flux=2.177×10^{-9} erg/s/cm^2/$\mathring{A}$) can be done with SNR$\sim$135 in 1 hour of integration time. Further, considering the near-equal intensity distribution in o- and e-rays, for the spectro-polarimetry mode, it is estimated that $\sim$0.2% accuracy in polarization can be achieved for R=10 magnitudes source in 1 hour of integration time.

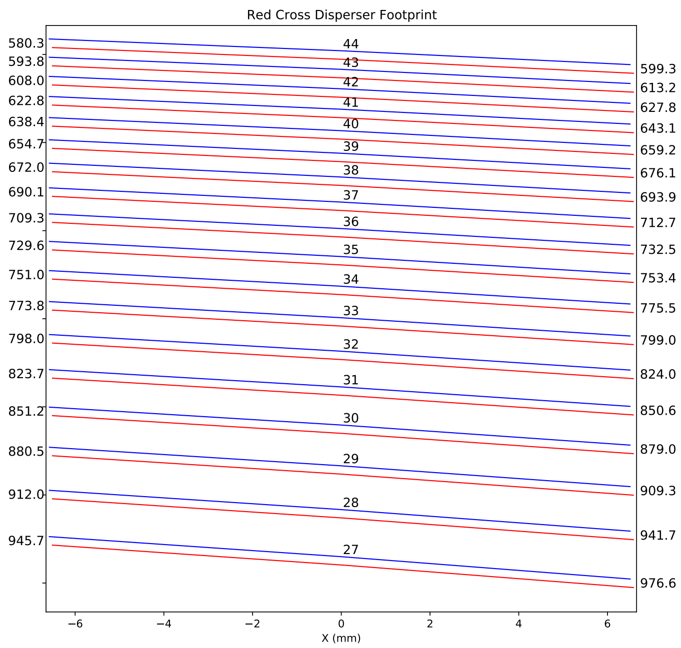

Figure 5.36: Echellogram footprint on 1K×1K detector in the red cross-disperser mode (numbers and color notations are same as in Fig.5.35)

5.3.4 Preliminary Opto-mechanical Design of ProtoPol

We had prepared the preliminary opto-mechanical design of the system in AUTOCAD/INVENTOR mechanical design software, considering the weight and volume constraints on the PRL 1.2m telescope. The final mechanical design and further engineering level fine-tuning of the mechanical system were done by the other mechanical engineers of our instrumentation team. Here we present the preliminary designs which we have developed. This includes the designs of calibration module, polarimeter unit and echelle-spectrometer unit. These modules are discussed below.

5.3.4.1 Calibration Unit

The calibration unit is used for the calibration of the instrument's polarization, as well as for the wavelength calibration of the spectra. For the calibration of the polarization, a Glan-Taylor prism is used, while spectral calibration lamps are used for the wavelength calibration. These lamps are used with an integrating sphere, which helps to diffuse the light so that the instrument cannot see any filament or other structure within the lamps. The opening of this integrating sphere is placed at the object plane of a calibration re-imaging optics, designed with two off-the-shelf achromat doublet lenses and two fold-mirrors (see panel A of Fig. 5.37). Calibration optics simulate the telescope's beam and maps the flat intensity profile of the opening of the integrating sphere onto the focal plane of the telescope. One of the fold-mirror is mounted on a linear translational stage to enable the calibration mode of the instrument by blocking the incoming telescope beam.

5.3.4.2 Field viewer and associated motorized stage

A field viewer ($\sim$5 arc-minute in diameter) is also provided in the calibration module with a separate field viewer optics and detector to identify the science target in the sky. The incoming field is directed to the field viewer with a movable fold-mirror required to identify the science target. The field viewer assembly consists of a CCD Model No.- SBIG STF-8300M[13], 3326 $\times$ 2504 pixels) and a COTS re-imaging lens system (Model no.- #33-814, M/S Edmund Optics). The lens system has been selected so that the magnification of the

[13] https://telescopes.net/sbig-stf-8300-monochrome-camera-complete-imaging-system-used.html

optics gives at least 2-3 pixel sampling of the seeing profile and with minimum object distance to make a compact system. A linear translational stage is provided in the calibration unit, which hosts the calibration fold mirror, a fold-mirror for the field-viewer, the Glan-Taylor prism and an open aperture for different calibration, field viewing and observing modes.

5.3.4.3 Polarimeter module and slit viewer optics

The light from the telescope enters the polarimeter section through the slit mounted at the telescope's focal plane. The slit is mounted within a cage-rod system of the collimator and polarization optics (see Fig. 5.37). A couple of fold mirrors are placed just after the polarization components mechanical fold the design and guide the separated o- and e-rays into the echelle-spectrometer section.

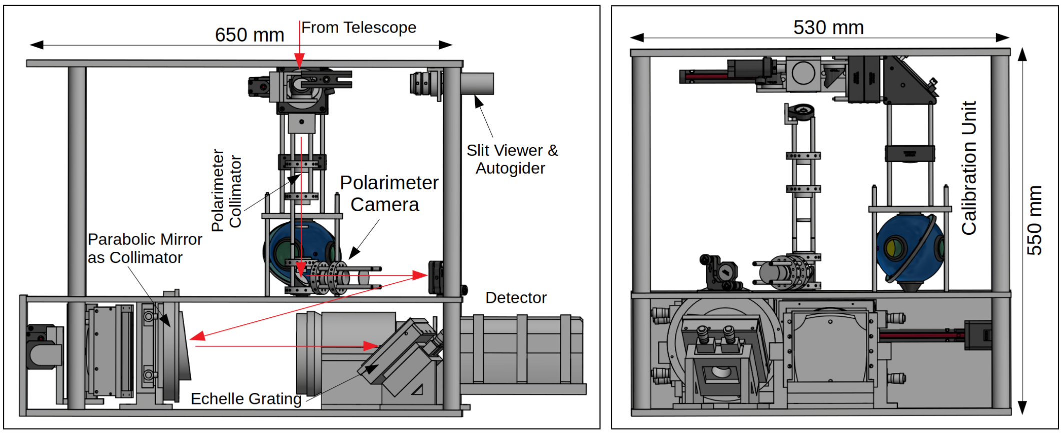

Figure 5.37: Two different views (Left:front view, Right:side view) of the mechanical CAD model of ProtoPol instrument for 2.5m telescope

Except for the half-wave plate (HWP), which would be rotated with a motorized stage, all other components of this module are rigidly fixed to the instrument base plate. A slit-viewer is provided in the polarimeter section to monitor and, if necessary, guide the telescope with the science target itself. The slit is rotated at 45 degrees for the slit-viewing mode. It consists of a machine vision camera optics (Model no.- #85-363, M/S Edmund Optics) and CCD (Starlight Xpress Camera Lodestar X2[14]) (see Fig.5.38 right panel).

[14]https://www.astroshop.eu/astronomical-cameras/starlight-xpress-camera-lodestar-x2-

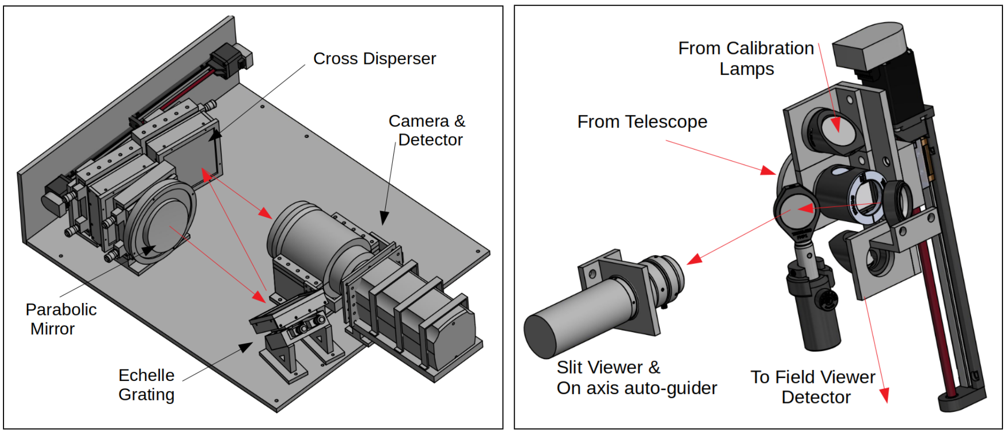

Figure 5.38: Left panel shows the bottom plate view showing the components mounted on the base plate and the light path to the detector, Right panel shows top plate assembly showing the different mode of the observations.

5.3.4.4 Spectrometer Section

In the spectrograph section, there are four sub-systems mounted on the horizontal base plate (see left panel of Fig. 5.38) of the instrument. It consists of a parabolic mirror as a collimator, echelle grating, cross disperser gratings, and a Canon lens system with CCD camera assembly. The incoming beam to this section would be first collimated by an off-axis parabolic mirror (with an off-axis angle of 30° in the plane of the horizontal base plate. The horizontal beam then falls on the echelle grating, which directs it towards the cross-disperser gratings. The off-

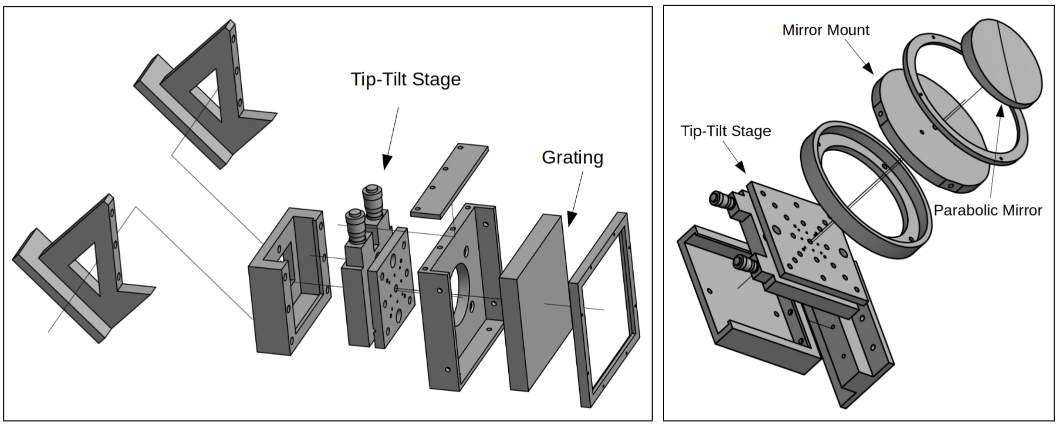

Figure 5.39: Left and right panels show the various parts of echelle grating mount and parabolic mirror mount respectively.

axis-parabola, echelle gratings and cross-disperser gratings are mounted on the tip-tilt stages for fine adjustment during the optical alignment. The two cross-

autoguider-mono/p,44835

disperser reflection gratings are placed on a linear motorized stage to select any of them as required to put them into the beam path. After the cross dispersion of light, the beam is directed to the Canon lens system, which is coupled with the CCD detector system. The lens system and CCD camera form a sub-assembly that is coupled to the spectrometer base plate. For ease of aligning, during the assembly process in the laboratory, the parabolic mirror, echelle grating and cross-disperser gratings are mounted on the tip-tilt stages. Various mechanical parts of the echelle grating mount and parabolic mirror mount are shown in Fig.5.39.

5.4 Chapter Conclusions

The optical design and analyses of the M-FOSC-EP and its prototype instrument-ProtoPol are presented in this chapter. M-FOSC-EP is a multi-mode instrument that has been designed to provide the capability of seeing limited imaging in various filters, low resolution (R∼500-800) spectroscopy, and intermediate resolution spectro-polarimetry (R∼15000) on PRL 2.5m optical telescope. The optical design is developed to achieve RMS spot diameters in the range of 1 to 1.5 pixels, including the effects of tolerances and temperature variations for all the instrument modes. Various other aspects of the optical design, like efficiency, resolutions, cross-talk, etc., are also evaluated and discussed. The optical and preliminary opto-mechanical designs of the ProtoPol have been discussed in the later part of this chapter. ProtoPol has been successfully designed with commercially available off-the-shelf optical and mechanical components., a goal set at the start of the project. It provides moderate resolution (∼6000-7000) spectro-polarimetry and is designed to be used on the upcoming PRL 2.5m telescope as well as on the existing PRL 1.2m telescope.

Chapter 6

Summary and Future Work

The research projects included in this thesis work are focused on the design, instrumentation, calibration, data analysis, and observational aspects of the back-end instruments like imagers, spectrometers, and spectro-polarimeters for ground-based optical/NIR telescopes. The early part of the thesis describes the Assembly-Integration-Test (AIT) of an in-house developed instrument named: Mount-Abu Faint Object Spectrograph & Camera - Pathfinder (MFOSC-P) for PRL 1.2m telescope for seeing limited imaging as well as low-resolution spectroscopy (resolutions ∼500, 1000, 2000). It includes quality tests for various components, instrument integration, laboratory, on-sky characterization, etc. The next part of the thesis was to perform the performance & science verification of MFOSC-P using a variety of astrophysical objects like M dwarfs, symbiotic stars, novae, etc. A data reduction pipeline of MFOSC-P was also developed during the performance verification. Subsequently, an optical design of a two-channel multi-mode instrument named Mt. Abu Faint Object Spectrograph and Camera - Echelle Polarimeter (M-FOSC-EP) has been developed to provide imaging, low-resolution spectroscopy (R∼500) & intermediate-resolution spectro-polarimetry (R∼15000) on the Cassegrain port of the 2.5m telescope. As a part of M-FOSC-EP development, an optical & opto-mechanical design of ProtoPol - a prototype spectro-polarimeter (R∼6000-7000) for PRL telescopes has been designed with commercial "off-the-shelf" optical components.

In this chapter, we summarize the presented work of the thesis. Later we will also discuss some future perspectives with reference to the research work presented here.

6.1 Summary

6.1.1 Assembly-Integration-Test & Characterization of MFOSC-P

MFOSC-P has been developed as a pathfinder instrument on PRL 1.2m telescope to develop the next generation FOSC type of instrument for the upcoming PRL 2.5m telescope. It provides seeing limited imaging in Bessell's filters and low-resolution spectroscopy in the visible domain. At the time of the beginning of this thesis work in mid-2018, the design of MFOSC-P was completed, and various components were being procured. Thus, the next step was to assemble and characterize the instrument in the laboratory.

The first project of the thesis work, i.e., the Assembly-Integration-Test (AIT) and laboratory/on-sky characterization of MFOSC-P, were completed from October 2018 to January 2019. The performance verification of various optics components (e.g., lenses and lens sub-assemblies), motion sub-systems testing, imaging and spectroscopy performance verification, etc., were done in this period. The instrument was assembled, integrated, and characterized in the laboratory. Subsequently, MFOSC-P was commissioned on the PRL 1.2m telescope in February 2019. Its on-sky characterization was done subsequently, and an automated data reduction pipeline was developed to reduce and analyze the raw observational data. The performance of MFOSC-P was determined as per the designed specifications.

The experience gained from MFOSC-P design and AIT is most helpful in developing the next FOSC instrument for the 2.5m telescope. The design and development approach adopted here is well suited for any small aperture telescope, which requires a simple yet versatile instrument within a short development period. As the instrument has been successfully used for a range of astronomical observations, the MFOSC-P presents a successful FOSC design, which could be adapted with minimal modifications to similar telescopes worldwide.

MFOSC-P is a pathfinder instrument, which is purposefully built to retire risks, learn lessons, and develop a better strategy for the next-generation instrument. We learned about our in-house workshop's tolerance capabilities while manufacturing and assembling MFOSC-P. These known capabilities aid in providing input for the new instrument design from the very beginning of the project, as well as in determining which pieces of work should be outsourced. The pathfinder assembly procedure provides a realistic understanding of the tools and accessories required to achieve precision in the orientations and positions of different components of the instrument. It also aids in the upgradation of the optical mount designs, several tests assuring the performance in the laboratory, and AIT plans for the next-generation instrument. One such example is the inclusion of an on-axis guiding and slit viewer in the next generation instrument, as we sometimes see the flexure effect caused by gravity in the off-axis guiding system creating star offset in the slit. As a result, the MFOSC-P instrument contributes significantly to the next-generation instrument.

6.1.2 Performance verification of MFOSC-P with the statistical studies of the samples of M dwarfs

The performance verification (PV) observations with MFOSC-P were aimed to establish and characterize the instrument's performance in various observing conditions, with sources of varying magnitudes, etc. M dwarfs were found to be suitable targets for the PV phase of MFOSC-P. They are among the most abundant stellar species of our Galaxy, and therefore, a good number of them would be available for observations at any given time of the year. Their spectra are rich in absorption features, and subtle differences are seen in M dwarfs of different spectral types. Further, for each sub-spectral class, a good number of M dwarfs could be found in the magnitude range suitable to be observed with the 1.2m aperture PRL telescope.

The PV observations of MFOSC-P were executed with statistical studies of a sample of M dwarfs during the commissioning run of MFOSC-P in February-June 2019. In this study, we provide a low-resolution (R$\sim$500) spectroscopic catalog of 80 bright M dwarfs (J $<$ 10) and classify them using their optical spectra. We have also performed the spectral synthesis and χ^2 minimization techniques to determine their fundamental parameters regarding effective temperature and surface gravity by comparing the observed spectra with the most recent BT-Settl synthetic spectra. Our sample's spectral type of M dwarfs ranges from M0 to M5. The derived effective temperature and surface gravity range from 4000-3000 K and 4.5-5.5 dex, respectively.

Out of 80 sources of the M dwarf sample of the PV observations, Hα emissions were detected in 10 sources which led us to plan another similar program to study the short-term variability in Hα / Hβ emissions. The 83 M dwarfs (M0-M6.5 sub-spectral classes) were observed over the time scales from $\sim$0.7 to 2.3 hours with a cadence of $\sim$3-10 minutes. The 53 of the objects in our sample ($\sim$64%) show statistically significant short-term variability in Hα , in which 38 are most likely related to the flaring events. Data were also collected for a complementary set of 43 M dwarfs, in the M3.5-M8.5 sub-spectral class, from the earlier published results of Lee et al. (2010). Various variability indicators were derived from a total of 126 sources spanning a full spectral range from M0 to M8.5 and were studied with respect to their sub-spectral classes. The archival photometric data from the TESS and Kepler/K2 missions were also used to relate the derived variability parameters with their rotation periods and star-spot filling factors. The variability indicators clearly show higher variability in late-type M dwarfs (M5-M8.5) with shorter rotation periods ($<$2 days). A similar trend is seen for the star-spot filling factors as well.

The performance verification of MFOSC-P was completed by observing and later characterizing a sample of M dwarfs. It was shown that MFOSC-P could be utilized in various observing conditions, magnitude range, air-mass range, etc. The data collected in this phase was also used to characterize the instrument as well, like determination of SNR, efficiency, etc.

6.1.3 Science verification of MFOSC-P with studies of Nova V2891 Cyg & Suspected Symbiotic - SU Lyn

A science verification (SV) program was undertaken with MFOSC-P to probe the physics of a suitable astrophysical source. The goal of the SV program is to demonstrate the instrument's scientific potential, capabilities, and performance which usually happens at the end of the commissioning phase when the instrument is well characterized. As novae evolve in many ways (its spectrum and photometric light curve) since their outbursts and then fade below the detection limits, their scientific studies with a new instrument were found most suitable to have a good scientific impact and push the instrument close to its observational limits.

Nova V2891 Cyg has been studied for its long spectroscopy and photometric evolution for nearly 13 months with various modes of MFOSC-P and with several other observing facilities worldwide. In this study, we have explored the optical and NIR spectroscopic evolution of the nova V2891 Cyg, one of the slowest novae recorded in recent times. During this period, we could even trace the faint continuum in the R500 mode spectroscopy mode of MFOSC-P when its V-band magnitude was around $\sim$18 (with 3-5 SNR in 60 minutes of integration time). The nova's light curve is having a couple of episodes of re-brightening, which we propose is due to periodic mass ejection, as manifested in the line profile of the O I 7773$\AA$ line. Strong evidence suggests that the coronal lines are created by shock heating rather than photoionization. The simultaneous occurrence of the dust and coronal lines supports the possibility that dust formation is shock-induced. Such a route for dust formation has not previously been seen in a nova. Thus, the presented data set and our associated analysis would be of interest to the community to explore the physics of the nova phenomenon.

Another opportunity to utilize MFOSC-P data for the studies of a similar kind of system had come with the timely ultra-violet spectroscopy observations of SU Lyn - a suspected symbiotic system. As the constituents of a symbiotic system are similar to the novae systems, i.e., a white dwarf in association with the main sequence or red giant star, a short study of SU Lyn was also undertaken as an auxiliary science program which included MFOSC-P observations as well. SU Lyn was suspected of harbouring a white dwarf based on its hard X-ray properties, thereby making it a symbiotic system. The star does not display, in low-resolution optical spectra, the high excitation lines typically seen in the spectra of symbiotic stars. The slitless UV spectra of SU Lyn from the ultra-violet imaging telescope (UVIT) aboard the AstroSat space mission show various emission lines, which are usually seen in a typical spectrum of symbiotic stars. The UV spectrum robustly confirms SU Lyn's symbiotic nature. The continuum variability is seen in the optical spectra of SU Lyn using MFOSC-P further strengthens these arguments of SU Lyn being a symbiotic system.

Thus, MFOSC-P has been successfully utilized to study the physics of Nova V2891 Cyg and suspected symbiotic SU Lyn. It has been regularly used on PRL 1.2m telescope since 2019 for various other observational programs as well.

6.1.4 Designs of spectro-polarimeters for PRL telescopes

The upcoming 2.5m PRL telescope would be a major observational facility to boost the ongoing observing programs of the observatory. Thanks to its larger aperture, it would also enhance the prospects of several specific research areas, such as studies of transients (novae, supernovae, etc.), exo-planets, M dwarfs, etc. To utilize the potential of this new telescope, a new multi-mode instrument (named Mt. Abu Faint Object Spectrograph and Camera - Echelle Polarimeter: M-FOSC-EP) was conceived for the visible bands, with basic FOSC-like observing modes of imaging and spectroscopy with quick switchover time. In addition, another spectro-polarimetry (resolutions$\sim$10000-15000) optical arm was embedded into it. Several scientific cases for objects like symbiotic systems, M dwarfs, AGNs, novae, supernovae, etc., would greatly benefit from having a higher resolution mode (resolutions$\sim$10000-15000) and/or having a spectro-polarimetry capability on the telescope.

M-FOSC-EP is a multi-mode instrument that would fulfill the requirements of seeing limited imaging in various filters, low resolution (R$\sim$500-800) spectroscopy, and intermediate resolution spectro-polarimetry (R$\sim$15000) on PRL 2.5m optical telescope. This design uses common collimator optics, followed by a movable fold mirror to direct the incoming telescope beam into either of the low-resolution and spectro-polarimetry modules, which are equipped with their separate detector system. The spectro-polarimetry mode was conceptualized with a traditional half-wave-plate plus Wollaston prism-based polarization measurement set-up in conjunction with an intermediate resolution Echelle spectrometer. The optical design of the instrument has successfully been developed, and the derived performance values are most suitable to achieve the scientific objectives of the instrument. The optical design is developed to achieve RMS spot diameters in the range of 1 to 1.5 pixels, including the effects of tolerances and temperature variations for all the instrument modes. Various other aspects of the optical design, like efficiency, resolutions, cross-talk, etc., are also evaluated. Currently, the mechanical system of M-FOSC-EP is being designed and will be commissioned around late 2023/early 2024.

As a precursor of M-FOSC-EP, a prototype spectro-polarimeter named ProtoPol is also being developed with commercially off-the-shelf optical components, which help immensely in the rapid development of this instrument. It provides moderate resolution (R$\sim$6000-7000) spectro-polarimetry and could be used on existing 1.2m as well as on upcoming 2.5m PRL telescopes. We have also developed the preliminary mechanical system design (CAD model) for the ProtoPol. The engineering team of ProtoPol later developed a full-fledged mechanical system. At the time of writing this thesis, the mechanical design of ProtoPol was completed, most of the optical components were procured, and its various mechanical parts were fabricated. ProtoPol is expected to be on the telescope by the end of 2022.

M-FOSC-EP and ProtoPol are being developed as facility instruments and would cater to the general requirements of Astronomy and Astrophysics (A&A) PRL division for imaging and spectroscopy in visible wavebands. It should be mentioned that the optical design of the M-FOSC-EP instrument described in this thesis has been discussed and approved by a national-level Technical Evaluation Committee (TEC) for the M-FOSC-EP instrument (constituted by Director, Physical Research Laboratory, Ahmedabad) for its realization.

6.2 Future Work

The successful completion of the projects that were set at the onset of this thesis work paved the way for several research projects that would be explored in the immediate future. These belong to both the instrumentation, simulations, and observational domains. Below we are describing some of them:

- **Development of ProtoPol:** The optical and preliminary opto-mechanical design of ProtoPol has been completed during this thesis work. The other mechanical engineers in the team did the final mechanical design and engineering level fine-tuning of the mechanical system, and the instrument is currently being fabricated. The optical and opto-mechanical components of the instrument have been procured and available in the laboratory. In the near future, the plan is to start the assembly-integration-test of the instrument in the laboratory and commission it on PRL 2.5m telescope along with a suitable observing characterization program.

- **Polarization aspects in novae and symbiotic system with ProtoPol:** The line profile variation in novae & symbiotics could arise due to changes in the optical depth morphology. Spectro-polarimetry is a suitable technique to explore such possibilities by measuring the wavelength-dependent polarization. The temporal variation in line polarization and intrinsic continuum polarization in novae may help us to understand the nova ejecta geometry (Kawakita et al., 2019). Further, the symbiotic systems show the O VI Raman scattered line, which is polarized in nature. Harries & Howarth (1996) shows that the line was found to be stable in intensity profiles for the line, but there were significant changes in both magnitude and direction of the polarization. It would be interesting to do such kinds of studies with the ProtoPol instrument.

- **Detailed science and performance simulation of M-FOSC-EP:** The optical design of M-FOSC-EP and various design analyses have been completed during this thesis work. While basic simulations were done to estimate the expected performance of the instrument, more detailed science simulations are essential to evaluate the final performance of the instrument in terms of the various instrument and observing parameters. Such simulation studies are extremely useful to further optimize the instrument performance with respect to various types of proposed science cases. This will also provide the observing limitations of the instrument to study various astrophysical objects with their required polarization accuracy, signal-to-noise ratio, etc. The performance simulations would involve the mathematical modeling of the instrument, its optics, detector, etc., to produce the final simulated spectra on the detector. Some parts of the data analysis pipeline may be developed using these simulated data.

- **High-resolution spectroscopy instrumentation:** During the commissioning observations & performance verification of MFOSC-P, two observational programs were completed with large samples of M dwarfs. Interestingly, suitable instrumentation is required to study the M dwarfs and the detection of exoplanets around them. The high-resolution spectroscopy in the optical/NIR regime may help to explore the stellar properties of M dwarfs like effective temperature, surface gravity, metallicity, magnetic field strength, etc. It may also help to detect the exoplanet around M dwarfs. After a good working experience with low/intermediate spectrographs, it would be interesting to explore the high-resolution spectrograph's instrumentation, design, and development aspects.

The success of MFOSC-P on the 1.2m PRL telescope has proved that the small aperture telescopes, once equipped with suitable instrumentation, can be extremely productive. Such telescopes - being larger in number, usually have the advantage of offering ample observing time for high-cadence science cases such as novae and supernovae, etc. The high cadence observations of nova V2891 Cyg with MFOSC-P and the studies of its rare spectral evolution is one such example that shows the importance of having such a combination for transient studies. Studies of a large sample, such as M dwarfs (in this case), are also suitable projects where dedicated instrumentation and a good amount of telescope time are required. With the ongoing development of M-FOSC-EP and ProtoPol for the upcoming 2.5m telescope, we do hope that several such high cadence science cases would be explored for their spectro-polarimetry- a domain that has been relatively less explored.

Appendix A

Data Reduction Pipeline GUI

This appendix is presented for chapter 2

The figure shows graphical user interface (GUI), developed by the MFOSC-P engineering team, which provides the front end of the data reduction software.

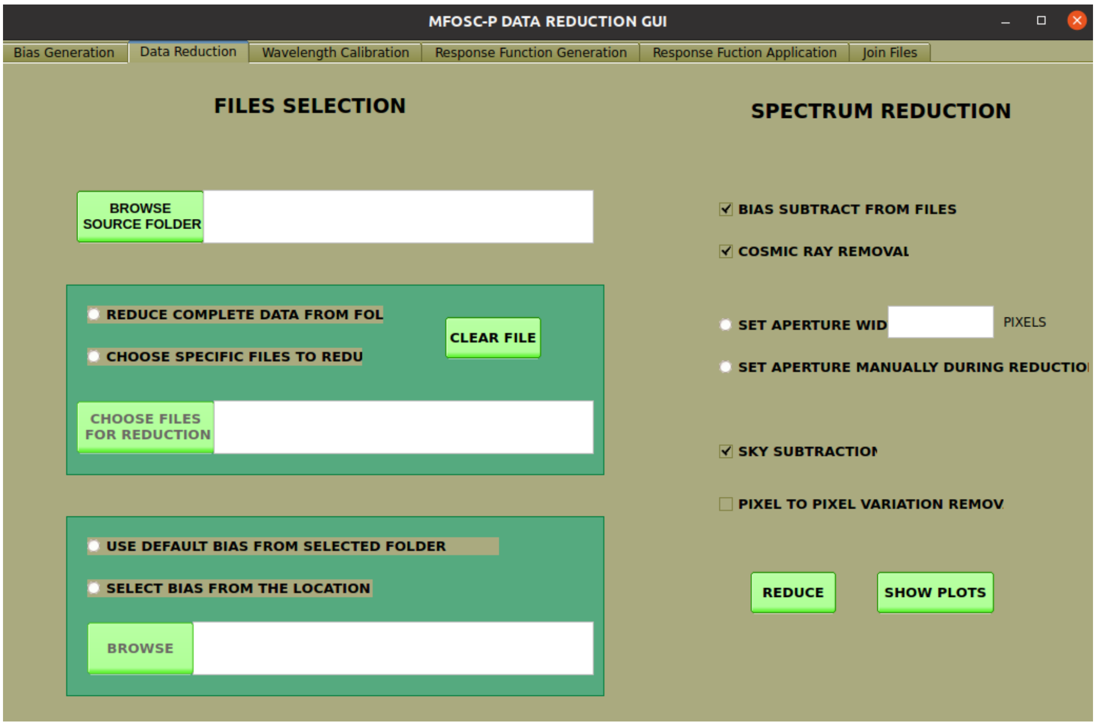

Figure A.1: The figure shows graphical user interface (GUI), developed by the MFOSC-P engineering team.

Appendix B

This appendix is presented for chapter 3

B.1 Extension of Table 3.1

Table B.1:

Source Name	RA	Dec	V (mag)	R (mag)	I (mag)	J (mag)	H (mag)	K (mag)	GAIA parallex (mas)	Distance (parsec)
Css833	13h48m34.02s	+31d59m56.89s	12.34	11.91	-	9.02	8.43	8.22	34.083	29.34
G123-74	12h57m32.41s	+40d57m00.89s	13.23	12.43	10.20	9.22	8.57	8.38	24.400	40.98
G138-64	16h46m13.76s	+16d28m41.08s	11.65	10.60	9.27	7.95	7.29	7.09	63.407	15.77
G138-7	16h11m28.10s	+07d03m59.98s	14.08	13.41	10.60	9.77	9.28	9.02	36.411	27.46
G177-8	12h58m17.17s	+52d36m43.70s	13.19	12.40	10.40	9.29	8.72	8.50	38.105	26.24
G19-12	17h04m49.57s	+01d30m35.47s	13.47	12.92	10.90	9.60	8.97	8.75	-	-
GJ3584	10h04m32.76s	+05d33m41.25s	12.67	12.22	9.90	9.02	8.40	8.18	-	-
GJ3696	11h58m17.61s	+42d34m28.96s	14.43	13.76	10.60	9.59	8.98	8.71	46.028	21.73
GJ3697	11h58m59.45s	+42d39m39.81s	12.09	11.65	9.90	8.64	8.05	7.82	-	-
GJ3763	13h08m50.52s	+16d22m03.58s	13.48	12.71	10.20	9.26	8.65	8.41	35.918	27.84
GJ3793	13h34m49.35s	+20d11m38.67s	14.25	13.42	10.80	9.67	9.10	8.85	18.232	54.85
GJ3822	14h02m19.62s	+13d41m22.76s	10.64	9.69	8.68	7.56	6.89	6.71	49.175	20.34
GJ3873	14h54m27.92s	+35d32m56.94s	12.55	12.13	9.50	8.24	7.71	7.47	67.072	14.91
GJ3895	15h11m55.96s	+17d57m16.42s	13.98	12.90	10.60	9.56	9.06	8.77	41.228	24.26
LP324-18	13h51m45.13s	+31d42m57.67s	13.40	12.46	10.60	9.59	8.93	8.75	14.402	69.44
LP324-72	14h08m10.47s	+28d11m13.93s	12.75	12.31	10.60	9.73	9.06	8.90	19.749	50.64
LP378-897	13h16m40.56s	+23d15m42.43s	13.51	13.03	10.70	9.76	9.11	8.85	27.695	36.11
LP435-110	12h26m38.10s	+17d28m11.14s	13.63	12.74	10.50	9.64	9.01	8.79	25.938	38.55
LP671-33	10h46m07.05s	-08d22m14.77s	12.74	12.32	11.00	9.86	9.21	9.03	17.702	56.49
LP738-44	13h37m30.00s	-10d48m34.92s	12.46	12.10	-	9.73	9.09	8.91	-	-
StKM1-1125	14h08m40.58s	+23d50m54.94s	12.34	11.86	10.20	9.29	8.62	8.40	20.267	49.34
StKM1-1077	13h35m16.12s	+30d10m56.67s	11.67	11.30	-	8.76	8.14	7.91	25.689	38.93
StM186	13h41m27.65s	+48d54m45.87s	12.98	12.62	10.20	9.00	8.45	8.19	-	-
TYC2009-522-1	14h04m10.24s	+26d26m24.02s	12.33	11.92	-	9.83	9.21	9.03	14.545	68.75
UCAC3 160-122037	13h16m49.39s	-10d19m18.27s	13.92	13.71	11.29	9.97	9.43	9.11	-	10.00
UCAC4 396-055485	13h21m56.31s	-10d52m09.88s	13.90	13.70	11.00	9.52	8.82	8.62	18.818	53.14
UCAC4 407-056568	13h26m56.92s	-08d45m47.01s	12.99	12.58	-	9.45	8.86	8.59	-	-
UCAC4 407-057475	13h55m12.70s	-08d42m25.93s	13.00	12.80	-	9.25	8.65	8.40	28.976	34.51
UCAC4 421-056421	12h06m07.44s	-05d50m01.88s	13.16	12.77	-	9.97	9.33	9.06	18.425	54.27
UCAC4 436-076101	18h25m48.64s	-02d58m17.15s	13.05	12.64	-	9.62	8.95	8.75	21.076	47.45
UCAC4 448-055886	13h26m26.40s	-00d26m52.86s	12.48	12.07	-	9.89	9.28	9.08	13.105	76.31

Table B.2: Continue Table B.1

Source Name	RA	Dec	V (mag)	R (mag)	I (mag)	J (mag)	H (mag)	K (mag)	GAIA parallax (mas)	Distance (parsec)
UCAC4 450-057508	15h09m50.64s	-00d07m51.77s	12.33	11.91	-	9.51	8.90	8.69	19.318	51.77
UCAC4 451-054724	13h27m06.68s	+00d00m48.29s	13.02	12.57	-	9.74	9.13	8.91	23.360	42.81
UCAC4 451-055381	13h51m13.78s	+00d04m26.98s	13.06	12.82	-	9.90	9.25	9.04	18.456	54.18
UCAC4 451-081123	18h27m41.08s	+00d11m15.07s	12.92	12.65	-	9.48	8.89	8.60	-	-
UCAC4 467-056893	16h50m11.00s	+03d14m40.08s	14.03	13.30	-	9.72	9.19	8.92	-	-
UCAC4 484-057552	15h29m48.62s	+06d38m16.52s	12.69	12.23	-	9.99	9.34	9.16	10.529	94.97
UCAC4 496-060421	13h37m17.62s	+09d08m00.56s	12.86	12.48	-	9.34	8.77	8.50	27.347	36.57
UCAC4 528-054911	12h44m24.96s	+15d32m12.49s	13.86	13.45	-	9.99	9.40	9.16	23.280	42.96
UCAC4 534-051996	11h52m20.53s	+16d40m19.14s	13.54	13.16	-	9.73	9.17	8.92	34.955	28.61
UCAC4 540-054017	13h27m30.59s	+17d48m08.31s	12.66	12.27	-	9.83	9.18	9.01	15.333	65.22
UCAC4 546-052448	12h54m10.86s	+19d01m16.66s	13.50	13.27	-	9.59	8.94	8.69	31.123	32.13
UCAC4 548-070636	18h20m35.82s	+19d27m55.67s	12.81	12.21	10.30	9.57	8.88	8.70	17.700	56.50
UCAC4 550-052262	13h15m49.21s	+19d57m07.95s	13.58	13.15	-	9.87	9.25	8.99	28.602	34.96
UCAC4 570-051422	14h08m40.58s	+23d50m54.94s	12.34	11.86	10.20	9.29	8.62	8.40	20.267	49.34
UCAC4 570-051538	14h14m35.09s	+23d57m24.84s	12.53	12.39	10.70	9.78	9.13	8.98	13.737	72.80
UCAC4 574-047909	12h35m33.43s	+24d39m18.44s	13.43	13.05	10.80	9.93	9.25	9.06	13.174	75.91
UCAC4 587-051209	15h11m04.82s	+27d12m44.71s	13.13	12.58	10.60	9.53	8.93	8.70	24.985	40.02
UCAC4 599-049146	11h59m13.54s	+29d36m09.07s	13.26	12.64	-	9.89	9.34	9.11	-	-
UCAC4 605-050828	14h04m08.56s	+30d49m34.50s	13.03	12.54	-	9.43	8.76	8.52	26.001	38.46
UCAC4 607-049137	14h10m15.46s	+31d15m36.55s	13.86	13.26	-	9.96	9.30	9.03	-	-
UCAC4 615-064218	18h44m20.37s	+32d50m46.33s	13.73	13.06	-	9.65	9.05	8.80	29.039	34.44
UCAC4 629-047283	13h25m55.16s	+35d46m42.88s	13.48	12.82	10.40	9.64	9.09	8.84	29.349	34.07
UCAC4 630-046962	11h52m57.15s	+35d54m45.91s	13.69	13.41	11.20	9.96	9.35	9.13	25.112	39.82
UCAC4 640-048822	14h07m07.51s	+37d52m22.99s	12.57	12.17	10.50	9.67	9.02	8.83	17.232	58.03
UCAC4 641-058022	18h06m17.74s	+38d01m49.79s	12.23	11.55	10.20	9.32	8.66	8.48	8.670	115.34
UCAC4 647-050041	12h54m29.25s	+39d19m56.78s	13.32	12.89	10.70	9.97	9.35	9.13	19.221	52.03
UCAC4 687-054755	13h25m18.24s	+47d20m37.32s	12.68	12.16	10.50	9.74	9.12	8.89	17.925	55.79
UCAC4 719-054147	15h25m48.82s	+53d44m16.30s	12.70	12.26	-	9.86	9.21	9.02	17.079	58.55
UCAC4 724-051511	13h27m01.69s	+54d36m13.77s	12.88	12.61	10.90	9.87	9.27	9.04	19.643	50.91
UCAC4 731-051425	13h17m23.17s	+56d10m13.50s	13.38	13.09	10.80	9.80	9.22	8.98	26.768	37.36
UCAC4 780-025091	13h11m59.55s	+65d50m01.79s	12.95	12.58	10.60	9.71	9.06	8.84	27.740	36.05
UCAC4 413-059942	14h16m33.28s	-07d25m38.24s	13.76	13.47	-	9.81	9.20	8.94	17.242	58.00
UCAC4 413-060157	14h23m01.24s	-07d34m01.11s	13.20	12.92	10.38	9.59	8.99	8.73	31.004	32.25
UCAC4 457-046840	10h06m21.82s	+01d21m23.18s	13.77	13.57	-	9.53	9.00	8.70	39.547	25.29
UCAC4 462-046617	10h35m46.92s	+02d15m58.21s	13.57	13.23	-	9.83	9.22	8.97	-	-
UCAC4 492-058611	13h49m07.33s	+08d23m36.09s	12.18	11.67	-	9.34	8.76	8.55	17.878	55.94
UCAC4 518-059332	15h47m11.96s	+13d34m40.78s	13.15	12.78	-	9.89	9.20	9.03	-	-
UCAC4 529-059437	16h27m46.42s	+15d42m06.13s	13.16	12.70	11.10	9.98	9.38	9.17	20.594	48.56
UCAC4 536-067333	17h44m12.95s	+17d06m12.14s	13.32	12.81	10.80	9.94	9.32	9.11	19.410	51.52
UCAC4 537-053981	13h35m12.46s	+17d14m08.88s	13.19	12.73	10.80	9.87	9.21	9.03	13.898	71.95
UCAC4 544-056450	15h51m39.13s	+18d40m23.54s	13.05	12.53	10.60	9.80	9.11	8.90	20.595	48.56
UCAC4 547-049435	11h05m19.44s	+19d18m34.24s	13.82	13.35	-	9.87	9.28	9.01	23.696	42.20
UCAC4 562-051219	12h23m43.46s	+22d15m17.08s	12.36	11.95	10.50	9.89	9.31	9.14	10.281	97.27
UCAC4 562-057449	16h38m25.33s	+22d22m41.54s	13.06	12.54	10.80	9.61	9.05	8.82	30.562	32.72
UCAC4 598-053572	15h39m05.72s	+29d31m40.62s	13.11	12.65	-	9.76	9.18	8.94	23.604	42.37
UCAC4 629-050950	16h27m37.57s	+35d41m42.94s	13.71	13.31	10.60	9.60	9.02	8.74	35.924	27.84
UCAC4 647-048900	11h31m16.41s	+39d23m02.91s	13.05	12.64	10.60	9.70	9.12	8.88	27.390	36.51
UCAC4 682-053954	14h13m46.76s	+46d18m22.73s	13.14	12.64	10.40	9.43	8.80	8.59	25.434	39.32
UCAC4 507-054072	13h15m47.39s	+11d16m25.77s	13.20	12.77	-	9.76	9.16	8.95	19.186	52.12

B.2 Optical spectra of M dwarfs observed with the MFOSC-P

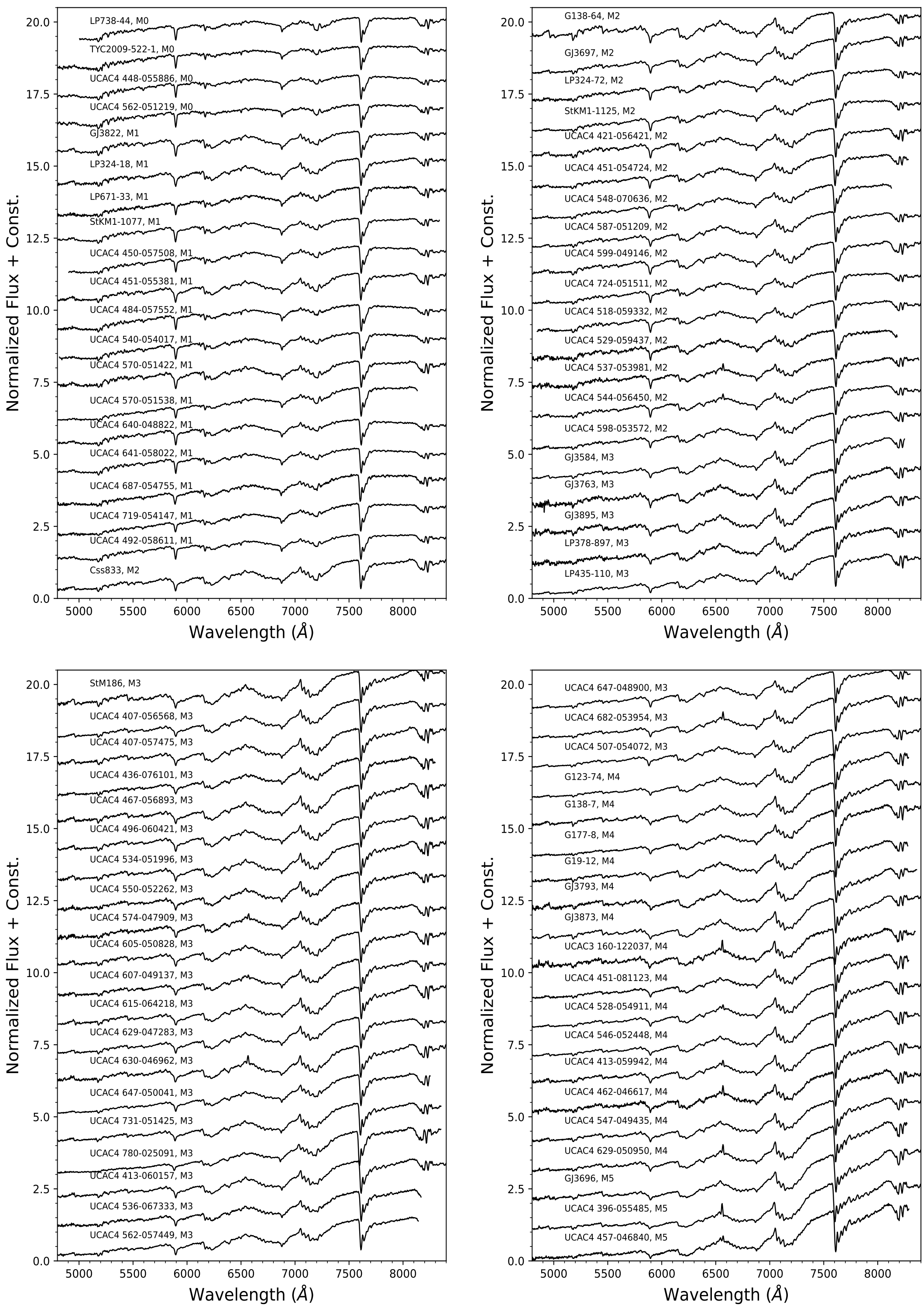

Figure B.1: Optical spectra of M dwarfs observed with the MFOSC-P.

B.3 Comparison of observed spectra

Comparison of observed spectra of M dwarfs (black) ranges from M0 to M5, with the best fit BT-Settl synthetic spectra (red). The model displayed here have log g ranges from 4.5 to 5.5 and T_{eff} ranges from 3900 K to 3100 K. Telluric features near 7600 to 7700 Å were ignored from the chi-square.

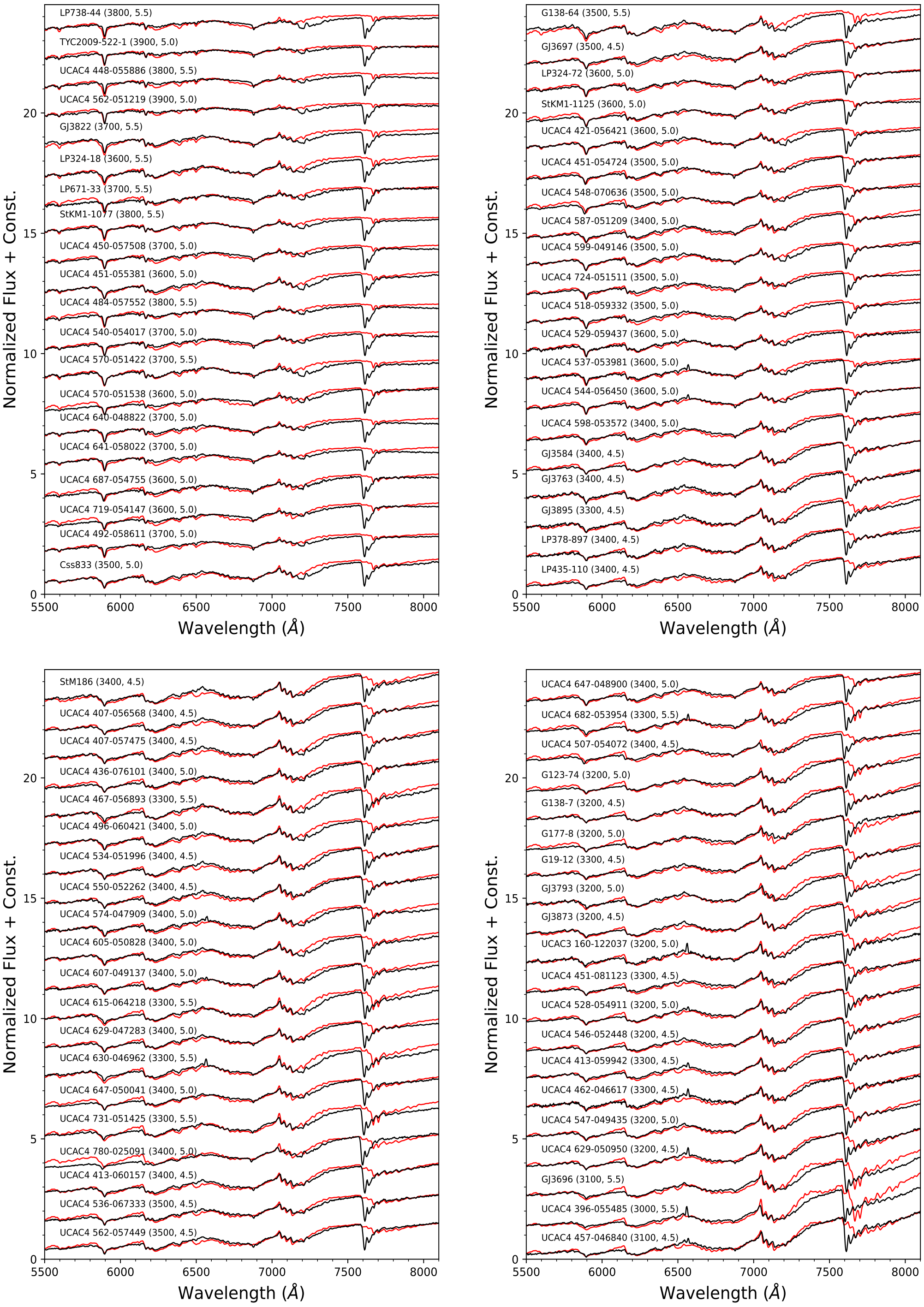

Figure B.2: Comparison of observed spectra of M dwarfs (black) ranges from M0 to M5, with the best fit BT-Settl synthetic spectra (red)

B.4 Extension of Table 3.2

Table B.3:

Source Name	Photometric Spectral Type (Lépine & Gaidos, 2011)	Derived Spectral Type (This study)	T_{eff} (K)	$\log g$ (cm/sec^2)	Source Name	Photometric Spectral Type (Lépine & Gaidos, 2011)	Derived Spectral Type (This study)	T_{eff} (K)	$\log g$ (cm/sec^2)
Css833	M2	M2	3500	5	UCAC4 540-054017	M0	M1	3700	5
G123-74	M3	M2	3500	5.5	UCAC4 546-052448	M4	M4	3200	4.5
G138-64	M3	M4	3200	5	UCAC4 548-070636	M2	M2	3500	5
G138-7	M4	M4	3200	5	UCAC4 550-052262	M3	M3	3400	4.5
G177-8	M3	M4	3200	5	UCAC4 570-051422	M1	M1	3700	5.5
G19-12	M3	M4	3300	5	UCAC4 570-051538	M1	M1	3600	5
GJ3584	M3	M3	3400	4.5	UCAC4 574-047909*	M3	M3	3400	5
GJ3696	M5	M5	3100	5.5	UCAC4 587-051209	M2	M2	3400	5
GJ3697	M2	M2	3500	4.5	UCAC4 599-049146	M2	M2	3500	5
GJ3763	M4	M3	3400	4.5	UCAC4 605-050828	M3	M3	3400	5
GJ3793	M4	M4	3200	5	UCAC4 607-049137	M3	M3	3400	5
GJ3822	M0	M1	3700	5.5	UCAC4 615-064218	M3	M3	3300	5
GJ3873	M4	M4	3200	5	UCAC4 629-047283	M3	M3	3400	5
GJ3895	M4	M3	3300	4.5	UCAC4 630-046962*	M3	M3	3300	5
LP324-18	M3	M1	3600	5.5	UCAC4 640-048822	M1	M1	3700	5
LP324-72	M0	M2	3600	5	UCAC4 641-058022	M0	M1	3700	5
LP378-897	M4	M3	3300	5	UCAC4 647-050041	M2	M3	3400	5
LP435-110	M3	M3	3400	4.5	UCAC4 687-054755	M1	M1	3600	5
LP671-33	M0	M1	3700	5.5	UCAC4 719-054147	M1	M1	3600	5
LP738-44	M0	M0	3800	5.5	UCAC4 724-051511	M2	M2	3500	5
StKM1-1125	M1	M2	3600	5	UCAC4 731-051425	M4	M3	3300	5
StKM1-1077	M0	M1	3800	5.5	UCAC4 780-025091	M2	M3	3300	5
StM186	M4	M3	3400	4.5	UCAC4 413-059942*	M4	M4	3300	5
TYC2009-522-1	M0	M0	3900	5	UCAC4 413-060157	M1	M3	3400	4.5
UCAC3 160-122037*	M4	M4	3200	5	UCAC4 457-046840	M4	M5	3100	5
UCAC4 396-055485*	M4	M5	3000	5	UCAC4 462-046617*	M3	M4	3300	5
UCAC4 407-056568	M3	M3	3400	4.5	UCAC4 492-058611	M0	M1	3700	5
UCAC4 407-057475	M3	M3	3400	4.5	UCAC4 518-059332	M3	M2	3500	5
UCAC4 421-056421	M3	M2	3600	5	UCAC4 529-059437	M3	M2	3600	5
UCAC4 436-076101	M2	M3	3400	5	UCAC4 536-067333	M3	M3	3500	4.5
UCAC4 448-055886	M1	M0	3800	5.5	UCAC4 537-053981*	M3	M2	3600	5
UCAC4 450-057508	M0	M1	3700	5	UCAC4 544-056450*	M2	M2	3600	5
UCAC4 451-054724	M2	M2	3500	5	UCAC4 547-049435	M4	M4	3200	5
UCAC4 451-055381	M2	M1	3600	5	UCAC4 562-051219	M0	M0	3900	5
UCAC4 451-081123	M3	M4	3300	5	UCAC4 562-057449	M3	M3	3500	4.5
UCAC4 467-056893	M4	M3	3300	5	UCAC4 598-053572	M3	M2	3400	5
UCAC4 484-057552	M1	M1	3800	5.5	UCAC4 629-050950*	M4	M4	3200	5
UCAC4 496-060421	M0	M3	3400	5	UCAC4 647-048900	M2	M3	3400	5
UCAC4 528-054911	M4	M4	3200	5	UCAC4 682-053954*	M3	M3	3300	5
UCAC4 534-051996	M4	M3	3300	5	UCAC4 507-054072	M3	M3	3400	4.5

* Hα emission at 6563 Å is detected.

B.5 Extension of Table 3.3

Table B.4: Extension of Table 3.3

Source ID	Source name	Spectral type	Magnitude (V-band)	Date of observation (UT)	Frame exposure time × No. of frames (s)	log g (cm s^{-2})	T_{eff} (K)
1	PM J03332+4615S	M0.0	13.09	2020-12-29.602	300sx14	5.0	3900
2	PM J03416+5513	M0.0	-	2021-02-01.600	300sx18	5.0	3800
3	PM J07151+1555	M0.0	11.37	2021-01-30.754	300sx18	5.0	4000
4	PM J23083-1524	M0.0	10.87	2020-11-26.563	300sx14	4.5	3900
5	PM J03322+4914S	M0.5	11.94	2021-02-03.680	300sx18	5.0	3700
6	PM J04595+0147	M0.5	10.11	2021-01-31.618	300sx18	5.0	3900
7	PM J10143+2104	M0.5	10.08	2020-12-29.882	300sx13	5.0	3800
8	PM J19026+3231	M0.5	11.57	2021-03-23.963	300sx16	5.0	3700
9	PM J23060+6355	M0.5	10.96	2020-12-27.599	300sx12	5.0	3700
10	PM J06310+5002	M1.0	-	2021-01-31.711	300sx19	5.0	3700
11	PM J08317+0545	M1.0	11.93	2021-01-30.854	300sx16	5.0	3800
12	PM J09193+6203	M1.0	-	2021-03-08.811	300sx16	5.5	3600
13	PM J12576+3513E	M1.0	-	2020-03-20.846	300sx15	5.0	3600
14	PM J15238+5609	M1.0	11.68	2021-03-22.832	300sx18	5.0	3800
15	PM J15581+4927	M1.0	-	2020-05-06.890	450sx8	5.5	3600
16	PM J04376-0229	M1.0	10.59	2020-12-29.755	300sx13	5.0	3600
17	PM J00428+3532	M1.5	-	2020-12-29.679	300sx13	5.0	3500
18	PM J05402+1239	M1.5	11.35	2021-03-02.606	300sx18	5.0	3700
19	PM J06262+2349	M1.5	11.82	2021-03-26.681	300sx15	5.0	3500
20	PM J07295+3556	M1.5	11.88	2021-02-03.787	300sx18	5.0	3600
21	PM J13007+1222	M1.5	9.75	2021-01-31.905	300sx18	4.5	3900
22	PM J15416+1828	M1.5	12.32	2021-02-01.007	300sx12	5.0	3600
23	PM J16220+2250	M1.5	12.12	2021-03-25.850	300sx18	5.0	3700
24	PM J22387-2037	M1.5	9.08	2020-12-02.626	200sx18	5.0	3600
25	PM J04284+1741	M2.0	12.12	2021-02-01.683	300sx18	5.0	3500
26	PM J06212+4414	M2.0	-	2021-01-31.825	300sx9	5.0	3500
27	PM J11201-1029	M2.0	11.25	2021-03-23.772	300sx18	5.0	3500
28	PM J13518+1247	M2.0	12.25	2021-02-01.940	300sx18	5.0	3800
29	PM J15218+2058	M2.0	10.00	2021-03-08.973	200sx22	5.0	3600
30	PM J16170+5516	M2.0	9.46	2020-05-06.752	200sx16	5.0	3600
31	PM J06596+0545	M2.5	12.50	2021-02-01.764	300sx18	5.0	3500
32	PM J09177+4612	M2.5	11.58	2021-01-28.857	300sx20	5.0	3500
33	PM J10043+5023	M2.5	-	2021-02-01.851	300sx18	5.0	3500
34	PM J11519+0731	M2.5	12.42	2021-03-08.902	300sx15	5.0	3500
35	PM J15557+6840	M2.5	11.97	2020-05-22.902	300sx12	5.0	3400
36	PM J04333+2359	M3.0	12.66	2021-02-02.597	300sx18	4.5	3500
37	PM J05091+1527	M3.0	-	2021-02-02.685	300sx17	5.0	3400
38	PM J05337+0156	M3.0	11.50	2020-11-27.854	200sx13	5.0	3400
39	PM J05547+1055	M3.0	-	2021-03-27.613	300sx18	4.5	3500
40	PM J07319+3613S	M3.0	-	2021-03-25.611	300sx18	5.0	3400
41	PM J07349+1445	M3.0	11.15	2021-02-02.786	300sx18	5.0	3400

Table B.5: Table B.4 continue...

Source ID	Source name	Spectral type	Magnitude (V-band)	Date of observation (UT)	Frame exposure time × No. of frames (s)	log g (cm s^{-2})	T_{eff} (K)
42	PM J11529+3554*	M3.0	13.69	2020-05-21.751	600sx9	5.0	3300
43	PM J12355+2439*	M3.0	13.43	2020-03-08.784	600sx10	5.0	3500
44	PM J13352+1714*	M3.0	13.19	2020-05-24.730	600sx9	5.0	3600
45	PM J14137+4618*	M3.0	13.14	2020-05-21.873	600sx9	5.0	3400
46	PM J04238+1455	M3.5	13.35	2020-11-26.785	500sx10	4.5	3500
47	PM J09302+2630	M3.5	-	2021-02-02.870	300sx18	4.5	3400
48	PM J09557+3521	M3.5	-	2021-02-02.967	300sx15	5.0	3300
49	PM J12485+4933	M3.5	12.51	2021-02-03.977	300sx15	5.0	3400
50	PM J12490+6606	M3.5	-	2021-03-26.764	300sx18	4.5	3500
51	PM J13417+5815	M3.5	12.54	2021-03-23.871	300sx18	5.0	3300
52	PM J16591+2058	M3.5	12.45	2021-03-26.892	300sx18	5.0	3400
53	PM J00325+0729	M4.0	12.80	2020-11-27.723	300sx12	4.5	3200
54	PM J01593+5831	M4.0	12.15	2020-11-27.786	300sx14	5.0	3200
55	PM J02088+4926	M4.0	12.45	2020-12-02.827	300sx14	5.0	3300
56	PM J05062+0439	M4.0	13.46	2021-02-12.597	300sx18	4.0	3200
57	PM J06000+0242	M4.0	11.31	2021-03-26.601	300sx18	5.0	3200
58	PM J07033+3441	M4.0	-	2021-02-12.685	300sx18	5.0	3200
59	PM J07100+3831	M4.0	11.52	2021-03-27.697	300sx18	5.0	3100
60	PM J09161+0153	M4.0	13.03	2021-02-24.75	300sx16	5.0	3300
61	PM J10357+0215*	M4.0	13.57	2020-05-22.665	600sx5	5.0	3400
62	PM J10360+0507	M4.0	12.64	2021-02-23.784	300sx18	5.0	3300
63	PM J11033+1337	M4.0	-	2021-03-24.744	300sx18	5.0	3300
64	PM J11118+3332S	M4.0	-	2021-02-24.827	300sx10	5.0	3300
65	PM J12156+5239	M4.0	12.56	2021-02-12.863	300sx18	5.0	3400
66	PM J13536+7737	M4.0	-	2021-02-12.971	300sx18	5.0	3100
67	PM J14165-0725*	M4.0	13.76	2020-05-22.806	600sx10	4.5	3400
68	PM J15126+4543	M4.0	13.33	2021-02-24.975	300sx15	5.0	3200
69	PM J05243-1601	M4.5	13.57	2020-12-02.899	300sx14	4.0	3000
70	PM J13317+2916	M4.5	12.02	2021-02-24.900	300sx15	5.0	3200
71	PM J17199+2630W	M4.5	11.34	2020-05-21.956	300sx9	5.0	3200
72	PM J01033+6221	M5.0	13.21	2020-11-28.675	400sx13	4.0	3000
73	PM J02002+1303	M5.0	12.30	2021-02-23.597	300sx13	5.0	3100
74	PM J06579+6219	M5.0	-	2021-02-24.600	300sx18	4.0	3000
75	PM J07364+0704	M5.0	13.24	2020-12-02.970	300sx16	5.5	3000
76	PM J09449-1220	M5.0	13.65	2020-11-27.914	300sx15	4.0	3200
77	PM J12142+0037	M5.0	-	2021-02-23.879	300sx18	4.0	3100
78	PM J13005+0541	M5.0	-	2021-02-23.972	300sx17	4.5	3100
79	PM J20298+0941	M5.0	-	2020-11-28.570	400sx12	5.0	3000
80	PM J12332+0901	M5.5	12.47	2020-12-29.950	300sx11	4.0	3200
81	PM J17338+1655	M5.5	14.38	2021-03-25.944	300sx18	5.5	3000
82	PM J10564+0700	M6.0	13.51	2020-11-27.989	300sx12	4.0	3000
83	PM J11055+4331	M6.5	14.45	2020-12-31.011	400sx9	5.5	3000

B.6 Time-varying Spectra of M dwarfs

The figures show the spectral times series (panel a), photometric light curves from TESS and Kepler/K2 databases (panel b), EWs light-curves for Hα and Hβ emissions (panel c) and their computed fractional structure functions (SFs) (panel d) for each of the sources observed with MFOSC-P instrument on PRL 1.2m telescope at Mt. Abu. Source ID, spectral type, and rotation period are also mentioned at the top of the panel (a). Data for Hα and Hβ are shown in red circles and black triangles, respectively. The Y-axis (ordinate) of the panel (a) is in arbitrary units of flux. Y-axes of panel (c) are in units of $\AA$ for Hα (left) and Hβ (right). Y-axes of the panel (d) are the fractional structure function (SF) for Hα (left) and Hβ (right). Units of X-axes (abscissa) of the panel (a), (c), and (d) are given at the bottom of these plots. The X-axis of the panel (b) - photometric light curves - is in units of days, and Y-axis is in arbitrary units of flux. See Fig.4 of the main text also for these units. For some sources, either light curves were not found or rotation periods could not be determined, and/or Hβ emission was not covered. Thus, these data are not presented for some of the sources.

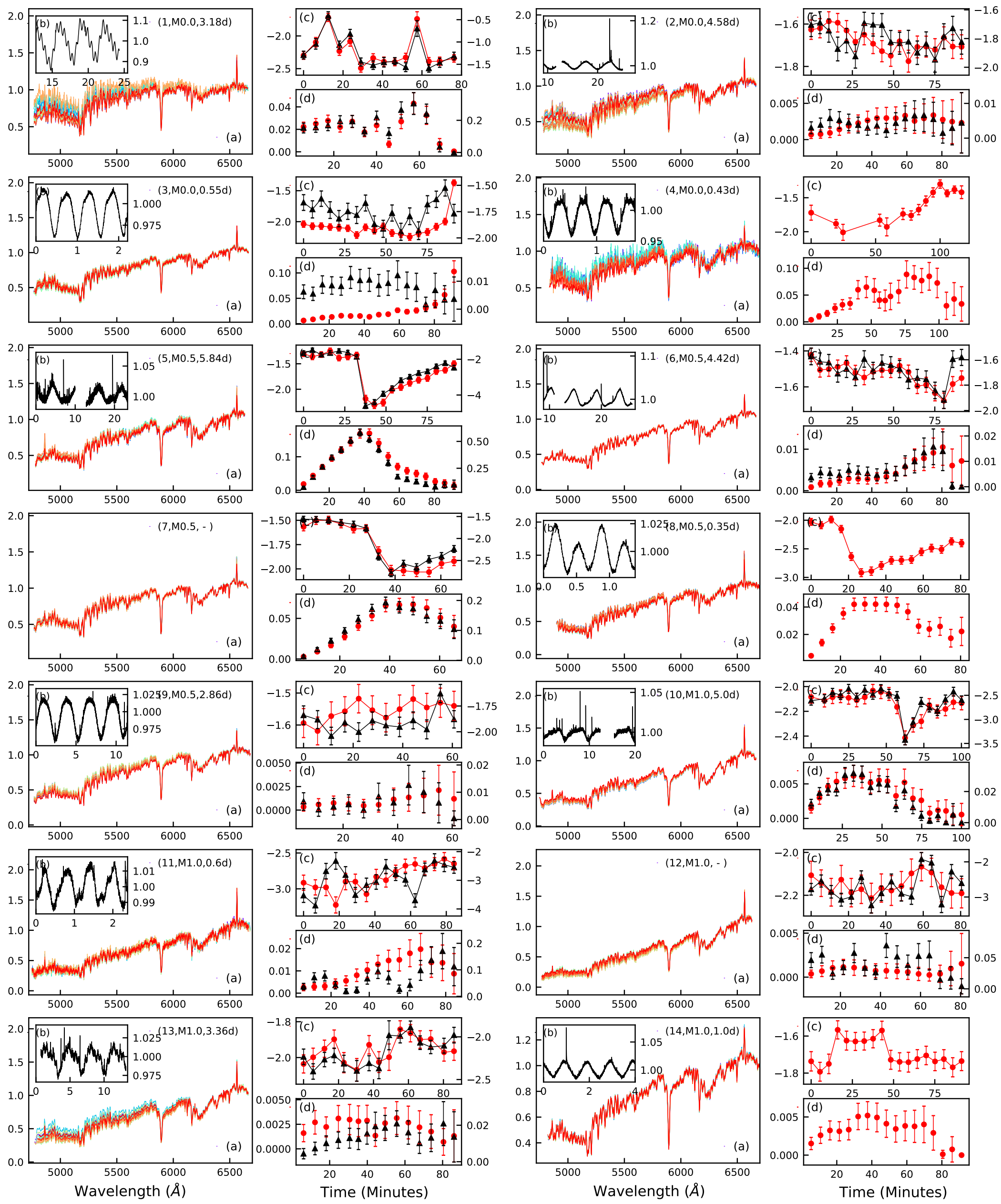

Figure B.3: Time-varying Spectra of M dwarfs

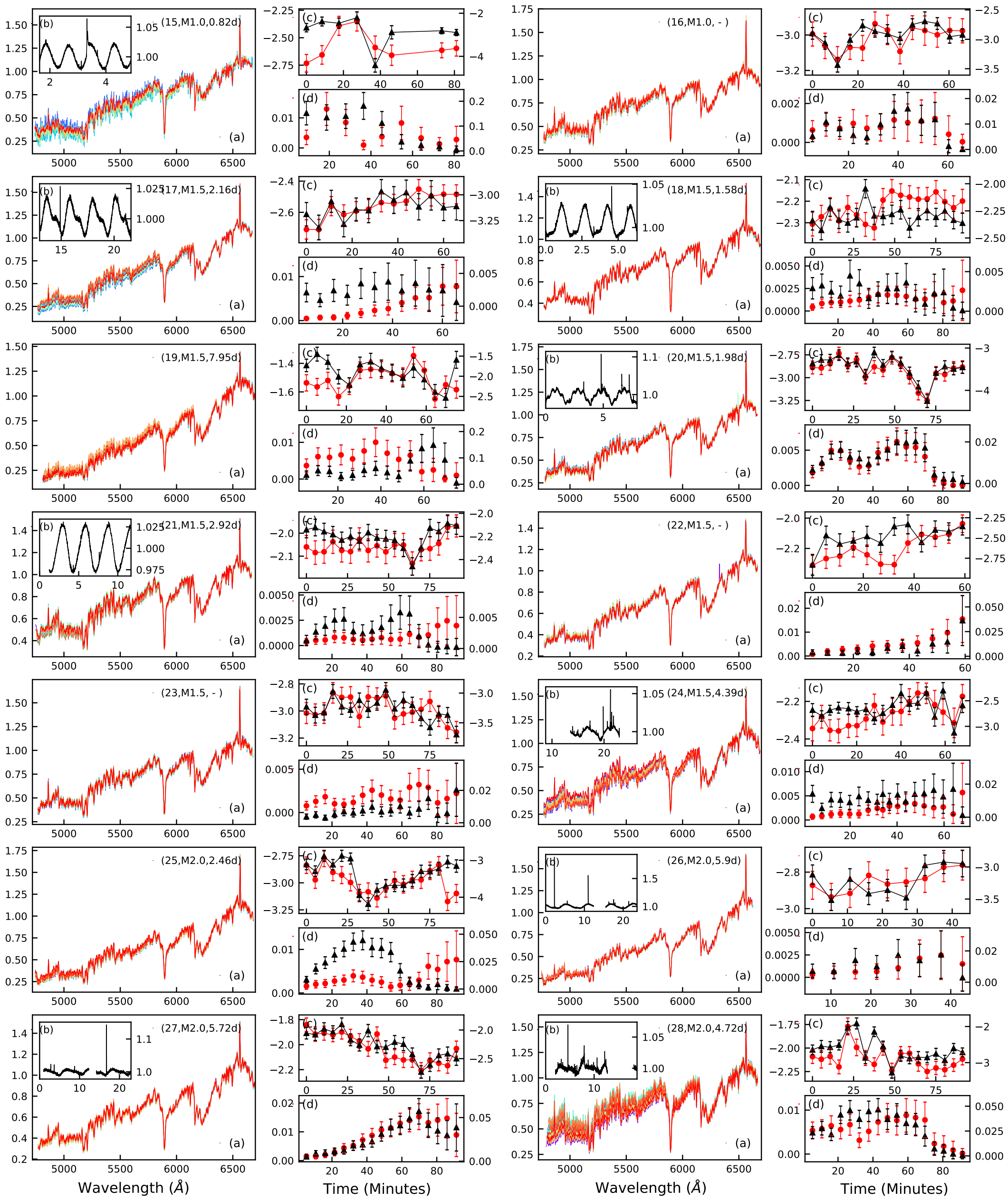

Figure B.4: Figure B.3 continue...

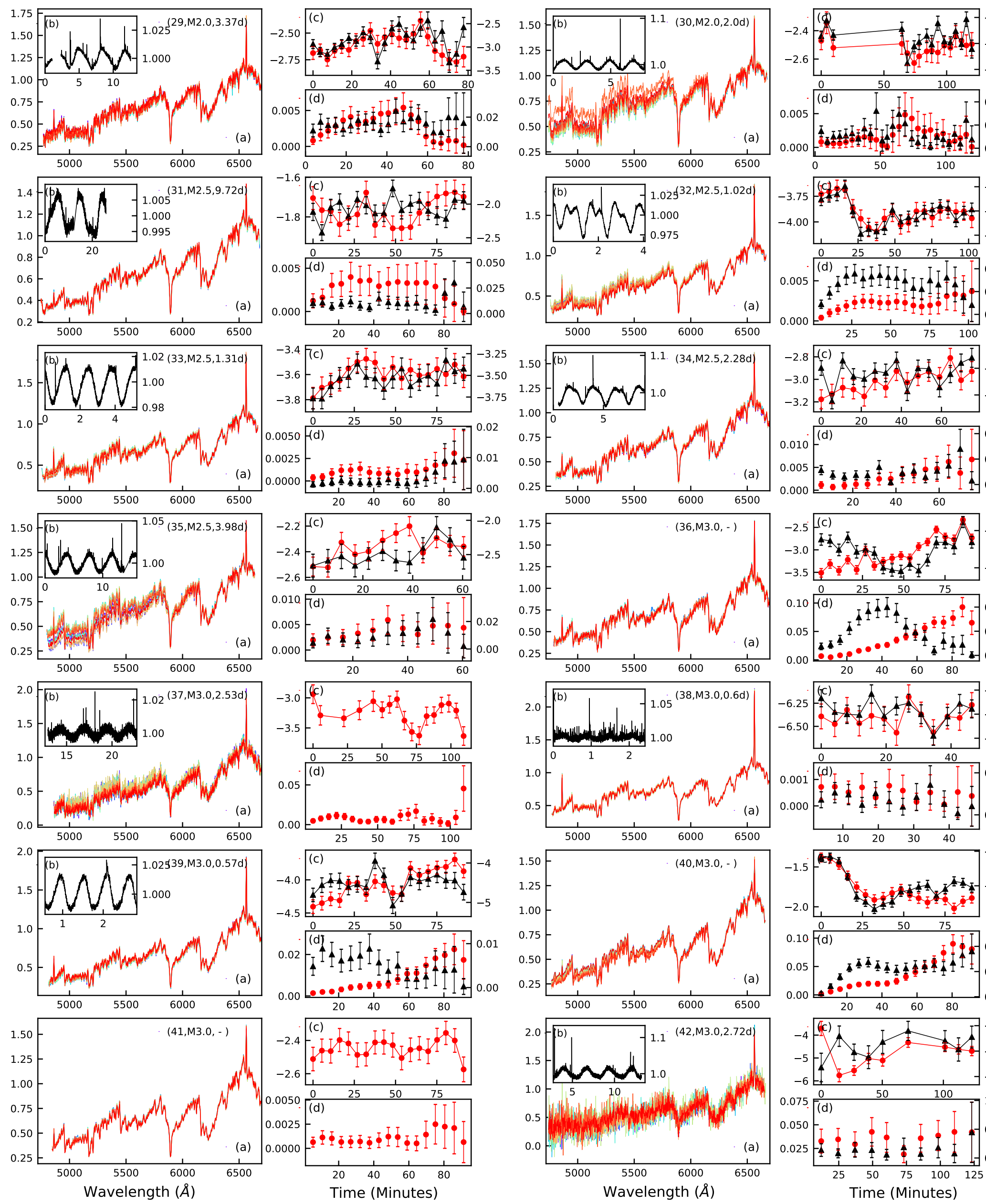

Figure B.5: Figure B.4 continue...

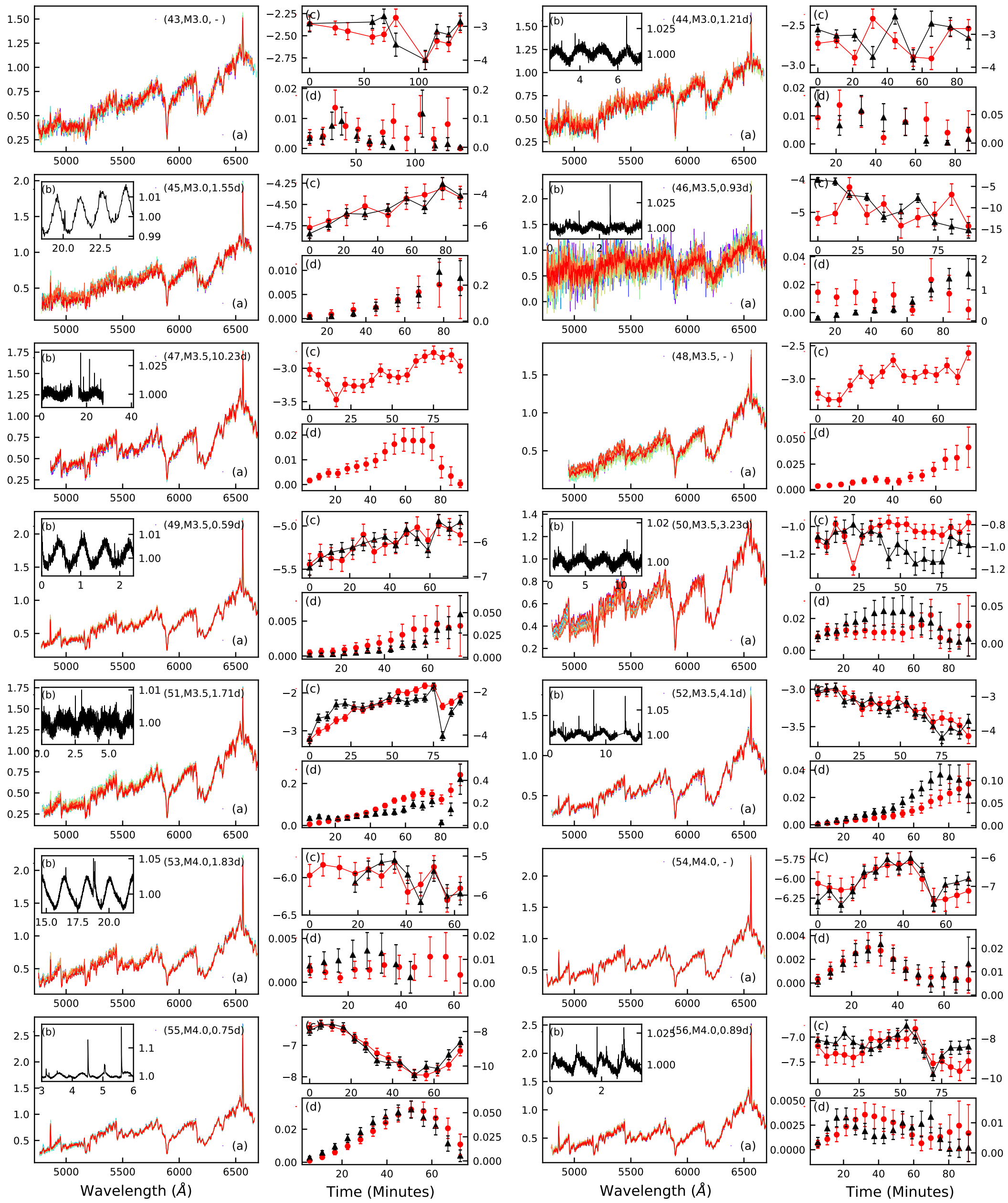

Figure B.6: Figure B.5 continue...

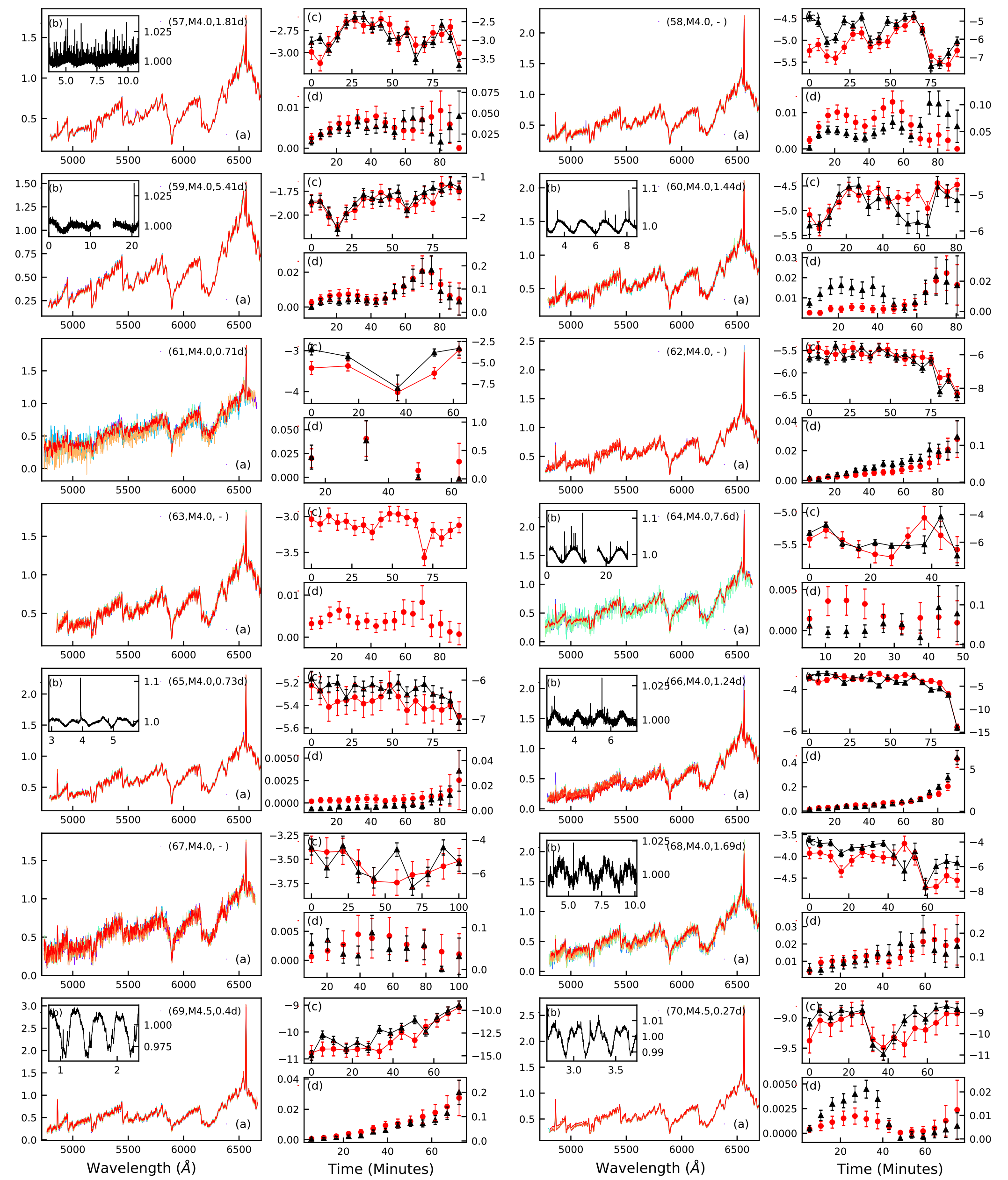

Figure B.7: Figure B.6 continue...

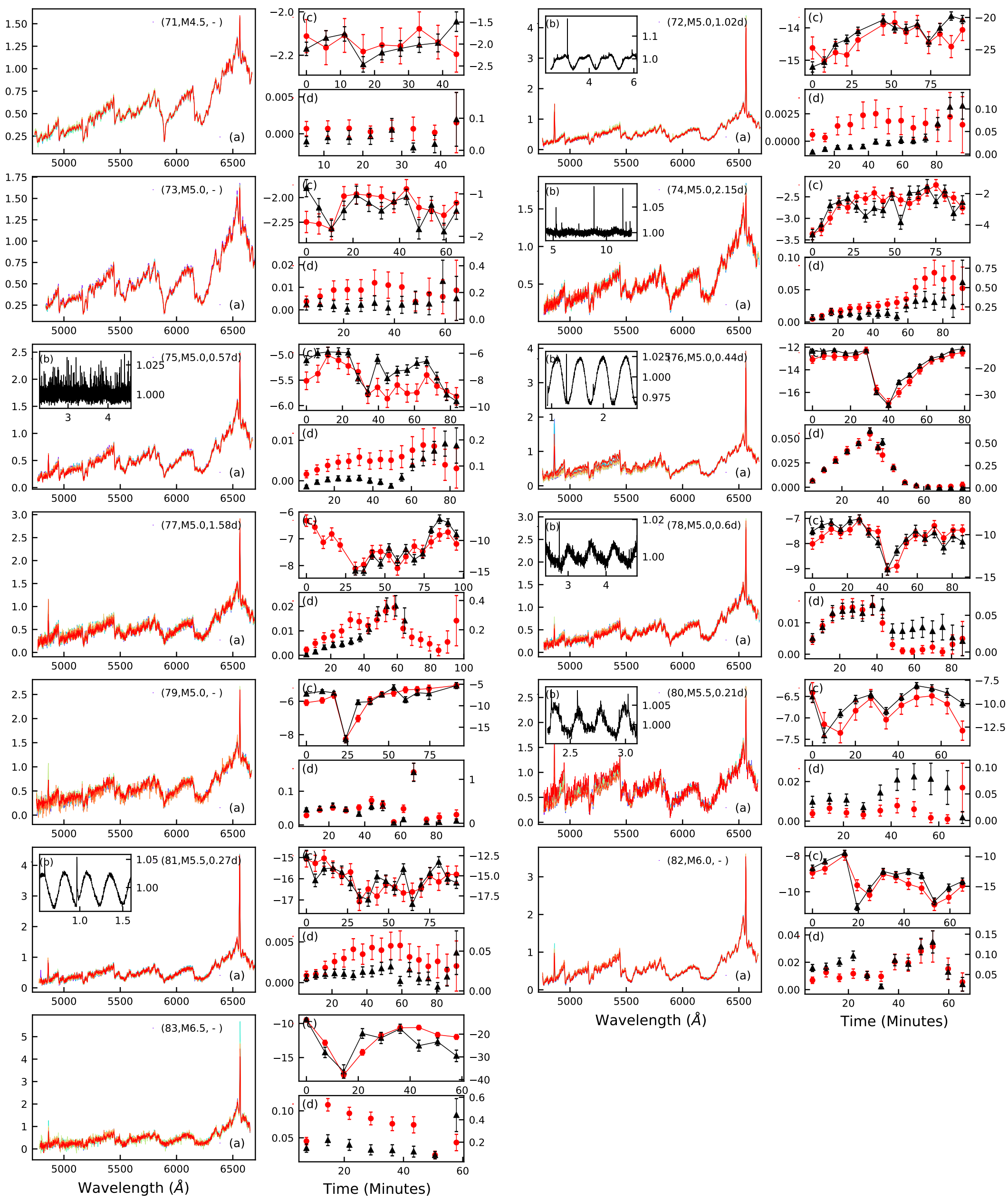

Figure B.8: Figure B.7 continue...

B.7 Extension of Table 3.4

Table B.6: Extension of Table 3.4

Source ID	Source name	emission line	Median Hα EW Hβ EW	Minimum Hα EW Hβ EW	Maximum Hα EW Hβ EW	Δ Hα EW Hβ EW	RMS Hα EW Hβ EW	Mean $\log_{10}(L_{H\alpha}/L_{bol})$ $\log_{10}(L_{H\beta}/L_{bol})$	P-value Hα Hβ
1	PM J03332+4615S*	Hα	-2.333 ± 0.065	-1.717 ± 0.062	-2.492 ± 0.061	0.775 ± 0.087	0.232 ± 0.022	-3.883	0.0000
		Hβ	-1.372 ± 0.085	-0.413 ± 0.091	-1.590 ± 0.086	1.177 ± 0.125	0.349 ± 0.031	-4.199	0.0000
2	PM J03416+5513	Hα	-1.688 ± 0.047	-1.587 ± 0.045	-1.775 ± 0.052	0.188 ± 0.068	0.051 ± 0.012	-3.984	0.2298
		Hβ	-1.818 ± 0.085	-1.690 ± 0.076	-1.947 ± 0.087	0.258 ± 0.116	0.080 ± 0.020	-3.981	0.4134
3	PM J07151+1555*	Hα	-2.094 ± 0.052	-1.372 ± 0.046	-2.246 ± 0.055	0.874 ± 0.072	0.183 ± 0.012	-3.854	0.0000
		Hβ	-1.755 ± 0.076	-1.525 ± 0.077	-1.942 ± 0.081	0.417 ± 0.111	0.110 ± 0.019	-3.905	0.0062
4	PM J23083-1524*	Hα	-1.698 ± 0.110	-1.298 ± 0.061	-2.010 ± 0.117	0.711 ± 0.132	0.220 ± 0.025	-3.980	0.0000
		Hβ	-	-	-	-	-	-	-
5	PM J03322+4914S*	Hα	-1.637 ± 0.059	-1.249 ± 0.056	-2.311 ± 0.066	1.062 ± 0.087	0.346 ± 0.015	-3.960	0.0000
		Hβ	-2.431 ± 0.121	-1.486 ± 0.111	-4.612 ± 0.141	3.127 ± 0.179	0.979 ± 0.032	-3.766	0.0000
6	PM J04595+0147*	Hα	-1.516 ± 0.039	-1.421 ± 0.037	-1.677 ± 0.043	0.256 ± 0.057	0.061 ± 0.010	-4.033	0.0012
		Hβ	-1.673 ± 0.067	-1.574 ± 0.065	-1.916 ± 0.068	0.342 ± 0.094	0.091 ± 0.016	-4.030	0.0083
7	PM J10143+2104*	Hα	-1.817 ± 0.044	-1.499 ± 0.041	-2.033 ± 0.048	0.533 ± 0.063	0.219 ± 0.013	-3.973	0.0000
		Hβ	-2.239 ± 0.078	-1.560 ± 0.066	-2.787 ± 0.082	1.226 ± 0.105	0.456 ± 0.022	-3.940	0.0000
8	PM J19026+3231*	Hα	-2.532 ± 0.064	-1.988 ± 0.057	-2.918 ± 0.069	0.930 ± 0.090	0.290 ± 0.016	-3.815	0.0000
		Hβ	-	-	-	-	-	-	-
9	PM J23060+6355	Hα	-1.552 ± 0.045	-1.518 ± 0.045	-1.619 ± 0.043	0.101 ± 0.062	0.029 ± 0.013	-4.057	0.9234
		Hβ	-1.902 ± 0.091	-1.629 ± 0.089	-2.042 ± 0.085	0.413 ± 0.123	0.100 ± 0.027	-4.046	0.1749
10	PM J06310+5002*	Hα	-2.112 ± 0.053	-2.032 ± 0.049	-2.415 ± 0.056	0.382 ± 0.075	0.096 ± 0.013	-3.907	0.0000
		Hβ	-2.541 ± 0.086	-2.364 ± 0.086	-3.426 ± 0.102	1.062 ± 0.133	0.255 ± 0.023	-3.884	0.0000
11	PM J08317+0545*	Hα	-2.855 ± 0.096	-2.583 ± 0.088	-3.225 ± 0.112	0.642 ± 0.143	0.173 ± 0.026	-3.781	0.0000
		Hβ	-2.799 ± 0.221	-2.322 ± 0.248	-3.882 ± 0.259	1.560 ± 0.359	0.484 ± 0.065	-3.823	0.0000
12	PM J09193+6203	Hα	-2.164 ± 0.066	-2.067 ± 0.066	-2.213 ± 0.069	0.146 ± 0.096	0.041 ± 0.017	-3.865	0.9796
		Hβ	-2.816 ± 0.178	-1.923 ± 0.186	-3.238 ± 0.217	1.315 ± 0.286	0.382 ± 0.052	-3.776	0.0000
13	PM J12576+3513E*	Hα	-1.965 ± 0.051	-1.842 ± 0.047	-2.068 ± 0.063	0.226 ± 0.079	0.066 ± 0.014	-3.928	0.0479
		Hβ	-2.217 ± 0.085	-1.889 ± 0.074	-2.405 ± 0.090	0.517 ± 0.117	0.164 ± 0.028	-3.923	0.0000
14	PM J15238+5609*	Hα	-1.726 ± 0.051	-1.567 ± 0.049	-1.793 ± 0.051	0.226 ± 0.071	0.068 ± 0.012	-3.994	0.0112
		Hβ	-	-	-	-	-	-	-
15	PM J15581+4927*	Hα	-2.606 ± 0.068	-2.352 ± 0.087	-2.733 ± 0.080	0.381 ± 0.119	0.125 ± 0.032	-3.897	0.0162
		Hβ	-2.743 ± 0.139	-2.208 ± 0.270	-4.415 ± 0.316	2.207 ± 0.416	0.639 ± 0.110	-3.998	0.0000
16	PM J04376-0229	Hα	-2.994 ± 0.068	-2.936 ± 0.067	-3.137 ± 0.072	0.201 ± 0.098	0.060 ± 0.020	-3.720	0.6793
		Hβ	-2.911 ± 0.160	-2.695 ± 0.161	-3.437 ± 0.120	0.743 ± 0.201	0.185 ± 0.035	-3.753	0.0010
17	PM J00428+3532	Hα	-2.545 ± 0.061	-2.451 ± 0.061	-2.711 ± 0.065	0.260 ± 0.089	0.078 ± 0.018	-3.878	0.0655
		Hβ	-3.116 ± 0.128	-2.968 ± 0.116	-3.317 ± 0.120	0.349 ± 0.167	0.103 ± 0.035	-3.911	0.6763
18	PM J05402+1239	Hα	-2.215 ± 0.054	-2.153 ± 0.053	-2.324 ± 0.055	0.171 ± 0.077	0.053 ± 0.013	-3.931	0.4400
		Hβ	-2.309 ± 0.080	-2.046 ± 0.084	-2.429 ± 0.088	0.383 ± 0.122	0.082 ± 0.021	-4.028	0.4803
19	PM J06262+2349*	Hα	-1.520 ± 0.057	-1.346 ± 0.059	-1.649 ± 0.060	0.303 ± 0.084	0.079 ± 0.016	-4.039	0.0232
		Hβ	-1.804 ± 0.206	-1.452 ± 0.171	-2.538 ± 0.237	1.086 ± 0.292	0.297 ± 0.054	-3.976	0.0018
20	PM J07295+3556*	Hα	-2.892 ± 0.070	-2.733 ± 0.067	-3.249 ± 0.078	0.515 ± 0.102	0.122 ± 0.018	-3.775	0.0000
		Hβ	-3.381 ± 0.133	-3.103 ± 0.123	-4.253 ± 0.151	1.149 ± 0.195	0.268 ± 0.034	-3.766	0.0000
21	PM J13007+1222	Hα	-2.063 ± 0.050	-1.969 ± 0.048	-2.132 ± 0.051	0.164 ± 0.070	0.037 ± 0.012	-3.986	0.8947
		Hβ	-2.192 ± 0.074	-2.088 ± 0.075	-2.460 ± 0.075	0.371 ± 0.106	0.086 ± 0.018	-4.090	0.1217
22	PM J15416+1828*	Hα	-2.218 ± 0.065	-2.037 ± 0.058	-2.311 ± 0.065	0.274 ± 0.087	0.088 ± 0.018	-3.965	0.0086
		Hβ	-2.475 ± 0.115	-2.333 ± 0.117	-2.831 ± 0.128	0.498 ± 0.173	0.132 ± 0.036	-4.054	0.2102
23	PM J16220+2250	Hα	-3.012 ± 0.075	-2.866 ± 0.076	-3.156 ± 0.079	0.290 ± 0.109	0.082 ± 0.019	-3.761	0.2604
		Hβ	-3.268 ± 0.130	-2.946 ± 0.123	-3.698 ± 0.139	0.751 ± 0.185	0.181 ± 0.031	-3.781	0.0051
24	PM J22387-2037	Hα	-2.269 ± 0.061	-2.156 ± 0.056	-2.357 ± 0.063	0.202 ± 0.084	0.065 ± 0.015	-3.869	0.2155
		Hβ	-2.660 ± 0.118	-2.302 ± 0.155	-3.125 ± 0.196	0.823 ± 0.250	0.190 ± 0.040	-3.847	0.0360
25	PM J04284+1741*	Hα	-2.976 ± 0.079	-2.775 ± 0.076	-3.172 ± 0.083	0.398 ± 0.113	0.107 ± 0.019	-3.859	0.0103
		Hβ	-3.296 ± 0.142	-2.881 ± 0.150	-4.188 ± 0.171	1.307 ± 0.228	0.370 ± 0.039	-3.976	0.0000
26	PM J06212+4414	Hα	-2.854 ± 0.076	-2.762 ± 0.082	-2.936 ± 0.074	0.174 ± 0.110	0.055 ± 0.027	-3.841	0.8049
		Hβ	-3.188 ± 0.160	-2.923 ± 0.180	-3.517 ± 0.162	0.594 ± 0.242	0.223 ± 0.062	-3.917	0.0634
27	PM J11201-1029*	Hα	-2.033 ± 0.059	-1.841 ± 0.054	-2.206 ± 0.062	0.365 ± 0.082	0.111 ± 0.014	-3.976	0.0000
		Hβ	-2.254 ± 0.104	-1.899 ± 0.110	-2.733 ± 0.108	0.834 ± 0.154	0.223 ± 0.027	-4.045	0.0000

Table B.7: Table B.6 continues...

Source ID	Source name	emission line	Median Hα EW Hβ EW	Minimum Hα EW Hβ EW	Maximum Hα EW Hβ EW	Δ Hα EW Hβ EW	RMS Hα EW Hβ EW	Mean $\log_{10}(L_{H\alpha}/L_{bol})$ $\log_{10}(L_{H\beta}/L_{bol})$	P-value Hα Hβ
28	PM J13518+1247*	Hα	-2.118 ± 0.062	-1.771 ± 0.091	-2.248 ± 0.072	0.478 ± 0.115	0.112 ± 0.020	-3.997	0.0071
		Hβ	-2.680 ± 0.132	-1.915 ± 0.152	-3.277 ± 0.153	1.363 ± 0.216	0.327 ± 0.037	-4.059	0.0000
29	PM J15218+2058*	Hα	-2.615 ± 0.060	-2.383 ± 0.081	-2.771 ± 0.097	0.388 ± 0.126	0.099 ± 0.018	-3.866	0.0351
		Hβ	-2.864 ± 0.216	-2.430 ± 0.182	-3.331 ± 0.213	0.901 ± 0.280	0.244 ± 0.039	-3.943	0.0000
30	PM J16170+5516	Hα	-2.513 ± 0.064	-2.344 ± 0.077	-2.628 ± 0.066	0.284 ± 0.101	0.062 ± 0.019	-3.900	0.7030
		Hβ	-2.909 ± 0.096	-2.533 ± 0.140	-3.380 ± 0.176	0.847 ± 0.224	0.214 ± 0.039	-3.974	0.0020
31	PM J06596+0545	Hα	-1.775 ± 0.062	-1.675 ± 0.061	-1.858 ± 0.062	0.182 ± 0.087	0.065 ± 0.015	-4.062	0.2529
		Hβ	-2.069 ± 0.120	-1.767 ± 0.123	-2.424 ± 0.118	0.657 ± 0.170	0.141 ± 0.030	-4.139	0.1106
32	PM J09177+4612*	Hα	-3.899 ± 0.085	-3.674 ± 0.081	-4.093 ± 0.089	0.419 ± 0.120	0.117 ± 0.019	-3.693	0.0049
		Hβ	-4.515 ± 0.134	-3.989 ± 0.124	-4.974 ± 0.137	0.986 ± 0.185	0.258 ± 0.030	-3.744	0.0000
33	PM J10043+5023	Hα	-3.600 ± 0.088	-3.475 ± 0.083	-3.788 ± 0.085	0.313 ± 0.119	0.077 ± 0.020	-3.739	0.5912
		Hβ	-3.528 ± 0.121	-3.322 ± 0.133	-3.768 ± 0.117	0.446 ± 0.177	0.118 ± 0.030	-3.874	0.4600
34	PM J11519+0731	Hα	-3.009 ± 0.083	-2.810 ± 0.085	-3.177 ± 0.084	0.367 ± 0.120	0.096 ± 0.023	-3.858	0.1592
		Hβ	-3.051 ± 0.150	-2.805 ± 0.177	-3.617 ± 0.142	0.812 ± 0.227	0.221 ± 0.042	-4.023	0.0063
35	PM J15557+6840	Hα	-2.355 ± 0.076	-2.201 ± 0.074	-2.523 ± 0.075	0.322 ± 0.105	0.092 ± 0.022	-3.907	0.0708
		Hβ	-2.552 ± 0.157	-2.104 ± 0.157	-2.662 ± 0.163	0.558 ± 0.226	0.159 ± 0.048	-3.996	0.3764
36	PM J04333+2359*	Hα	-3.156 ± 0.086	-2.333 ± 0.072	-3.511 ± 0.094	1.178 ± 0.118	0.329 ± 0.020	-3.846	0.0000
		Hβ	-3.518 ± 0.155	-2.772 ± 0.146	-4.090 ± 0.158	1.319 ± 0.215	0.358 ± 0.038	-3.948	0.0000
37	PM J05091+1527*	Hα	-3.211 ± 0.122	-2.940 ± 0.155	-3.635 ± 0.154	0.695 ± 0.219	0.199 ± 0.037	-3.829	0.0150
		Hβ	-	-	-	-	-	-	-
38	PM J05337+0156	Hα	-6.394 ± 0.134	-6.182 ± 0.130	-6.568 ± 0.136	0.386 ± 0.189	0.103 ± 0.038	-3.510	0.8028
		Hβ	-6.956 ± 0.191	-6.580 ± 0.189	-7.451 ± 0.196	0.871 ± 0.272	0.208 ± 0.055	-3.628	0.2125
39	PM J05547+1055*	Hα	-4.045 ± 0.099	-3.692 ± 0.096	-4.405 ± 0.103	0.713 ± 0.141	0.210 ± 0.024	-3.739	0.0000
		Hβ	-4.459 ± 0.199	-3.945 ± 0.196	-5.078 ± 0.204	1.132 ± 0.282	0.238 ± 0.047	-3.877	0.0594
40	PM J07319+3613S*	Hα	-1.871 ± 0.065	-1.382 ± 0.055	-2.020 ± 0.065	0.639 ± 0.085	0.187 ± 0.014	-4.136	0.0000
		Hβ	-2.072 ± 0.131	-1.146 ± 0.093	-2.676 ± 0.127	1.530 ± 0.158	0.434 ± 0.028	-4.311	0.0000
41	PM J07349+1445	Hα	-2.451 ± 0.071	-2.355 ± 0.070	-2.574 ± 0.074	0.219 ± 0.102	0.051 ± 0.017	-3.967	0.9333
		Hβ	-	-	-	-	-	-	-
42	PM J11529+3554*	Hα	-4.697 ± 0.202	-3.708 ± 0.310	-5.760 ± 0.280	2.052 ± 0.417	0.593 ± 0.094	-3.628	0.0000
		Hβ	-4.100 ± 1.131	-3.013 ± 0.937	-6.610 ± 1.401	3.598 ± 1.686	1.080 ± 0.415	-3.805	0.3939
43	PM J12355+2439*	Hα	-2.467 ± 0.096	-2.297 ± 0.098	-2.779 ± 0.102	0.482 ± 0.141	0.132 ± 0.032	-3.913	0.0263
		Hβ	-3.036 ± 0.249	-2.703 ± 0.213	-3.996 ± 0.284	1.292 ± 0.355	0.402 ± 0.101	-3.952	0.0074
44	PM J13352+1714*	Hα	-2.696 ± 0.083	-2.417 ± 0.120	-2.917 ± 0.139	0.500 ± 0.184	0.170 ± 0.041	-	0.0082
		Hβ	-3.025 ± 0.175	-2.460 ± 0.229	-3.773 ± 0.302	1.313 ± 0.378	0.414 ± 0.103	-	0.0107
45	PM J14137+4618	Hα	-4.520 ± 0.119	-4.313 ± 0.129	-4.774 ± 0.122	0.461 ± 0.178	0.148 ± 0.044	-3.768	0.1292
		Hβ	-4.966 ± 0.342	-3.373 ± 0.410	-6.525 ± 0.282	3.152 ± 0.498	0.906 ± 0.123	-3.992	0.0000
46	PM J04238+1455	Hα	-5.064 ± 0.360	-4.235 ± 0.292	-5.419 ± 0.294	1.184 ± 0.414	0.367 ± 0.102	-3.711	0.0919
		Hβ	-9.320 ± 1.001	-3.474 ± 0.545	-15.323 ± 1.809	11.849 ± 1.890	4.045 ± 0.438	-3.672	0.0000
47	PM J09302+2630*	Hα	-3.100 ± 0.095	-2.765 ± 0.098	-3.470 ± 0.104	0.705 ± 0.143	0.189 ± 0.024	-3.893	0.0000
		Hβ	-	-	-	-	-	-	-
48	PM J09557+3521*	Hα	-2.956 ± 0.096	-2.610 ± 0.104	-3.316 ± 0.102	0.706 ± 0.146	0.193 ± 0.027	-3.915	0.0000
		Hβ	-	-	-	-	-	-	-
49	PM J12485+4933	Hα	-5.196 ± 0.124	-4.989 ± 0.121	-5.444 ± 0.124	0.455 ± 0.173	0.142 ± 0.033	-3.641	0.1323
		Hβ	-6.051 ± 0.206	-5.407 ± 0.193	-6.749 ± 0.213	1.342 ± 0.288	0.368 ± 0.054	-3.774	0.0000
50	PM J12490+6606*	Hα	-1.038 ± 0.052	-0.968 ± 0.050	-1.302 ± 0.050	0.334 ± 0.071	0.078 ± 0.012	-4.387	0.0007
		Hβ	-0.960 ± 0.095	-0.802 ± 0.092	-1.152 ± 0.104	0.350 ± 0.138	0.110 ± 0.024	-4.662	0.1525
51	PM J13417+5815*	Hα	-2.323 ± 0.083	-1.813 ± 0.072	-3.243 ± 0.095	1.430 ± 0.119	0.403 ± 0.021	-4.008	0.0000
		Hβ	-2.575 ± 0.208	-1.788 ± 0.179	-4.175 ± 0.217	2.387 ± 0.282	0.585 ± 0.049	-4.164	0.0000
52	PM J16591+2058*	Hα	-3.206 ± 0.091	-3.007 ± 0.088	-3.626 ± 0.101	0.619 ± 0.134	0.169 ± 0.023	-3.880	0.0000
		Hβ	-3.311 ± 0.161	-2.753 ± 0.143	-4.216 ± 0.172	1.463 ± 0.224	0.424 ± 0.041	-4.091	0.0000
53	PM J00325+0729	Hα	-5.958 ± 0.147	-5.796 ± 0.144	-6.302 ± 0.160	0.506 ± 0.215	0.153 ± 0.046	-3.629	0.3676
		Hβ	-5.477 ± 0.222	-5.111 ± 0.226	-6.179 ± 0.255	1.068 ± 0.341	0.367 ± 0.089	-3.903	0.0113
54	PM J01593+5831	Hα	-6.089 ± 0.146	-5.796 ± 0.144	-6.277 ± 0.153	0.480 ± 0.210	0.161 ± 0.041	-3.700	0.2252
		Hβ	-6.800 ± 0.240	-6.022 ± 0.225	-7.646 ± 0.243	1.624 ± 0.331	0.522 ± 0.065	-3.963	0.0000
55	PM J02088+4926*	Hα	-7.213 ± 0.157	-6.340 ± 0.144	-7.947 ± 0.172	1.607 ± 0.225	0.569 ± 0.044	-3.534	0.0000
		Hβ	-9.140 ± 0.273	-7.573 ± 0.237	-10.534 ± 0.308	2.961 ± 0.388	0.986 ± 0.075	-3.661	0.0000
56	PM J05062+0439*	Hα	-7.327 ± 0.183	-6.835 ± 0.175	-7.682 ± 0.189	0.847 ± 0.258	0.227 ± 0.044	-3.662	0.0422
		Hβ	-8.301 ± 0.306	-7.359 ± 0.291	-9.795 ± 0.323	2.436 ± 0.434	0.504 ± 0.076	-3.957	0.0001

Table B.8: Table B.7 continues...

Source	Source	emission	Median	Minimum	Maximum	Δ	RMS	Mean	P-value
ID	name	line	Hα EW	Hα EW	Hα EW	Hα EW	Hα EW	$\log_{10}(L_{H\alpha}/L_{bol})$	Hα
			Hβ EW	Hβ EW	Hβ EW	Hβ EW	Hβ EW	$\log_{10}(L_{H\beta}/L_{bol})$	Hβ
57	PM J06000+0242*	Hα	-2.782 ± 0.085	-2.618 ± 0.083	-3.119 ± 0.088	0.501 ± 0.121	0.142 ± 0.021	-4.042	0.0001
		Hβ	-2.928 ± 0.147	-2.368 ± 0.133	-3.680 ± 0.149	1.312 ± 0.200	0.348 ± 0.035	-4.351	0.0000
58	PM J07033+3441*	Hα	-5.124 ± 0.137	-4.467 ± 0.121	-5.559 ± 0.143	1.091 ± 0.188	0.301 ± 0.032	-3.730	0.0000
		Hβ	-5.389 ± 0.246	-4.700 ± 0.222	-7.483 ± 0.275	2.782 ± 0.353	0.859 ± 0.061	-3.957	0.0000
59	PM J07100+3831	Hα	-1.850 ± 0.091	-1.682 ± 0.087	-2.121 ± 0.096	0.439 ± 0.130	0.109 ± 0.022	-4.296	0.0719
		Hβ	-1.518 ± 0.144	-1.159 ± 0.162	-2.295 ± 0.158	1.135 ± 0.226	0.273 ± 0.038	-4.760	0.0000
60	PM J09161+0153*	Hα	-4.709 ± 0.132	-4.443 ± 0.132	-5.361 ± 0.146	0.918 ± 0.197	0.239 ± 0.035	-3.751	0.0000
		Hβ	-5.232 ± 0.314	-4.748 ± 0.236	-5.850 ± 0.246	1.102 ± 0.341	0.403 ± 0.070	-3.968	0.0013
61	PM J10357+0215*	Hα	-3.423 ± 0.160	-2.978 ± 0.204	-4.019 ± 0.202	1.040 ± 0.287	0.335 ± 0.096	-3.791	0.0067
		Hβ	-3.811 ± 0.419	-3.313 ± 0.806	-7.983 ± 1.511	4.670 ± 1.713	1.738 ± 0.635	-3.840	0.0061
62	PM J10360+0507*	Hα	-5.604 ± 0.140	-5.435 ± 0.134	-6.462 ± 0.158	1.027 ± 0.208	0.262 ± 0.037	-3.670	0.0000
		Hβ	-6.182 ± 0.247	-5.458 ± 0.249	-8.427 ± 0.313	2.969 ± 0.400	0.808 ± 0.067	-3.880	0.0000
63	PM J11033+1337*	Hα	-3.094 ± 0.102	-2.961 ± 0.102	-3.572 ± 0.111	0.612 ± 0.151	0.141 ± 0.026	-3.909	0.0271
		Hβ	-	-	-	-	-	-	-
64	PM J11118+3332S	Hα	-5.423 ± 0.126	-5.086 ± 0.178	-5.696 ± 0.132	0.611 ± 0.222	0.177 ± 0.053	-3.682	0.1206
		Hβ	-6.126 ± 0.204	-4.150 ± 0.739	-6.964 ± 0.714	2.814 ± 1.028	0.801 ± 0.195	-3.908	0.0000
65	PM J12156+5239	Hα	-5.364 ± 0.124	-5.219 ± 0.122	-5.496 ± 0.127	0.277 ± 0.176	0.073 ± 0.030	-3.731	0.9915
		Hβ	-6.213 ± 0.193	-5.962 ± 0.190	-7.080 ± 0.214	1.117 ± 0.286	0.245 ± 0.050	-3.960	0.0873
66	PM J13536+7737*	Hα	-3.485 ± 0.121	-3.226 ± 0.110	-5.818 ± 0.150	2.593 ± 0.186	0.574 ± 0.035	-3.926	0.0000
		Hβ	-3.837 ± 0.401	-2.199 ± 0.430	-14.037 ± 0.576	11.838 ± 0.718	2.654 ± 0.130	-4.160	0.0000
67	PM J14165-0725	Hα	-3.559 ± 0.143	-3.401 ± 0.141	-3.742 ± 0.132	0.341 ± 0.194	0.120 ± 0.046	-3.890	0.5877
		Hβ	-5.528 ± 0.573	-4.366 ± 0.569	-6.791 ± 0.498	2.426 ± 0.756	0.833 ± 0.168	-3.988	0.0007
68	PM J15126+4543*	Hα	-4.034 ± 0.179	-3.706 ± 0.172	-4.725 ± 0.173	1.019 ± 0.244	0.302 ± 0.042	-3.840	0.0000
		Hβ	-4.759 ± 0.664	-3.784 ± 0.263	-7.641 ± 0.695	3.858 ± 0.743	1.023 ± 0.154	-4.054	0.0000
69	PM J05243-1601*	Hα	-10.500 ± 0.256	-9.080 ± 0.233	-10.776 ± 0.272	1.696 ± 0.359	0.549 ± 0.069	-3.502	0.0000
		Hβ	-12.443 ± 0.486	-9.432 ± 0.446	-14.962 ± 0.520	5.529 ± 0.685	1.561 ± 0.130	-3.762	0.0000
70	PM J13317+2916	Hα	-9.108 ± 0.201	-8.917 ± 0.195	-9.493 ± 0.207	0.576 ± 0.285	0.192 ± 0.054	-3.565	0.4687
		Hβ	-9.005 ± 0.239	-8.696 ± 0.241	-10.964 ± 0.280	2.268 ± 0.369	0.666 ± 0.070	-3.910	0.0000
71	PM J17199+2630W	Hα	-2.153 ± 0.080	-2.078 ± 0.078	-2.195 ± 0.082	0.117 ± 0.113	0.036 ± 0.028	-4.188	0.9852
		Hβ	-2.019 ± 0.172	-1.489 ± 0.222	-2.463 ± 0.177	0.974 ± 0.284	0.260 ± 0.068	-4.567	0.0284
72	PM J01033+6221	Hα	-14.374 ± 0.327	-13.836 ± 0.328	-15.019 ± 0.347	1.183 ± 0.477	0.369 ± 0.096	-3.424	0.2004
		Hβ	-21.756 ± 0.697	-19.777 ± 0.649	-27.742 ± 0.804	7.965 ± 1.033	2.373 ± 0.215	-3.626	0.0000
73	PM J02002+1303	Hα	-2.053 ± 0.104	-1.912 ± 0.095	-2.322 ± 0.106	0.410 ± 0.143	0.125 ± 0.029	-4.198	0.0742
		Hβ	-1.326 ± 0.215	-0.864 ± 0.203	-1.888 ± 0.194	1.023 ± 0.281	0.306 ± 0.058	-4.734	0.0027
74	PM J06579+6219*	Hα	-2.558 ± 0.127	-2.225 ± 0.125	-3.362 ± 0.135	1.137 ± 0.184	0.288 ± 0.032	-4.180	0.0000
		Hβ	-2.656 ± 0.410	-1.542 ± 0.440	-4.644 ± 0.330	3.102 ± 0.550	0.808 ± 0.094	-4.577	0.0000
75	PM J07364+0704*	Hα	-5.606 ± 0.174	-5.010 ± 0.159	-5.863 ± 0.174	0.853 ± 0.236	0.255 ± 0.043	-3.890	0.0011
		Hβ	-6.995 ± 0.389	-5.897 ± 0.345	-9.587 ± 0.462	3.689 ± 0.577	1.152 ± 0.102	-4.217	0.0000
76	PM J09449-1220*	Hα	-12.969 ± 0.313	-12.313 ± 0.302	-16.936 ± 0.389	4.623 ± 0.492	1.432 ± 0.095	-3.589	0.0000
		Hβ	-14.558 ± 0.450	-12.798 ± 0.555	-34.008 ± 0.857	21.210 ± 1.021	6.434 ± 0.191	-3.985	0.0000
77	PM J12142+0037*	Hα	-7.256 ± 0.233	-6.326 ± 0.214	-8.113 ± 0.241	1.787 ± 0.322	0.492 ± 0.057	-3.808	0.0000
		Hβ	-12.128 ± 0.765	-6.575 ± 0.681	-14.916 ± 0.666	8.341 ± 0.952	2.693 ± 0.193	-4.087	0.0000
78	PM J13005+0541*	Hα	-7.589 ± 0.208	-7.055 ± 0.195	-9.026 ± 0.232	1.971 ± 0.303	0.502 ± 0.056	-3.646	0.0000
		Hβ	-9.765 ± 0.518	-8.155 ± 0.482	-14.109 ± 0.660	5.954 ± 0.817	1.433 ± 0.147	-3.889	0.0000
79	PM J20298+0941*	Hα	-5.622 ± 0.158	-5.053 ± 0.171	-8.264 ± 0.222	3.212 ± 0.280	0.870 ± 0.062	-3.813	0.0000
		Hβ	-7.182 ± 0.336	-5.312 ± 0.699	-17.770 ± 0.861	12.458 ± 1.109	3.106 ± 0.245	-4.076	0.0000
80	PM J12332+0901*	Hα	-6.706 ± 0.210	-6.411 ± 0.233	-7.350 ± 0.232	0.939 ± 0.329	0.322 ± 0.072	-3.872	0.0123
		Hβ	-9.305 ± 0.355	-8.079 ± 0.329	-13.386 ± 0.791	5.307 ± 0.856	1.433 ± 0.201	-4.216	0.0000
81	PM J17338+1655*	Hα	-16.011 ± 0.394	-15.034 ± 0.376	-17.078 ± 0.419	2.044 ± 0.563	0.580 ± 0.096	-3.526	0.0019
		Hβ	-15.474 ± 0.780	-12.478 ± 0.651	-18.510 ± 0.799	6.032 ± 1.030	1.537 ± 0.182	-4.066	0.0000
82	PM J10564+0700*	Hα	-9.604 ± 0.303	-7.968 ± 0.276	-10.721 ± 0.322	2.753 ± 0.425	0.726 ± 0.090	-3.746	0.0000
		Hβ	-13.160 ± 0.499	-9.466 ± 0.433	-18.432 ± 0.572	8.966 ± 0.717	2.485 ± 0.155	-4.100	0.0000
83	PM J11055+4331*	Hα	-11.761 ± 0.357	-9.479 ± 0.288	-17.546 ± 0.478	8.067 ± 0.558	2.260 ± 0.147	-3.850	0.0000
		Hβ	-23.353 ± 1.646	-13.665 ± 0.782	-36.401 ± 2.937	22.736 ± 3.039	6.440 ± 0.806	-4.258	0.0000

B.8 Extension of Table 3.5

Table B.9: Extension of Table 3.5

Source ID	Source name	Mission/Year/Author	Exposure time (s)	Rotation period (days)	T_{spot} (K)	Filling factor (%)	Mean FLI Hα	Mean FLI Hβ
1	PM J03332+4615S*	T-18/2019/QLP	1800	3.184	3192	36.0	10.40 ± 1.72	2.65 ± 0.95
2	PM J03416+5513*	T-19/2019/SPOC	120	4.585	3145	6.2	6.97 ± 0.62	4.50 ± 0.45
3	PM J07151+1555*	T-33/2020/SPOC	120	0.554	3239	9.6	12.05 ± 1.83	4.67 ± 0.42
4	PM J23083-1524	T-42/2021/SPOC	20	0.431	3192	8.9	6.17 ± 1.25	-
5	PM J03322+4914S*	T-18/2019/SPOC	120	5.839	3097	5.0	7.09 ± 1.59	6.23 ± 2.72
6	PM J04595+0147*	T-32/2020/SPOC	120	4.421	3192	7.1	6.75 ± 0.43	4.63 ± 0.50
7	PM J10143+2104*	-	-	-	3145	-	8.00 ± 1.36	5.28 ± 1.25
8	PM J19026+3231	T-14/2019/SPOC	120	0.347	3097	7.6	11.91 ± 2.38	-
9	PM J23060+6355*	T-24/2020/SPOC	120	2.859	3097	11.3	6.96 ± 0.66	4.33 ± 0.55
10	PM J06310+5002*	T-20/2019/SPOC	120	5	3097	2.6	8.68 ± 1.04	6.32 ± 0.81
11	PM J08317+0545*	T-07/2019/SPOC	120	0.596	3145	4.6	10.06 ± 0.96	4.13 ± 1.06
12	PM J09193+6203*	T-21/2020/SPOC	120	-	3048	3.0	8.22 ± 0.60	4.03 ± 0.74
13	PM J12576+3513E*	T-22/2020/SPOC	120	3.364	3048	7.7	7.95 ± 0.79	5.09 ± 0.76
14	PM J15238+5609	T-24/2020/SPOC	120	1.001	3145	5.0	7.26 ± 0.64	-
15	PM J15581+4927*	T-24/2020/SPOC	120	0.816	3048	8.5	9.17 ± 1.28	3.97 ± 0.92
16	PM J04376-0229	T-05/2018/QLP	1800	-	3048	-	11.35 ± 0.65	6.48 ± 0.98
17	PM J00428+3532*	T-17/2019/SPOC	120	2.16	2998	6.4	10.02 ± 0.97	6.04 ± 0.76
18	PM J05402+1239*	T-06/2018/SPOC	120	1.576	3097	6.8	9.36 ± 0.77	6.02 ± 0.71
19	PM J06262+2349	K/2014/K2	1800	7.948	2998	5.8	5.20 ± 0.46	2.81 ± 0.81
20	PM J07295+3556*	T-20/2019/SPOC	120	1.984	3048	7.2	11.36 ± 1.07	7.40 ± 0.60
21	PM J13007+1222	T-23/2020/SPOC	120	2.923	3192	9.5	8.20 ± 0.57	6.15 ± 0.65
22	PM J15416+1828*	T-24/2020/TESS-SPOC	1800	-	3048	-	8.39 ± 0.74	5.90 ± 0.70
23	PM J16220+2250	T-25/2020/QLP	1800	-	3097	7.2	10.78 ± 0.72	8.12 ± 0.86
24	PM J22387-2037*	T-42/2021/SPOC	120	4.391	3048	3.7	7.76 ± 0.63	4.92 ± 0.82
25	PM J04284+1741*	K-13/2017/K2	1800	2.455	2998	10.6	10.10 ± 0.91	6.08 ± 0.88
26	PM J06212+4414	T-20/2019/SPOC	120	5.897	2998	16.1	9.33 ± 0.69	4.92 ± 0.75
27	PM J11201-1029*	T-09/2019/SPOC	120	5.722	2998	3.4	7.05 ± 0.64	4.93 ± 0.84
28	PM J13518+1247*	T-23/2020/SPOC	120	4.716	3145	2.2	7.70 ± 1.02	5.61 ± 0.95
29	PM J15218+2058*	T-24/2020/SPOC	120	3.367	3048	3.5	9.27 ± 1.24	5.85 ± 1.27
30	PM J16170+5516*	T-25/2020/SPOC	120	1.997	3048	3.7	8.79 ± 0.70	6.55 ± 0.98
31	PM J06596+0545*	T-33/2020/TESS-SPOC	600	9.716	2998	2.5	5.99 ± 0.46	3.94 ± 0.55
32	PM J09177+4612*	T-21/2020/SPOC	120	1.017	2998	7.4	13.47 ± 1.16	9.70 ± 1.14
33	PM J10043+5023*	T-21/2020/SPOC	120	1.31	2998	5.9	11.19 ± 0.79	7.30 ± 0.81
34	PM J11519+0731*	T-22/2020/SPOC	120	2.285	2998	10.1	9.59 ± 0.70	6.46 ± 1.23
35	PM J15557+6840	T-40/2021/SPOC	120	3.982	2948	4.4	7.73 ± 0.56	4.43 ± 0.55
36	PM J04333+2359*	-	-	-	2998	-	8.19 ± 0.62	6.46 ± 0.69
37	PM J05091+1527	T-32/2020/SPOC	120	2.526	2948	1.2	7.01 ± 0.92	-
38	PM J05337+0156*	T-32/2020/SPOC	20	0.604	2948	1.3	18.46 ± 1.40	12.84 ± 1.31
39	PM J05547+1055*	T-33/2020/SPOC	120	0.566	2998	5.5	11.63 ± 1.03	7.73 ± 1.78
40	PM J07319+3613S*	T-20/2019/QLP	1800	-	2948	9.3	4.37 ± 0.63	3.10 ± 0.88

a : K: K2 compaign; T: TESS sector.

Table B.10: Table B.9 continues...

Source ID	Source name	Mission/Year/ Author	Exposure time (s)	Rotation period (days)	T_{spot} (K)	Filling factor (%)	Mean FLI Hα	Mean FLI Hβ
41	PM J07349+1445	T-07/2019/SPOC	120	-	2948	2.3	5.80 ± 0.42	-
42	PM J11529+3554	T-22/2020/SPOC	120	2.725	2896	6.0	8.36 ± 1.85	1.08 ± 0.53
43	PM J12355+2439	-	-	-	2998	-	7.79 ± 0.56	3.82 ± 0.49
44	PM J13352+1714*	T-23/2020/SPOC	120	1.209	3048	2.2	9.02 ± 1.49	4.75 ± 1.50
45	PM J14137+4618*	T-23/2020/TESS-SPOC	1800	1.546	2948	4.4	13.28 ± 1.55	5.31 ± 2.45
46	PM J04238+1455*	T-32/2020/SPOC	120	0.926	2998	1.1	5.65 ± 1.18	2.52 ± 0.94
47	PM J09302+2630	T-21/2020/SPOC	120	10.228	2948	1.3	6.36 ± 0.64	-
48	PM J09557+3521	T-21/2020/SPOC	120	-	2896	0.5	6.83 ± 0.59	-
49	PM J12485+4933*	T-15/2019/SPOC	120	0.588	2948	2.1	11.95 ± 1.02	9.57 ± 1.04
50	PM J12490+6606	T-22/2020/SPOC	120	3.232	2998	1.0	2.32 ± 0.35	1.39 ± 0.27
51	PM J13417+5815*	T-16/2019/SPOC	120	1.709	2896	0.9	5.66 ± 0.84	3.72 ± 1.07
52	PM J16591+2058*	T-25/2020/SPOC	120	4.103	2948	4.2	6.92 ± 0.59	4.86 ± 0.82
53	PM J00325+0729	T-42/2021/SPOC	120	1.829	2845	11.3	9.89 ± 0.63	6.41 ± 0.80
54	PM J01593+5831	-	-	-	2845	-	9.41 ± 0.72	7.90 ± 0.90
55	PM J02088+4926*	T-18/2019/SPOC	120	0.75	2896	4.1	15.00 ± 1.37	11.00 ± 1.28
56	PM J05062+0439	T-05/2018/SPOC	120	0.888	2845	4.0	10.80 ± 0.87	9.28 ± 1.42
57	PM J06000+0242*	T-33/2020/SPOC	20	1.812	2845	1.1	4.89 ± 0.49	3.72 ± 0.67
58	PM J07033+3441*	T-20/2019/SPOC	120	-	2845	3.4	8.59 ± 0.66	6.95 ± 0.87
59	PM J07100+3831	T-20/2019/SPOC	120	5.412	2792	1.7	2.44 ± 0.22	1.39 ± 0.33
60	PM J09161+0153*	T-08/2019/SPOC	120	1.439	2896	8.2	8.61 ± 0.77	6.44 ± 1.39
61	PM J10357+0215	K-14/2017/K2	1800	0.708	2948	4.0	6.56 ± 1.40	1.98 ± 0.89
62	PM J10360+0507	-	-	-	2896	-	10.42 ± 0.62	8.04 ± 1.56
63	PM J11033+1337	T-22/2020/SPOC	120	-	2896	0.5	6.03 ± 0.64	-
64	PM J11118+3332S*	T-22/2020/SPOC	120	7.6	2896	9.3	10.39 ± 1.28	6.93 ± 3.01
65	PM J12156+5239	T-22/2020/SPOC	120	0.728	2948	3.4	12.16 ± 0.94	10.23 ± 0.94
66	PM J13536+7737*	T-41/2021/SPOC	120	1.239	2792	2.0	6.78 ± 1.44	3.09 ± 2.02
67	PM J14165-0725*	-	-	-	2948	-	7.61 ± 0.68	3.50 ± 1.13
68	PM J15126+4543*	T-24/2020/SPOC	120	1.691	2845	3.9	6.64 ± 0.80	4.22 ± 1.41
69	PM J05243-1601*	T-32/2020/SPOC	120	0.397	2739	15.9	11.90 ± 1.15	10.24 ± 1.73
70	PM J13317+2916	T-23/2020/SPOC	120	0.268	2845	3.5	14.97 ± 0.87	13.42 ± 2.09
71	PM J17199+2630W	T-25/2020/SPOC	120	-	2845	5.7	4.20 ± 0.27	2.27 ± 0.57
72	PM J01033+6221	T-24/2020/SPOC	120	1.024	2739	20.1	16.70 ± 1.19	18.53 ± 3.05
73	PM J02002+1303	-	-	-	2792	-	2.62 ± 0.27	1.10 ± 0.64
74	PM J06579+6219	T-20/2019/SPOC	120	2.146	2739	1.6	3.12 ± 0.42	1.57 ± 0.98
75	PM J07364+0704*	T-34/2021/SPOC	20	0.572	2739	0.6	6.20 ± 0.60	5.85 ± 1.13
76	PM J09449-1220*	T-35/2021/SPOC	120	0.442	2845	14.9	14.35 ± 1.51	16.30 ± 7.87
77	PM J12142+0037*	K-102/2016/K2SFF	1800	1.581	2792	5.1	7.77 ± 0.67	6.41 ± 2.18
78	PM J13005+0541*	T-23/2020/SPOC	120	0.602	2792	2.9	9.82 ± 0.88	7.06 ± 1.57
79	PM J20298+0941*	-	-	-	2739	-	7.88 ± 1.32	5.05 ± 2.44
80	PM J12332+0901	T-23/2020/SPOC	120	0.207	2845	1.5	6.39 ± 0.37	7.62 ± 1.28
81	PM J17338+1655*	T-26/2020/SPOC	120	0.266	2739	18.5	15.48 ± 1.28	9.33 ± 1.15
82	PM J10564+0700*	K-14/2017/K2SFF	1800	-	2739	6.2	6.53 ± 0.71	10.03 ± 2.96
83	PM J11055+4331*	T-21/2020/QLP	1800	-	2739	-	9.58 ± 1.62	5.63 ± 1.37

Appendix C

ProtoPol Mechanical design

This appendix is presented for chapter 5

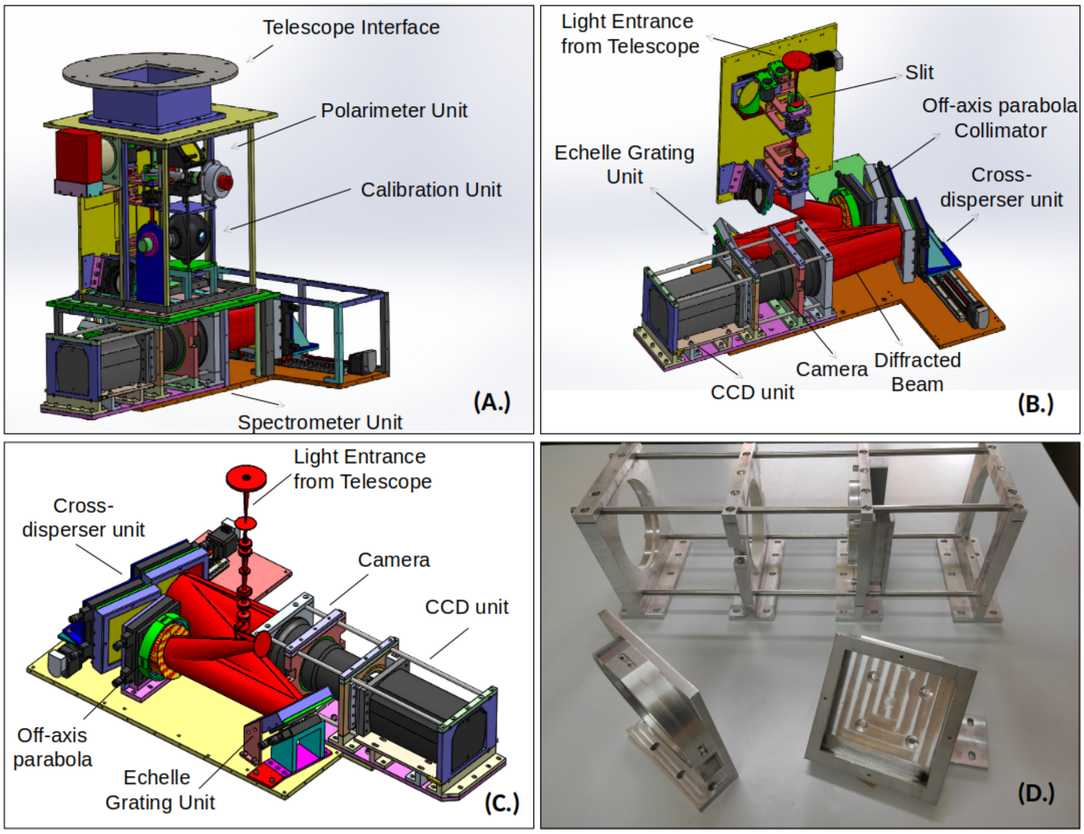

Figure C.1: The figure shows a full-fledged mechanical system, developed by the engineering team of ProtoPol.

Bibliography

Allard, F., Guillot, T., Ludwig, H.-G., et al. 2003, in IAU Symposium, Vol. 211, Brown Dwarfs, ed. E. Martín, 325–+ [Cited on page 85.]

Allard, F., & Hauschildt, P. H. 1995, *The Astrophysical Journal*, 445, 433, doi: 10.1086/175708 [Cited on page 85.]

Allard, F., Hauschildt, P. H., & Schwenke, D. 2000, *The Astrophysical Journal*, 540, 1005, doi: 10.1086/309366 [Cited on page 87.]

Allard, F., Homeier, D., & Freytag, B. 2011, in Astronomical Society of the Pacific Conference Series, Vol. 448, Astronomical Society of the Pacific Conference Series, ed. C. Johns-Krull, M. K. Browning, & A. A. West, 91 [Cited on pages 89 and 97.]

Allard, F., Homeier, D., Freytag, B., et al. 2013, Memorie della Societa Astronomica Italiana Supplementi, 24, 128. https://arxiv.org/abs/1302.6559 [Cited on pages 70, 85, 89, 97, and 115.]

Allard, F., Homeier, D., Freytag, B., & Sharp, C. M. 2012, in EAS Publications Series, Vol. 57, EAS Publications Series, ed. C. Reylé, C. Charbonnel, & M. Schultheis, 3–43 [Cited on pages 85 and 90.]

Almeida, L. A., Jablonski, F., & Martioli, E. 2011, *Astronomy & Astrophysics*, 525, A84, doi: 10.1051/0004-6361/201014219 [Cited on pages 93 and 113.]

Andersen, J., Andersen, M. I., Klougart, J., et al. 1995, The Messenger, 79, 12 [Cited on page 7.]

Anupama, G. C., & Mikołajewska, J. 1999, *Astronomy & Astrophysics*, 344, 177. https://arxiv.org/abs/astro-ph/9812432 [Cited on page 68.]

Arai, A., Kawakita, H., Shinnaka, Y., & Tajitsu, A. 2016, *The Astrophysical Journal*, 830, 30, doi: 10.3847/0004-637X/830/1/30 [Cited on page 138.]

Aydi, E., Sokolovsky, K. V., Chomiuk, L., et al. 2020, Nature Astronomy, 4, 776, doi: 10.1038/s41550-020-1070-y [Cited on page 154.]

Banerjee, D. P. K., & Ashok, N. M. 2012, Bulletin of the Astronomical Society of India, 40, 243. https://arxiv.org/abs/1306.0343 [Cited on pages 11 and 144.]

Banerjee, D. P. K., Bobra, A. D., & Subhedar, D. V. 1997, Bulletin of the Astronomical Society of India, 25, 555 [Cited on page 9.]

Banerjee, D. P. K., Srivastava, M. K., Ashok, N. M., et al. 2018a, *Monthly Notices of Royal Astronomical Society*, 473, 1895, doi: 10.1093/mnras/stx2459 [Cited on pages 11, 130, and 147.]

Banerjee, D. P. K., Joshi, V., Evans, A., et al. 2018b, *Monthly Notices of Royal Astronomical Society*, 481, 806, doi: 10.1093/mnras/sty2255 [Cited on pages 7 and 165.]

Barber, R. J., & Tennyson, J. 2008, in European Planetary Science Congress 2008, 870 [Cited on page 90.]

Barber, R. J., Tennyson, J., Harris, G. J., & Tolchenov, R. N. 2006, *Monthly Notices of Royal Astronomical Society*, 368, 1087, doi: 10.1111/j.1365-2966.2006.10184.x [Cited on page 85.]

Baroch, D., Morales, J. C., Ribas, I., et al. 2021, *Astronomy & Astrophysics*, 653, A49, doi: 10.1051/0004-6361/202141031 [Cited on page 82.]

Bath, G. T., & Harkness, R. P. 1989, in Classical Novae, First Edition, ed. M. Bode & A. Evans (Wiley, Chichester), 61–72 [Cited on page 153.]

Bath, G. T., & Shaviv, G. 1976, *Monthly Notices of Royal Astronomical Society*, 175, 305, doi: 10.1093/mnras/175.2.305 [Cited on page 153.]

Bell, K. J., Hilton, E. J., Davenport, J. R. A., et al. 2012, *Publications of the Astronomical Society of the Pacific*, 124, 14, doi: 10.1086/664024 [Cited on pages 94, 99, 112, 113, and 114.]

Benjamin, R. A., & Dinerstein, H. L. 1990, *The Astronomical Journal*, 100, 1588, doi: 10.1086/115619 [Cited on page 152.]

Berdyugina, S. V. 2005, Living Reviews in Solar Physics, 2, 8, doi: 10.12942/lrsp-2005-8 [Cited on page 110.]

Berrington, K. A., Saraph, H. E., & Tully, J. A. 1998, *Astronomy and Astrophysics Supplement Series*, 129, 161, doi: 10.1051/aas:1998394 [Cited on page 156.]

Blaha, M. 1969, *Astronomy & Astrophysics*, 1, 42 [Cited on page 156.]

Bochanski, J. J., West, A. A., Hawley, S. L., & Covey, K. R. 2007, *The Astronomical Journal*, 133, 531, doi: 10.1086/510240 [Cited on pages xxiv, xxv, 71, 88, and 96.]

Bode, M. F., & Kahn, F. D. 1985, *Monthly Notices of Royal Astronomical Society*, 217, 205, doi: 10.1093/mnras/217.1.205 [Cited on page 12.]

Bonfils, X., Gillon, M., Udry, S., et al. 2012, ArXiv e-prints. https://arxiv.org/abs/1206.5307 [Cited on page 82.]

Bottema, M. 1981, in Society of Photo-Optical Instrumentation Engineers (SPIE) Conference Series, Vol. 240, Society of Photo-Optical Instrumentation Engineers (SPIE) Conference Series, ed. C. H. Chi, E. G. Loewen, & C. L. O'Bryan, 171–177 [Cited on pages 44 and 199.]

Bozzo, E., Bahramian, A., Ferrigno, C., et al. 2018, *Astronomy & Astrophysics*, 613, A22, doi: 10.1051/0004-6361/201832588 [Cited on page 160.]

Buzzoni, B., Delabre, B., Dekker, H., et al. 1984, The Messenger, 38, 9 [Cited on page 7.]

Caffau, E., Ludwig, H.-G., Steffen, M., Freytag, B., & Bonifacio, P. 2010, Solar Physics, 268, 255, doi: 10.1007/s11207-010-9541-4 [Cited on page 90.]

Caffau, E., Maiorca, E., Bonifacio, P., et al. 2009, *Astronomy & Astrophysics*, 498, 877, doi: 10.1051/0004-6361/200810859 [Cited on page 90.]

Caldwell, D. A., van Cleve, J. E., Jenkins, J. M., et al. 2010, in Society of Photo-Optical Instrumentation Engineers (SPIE) Conference Series, Vol. 7731, Space Telescopes and Instrumentation 2010: Optical, Infrared, and Millimeter Wave, ed. J. Oschmann, Jacobus M., M. C. Clampin, & H. A. MacEwen, 773117 [Cited on pages 93 and 105.]

Cardelli, J. A., Clayton, G. C., & Mathis, J. S. 1989, *The Astrophysical Journal*, 345, 245, doi: 10.1086/167900 [Cited on page 169.]

Chabrier, G. 2003, *The Astrophysical Journal Letters*, 586, L133, doi: 10.1086/374879 [Cited on page 82.]

Chakraborty, A., Roy, A., Sharma, R., et al. 2018a, *The Astronomical Journal*, 156, 3, doi: 10.3847/1538-3881/aac436 [Cited on page 7.]

Chakraborty, A., Thapa, N., Kumar, K., et al. 2018b, in Society of Photo-Optical Instrumentation Engineers (SPIE) Conference Series, Vol. 10702, Ground-based and Airborne Instrumentation for Astronomy VII, ed. C. J. Evans, L. Simard, & H. Takami, 107026G [Cited on page 25.]

Chambers, K. C., & Pan-STARRS Team. 2016, in American Astronomical Society Meeting Abstracts, Vol. 227, American Astronomical Society Meeting Abstracts #227, 324.07 [Cited on page 132.]

Chambers, K. C., Magnier, E. A., Metcalfe, N., et al. 2016, arXiv e-prints, arXiv:1612.05560. https://arxiv.org/abs/1612.05560 [Cited on page 125.]

Chandrasekhar, T., Ashok, N. M., & Ragland, S. 1993, Journal of Astrophysics and Astronomy, 14, 7, doi: 10.1007/BF02702277 [Cited on page 156.]

Chang, H. Y., Song, Y. H., Luo, A. L., et al. 2017, *The Astrophysical Journal*, 834, 92, doi: 10.3847/1538-4357/834/1/92 [Cited on pages 92, 93, and 113.]

Cohen, J. G. 1985, *The Astrophysical Journal*, 292, 90, doi: 10.1086/163135 [Cited on page 130.]

Cool, A. M., Piotto, G., & King, I. R. 1996, *The Astrophysical Journal*, 468, 655, doi: 10.1086/177723 [Cited on page 82.]

Coughlin, M. W., Dekany, R. G., Duev, D. A., et al. 2019, Monthly Notices of the Royal Astronomical Society, 485, 1412, doi: 10.1093/mnras/stz497 [Cited on page 182.]

Cox, A. N. 2000, Allen's astrophysical quantities; 4th ed. (New York, NY: AIP) [Cited on page 153.]

Csák, B., Kiss, L. L., Retter, A., Jacob, A., & Kaspi, S. 2005, *Astronomy & Astrophysics*, 429, 599, doi: 10.1051/0004-6361:20035751 [Cited on page 144.]

Cushing, M. C., Vacca, W. D., & Rayner, J. T. 2004, *Publications of the Astronomical Society of the Pacific*, 116, 362, doi: 10.1086/382907 [Cited on page 126.]

Das, R., Banerjee, D. P. K., Nandi, A., Ashok, N. M., & Mondal, S. 2015, *Monthly Notices of Royal Astronomical Society*, 447, 806, doi: 10.1093/mnras/stu2488 [Cited on page 130.]

Das, R. K., Banerjee, D. P. K., Ashok, N. M., & Chesneau, O. 2008, *Monthly Notices of Royal Astronomical Society*, 391, 1874, doi: 10.1111/j.1365-2966.2008.13998.x [Cited on pages 121 and 144.]

De, K., & Palomar Gattini-IR Collaboration. 2020, The Astronomer's Telegram, 13732, 1 [Cited on pages 121 and 149.]

De, K., Hankins, M., Kasliwal, M. M., et al. 2019, The Astronomer's Telegram, 13130, 1 [Cited on pages 71, 120, and 132.]

De Gennaro Aquino, I., Schröder, K. P., Mittag, M., et al. 2015, *Astronomy & Astrophysics*, 581, A134, doi: 10.1051/0004-6361/201525810 [Cited on page 140.]

Deen, C. P., Gully-Santiago, M., Wang, W., et al. 2017, *Publications of the Astronomical Society of the Pacific*, 129, 065004, doi: 10.1088/1538-3873/129/976/065004 [Cited on page 192.]

della Valle, M., & Livio, M. 1995, *The Astrophysical Journal*, 452, 704, doi: 10.1086/176342 [Cited on pages xxviii, 130, and 131.]

Derdzinski, A. M., Metzger, B. D., & Lazzati, D. 2017, *Monthly Notices of Royal Astronomical Society*, 469, 1314, doi: 10.1093/mnras/stx829 [Cited on pages 147, 158, and 159.]

Deshpande, M. R. 1995, Bulletin of the Astronomical Society of India, 23, 13 [Cited on page 9.]

Dessart, L., Leonard, D. C., John Hillier, D., & Pignata, G. 2021, *Astronomy & Astrophysics*, 651, A19, doi: 10.1051/0004-6361/202140281 [Cited on pages xix, 31, and 32.]

Dittmann, J. A., Irwin, J. M., Charbonneau, D., & Newton, E. R. 2016, *The Astrophysical Journal*, 818, 153, doi: 10.3847/0004-637X/818/2/153 [Cited on page 102.]

Douglas, S. T., Agüeros, M. A., Covey, K. R., et al. 2014, *The Astrophysical Journal*, 795, 161, doi: 10.1088/0004-637X/795/2/161 [Cited on pages 101, 102, and 109.]

Doyle, L., Ramsay, G., Doyle, J. G., & Wu, K. 2019, *Monthly Notices of Royal Astronomical Society*, 489, 437, doi: 10.1093/mnras/stz2205 [Cited on pages 93 and 94.]

Doyle, L., Ramsay, G., Doyle, J. G., Wu, K., & Scullion, E. 2018, *Monthly Notices of Royal Astronomical Society*, 480, 2153, doi: 10.1093/mnras/sty1963 [Cited on pages 93 and 94.]

Espey, B. R., Schulte-Ladbeck, R. E., Kriss, G. A., et al. 1995, *The Astrophysical Journal Letters*, 454, L61, doi: 10.1086/309764 [Cited on page 171.]

Evans, A., Tyne, V. H., Smith, O., et al. 2005, *Monthly Notices of Royal Astronomical Society*, 360, 1483, doi: 10.1111/j.1365-2966.2005.09146.x [Cited on page 153.]

Evans, A., Gehrz, R. D., Geballe, T. R., et al. 2003, *The Astronomical Journal*, 126, 1981, doi: 10.1086/377618 [Cited on pages 152, 153, 154, and 156.]

Evans, A., Banerjee, D. P. K., Gehrz, R. D., et al. 2017, *Monthly Notices of Royal Astronomical Society*, 466, 4221, doi: 10.1093/mnras/stw3334 [Cited on pages 147 and 159.]

Eversberg, T., & Vollmann, K. 2015, Spectroscopic Instrumentation: Fundamentals and Guidelines for Astronomers [Cited on pages xx, 33, 40, 43, and 192.]

Ferguson, J. W., Korista, K. T., & Ferland, G. J. 1997, *The Astrophysical Journal Supplement Series*, 110, 287, doi: 10.1086/312998 [Cited on page 155.]

Frith, J., Pinfield, D. J., Jones, H. R. A., et al. 2013, *Monthly Notices of Royal Astronomical Society*, 435, 2161, doi: 10.1093/mnras/stt1436 [Cited on page 84.]

Gaia Collaboration, Prusti, T., de Bruijne, J. H. J., et al. 2016, *Astronomy & Astrophysics*, 595, A1, doi: 10.1051/0004-6361/201629272 [Cited on page 131.]

Gałan, C., Mikołajewska, J., Iłkiewicz, K., et al. 2022, *Astronomy & Astrophysics*, 657, A137, doi: 10.1051/0004-6361/202142144 [Cited on pages xix and 28.]

Gehrels, N., Chincarini, G., Giommi, P., et al. 2004, *The Astrophysical Journal*, 611, 1005, doi: 10.1086/422091 [Cited on page 153.]

Gehrz, R. D., Evans, A., Helton, L. A., et al. 2015, *The Astrophysical Journal*, 812, 132, doi: 10.1088/0004-637X/812/2/132 [Cited on page 159.]

Gillon, M., Triaud, A. H. M. J., Demory, B.-O., et al. 2017, ArXiv e-prints. https://arxiv.org/abs/1703.01424 [Cited on page 82.]

Gizis, J. E. 1997, *The Astronomical Journal*, 113, 806, doi: 10.1086/118302 [Cited on page 88.]

Gizis, J. E., Reid, I. N., & Hawley, S. L. 2002, *The Astronomical Journal*, 123, 3356, doi: 10.1086/340465 [Cited on pages 84, 92, and 103.]

Glass, I. S. 1999, Handbook of Infrared Astronomy, Cambridge Observing Handbooks for Research Astronomers (Cambridge University Press), doi: 10.1017/CBO9780511564949 [Cited on pages xxviii and 131.]

Godon, P., Sion, E. M., Balman, Ş., & Blair, W. P. 2017, *The Astrophysical Journal*, 846, 52, doi: 10.3847/1538-4357/aa7f71 [Cited on page 168.]

Goldstein, D. 2003, Polarized light [Cited on pages 36 and 37.]

Green, P. J., & Margon, B. 1994, *The Astrophysical Journal*, 423, 723, doi: 10.1086/173851 [Cited on page 82.]

Greenhouse, M. A., Feldman, U., Smith, H. A., et al. 1993, *The Astrophysical Journal Supplement Series*, 88, 23, doi: 10.1086/191813 [Cited on page 155.]

Greenhouse, M. A., Grasdalen, G. L., Hayward, T. L., Gehrz, R. D., & Jones, T. J. 1988, *The Astronomical Journal*, 95, 172, doi: 10.1086/114625 [Cited on page 156.]

Greenhouse, M. A., Grasdalen, G. L., Woodward, C. E., et al. 1990, *The Astrophysical Journal*, 352, 307, doi: 10.1086/168537 [Cited on pages 152 and 153.]

Guenther, E. W., Wöckel, D., Chaturvedi, P., et al. 2021, *Monthly Notices of Royal Astronomical Society*, 507, 2103, doi: 10.1093/mnras/stab1973 [Cited on pages 109 and 110.]

Gupta, R., Burse, M., Das, H. K., et al. 2002, Bulletin of the Astronomical Society of India, 30, 785 [Cited on page 8.]

Gutierrez-Moreno, A., & Moreno, H. 1996, *Publications of the Astronomical Society of the Pacific*, 108, 972, doi: 10.1086/133822 [Cited on page 167.]

Harding, L. K., Hallinan, G., Milburn, J., et al. 2016, Monthly Notices of the Royal Astronomical Society, 457, 3036, doi: 10.1093/mnras/stw094 [Cited on page 230.]

Harries, T. J., & Howarth, I. D. 1996, *Astronomy and Astrophysics Supplement Series*, 119, 61 [Cited on pages xix, 28, 29, and 242.]

Harvey, E. J., Redman, M. P., Darnley, M. J., et al. 2018, *Astronomy & Astrophysics*, 611, A3, doi: 10.1051/0004-6361/201731741 [Cited on page 159.]

Hawley, S. L., Davenport, J. R. A., Kowalski, A. F., et al. 2014, *The Astrophysical Journal*, 797, 121, doi: 10.1088/0004-637X/797/2/121 [Cited on pages 92, 93, and 113.]

Hawley, S. L., Gizis, J. E., & Reid, I. N. 1996, *The Astronomical Journal*, 112, 2799, doi: 10.1086/118222 [Cited on pages 84 and 92.]

Hayes, M. A., & Nussbaumer, H. 1986, *Astronomy & Astrophysics*, 161, 287 [Cited on page 163.]

Henden, A., & Munari, U. 2014, Contributions of the Astronomical Observatory Skalnate Pleso, 43, 518 [Cited on page 125.]

Henry, T. J., Ianna, P. A., Kirkpatrick, J. D., & Jahreiss, H. 1997, *The Astronomical Journal*, 114, 388, doi: 10.1086/118482 [Cited on page 82.]

Henry, T. J., Walkowicz, L. M., Barto, T. C., & Golimowski, D. A. 2002, *The Astronomical Journal*, 123, 2002, doi: 10.1086/339315 [Cited on page 87.]

Hilton, E. J., West, A. A., Hawley, S. L., & Kowalski, A. F. 2010, *The Astronomical Journal*, 140, 1402, doi: 10.1088/0004-6256/140/5/1402 [Cited on pages 93, 94, 98, 101, 103, 104, 105, and 113.]

Howell, S. B., Sobeck, C., Haas, M., et al. 2014, *Publications of the Astronomical Society of the Pacific*, 126, 398, doi: 10.1086/676406 [Cited on pages 93 and 105.]

Huang, C. X., Vanderburg, A., Pál, A., et al. 2020, Research Notes of the AAS, 4, 204, doi: 10.3847/2515-5172/abca2e [Cited on page 106.]

Hummer, D. G., & Storey, P. J. 1987, *Monthly Notices of Royal Astronomical Society*, 224, 801, doi: 10.1093/mnras/224.3.801 [Cited on page 146.]

Iłkiewicz, K., Mikołajewska, J., Stoyanov, K., Manousakis, A., & Miszalski, B. 2016, *Monthly Notices of Royal Astronomical Society*, 462, 2695, doi: 10.1093/mnras/stw1837 [Cited on page 68.]

Ivison, R. J., Bode, M. F., & Meaburn, J. 1994, *Astronomy and Astrophysics Supplement Series*, 103, 201 [Cited on page 174.]

Jackson, R. J., & Jeffries, R. D. 2013, *Monthly Notices of Royal Astronomical Society*, 431, 1883, doi: 10.1093/mnras/stt304 [Cited on page 109.]

Jain, N. K., & Narain, U. 1978, *Astronomy and Astrophysics Supplement Series*, 31, 1 [Cited on page 156.]

Jeffers, S. V., Schöfer, P., Lamert, A., et al. 2018, *Astronomy & Astrophysics*, 614, A76, doi: 10.1051/0004-6361/201629599 [Cited on pages xl, 95, 96, 97, 107, and 109.]

Jenkins, J. M., Twicken, J. D., McCauliff, S., et al. 2016, in Software and Cyberinfrastructure for Astronomy IV, ed. G. Chiozzi & J. C. Guzman, Vol. 9913, International Society for Optics and Photonics (SPIE), 1232 – 1251. https://doi.org/10.1117/12.2233418 [Cited on page 106.]

Jenkins, J. S., Ramsey, L. W., Jones, H. R. A., et al. 2009, *The Astrophysical Journal*, 704, 975, doi: 10.1088/0004-637X/704/2/975 [Cited on page 93.]

Jordan, C. 1969, *Monthly Notices of Royal Astronomical Society*, 142, 501, doi: 10.1093/mnras/142.4.501 [Cited on page 156.]

José, J., & Hernanz, M. 1998, *The Astrophysical Journal*, 494, 680, doi: 10.1086/305244 [Cited on page 157.]

Joshi, V., Banerjee, D. P. K., & Ashok, N. M. 2014, *Monthly Notices of Royal Astronomical Society*, 443, 559, doi: 10.1093/mnras/stu1168 [Cited on page 126.]

Joshi, V., Banerjee, D. P. K., & Srivastava, M. 2017, *The Astrophysical Journal Letters*, 851, L30, doi: 10.3847/2041-8213/aa9d86 [Cited on page 7.]

—. 2019, The Astronomer's Telegram, 13301, 1 [Cited on page 121.]

Kashikawa, N., Inata, M., Iye, M., et al. 2000, in Optical and IR Telescope Instrumentation and Detectors, ed. M. Iye & A. F. M. Moorwood, Vol. 4008, International Society for Optics and Photonics (SPIE), 104 – 113. https://doi.org/10.1117/12.395414 [Cited on page 7.]

Kaur, N., Chandra, S., Baliyan, K. S., Sameer, & Ganesh, S. 2017, *The Astrophysical Journal*, 846, 158, doi: 10.3847/1538-4357/aa86b0 [Cited on page 7.]

Kawakita, H., Shinnaka, Y., Arai, A., Arasaki, T., & Ikeda, Y. 2019, The Astrophysical Journal, 872, 120, doi: 10.3847/1538-4357/aaff68 [Cited on pages 221 and 242.]

Keenan, F. P., Ahmed, S., Brage, T., et al. 2002, *Monthly Notices of Royal Astronomical Society*, 337, 901, doi: 10.1046/j.1365-8711.2002.05988.x [Cited on page 167.]

Kenyon, S. J. 1986, The Symbiotic Stars, Cambridge Astrophysics (Cambridge University Press), doi: 10.1017/CBO9780511586071 [Cited on page 161.]

Kenyon, S. J., & Webbink, R. F. 1984, *The Astrophysical Journal*, 279, 252, doi: 10.1086/161888 [Cited on pages 162 and 176.]

Kiman, R., Faherty, J. K., Cruz, K. L., et al. 2021, *The Astronomical Journal*, 161, 277, doi: 10.3847/1538-3881/abf561 [Cited on page 113.]

Kiraga, M., & Stepien, K. 2007, *ACTA ASTRONOMICA*, 57, 149. https://arxiv.org/abs/0707.2577 [Cited on pages 93 and 113.]

Kirkpatrick, J. D., Henry, T. J., & McCarthy, Jr., D. W. 1991, *The Astrophysical Journal Supplement Series*, 77, 417, doi: 10.1086/191611 [Cited on page 87.]

Kirkpatrick, J. D., Henry, T. J., & Simons, D. A. 1995, *The Astronomical Journal*, 109, 797, doi: 10.1086/117323 [Cited on pages 88 and 89.]

Koch, D. G., Borucki, W. J., Basri, G., et al. 2010, *The Astrophysical Journal Letters*, 713, L79, doi: 10.1088/2041-8205/713/2/L79 [Cited on pages 93 and 105.]

Kowalski, A. F., Hawley, S. L., Holtzman, J. A., Wisniewski, J. P., & Hilton, E. J. 2010, *The Astrophysical Journal Letters*, 714, L98, doi: 10.1088/2041-8205/714/1/L98 [Cited on pages 80 and 93.]

Kruse, E. A., Berger, E., Knapp, G. R., et al. 2010, *The Astrophysical Journal*, 722, 1352, doi: 10.1088/0004-637X/722/2/1352 [Cited on pages 94, 98, 105, and 113.]

Kumar, T. S. 2016, in Ground-based and Airborne Instrumentation for Astronomy VI, ed. C. J. Evans, L. Simard, & H. Takami, Vol. 9908, International Society for Optics and Photonics (SPIE), 1515 – 1520. https://doi.org/10.1117/12.2233082 [Cited on page 8.]

Landolt, A. U. 1992, *The Astronomical Journal*, 104, 340, doi: 10.1086/116242 [Cited on page 125.]

Lang, K. R. 1980, Astrophysical Formulae. A Compendium for the Physicist and Astrophysicist. (Springer-Verlag, Berlin (Heidelberg, New York)) [Cited on page 156.]

Lee, C.-H., Soraisam, M., Narayan, G., et al. 2019, The Astronomer's Telegram, 13149, 1 [Cited on pages 71, 120, and 121.]

Lee, K.-G., Berger, E., & Knapp, G. R. 2010, *The Astrophysical Journal*, 708, 1482, doi: 10.1088/0004-637X/708/2/1482 [Cited on pages xxvi, xxvii, xl, 80, 93, 94, 95, 96, 98, 99, 100, 101, 103, 105, 106, 107, 109, 110, 112, 113, 115, and 238.]

Lépine, S., & Gaidos, E. 2011, *The Astronomical Journal*, 142, 138, doi: 10.1088/0004-6256/142/4/138 [Cited on pages xxxix, 70, 84, 85, 86, 89, 90, 91, 95, 115, and 251.]

Lépine, S., Hilton, E. J., Mann, A. W., et al. 2013, *The Astronomical Journal*, 145, 102, doi: 10.1088/0004-6256/145/4/102 [Cited on pages xl, 84, 96, and 97.]

Lépine, S., Rich, R. M., & Shara, M. M. 2007, *The Astrophysical Journal*, 669, 1235, doi: 10.1086/521614 [Cited on page 88.]

Lépine, S., Shara, M. M., & Rich, R. M. 2003, *The Astronomical Journal*, 126, 921, doi: 10.1086/376745 [Cited on page 88.]

Lightkurve Collaboration, Cardoso, J. V. d. M., Hedges, C., et al. 2018, Lightkurve: Kepler and TESS time series analysis in Python, Astrophysics Source Code Library. http://ascl.net/1812.013 [Cited on page 106.]

Lodders, K. 2021, *Space Science Reviews*, 217, 44, doi: 10.1007/s11214-021-00825-8 [Cited on page 157.]

Lomb, N. R. 1976, *Astrophysics and Space Science*, 39, 447, doi: 10.1007/BF00648343 [Cited on page 106.]

Lopes de Oliveira, R., Sokoloski, J. L., Luna, G. J. M., Mukai, K., & Nelson, T. 2018, *The Astrophysical Journal*, 864, 46, doi: 10.3847/1538-4357/aad2d5 [Cited on pages 161, 162, 167, and 169.]

Luna, G. J. M., Sokoloski, J. L., Mukai, K., & Nelson, T. 2013, *Astronomy & Astrophysics*, 559, A6, doi: 10.1051/0004-6361/201220792 [Cited on pages 162 and 167.]

Luri, X., Brown, A. G. A., Sarro, L. M., et al. 2018, *Astronomy & Astrophysics*, 616, A9, doi: 10.1051/0004-6361/201832964 [Cited on pages xxxix and 86.]

Maehara, H., Notsu, Y., Notsu, S., et al. 2017, *Publications of the Astronomical Society of Japan*, 69, 41, doi: 10.1093/pasj/psx013 [Cited on pages 109 and 110.]

Marshall, D. J., Robin, A. C., Reylé, C., Schultheis, M., & Picaud, S. 2006, *Astronomy & Astrophysics*, 453, 635, doi: 10.1051/0004-6361:20053842 [Cited on pages xxviii, 130, and 131.]

Martín, E. L., Delfosse, X., Basri, G., et al. 1999, *The Astronomical Journal*, 118, 2466, doi: 10.1086/301107 [Cited on page 88.]

Masetti, N., Orlandini, M., Palazzi, E., Amati, L., & Frontera, F. 2006, A&A, 453, 295, doi: 10.1051/0004-6361:20065025 [Cited on page 160.]

McLaughlin, D. B. 1964, Annales d'Astrophysique, 27, 450 [Cited on page 137.]

Meier, S. R., Kafatos, M., Fahey, R. P., & Michalitsianos, A. G. 1994, *The Astrophysical Journal Supplement Series*, 94, 183, doi: 10.1086/192078 [Cited on pages 162 and 166.]

Mercer, A., & Stamatellos, D. 2020, *Astronomy & Astrophysics*, 633, A116, doi: 10.1051/0004-6361/201936954 [Cited on page 82.]

Michalitsianos, A. G., Kafatos, M., Feibelman, W. A., & Hobbs, R. W. 1982, *The Astrophysical Journal*, 253, 735, doi: 10.1086/159674 [Cited on pages 166 and 176.]

Mikołajewska, J., Friedjung, M., & Quiroga, C. 2006, *Astronomy & Astrophysics*, 460, 191, doi: 10.1051/0004-6361:20052655 [Cited on page 171.]

Mikolajewska, J., Kenyon, S. J., & Mikolajewski, M. 1989, *The Astronomical Journal*, 98, 1427, doi: 10.1086/115229 [Cited on pages 162 and 173.]

Moore, A. M., & Kasliwal, M. M. 2019, Nature Astronomy, 3, 109, doi: 10.1038/s41550-018-0675-x [Cited on page 71.]

Moro, D., & Munari, U. 2000, *Astronomy and Astrophysics Supplement Series*, 147, 361, doi: 10.1051/aas:2000370 [Cited on page 125.]

Mukai, K., Luna, G. J. M., Cusumano, G., et al. 2016, *Monthly Notices of Royal Astronomical Society*, 461, L1, doi: 10.1093/mnrasl/slw087 [Cited on pages 29, 161, 162, 167, 169, and 171.]

Munari, U. 2014, in Astronomical Society of the Pacific Conference Series, Vol. 490, Stellar Novae: Past and Future Decades, ed. P. A. Woudt & V. A. R. M. Ribeiro, 183 [Cited on page 130.]

Munari, U. 2019, The Astronomer's Telegram, 13283, 1 [Cited on pages 121, 171, 174, and 176.]

Munari, U., Cotar, K., Andreoli, V., Dallaporta, S., & Yalyalieva, L. N. 2019, The Astronomer's Telegram, 13340, 1 [Cited on page 121.]

Munari, U., Dallaporta, S., & Cherini, G. 2016, *New Astronomy*, 47, 7, doi: 10.1016/j.newast.2016.01.002 [Cited on page 68.]

Munari, U., Hambsch, F. J., & Frigo, A. 2017, *Monthly Notices of Royal Astronomical Society*, 469, 4341, doi: 10.1093/mnras/stx1116 [Cited on page 127.]

Munari, U., Henden, A., Frigo, A., & Dallaporta, S. 2014, Journal of Astronomical Data, 20, 4 [Cited on page 125.]

Munari, U., & Moretti, S. 2012, Baltic Astronomy, 21, 22, doi: 10.1515/astro-2017-0354 [Cited on page 125.]

Munari, U., & Renzini, A. 1992, *The Astrophysical Journal Letters*, 397, L87, doi: 10.1086/186551 [Cited on page 176.]

Munari, U., & Zwitter, T. 2002, *Astronomy & Astrophysics*, 383, 188, doi: 10.1051/0004-6361:20011724 [Cited on pages 167 and 176.]

Munari, U., Bacci, S., Baldinelli, L., et al. 2012, Baltic Astronomy, 21, 13, doi: 10.1515/astro-2017-0353 [Cited on pages 122 and 125.]

Nauenberg, M. 1972, *The Astrophysical Journal*, 175, 417, doi: 10.1086/151568 [Cited on page 168.]

Newton, E. R., Irwin, J., Charbonneau, D., et al. 2017, *The Astrophysical Journal*, 834, 85, doi: 10.3847/1538-4357/834/1/85 [Cited on pages 80, 92, 93, 101, 102, 107, 109, 113, and 114.]

Notsu, Y., Maehara, H., Honda, S., et al. 2019, The Astrophysical Journal, 876, 58, doi: 10.3847/1538-4357/ab14e6 [Cited on page 110.]

Nussbaumer, H., & Storey, P. J. 1987, *Astronomy and Astrophysics Supplement Series*, 69, 123 [Cited on page 163.]

Nussbaumer, H., & Vogel, M. 1989, *Astronomy & Astrophysics*, 213, 137 [Cited on pages 162, 163, and 171.]

Ochsenbein, F., Bauer, P., & Marcout, J. 2000, *Astronomy and Astrophysics Supplement Series*, 143, 23, doi: 10.1051/aas:2000169 [Cited on pages xxxix and 86.]

Ojha, D., Ghosh, S. K., Sharma, S., et al. 2018, Bulletin de la Societe Royale des Sciences de Liege, 87, 58 [Cited on page 126.]

Omar, A., Kumar, B., Gopinathan, M., & Sagar, R. 2017, Current Science, 113, 682. https://arxiv.org/abs/1710.01050 [Cited on page 8.]

Osterbrock, D. E. 1989, Astrophysics of gaseous nebulae and active galactic nuclei (University Science Books, Melville, NY, USA) [Cited on page 136.]

Passegger, V. M., Wende-von Berg, S., & Reiners, A. 2016, *Astronomy & Astrophysics*, 587, A19, doi: 10.1051/0004-6361/201322261 [Cited on page 85.]

Passegger, V. M., Schweitzer, A., Shulyak, D., et al. 2019, arXiv e-prints, arXiv:1907.00807. https://arxiv.org/abs/1907.00807 [Cited on page 85.]

Patra, K. C., Yang, Y., Brink, T. G., et al. 2022, *Monthly Notices of Royal Astronomical Society*, 509, 4058, doi: 10.1093/mnras/stab3136 [Cited on page 32.]

Pejcha, O. 2009, *The Astrophysical Journal Letters*, 701, L119, doi: 10.1088/0004-637X/701/2/L119 [Cited on page 144.]

Pereira, C. B., Vogel, M., & Nussbaumer, H. 1995, *Astronomy & Astrophysics*, 293, 783 [Cited on page 167.]

Pirnay, O., Lousberg, G. P., Lanotte, A., et al. 2018, in Society of Photo-Optical Instrumentation Engineers (SPIE) Conference Series, Vol. 10700, *SPIE Conference Proceedings*, 107005S [Cited on page 9.]

Plez, B. 1998, *Astronomy & Astrophysics*, 337, 495 [Cited on page 85.]

Prabhu, T. P., & Anupama, G. C. 2010, in Astronomical Society of India Conference Series, Vol. 1, Astronomical Society of India Conference Series, 193–201 [Cited on page 8.]

Pringle, J. E. 1981, *Annual Review of Astronomy and Astrophysics*, 19, 137, doi: 10.1146/annurev.aa.19.090181.001033 [Cited on page 168.]

Proga, D., Kenyon, S. J., Raymond, J. C., & Mikolajewska, J. 1996, *The Astrophysical Journal*, 471, 930, doi: 10.1086/178020 [Cited on page 171.]

Raetz, S., Stelzer, B., Damasso, M., & Scholz, A. 2020, *Astronomy & Astrophysics*, 637, A22, doi: 10.1051/0004-6361/201937350 [Cited on page 114.]

Rai, A., Ganesh, S., Paul, S. K., et al. 2020, in Ground-based and Airborne Instrumentation for Astronomy VIII, ed. C. J. Evans, J. J. Bryant, & K. Motohara, Vol. 11447, International Society for Optics and Photonics (SPIE), 1370 – 1377. https://doi.org/10.1117/12.2560988 [Cited on page 25.]

Rajpurohit, A. S., Allard, F., Rajpurohit, S., et al. 2018a, *Astronomy & Astrophysics*, 620, A180, doi: 10.1051/0004-6361/201833500 [Cited on pages xix, 31, 85, and 90.]

Rajpurohit, A. S., Allard, F., Teixeira, G. D. C., et al. 2018b, *Astronomy & Astrophysics*, 610, A19, doi: 10.1051/0004-6361/201731507 [Cited on pages 85 and 90.]

Rajpurohit, A. S., Kumar, V., Srivastava, M. K., et al. 2020, *Monthly Notices of Royal Astronomical Society*, 492, 5844, doi: 10.1093/mnras/staa163 [Cited on pages 95 and 122.]

Rajpurohit, A. S., Reylé, C., Allard, F., et al. 2016, *Astronomy & Astrophysics*, 596, A33, doi: 10.1051/0004-6361/201526776 [Cited on page 85.]

—. 2013, *Astronomy & Astrophysics*, 556, A15, doi: 10.1051/0004-6361/201321346 [Cited on pages xxvi, xl, 85, 90, 91, 110, and 112.]

—. 2014, *Astronomy & Astrophysics*, 564, A90, doi: 10.1051/0004-6361/201322881 [Cited on pages 85 and 90.]

Rajpurohit, A. S., Reylé, C., Schultheis, M., et al. 2012, *Astronomy & Astrophysics*, 545, A85, doi: 10.1051/0004-6361/201219029 [Cited on pages 85, 90, and 97.]

Rayner, J. T., Toomey, D. W., Onaka, P. M., et al. 2003, *Publications of the Astronomical Society of the Pacific*, 115, 362, doi: 10.1086/367745 [Cited on page 126.]

Reid, I. N., Hawley, S. L., & Gizis, J. E. 1995a, *The Astronomical Journal*, 110, 1838, doi: 10.1086/117655 [Cited on pages 84, 87, and 89.]

Reid, N., Hawley, S. L., & Mateo, M. 1995b, *Monthly Notices of Royal Astronomical Society*, 272, 828, doi: 10.1093/mnras/272.4.828 [Cited on page 101.]

Reiners, A., Joshi, N., & Goldman, B. 2012, *The Astronomical Journal*, 143, 93, doi: 10.1088/0004-6256/143/4/93 [Cited on pages 92 and 113.]

Reiners, A., Schüssler, M., & Passegger, V. M. 2014, *The Astrophysical Journal*, 794, 144, doi: 10.1088/0004-637X/794/2/144 [Cited on pages 92 and 113.]

Renzini, A., Bragaglia, A., Ferraro, F. R., et al. 1996, *The Astrophysical Journal Letters*, 465, L23+, doi: 10.1086/310128 [Cited on page 82.]

Ricker, G. R., Winn, J. N., Vanderspek, R., et al. 2015, Journal of Astronomical Telescopes, Instruments, and Systems, 1, 014003, doi: 10.1117/1.JATIS.1.1.014003 [Cited on pages 93 and 105.]

Scargle, J. D. 1982, *The Astrophysical Journal*, 263, 835, doi: 10.1086/160554 [Cited on page 106.]

Schlafly, E. F., & Finkbeiner, D. P. 2011, *The Astrophysical Journal*, 737, 103, doi: 10.1088/0004-637X/737/2/103 [Cited on page 130.]

Schlegel, D. J., Finkbeiner, D. P., & Davis, M. 1998, *The Astrophysical Journal*, 500, 525, doi: 10.1086/305772 [Cited on page 130.]

Schmid, H. M. 1989, *Astronomy & Astrophysics*, 211, L31 [Cited on page 161.]

Scholz, R. D., Meusinger, H., & Jahreiß, H. 2005, *Astronomy & Astrophysics*, 442, 211, doi: 10.1051/0004-6361:20053004 [Cited on pages 87, 88, and 89.]

Schwarz, G. J., Ness, J.-U., Osborne, J. P., et al. 2011, *The Astrophysical Journal Supplement Series*, 197, 31, doi: 10.1088/0067-0049/197/2/31 [Cited on page 153.]

Schweizer, F. 1979, *Publications of the Astronomical Society of the Pacific*, 91, 149, doi: 10.1086/130458 [Cited on page 14.]

Selvelli, P., & Gilmozzi, R. 2013, *Astronomy & Astrophysics*, 560, A49, doi: 10.1051/0004-6361/201220627 [Cited on page 132.]

—. 2019, *Astronomy & Astrophysics*, 622, A186, doi: 10.1051/0004-6361/201834238 [Cited on page 131.]

Shu, F. H. 1992, Physics of Astrophysics, Vol. II:Gas Dynamics (University Science Books) [Cited on page 154.]

Shull, J. M., & van Steenberg, M. 1982, *The Astrophysical Journal Supplement Series*, 48, 95, doi: 10.1086/190769 [Cited on page 156.]

Silvestri, N. M., Hawley, S. L., & Oswalt, T. D. 2005, *The Astronomical Journal*, 129, 2428, doi: 10.1086/429593 [Cited on page 113.]

Simon, M. C. 1986, Appl. Opt., 25, 369, doi: 10.1364/AO.25.000369 [Cited on page 38.]

Skopal, A. 2008, How to understand the light curves of symbiotic stars, arXiv, doi: 10.48550/ARXIV.0805.1222. https://arxiv.org/abs/0805.1222 [Cited on page 172.]

Skrutskie, M. F., Cutri, R. M., Stiening, R., et al. 2006, *The Astronomical Journal*, 131, 1163, doi: 10.1086/498708 [Cited on page 84.]

Smith, A. R., McDonald, R. J., Hurley, D. C., et al. 2002, in Society of Photo-Optical Instrumentation Engineers (SPIE) Conference Series, Vol. 4669, Sensors and Camera Systems for Scientific, Industrial, and Digital Photography Applications III, ed. M. M. Blouke, J. Canosa, & N. Sampat, 172–183 [Cited on page 210.]

Smith, N., Giltinan, A., O'Connor, A., et al. 2008, in Astrophysics and Space Science Library, Vol. 351, Astrophysics and Space Science Library, ed. D. Phelan, O. Ryan, & A. Shearer, 257 [Cited on page 182.]

Sokolovsky, K., Babul, A.-N., Sokoloski, J., et al. 2020, The Astronomer's Telegram, 13653, 1 [Cited on page 121.]

Songsheng, Y.-Y., & Wang, J.-M. 2018, *Monthly Notices of Royal Astronomical Society*, 473, L1, doi: 10.1093/mnrasl/slx154 [Cited on page 32.]

Sordo, R., & Munari, U. 2006, *Astronomy & Astrophysics*, 452, 735, doi: 10.1051/0004-6361:20054619 [Cited on page 125.]

Sparks, W. M., Starrfield, S., & Truran, J. W. 1976, *The Astrophysical Journal*, 208, 819, doi: 10.1086/154668 [Cited on page 119.]

Spinoglio, L., & Malkan, M. A. 1992, *The Astrophysical Journal*, 399, 504, doi: 10.1086/171943 [Cited on page 155.]

Srivastava, M. K., Ashok, N. M., Banerjee, D. P. K., & Sand, D. 2015, *Monthly Notices of Royal Astronomical Society*, 454, 1297, doi: 10.1093/mnras/stv2094 [Cited on pages 11, 68, 140, and 146.]

Srivastava, M. K., Banerjee, D. P. K., Ashok, N. M., et al. 2016, *Monthly Notices of Royal Astronomical Society*, 462, 2074, doi: 10.1093/mnras/stw1807 [Cited on pages 7, 126, and 165.]

Srivastava, M. K., Jangra, M., Dixit, V., et al. 2018, in Society of Photo-Optical Instrumentation Engineers (SPIE) Conference Series, Vol. 10702, Ground-based and Airborne Instrumentation for Astronomy VII, 107024I [Cited on pages 21, 95, 122, and 165.]

Srivastava, M. K., Kumar, V., Banerjee, D. P. K., & Joshi, V. 2019, The Astronomer's Telegram, 13258, 1 [Cited on pages 72, 121, and 134.]

Srivastava, M. K., Kumar, V., Dixit, V., et al. 2021, Experimental Astronomy, 51, 345–382, doi: 10.1007/s10686-021-09753-5 [Cited on pages xviii, xix, xxxix, 13, 14, 15, 16, 17, 19, 20, 21, 22, 23, 95, and 122.]

Srivastava, M. K., Prabhudesai, S. M., & Tandon, S. N. 2009, Publications of the Astronomical Society of the Pacific, 121, 621, doi: 10.1086/603543 [Cited on page 169.]

Starrfield, S., Gehrz, R. D., & Truran, J. W. 1997, in American Institute of Physics Conference Series, Vol. 402, Astrophysical implications of the laboratory study of presolar materials, ed. T. J. Bernatowicz & E. Zinner, 203–234 [Cited on page 157.]

Storey, P. J., & Hummer, D. G. 1995, *Monthly Notices of Royal Astronomical Society*, 272, 41, doi: 10.1093/mnras/272.1.41 [Cited on pages 144, 146, and 149.]

Stoyanov, K. A., Martí, J., Zamanov, R., et al. 2018, Bulgarian Astronomical Journal, 28, 42. https://arxiv.org/abs/1711.01749 [Cited on page 172.]

Strope, R. J., Schaefer, B. E., & Henden, A. A. 2010, *The Astronomical Journal*, 140, 34, doi: 10.1088/0004-6256/140/1/34 [Cited on page 127.]

Subramaniam, A., Tandon, S. N., Hutchings, J., et al. 2016, in Space Telescopes and Instrumentation 2016: Ultraviolet to Gamma Ray, ed. J.-W. A. den Herder, T. Takahashi, & M. Bautz, Vol. 9905, International Society for Optics and Photonics (SPIE), 399 – 408. https://doi.org/10.1117/12.2235271 [Cited on page 163.]

Tanaka, J., Nogami, D., Fujii, M., et al. 2011, *Publications of the Astronomical Society of Japan*, 63, 911, doi: 10.1093/pasj/63.4.911 [Cited on pages 142 and 144.]

Tandon, S. N., Hutchings, J. B., Ghosh, S. K., et al. 2017a, Journal of Astrophysics and Astronomy, 38, 28, doi: 10.1007/s12036-017-9445-x [Cited on pages 163 and 164.]

Tandon, S. N., Subramaniam, A., Girish, V., et al. 2017b, *The Astronomical Journal*, 154, 128, doi: 10.3847/1538-3881/aa8451 [Cited on pages 163 and 164.]

Tandon, S. N., Postma, J., Joseph, P., et al. 2020, *The Astronomical Journal*, 159, 158, doi: 10.3847/1538-3881/ab72a3 [Cited on pages 163 and 164.]

Tatischeff, V., & Hernanz, M. 2007, *The Astrophysical Journal Letters*, 663, L101, doi: 10.1086/520049 [Cited on page 154.]

Tody, D. 1986, in Society of Photo-Optical Instrumentation Engineers (SPIE) Conference Series, Vol. 627, Instrumentation in astronomy VI, ed. D. L. Crawford, 733 [Cited on page 125.]

Tulloch, S. M., & Dhillon, V. S. 2011, Monthly Notices of the Royal Astronomical Society, 411, 211, doi: 10.1111/j.1365-2966.2010.17675.x [Cited on page 182.]

UKIDSS Consortium. 2012, VizieR Online Data Catalog, II/316 [Cited on page 132.]

Vacca, W. D., Cushing, M. C., & Rayner, J. T. 2003, *Publications of the Astronomical Society of the Pacific*, 115, 389, doi: 10.1086/346193 [Cited on page 126.]

van den Bergh, S., & Younger, P. F. 1987, *Astronomy and Astrophysics Supplement Series*, 70, 125 [Cited on page 130.]

VanderPlas, J. T. 2018, *The Astrophysical Journal Supplement Series*, 236, 16, doi: 10.3847/1538-4365/aab766 [Cited on page 106.]

Venkataramani, K., Ganesh, S., Rai, A., et al. 2019, *The Astronomical Journal*, 157, 199, doi: 10.3847/1538-3881/ab0f26 [Cited on page 7.]

Vogel, M., & Nussbaumer, H. 1994, *Astronomy & Astrophysics*, 284, 145 [Cited on page 163.]

Walkowicz, L. M., & Hawley, S. L. 2009, *The Astronomical Journal*, 137, 3297, doi: 10.1088/0004-6256/137/2/3297 [Cited on page 93.]

Walkowicz, L. M., Hawley, S. L., & West, A. A. 2004, *Publications of the Astronomical Society of the Pacific*, 116, 1105, doi: 10.1086/426792 [Cited on page 102.]

Walkowicz, L. M., Basri, G., Batalha, N., et al. 2011, *The Astronomical Journal*, 141, 50, doi: 10.1088/0004-6256/141/2/50 [Cited on pages 93 and 113.]

Warner, B. 1995, Cambridge Astrophysics Series, 28 [Cited on page 132.]

West, A. A., & Hawley, S. L. 2008, *Publications of the Astronomical Society of the Pacific*, 120, 1161, doi: 10.1086/593024 [Cited on page 102.]

West, A. A., Hawley, S. L., Bochanski, J. J., et al. 2008, *The Astronomical Journal*, 135, 785, doi: 10.1088/0004-6256/135/3/785 [Cited on pages 80, 92, 93, 101, and 109.]

West, A. A., Weisenburger, K. L., Irwin, J., et al. 2015, *The Astrophysical Journal*, 812, 3, doi: 10.1088/0004-637X/812/1/3 [Cited on pages 92, 107, 109, and 114.]

West, A. A., Hawley, S. L., Walkowicz, L. M., et al. 2004, *The Astronomical Journal*, 128, 426, doi: 10.1086/421364 [Cited on page 93.]

Williams, R., & Mason, E. 2010, *Astrophysics and Space Science*, 327, 207, doi: 10.1007/s10509-010-0318-x [Cited on page 138.]

Williams, R., Mason, E., Della Valle, M., & Ederoclite, A. 2008, *The Astrophysical Journal*, 685, 451, doi: 10.1086/590056 [Cited on pages 138 and 139.]

Williams, R. E. 1992, *The Astronomical Journal*, 104, 725, doi: 10.1086/116268 [Cited on pages 11 and 120.]

—. 1994, *The Astrophysical Journal*, 426, 279, doi: 10.1086/174062 [Cited on page 141.]

Woodward, C. E., Banerjee, D. P. K., & Evans, A. 2020a, The Astronomer's Telegram, 13759, 1 [Cited on pages 121 and 149.]

—. 2020b, The Astronomer's Telegram, 14033, 1 [Cited on pages 149 and 152.]

Wright, E. L., Eisenhardt, P. R. M., Mainzer, A. K., et al. 2010, *The Astronomical Journal*, 140, 1868, doi: 10.1088/0004-6256/140/6/1868 [Cited on pages xxviii, 84, 132, and 133.]

Wright, N. J., Newton, E. R., Williams, P. K. G., Drake, J. J., & Yadav, R. K. 2018, *Monthly Notices of Royal Astronomical Society*, 479, 2351, doi: 10.1093/mnras/sty1670 [Cited on pages 92, 113, and 114.]

Yang, H., Liu, J., Gao, Q., et al. 2017, *The Astrophysical Journal*, 849, 36, doi: 10.3847/1538-4357/aa8ea2 [Cited on pages 80 and 93.]

York, D. G., Adelman, J., Anderson, Jr., J. E., et al. 2000, *The Astronomical Journal*, 120, 1579, doi: 10.1086/301513 [Cited on page 84.]

Zamanov, R. K., Bode, M. F., Tomov, N. A., & Porter, J. M. 2005, *Monthly Notices of Royal Astronomical Society*, 363, L26, doi: 10.1111/j.1745-3933.2005.00077.x [Cited on page 69.]

Zamanov, R. K., Stoyanov, K. A., Kostov, A., et al. 2021, Astronomische Nachrichten, 342, 952, doi: 10.1002/asna.202113975 [Cited on pages xix, 30, and 182.]

Zhang, H. L., Graziani, M., & Pradhan, A. K. 1994, *Astronomy & Astrophysics*, 283, 319 [Cited on page 156.]

Zwitter, T., & Munari, U. 2000, An introduction to analysis of single dispersion spectra with IRAF, Asiago monografie ; vol. 1 (Osservatori Astronomici di Padova e Asiago, Dipartimento di Astronomia dell'Universita di Padova) [Cited on page 125.]